



VNIVERSITATIS VALÈNCIA

FACULTAD DE QUÍMICA
Departamento de Química Inorgánica
Instituto de Ciencia Molecular (ICMol)

RETICULAR METAL-ORGANIC FRAMEWORKS FOR SUSTAINABLE APPLICATIONS

PhD Thesis

Programa de Doctorado en Química (RD 99/2011)

Cristina Negro Ruiz

May 2023

Directors:

Dr. Emilio Pardo Marín

Dr. Jesús Ferrando Soria

D. **Emilio Pardo Marín**, Doctor en Química, Profesor Titular e investigador ERC y D. **Jesús Ferrando Soria**, Doctor en Química e investigador Ramón y Cajal, ambos miembros del Instituto de Ciencia Molecular y del Departamento de Química Inorgánica de la Facultad de Química de la Universidad de Valencia.

CERTIFICAN:

Que el trabajo que presenta **Cristina Negro Ruiz** en esta memoria titulada “**Reticular Metal-Organic Frameworks for Sustainable Applications**”, en el marco del programa de doctorado en Química ha sido realizado bajo nuestra dirección en el Instituto de Ciencia Molecular y Departamento de Química Inorgánica de la Universidad de Valencia para optar al título de Doctora en Química.

Y para que así conste, firmamos el presente certificado en Paterna a 10 de Mayo de 2023.

Fdo.: **Dr. Emilio Pardo Marín**

Fdo.: **Dr. Jesús Ferrando Soria**

AGRADECIMIENTOS

Quiero expresar mi agradecimiento a todas las personas que, de una forma u otra, contribuyeron a la realización de esta tesis. Sin su saber y guía crítica, sin su apoyo, sin su afecto, no habría sido posible culminar este trabajo.

En primer lugar, quiero agradecer a mis directores, Emilio y Jesús, cuya supervisión y dedicación fueron determinantes; así como a nuestros colaboradores externos, en especial a Donatella Armentano, Antonio Leyva, José Manuel Herrero y Ernesto Simó, por sus aportaciones en la resolución estructural, ensayos catalíticos y analíticos; y a mis compañeros de laboratorio: Fani, Renato, Paula, Xavi, Nuria, Loli, Nico, Nadia, Marta, Walter y Thais, por los momentos de risas, trabajo, tensión y compañerismo que vivimos.

En segundo lugar, agradezco al grupo *Functional Materials Design, Discovery and Development* por invitarme a realizar mi estancia en KAUST. En especial a Vincent Guillerme por confiar en mi y darme la oportunidad de explorar todo un mundo nuevo, tanto en lo científico como en lo cultural. A Mickaela, Ahlem, Maram, Taslim, Hadi, Rawan y Salma, por acogerme y regalarme una experiencia inolvidable.

Agradezco especialmente a mi pequeña familia del *ICMol*: Abhi, Bella, Lorenzo y Ana, sin vuestra ayuda esto no habría sido posible. A MariLuz, por sus sonrisas y abrazos. A Xuso, por los “dibujitos” que dan vida a esta tesis. A Nadia y Angela, por estar siempre. Y a Alberto, por su contagiosa pasión por la química orgánica y los años compartidos.

Finalmente quiero dar las gracias a mi familia. A mi madre, a mi hermano, y especialmente a mi abuelo, siempre en mi corazón. A Spin mi compañero peludo de vida. A MariCruz por sus bálsamos para el estrés. A Pepa por sus consejos, amor y complicidad. Y sobre todo a mi padre, por enseñarme el “valor” de las cosas y mostrarme que el camino del conocimiento es inagotable y apasionante.

ABSTRACT

The main objective of this thesis is to design and synthesize new multifunctional Metal-Organic Frameworks (MOFs) and multivariate MOFs (MTV-MOFs) for two purposes: first, to reduce the level of pollutants in aquatic ecosystems to meet the acceptable standards set by the World Health Organization (WHO), and second, to use them as heterogeneous catalysts to carry out reactions in a more sustainable way. To achieve this objective, functionalized oxamidato derivatives were used to build high-dimensional MOFs through the metalloligand strategy. In particular, dinuclear Cu^{II} complexes were employed as metalloligands to assemble heterobimetallic three-dimensional (3D) MOFs with functional pores decorated with amino acid residues, which provide flexibility to the framework, thereby influencing the properties and potential applications of these materials.

In general, the following steps were carried out:

- Design and synthesis of oxamidato-based proligands derived from enantiopure natural amino acids that can coordinate Cu(II) to yield *trans*-oxamidato dicopper(II) precursors.
- Synthesis of water-stable oxamidato-based MOFs and MTV-MOFs with different oxamidato precursors, either in polycrystalline powder or in single crystals.
- Study the properties of the MOFs and MTV-MOFs obtained. In particular, investigating the effect of different functional groups to introduce new or improved physical properties.
- Study of their use for capturing pollutants in water and as heterogeneous catalysts, either by synthesizing catalytically active MOFs containing metal complexes using Post-Synthetic Methodologies (PSMs) or by using them as templates to catalyze reactions.

The physical characterization of the obtained materials has been performed using infrared spectroscopy (IR), nuclear magnetic resonance (NMR), thermogravimetric analysis (TGA), powder X-ray diffraction (PXRD), N₂ and CO₂ adsorption, and scanning electron microscopy (SEM). However, the resolution of crystal structures through single crystal X-ray diffraction (SCXRD), as well as studies of catalytic activity and solid-phase extraction (SPE), were carried out in collaboration with other research groups.

For clarity, the thesis is divided into the following sections:

Chapter 1 provides a general context to the materials developed during this thesis, that is, oxamidato-based MOFs. In this chapter, an overview entitled “From Coordination Chemistry to Reticular Chemistry” is presented, which focuses on the increasing interest in the field of MOFs. The most common synthetic and characterization methodologies are also briefly described, and the most remarkable properties of MOFs are discussed, with representative examples described in more detail. Additionally, a particular and emerging type of MOF, the so-called Multivariate MOFs (MTV-MOFs), is highlighted, as it shows unique properties and applications and has played a key role in this thesis. Finally, the related previous work developed within my research group is also described, emphasizing the advantages of using oxamidato-based ligands derived from amino acids to build up 3D MOFs through the metalloligand approach.

Chapters 2 and 3 present the main results obtained during this thesis, which have been collected and published in some important scientific journals. In chapter 2, two objectives were pursued. Firstly, the change in reactivity in organometallic catalysts was studied to reveal the nature of catalytically active species and reaction mechanisms, taking advantage of the steric constraint effects induced by the MOF network. Secondly, drawing inspiration from the active centers of enzymes, where different organic functionalities can act synergetically, the effects on catalytic reactions of industrial

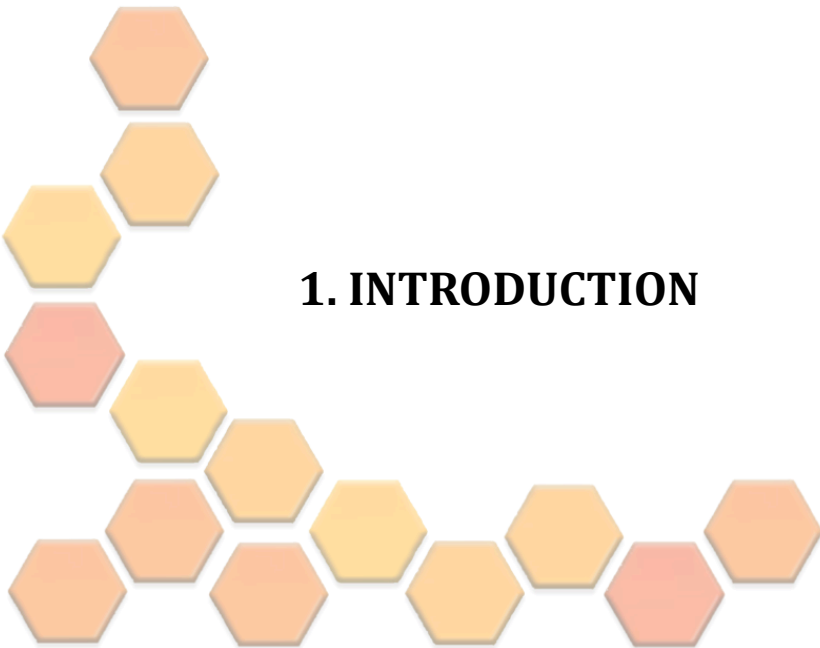
relevance when functional channels are decorated with more than one distinct amino acid residues were explored. In chapter 3, the rich host-guest chemistry of these MOFs was exploited for the efficient capture of some of the most common organic contaminants found in aquatic environments, such as organic dyes and neonicotinoids insecticides (NEOs). The crystal structures of the host-guest aggregates provided evidence of the synergistic interactions between the different functional groups of the MOFs and the guest contaminants, allowing us to understand the exceptional capture properties of these materials.

Finally, **chapter 4** presents the conclusions, as well as plans for future work and perspectives.

Table of Contents

1. INTRODUCTION	13
1.1. General Overview of MOFs	15
1.1.1. From Coordination Chemistry to Reticular Chemistry	15
1.1.2. Properties and Applications of MOFs	19
1.1.3. Biocompatible MOFs	26
1.1.4. Mixed-Component MOFs: Multivariate MTV-MOFs	29
1.1.5. Synthetic Strategies for MOFs	33
1.1.6. Post-Synthetic Methodologies	35
1.1.7. Characterization	37
1.2. Previous Work	40
1.2.1. Oxamato and Oxamidato-Based MOFs	41
1.2.2. Amino Acid-Derived Oxamidato-Based MOFs	48
1.3. Aim of the Thesis	55
1.4. References	60
2. MOFs AND MTV-MOFs FOR CATALYSIS	81
2.1. Introduction	83
2.2. References	85
2.3. Epoxidation vs Dehydrogenation of Allylic Alcohols: Heterogenization of the VO(acac)₂ Catalyst in a Metal-Organic Framework (Publication 1)	86
2.3.1. Introduction	86
2.3.2. Results and Discussion	88
2.3.3. Conclusions	95
2.3.4. References	95
2.4. Exploring the Role of Amino Acid-Derived Multivariate Metal-Organic Frameworks as Catalyst in (Hemi)-Ketalization Reactions (Publication 2)	98
2.4.1. Introduction	98
2.4.2. Results and Discussion	102
2.4.3. Conclusions	108
2.4.4. References	109
3. MOFs AND MTV-MOFs FOR WATER REMEDIATION	113
3.1. Introduction	115
3.2. References	117

3.3. Metal-Organic Frameworks as Unique Platforms to Gain Insight of σ-Hole Interactions for the Removal of Organic Dyes from Aquatic Ecosystems (Publication 3)	118
3.3.1. Introduction	119
3.3.2. Results and Discussion	122
3.3.3. Conclusions	132
3.3.4. References	132
3.4. Highly Efficient Removal of Neonicotinoid Insecticides by Thioether-Based (Multivariate) Metal-Organic Frameworks (Publication 4)	139
3.4.1. Introduction	139
3.4.2. Results and Discussion	142
3.4.3. Conclusions	153
3.4.4. References	154
4. CONCLUDING REMARKS AND PERSPECTIVES	159
5. RESUMEN	167
6. APPENDIX	187
6.1. Index of Abbreviations	189
6.2. List of Publications	193
PUBLICATION 1: Epoxidation vs Dehydrogenation of Allylic Alcohols: Heterogenization of the VO(acac) ₂ Catalyst in a Metal-Organic Framework	195
PUBLICATION 2: Exploring the Role of Amino Acid-Derived Multivariate Metal-Organic Frameworks as Catalyst in (Hemi)-Ketalization Reactions	239
PUBLICATION 3: Metal-Organic Frameworks as Unique Platforms to Gain Insight of σ -Hole Interactions for the Removal of Organic Dyes from Aquatic Ecosystems	265
PUBLICATION 4: Highly Efficient Removal of Neonicotinoid Insecticides by Thioether-Based (Multivariate) Metal-Organic Frameworks	297



1. INTRODUCTION

1.1. General Overview of MOFs

1.1.1. From Coordination Chemistry to Reticular Chemistry

Coordination Chemistry (derived from the Latin word “coordinatio”, meaning “to set in order” or “orderly combination”) is primarily concerned with the arrangement of atoms and molecules in space. A. Werner is credited with laying the foundation of coordination chemistry with his work *Contribution to the Constitution of Inorganic Compounds*, published in 1893,¹ that focused on establishing the geometry of metal ions and ligands in coordination complexes. Later, Hofmann and Küspert introduced the concept of a “framework” in 1897.^{2,3}

In 1916, G. N. Lewis published *The Atom and the Molecule*,⁴ which developed the theory of covalent bonding and popularized the term “coordination polymer” (CPs).⁵ However, the structures of many coordination polymers remained veiled throughout the last century,⁶ as many works reported non-crystalline CPs whose structures were difficult to characterize.^{7,8}

Following the principles of crystal chemistry reported by A. F. Wells in 1954,⁹ the first crystal structure of one-dimensional (1D), two-dimensional (2D), and three-dimensional (3D) networks was reported in 1959.^{10,11} Later, Robson and Hoskins proposed that these CPs, which are extended solid materials with large empty cavities and low densities, may possess accessible spaces while maintaining high thermal, chemical, and mechanical stability.¹²⁻¹⁴ Since then, many Porous Coordination Polymers (PCPs) have been synthesized using rational molecular-level design and characterized using X-ray crystallography. In this context, Reticular Chemistry (derived from the Latin word “reticulum”, meaning “having the form of a net” or “netlike”) has emerged as a promising bottom-up synthetic approach for developing pre-designed extended 2D and 3D frameworks.

1. INTRODUCTION

This approach involves deconstructing a target structure into its building units to determine the net's topology (called "reticular synthesis") and identify molecular constituents that represent these units.¹⁵ Both organic and inorganic components are linked by strong directional bonds, which impart architectural, thermal, and chemical stability in the final assembly.

Linkers are typically organic components bearing strongly coordinating functional groups, such as carboxylates, azolates, phosphates, and catecholates. Thermodynamic control over inorganic synthesis enables obtaining highly symmetric extended structures in a single step, enhancing the rational design and promoting the formation of dense crystals. The high crystallinity of these materials allows their characterization by X-ray or electron diffraction techniques, further proving the effectiveness of this approach.¹⁶

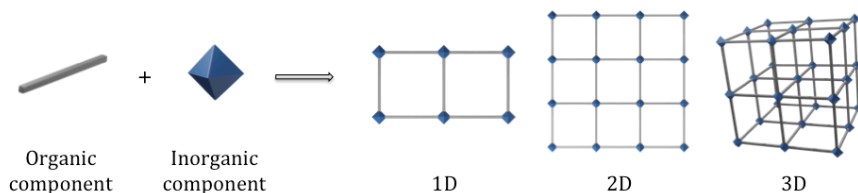


Figure 1. Schematic representation of the components (organic ligands and metal ions/clusters) used to assemble MOFs.

Based on these developments, O. M. Yagui reported the very first reticular material, coined as "Metal-Organic Framework" (MOF),¹⁷ which was initially named PCP by Robson.¹⁸⁻²⁰ Later, S. Kitawaga²¹ demonstrated that it was possible to maintain the network structure after removing the guest molecule.²² However, the surface area and pore volume could not be accurately determined, as the gas sorption experiments were carried out at high pressures.

1. INTRODUCTION

Shortly after, O. M. Yagui demonstrated in MOF-2²³ that MOFs have permanent porosity, by measuring under low pressure and providing the first proof of their porosity.²⁴ Subsequently, MOF-5²⁵ broke records with its extremely high porosity, presenting a higher surface area and pore volume than most porous crystalline zeolites. Soon after, its 16 isorecticular frameworks (IRMOF-1 to IRMOF-16),²⁶ triggered such a strong interest in this field (Figure 2).

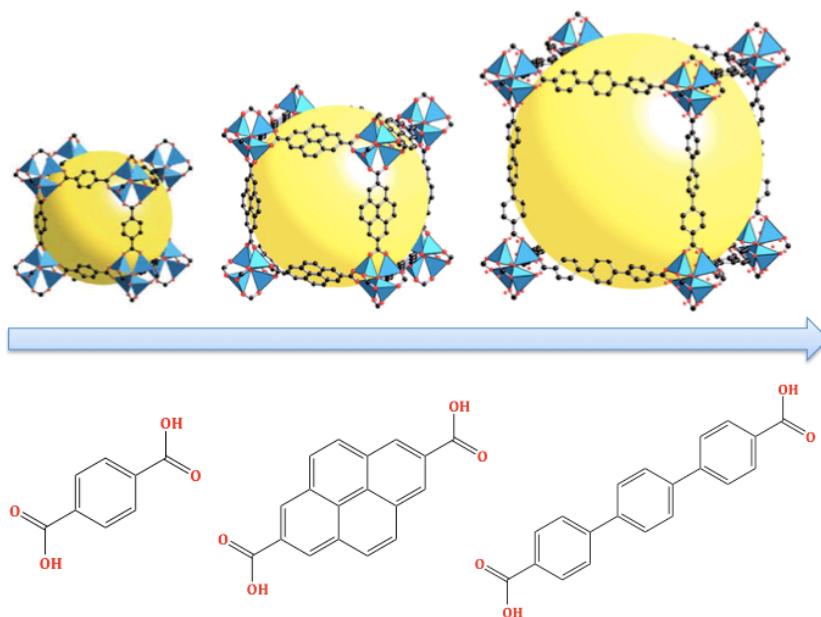


Figure 2. Single crystal X-ray structure of MOF-5 (IRMOF-1; left) and IRMOF-n, where n = 14 (center) and 16 (right). The large spheres represent the largest Van der Waals spheres that could fit in the cavities of the framework.

As previously mentioned, the development of MOFs has greatly benefited from the principles of reticular chemistry. To have control over the design and construction of MOF frameworks, it is essential to understand the structural features of the building blocks that make up the framework. These building blocks can be reduced to nodes (vertices) and linkers (edges) based on the underlying net topology of any periodic structure.²⁷

1. INTRODUCTION

The diversity of building blocks provides endless opportunities for reticular chemistry, and the discovery of new building blocks with specific geometries and connectivities is crucial for designing new materials with different compositions, topologies, and chemical and physical properties.²⁸ It is important to note that, unlike Molecular Building Blocks (MBBs) in general,^{29,30} Secondary Building Units (SBUs) are aggregates of metal ions linked together by multidentate functional groups, such as carboxylates, into clusters.³¹

The modification of building blocks, without altering the underlying topology of the network, has led to the development of “isorecticular” frameworks with the same connectivity/topology but different pore size/functionality. The first example of such frameworks was the previously mentioned series of IRMOFs derived from MOF-5, where multiple components were incorporated.²⁵ Over the years, isorecticular chemistry has been applied to a large number of structures, although the fundamental design principles have remained the same.³²

The expansion and contraction of building blocks rely mostly on organic linkers, which are limited by size constraint, since inserting metal atoms to obtain larger clusters while keeping the same geometry remains challenging. Although expansion can effectively increase pore volume, an excess of it may reduce structural stability and facilitate interpenetration. Thus, it is important to balance pore volume and stability. For example, expanding organic linkers from one to eleven units in the MOF-74 family resulted in an isorecticular family without interpenetration because the structure is based on a 1D rod topology of inorganic building blocks, which prevents structural interpenetration. In most cases, alternatives to reduce interpenetration are needed, such as using more diluted conditions³³ and adjusting reaction times,³⁴ among others.^{35,36} However, for some applications such as gas storage³⁷ and separation³⁸ or catalysis,³⁹ interpenetration might be favorable.

On the other hand, contraction reduces the pore sizes, which is suitable for some applications such as gas separation, as MOFs with small pore sizes allow for selective molecular exclusion and maximize host-guest interactions, increasing stability.⁴⁰

1.1.2. Properties and Applications of MOFs

Undoubtedly, the most prominent class of porous molecular-based materials is MOFs.

In contrast to Supramolecular Chemistry,⁴¹ which involves controlling non-covalent interactions and linking molecules through weak bonds, MOFs are assembled by strong bonds between metal ions and charged linkers. The transition from weak to strong bonds results in improved thermal and chemical stabilities. Consequently, MOFs can withstand temperatures up to 300-400 °C in air, and many of them are stable in acidic, basic, aqueous, and non-aqueous media, often at refluxing temperatures. This allows for organic and inorganic reactions to take place within their pores while retaining their fundamental properties of porosity and crystallinity.⁴²

The wide variety of MOFs is due to the different possibilities of connectivity of the building units. MOFs have exhibited extensive connectivity from 3 to 24 or even infinity for 1D rods and 2D arrays.⁴³ Additionally, the fascinating host-guest chemistry of MOFs can be tuned by fine control over the size, shape, and functionality of their channels. Another important feature is that they can have interconnected pores, which allows for the maximization of their internal surface area. Besides, unlike other porous materials, the crystalline nature of MOFs allows the possibility of using X-ray crystallography to observe what is happening within their channels.⁴⁴

As a result, the developments in the field of MOFs have had a significant impact, with thousands of papers on their synthesis, structure, and applications being published every year.

1. INTRODUCTION

Over one hundred thousand MOF structures have been reported in the Cambridge Structural Database (CSD) since 1995, demonstrating the wide variety of MOFs available.^{45,46}

MOFs have demonstrated excellent performance as platforms for various applications in fields such as gas storage⁴⁷⁻⁴⁹ and separation,^{50,51} catalysis,^{52,53} sensing,⁵⁴ ion-exchange,⁵⁵ conductivity,^{56,57} magnetism,^{58,59} and light⁶⁰ and water harvesting,^{61,62} among others.

Of particular interest in this thesis are catalysis and water remediation, which will be further discussed in the following chapters.

1.1.2.1. Catalysis

The objective of the chemical industry is to transform natural compounds or raw materials into derived compounds with new characteristics or utilities, thus creating greater economic value. In term of cost analysis, minimizing the time and energy required to achieve a certain degree of conversion is crucial. The use of catalysts to accelerate chemical reactions has been applied since ancient times, but it was not until the 19th century that the catalytic phenomenon was recognized and began to be studied in depth.⁶³

By definition, “catalysts” are materials that increase the rate of a chemical reaction without being consumed during the process,⁶⁴ and can be used in subsequent cycles. Additionally, only small amounts of catalysts relative to the substrate are needed, making them even more convenient.⁶⁵ However, this is an “ideal” definition since, in real systems, the catalyst can degrade or reduce its activity, as is the case with the thermal denaturation of enzymes, or it can react irreversibly with impurities, a phenomenon known as catalyst poisoning. Usually, the substrate/catalyst ratio indicates the catalyst efficiency, which is measured as the turnover number (TON) or turnover frequency (TOF).

1. INTRODUCTION

Generally, catalysts are composed of a metal atom stabilized by organic ligands bearing a specific atom with the capability of binding the metal. Additionally, their performance (activity, selectivity, and stability) can be perfectly adjusted by selecting the proper metal, ligand, or process conditions. Aiming to reduce the ecological footprint associated with the traditional use of noble scarce metals (such as Pd, Pt, or Ru) in multiton industrial processes,⁶⁶ further efforts are required to develop novel catalysts based on more abundant and less expensive metals such as transition ones.⁶⁷

Catalysts can be classified into homogeneous and heterogeneous based on the physical phase of the catalyst and the reactants (Figure 3).

In homogeneous catalysis, the catalyst, reactants (also called substrates), and products are in the same phase. One of the biggest advantages of homogeneous catalysts is that the behavior of the catalyst can be studied at a molecular level, thanks to the easy identification of the active species using common spectroscopic techniques such as Infrared (IR) and Nuclear Magnetic Resonance (NMR). However, the main drawback of homogeneous catalysts is the difficulty in separating the catalyst after the reaction, which is why the industry often tries to replace homogeneous with heterogeneous catalysts.⁶⁸

In heterogeneous catalysis, the catalyst and the substrate are in different phases. One important benefit of heterogeneous catalysis is the ease of catalyst recovery by separating it from the substrates or products.⁶⁹ It is worth noting that more than 90 % of the chemical processes use heterogeneous catalysts, including the manufacturing of food and medicines, the production of fabrics, building materials, and almost all the fuels for our transport systems. One example is the Methanol To Gasoline (MTG) process, which uses the zeolite ZSM-5 as a heterogeneous catalyst to synthesize petrol from methanol.⁷⁰

1. INTRODUCTION

Biocatalysis shares certain characteristics of both homogeneous and heterogeneous catalysis. Formally, both the catalyst and the substrate are in the same phase, but due to the large difference in size and the reduced extension of the active center, the way of reacting resembles that of heterogeneous catalysis. The biocatalyst is mainly an enzyme and can catalyze reactions in biological systems, such as living cells. Usually, enzymes can complete 1.000 catalytic cycles in one second, making them highly productive compared to homogeneous or heterogeneous catalysts, which can complete between 100 and 10.000 cycles per hour. Moreover, biocatalytic reactions are often carried out in mild conditions and water because of the enzyme's vulnerability to denaturation. Even though these catalysts are more expensive than homogeneous and heterogeneous ones, they are applied in some industrial processes because of their enormous activity.

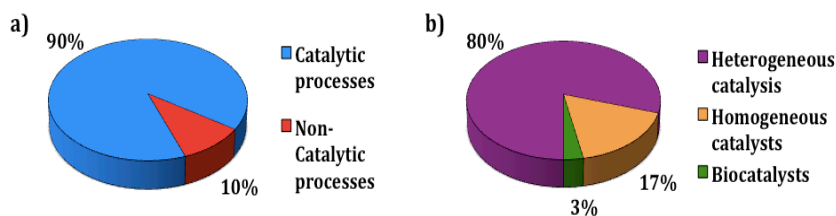


Figure 3. Contribution of catalytic processes to the chemical industry (a) and proportion of heterogeneous, homogeneous, and biocatalysts in the industrial catalytic processes (b).⁷¹

The high surface areas, tunable pore sizes and shapes, and high density of active sites within the very open structures of the MOFs⁷² make them ideal candidates as catalysts for industrial applications. Furthermore, they can be recycled and reused several times, providing important economic and environmental advantages. Indeed, the catalytic applications of MOFs⁷³ were proposed and demonstrated early on.⁷⁴

1. INTRODUCTION

It is known that catalytically active MOFs can be originated either from active sites⁷⁵ of the coordination network, such as Open Metal Sites (OMS) or Coordinatively Unsaturated Sites (CUS), as well as from organic ligands functionalities. Alternatively, MOFs can take advantage of their rich host-guest chemistry by encapsulating catalytic guest species in the pores⁷⁶ (Figure 4).

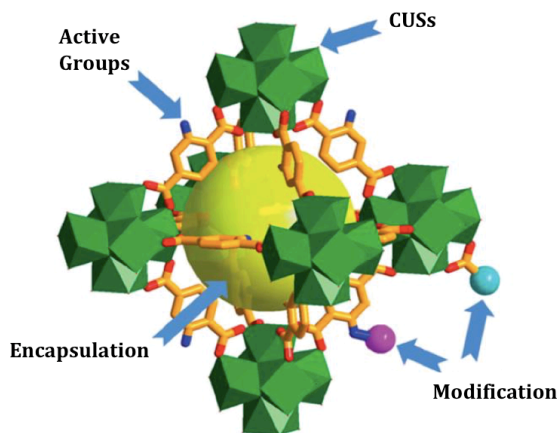


Figure 4. Various possibilities that MOFs offer to locate active sites for catalysis.⁷⁷

Bridging ligands containing active functional groups such as alcohols, amides, amines, carboxylates, and pyridines,^{78,79} as well as metal centers with unsaturated coordination environments, can act as active sites for catalysis.^{80,81} OMS or CUS can be created by removing the coordinated guest solvent molecules without collapsing the framework.⁸² Several MOFs have exploited the presence of OMS, such as HKUST-1,^{83,84} MIL-100,⁸⁵ MIL-101,^{86,87} and UiO-66.⁸⁸ Moreover, the versatility of MOFs allows for the introduction of multiple active sites in their structure, enabling the preparation of multifunctional MOFs.⁸⁹ Additionally, chiral organic ligands can be used to create MOFs with chiral centers, which can exhibit catalytic activity for asymmetric catalysis.⁹⁰

MOFs also serve as excellent platforms for supporting active guest species in their pores, including metal cations,⁹¹ complexes,⁹² small clusters,⁹³ or enzymes,^{94,95} through the use of Post-Synthetic Methodologies (PSMs).⁹⁶

However, despite the vast diversity of MOFs in terms of their structure, composition, and functionality, their potential in catalysis has been underexplored, and more research is needed to fully understand how the chemical and steric environment of the host matrix affects the catalytic activity of guest species.

1.1.2.2. Water remediation

Water is a precious and essential natural resource that sustains life on earth. However, human activities, such as agricultural and industrial practices,^{97,98} have caused water scarcity and pollution, making access to clean water increasingly difficult.⁹⁹ Moreover, with the continuous growth of the world's population and industrial development, the challenge of ensuring sustainable access to clean water for future generations has become even more significant.¹⁰⁰ According to the World Health Organization (WHO), nearly half of the world's population lives in water-stressed regions, and this situation is expected to worsen in the coming decades due to global warming. Therefore, water contamination is one of the most pressing issues that our society currently faces.^{101,102} In fact, providing universal access to clean freshwater is one of the goals of the United Nations' Sustainable Development Agenda. However, although conventional methods for water remediation,¹⁰³ such as adsorption, filtration, precipitation, and biological and chemical processes, are available, they are not always effective, can generate secondary pollutants,¹⁰⁴ and have high operating costs.

Harvesting groundwater and desalination of seawater are two solutions that can help alleviate the world's water crisis.¹⁰⁵ However, these solutions are not always affordable worldwide. Furthermore, desalination plants can potentially become a source of contamination for coastal aquatic ecosystems.

1. INTRODUCTION

Therefore, developing technologies for the removal of contaminants from water is becoming increasingly important¹⁰⁶ to help restore the planet's environmental balance.¹⁰⁷

Common water contaminants can be broadly categorized into inorganic and organic contaminants based on their chemical composition. Inorganic contaminants are generally more persistent in the environment than organic ones and are highly soluble and mobile in water due to their charged nature. Additionally, they can easily accumulate in the human body and the food chain.¹⁰⁸ On the other hand, although organic contaminants are not as persistent as inorganic ones, their continuous production in large amounts in modern societies makes their removal from water streams an important consideration.¹⁰⁹

In the current context, the exceptional features of MOFs¹¹⁰ make them a promising alternative for addressing concerns related to environmental sustainability by removing contaminants from water.¹¹¹ Initially, MOFs were scarcely applied in the field due to water-stability issues of the early MOF generations.¹¹² However, recent studies have overcome this problem, and MOFs have shown potential for use in decontamination protocols.¹¹³⁻¹¹⁵ MOFs have already been employed to remove inorganic pollutants such as heavy¹¹⁶ and radioactive metal ions,^{117,118} inorganic acids, and oxyanions/cations,¹¹⁹ as well as organic pollutants¹²⁰ including organic dyes,¹²¹ Pharmaceutical and Personal Care Products (PPCPs),¹²² herbicides and pesticides,¹²³ and industrial compounds/byproducts. Additionally, MOFs have shown the potential for photocatalytic degradation of pollutants into non-harmful species.¹²⁴ However, the practical application of MOFs is still limited due to challenges in their synthesis, scale-up, and cost-effectiveness. Further research and development are necessary to make MOFs a feasible and cost-effective solution for water decontamination on a larger scale.

1.1.3. Biocompatible MOFs

The interest in exploring the use of MOFs in biologically relevant applications,¹²⁵ including Drug Delivery Systems (DDS),¹²⁶ biosensing, biocatalysis, and imaging,¹²⁷ is increasing each year. The porous nature and host-guest chemistry characteristics, combined with their tailorable and highly specific functionalities, make them ideal candidates for the encapsulation of large molecules such as Active Pharmaceutical Ingredients (APIs)¹²⁸ or endogenous molecules. The resultant degradation of the material within a physiological environment allows for the slow release of drugs.¹²⁹ Moreover, MOFs are not only used to bring drugs into the body, but they can also act as detoxifying agents by removing them.¹³⁰ Hydrophilicity and hydrophobicity are important parameters in drug design,¹³¹ and the tunable nature of MOFs allows them to be modified as needed. Additionally, toxicity issues can be addressed by the synthesis of biodegradable and toxicologically safe materials.

Biocompatible MOFs (BioMOFs)¹³² can be built up by aiming for two goals: the use of non-toxic metals centers (such as Fe(II/III), Zn(II), Ca(II), Mg(II), etc.)¹³³ and low-toxicity organic linkers (like carboxylate,¹³⁴ phosphonate,¹³⁵ and sulfonate¹³⁶ derivatives).¹³⁷ Thus far, using biologically relevant molecules as linkers for MOFs is less common, possibly because many examples of BioMOFs stable in aqueous and buffer conditions are not yet known. Many biomolecules, such as amino acids, oligopeptides, proteins, nucleobases, and saccharides, are naturally good ligands and have recently emerged as building blocks for constructing MOFs that can be either structurally rigid or flexible, which impacts the functional nature of the resulting material. They can have many different metal-binding sites, exhibiting different possible coordination modes, a feature that increases their structural diversity.

1. INTRODUCTION

However, the synthesis of permanently porous and stable MOFs from biomolecules is challenging, in part due to the flexibility of large molecules with high numbers of sp^3 carbons and a limited number of coordination sites.

In particular, there is increasing interest in controlling the synthesis of chiral materials. For example, in the pharmaceutical sector, chirality is crucial since chiral molecules' differently handed forms (enantiomers) can have extremely different effects. A common example is glucose: both enantiomers taste sweet, but the human body can only metabolize the right-handed form. The left-handed one, which is manufactured artificially, is used as a calorie-free sweetener.

The most widely used strategies for obtaining chiral MOFs are: (a) the use of chiral molecules as ligands to build MOFs,^{138,139} (b) the addition of a chiral induction agent (with an asymmetric α -carbon atom) that, although not incorporated into the MOF, can induce chirality,¹⁴⁰⁻¹⁴³ or (c) the use of PSM on MOFs to introduce chiral moieties and transform achiral MOFs into homochiral MOFs.

Due to the importance of using chiral building blocks for constructing chiral MOFs, this thesis takes advantage of the inherent chirality of amino acids (excluding glycine) to design and synthesize chiral MOFs,¹⁴⁴ which have already demonstrated interesting properties for recognition, separation and catalysis.¹⁴⁵

The basic unit of an amino acid consists of an α -carbon atom with an attached amino group and an acid group. They have two common metal binding sites from a coordination perspective: amino nitrogen and carboxylate oxygen atoms. However, other types of metal binding sites can also be present in the side chain residues (Figure 5).

1. INTRODUCTION

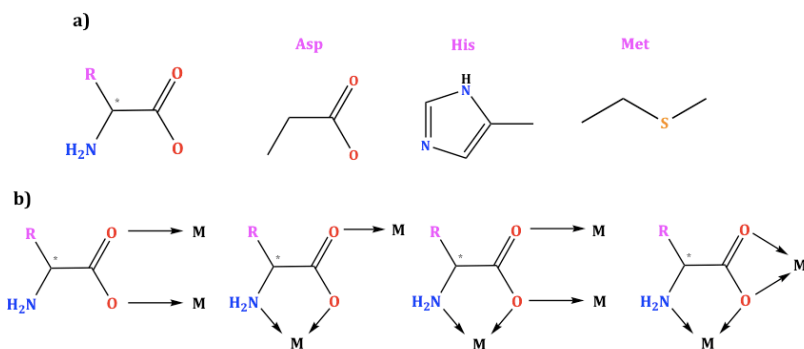


Figure 5. Illustration of the skeleton of a natural amino acid (a) where R is the organic side chain (left), and examples of the R-side chain of some amino acids highlighting potential coordination sites (right). Some of the coordination modes of α -amino acids (b).

Some amino acids have side chains that can coordinate with metal ions, such as the imidazole nitrogen atoms in *L*-histidine (His)¹⁴⁶ or thiolate and thioether sulfur atoms in *L*-cysteine (Cys) and *L*-methionine (Met),¹⁴⁷ respectively. β -carboxylic groups in aspartic acid (Asp)¹⁴⁸⁻¹⁵⁰ and glutamic acid (Glu) can also act as coordination sites.¹⁵¹⁻¹⁵⁴ Amino acids with R-side chains that have metal binding groups can increase the dimensionality of the resulting coordination polymer. Aspartic and glutamic acids, which have two carboxylate groups that can bridge metal ions, are the most common amino acids used to produce 3D MOFs. Natural amino acids can also be modified or incorporated into other organic molecules to extend the dimensionality and potential topologies of homochiral metal ion-amino acid frameworks. For example, phenylalanine (Phe) tends to form 1D and 2D structures, but modifying its phenyl ring with a tetrazole can allow the construction of 3D frameworks.¹⁵⁵⁻¹⁵⁷ In the case of the homochiral MOF of formula $[\text{Ni}_2(\text{L-Asp})_2(4,4'\text{-bipy})]$,¹⁵⁸ neutral chiral Ni(*L*-Asp) layers are connected by 4,4'-bipyridine ligands to form a pillared structure, where the channels are defined by the length of the bipyridine-type spacer, as shown in Figure 6.

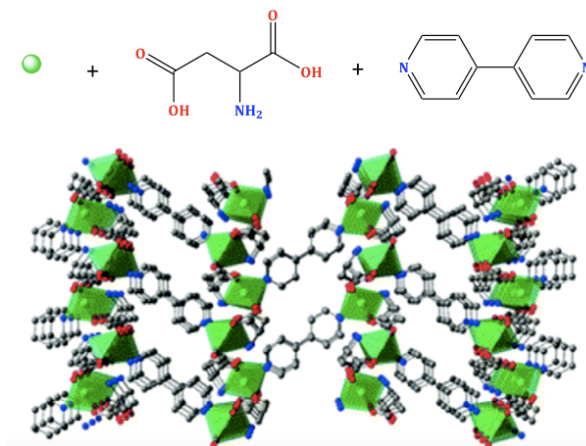


Figure 6. Representation of the pillared homochiral metal-Asp framework $[\text{Ni}_2(\text{L-Asp})_2(4,4'\text{-bipy})]$, showing the channels defined by the length of the bipyridine-type spacer.

Another interesting example is the family of homochiral MOFs based on Zn(II) and pyridyl functionalized valine (Val), alanine (Ala), and threonine (Threo), ranging from hydrophobic to hydrophilic.¹⁵⁹ The pyridyl groups, together with the amino and carboxylate groups of the ligand, connect the Zn(II) metal ions, forming a 3D network, while the remaining side arms can act as functional groups for applications such as sorption, sensing, or catalysis.

1.1.4. Mixed-Component MOFs: Multivariate MTV-MOFs

From a functional materials stand-point, MOFs possess several key features that make them highly useful, including their crystalline nature, chemical and structural diversity, permanent porosity,¹⁶⁰ and the ability to incorporate multiple functional groups that can act synergistically. This leads to unexpected properties that go beyond the sum of each individual component.¹⁶¹

1. INTRODUCTION

Heterogeneity in MOFs can be created by using different organic ligands and/or metal ions/SBUs,^{162,163} resulting in unique properties that are not found in single-component MOFs.¹⁶⁴⁻¹⁶⁷ Depending on the heterogeneity nature, they have been given different names such as mixed-metals MOFs,¹⁶⁸ Multivariate-MOFs (MTV-MOFs)^{169,170} and multicomponent MOFs^{171,172} (Figure 7). In most cases, this variance in functionality is obtained through direct synthesis in one-pot reactions. Nevertheless, different PSMs have also been successfully applied.

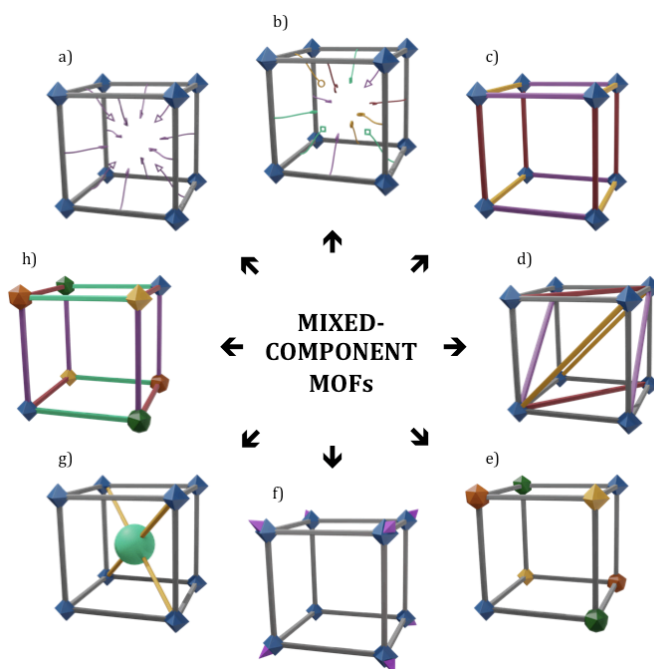


Figure 7. Schematic representation of the different types of mixed-component MOFs: (a) and (b) MTV-MOFs; (c) and (d) multicomponent MOFs; (e) and (f) mixed-metals MOFs and (g) and (h) mixed-ligands and metals MOFs.

There are four main approaches to building heterogeneous systems using metal ions/SBUs: varying the metals in the SBU, inserting different metals into the linkers through coordination bonds (metalloligands), attaching extraneous metals or metal clusters to

1. INTRODUCTION

the original SBUs, and altering SBU connectivity by metal-induced topological transformations. However, generating these MOFs can be challenging due to the sensitivity of SBU formation to synthetic conditions.¹⁷³

In multicomponent MOFs,^{174,175} since the linkers are topologically and compositionally distinct and occupy different crystallographic positions in the network,¹⁷⁶ they can be easily discriminated against and characterized by single-crystal X-ray crystallography.^{177,178} This allows generating complexity without sacrificing order and locating multiple functional groups in predefined positions. However, they have limited heterogeneity, which is intimately ligated to the number of defects/open coordination sites available to install different linkers, and can only accommodate a small number of distinct ligands. So far, this has been reduced to four distinct ligands.¹⁷⁹⁻¹⁸¹ Additionally, these MOFs have emerged as platforms for generating materials with high levels of vacancy defects,¹⁸² which can tune their adsorption properties.^{183,184}

The materials presented in this thesis are relevant to MTV-MOFs, where exceptional functional behavior has been observed.¹⁸⁵ MTV-MOFs allow for the incorporation of multiple types of functional groups and/or metals without altering the connectivity of the underlying structure, meaning that the components occupy topologically equivalent positions. However, assessing bulk purity and homogeneity can be challenging since MTV-MOFs share the same backbone as simple component MOFs. Therefore, it is difficult to differentiate the pure MTV-MOF phase from a mixture of its corresponding simple component MOFs using only Powder X-Ray Diffraction (PXRD). To ensure both the bulk purity and the homogeneity (or heterogeneity) of the MTV-MOFs, high-resolution elemental mapping of organic linkers should be provided by analyzing the interactions between different functionalities using advanced Solid-State NMR (SSNMR) and advanced fluorescent spectroscopic techniques.^{186,187}

1. INTRODUCTION

The MTV approach was first demonstrated by introducing up to eight different functional groups (-NH₂, -Br, -(Cl)₂, -NO₂, -(CH₃)₂, -C₄H₄, -(OC₃H₅)₂ and -(OC₇H₇)₂) into MOF-5 (Figure 8) by one-pot synthesis from equimolar amounts of the linkers. This led to a heterogeneous arrangement of functional groups throughout the ordered backbone of the framework with an enhancement in selectivity for sorption of CO₂ over CO compared to its single-linker analogs. Moreover, in the case of MTV-MOF-5-ABCD, it was demonstrated that the linker ratio could be controlled by modifying the reaction stoichiometry.¹⁸⁸

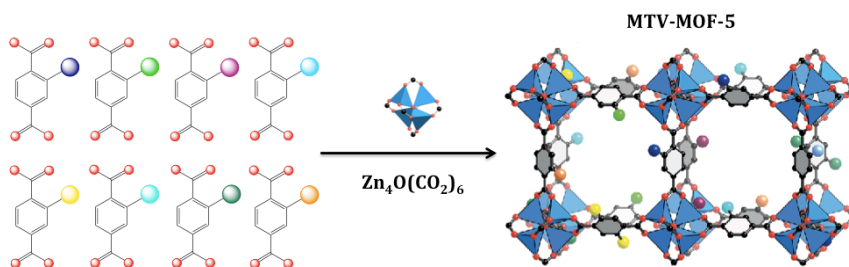


Figure 8. Schematic representation of the MTV-MOF-5 structure showing the multivariate arrangements of different functional groups.

Later on, the generality of the synergistic effects was confirmed for MTV-MOF-177, where a 25 % increase in volumetric H₂ uptake over linear combinations of single-linker analogs was observed.¹⁸⁹

Multimetal MTV-MOFs have also been reported. For example, ten different metals were introduced into the rod building blocks of MOF-74 (Figure 9).¹⁹⁰

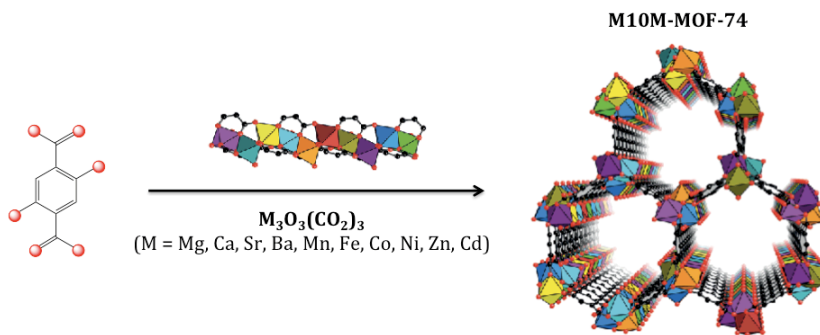


Figure 9. Schematic representation of the MTV-MOF-74 structure showing the multivariate arrangements of different metal ions.

In particular, this thesis focuses on the construction of MOFs with distinct organic linkers possessing identical backbones (same length, geometry, and connectivity), but different substituents and functionalities.^{191,192}

1.1.5. Synthetic Strategies for MOFs

Every new reticular structure begins with its synthesis.¹⁹³ Specifically, MOFs can be prepared as single crystal or polycrystalline powders, and at laboratory (milligram to gram quantities) or industrial (multi-ton quantities) scales.¹⁹⁴ Although the ideal way to prepare MOFs is at ambient pressure and temperature, as it allows for easier isolation without energy consumption, this is not always possible and may lead to poor crystallinity and reproducibility.¹⁹⁵ In order to obtain the desired phase purity and crystal size, several important parameters need to be tuned, including the fundamental characteristics of the starting materials (such as geometry and connectivity of organic ligand and coordination preferences of the metal ions), molar ratios, temperature, concentration, pH of the solution, presence or absence of modulators¹⁹⁶ or other organic ligands, polarity and boiling point of the solvents, and reaction time.

MOFs are typically synthesized by precipitating a metal salt with a multitopic organic ligand in solution.¹⁹⁷

1. INTRODUCTION

Ideally, the synthesis is solvent-free, allowing the organic linker to act as both a reagent and a solvent.¹⁹⁸ Metal-ligand dynamic bonds are crucial for forming ordered and crystalline materials, since they can be repeatedly formed and broken to correct any disorder or premature structure termination. Thus, small variations in the reaction mixture can have a significant impact on the final product. For example, combining a metal chloride (MCl_x) with a carboxylic acid can produce HCl as a byproduct, which can dissolve the MOF and affect crystal growth. In contrast, using a metal acetylacetonate ($M(acac)_x$) produces the milder byproduct acetylacetone.¹⁹⁹

Conventional synthesis refers to reactions carried out by conventional heating. Based on the temperature range, they can be divided into direct precipitation (temperature below or at the boiling point of the solvent at ambient pressure) and solvothermal (temperature above the boiling point of the solvent) methods. In the first case, different methods can be used, such as slow evaporation of the solvent at reduced temperature, controlled cooling, layering, or slow diffusion of the reagents through a membrane, a gel, or an H-shaped tube.²⁰⁰ Direct precipitation is a low-cost and versatile technique due to the mild conditions. However, higher density phases can be obtained upon heating, as the temperature provides energy to overcome the activation energy barrier to the assembly of a certain framework, with a direct influence on the product formation. In this regard, solvothermal methods, which have become increasingly popular,²⁰¹ are based on mixing the precursors diluted in polar solvents (*e.g.*, DMF, DEF, and DMSO) in hermetically sealed vials and heating above their boiling point, generating autogenous pressure. Although the solubility of the precursors is not needed at the beginning, they should become soluble when reaching the target temperature.

Alternatively, there are other synthetic routes that increase heating efficiency and reduce crystallization time, such as electrochemical,^{202,203} microwave-assisted,^{204,205} mechanochemical,^{206,207} or sonochemical methods.^{208,209}

Conventional hydrothermal and microwave-assisted hydrothermal approaches are the most commonly applied, while electrochemical, mechanochemistry, and ultrasound-assisted methods are relatively new. Other techniques involving the use of additives, such as ionic liquids^{210,211} or surfactants,²¹² have also been reported.

Despite zeolites being preferred as heterogeneous catalysts, adsorbents, and ion exchangers,²¹³ MOFs have become the most extensively studied family of porous materials in recent years, with a large number of patents reported, especially at the lab scale. Furthermore, they have been shown to be reusable adsorbents, making them highly attractive from environmental and industrial perspectives. Today, it is a reality that a small number of MOFs are being produced and applied in industrial applications with better performance compared to other porous materials, such as in the storage and secure handling of toxic gases.²¹⁴ Some examples of MOFs that have already been synthesized and marketed on a scale-up production level are HKUST-1,²¹⁵ ZIF-8, MIL-100, MIL-53,²¹⁶ and UiO-66.²¹⁷ However, this is not the general trend, and despite the remarkable advances that have been made, the widespread development of large-scale MOF production and shaping requires intensive attention to fully unleash the potential of MOFs.^{218,219} To achieve this, synthetic procedures should be optimized to use the minimum amount of solvents, to be cost-effective, and environmentally friendly, such as using water if the desired material is stable on it. Additionally, when considering MOFs' industrial scale production, costs and overall production time must be taken into account.

1.1.6. Post-Synthetic Methodologies

Alternative to direct synthetic methods, post-synthetic (PS) methods offer many possibilities for developing novel MOFs. PS methodologies (PSMs) can be applied to modify the pore of the MOF to introduce the desired properties into its backbone without altering the topology.²²⁰⁻²²²

1. INTRODUCTION

This approach allows for the heterogeneous functionalization of pre-synthesized MOFs, leading to improved or new chemical/physical properties, and even affording new materials that are difficult to obtain by direct synthesis.²²³ Furthermore, it is highly recommended that PSMs are applied in a Single-Crystal to Single-Crystal (SC to SC) manner, something that can only be done with MOFs, given their high crystallinity.²²⁴

The concept of PSM was first described in 1990,¹³ and since then, this area has witnessed continuous growth. Several design strategies for the modification and exchange, as well as insertion and polymerization of building blocks, have been described in the literature.²²⁵ It has also been demonstrated that the use of PSM offers the possibility of using the pores of the MOFs as templates to synthesize functional species. Recently, the influence of the solvent choice on PSMs was reported.²²⁶

The most extensively studied PSMs performed in MOFs are briefly described below:

- The PS covalent functionalization of organic linker targets to introduce chemical groups into pre-synthesized MOFs. These PSMs have been proven to successfully introduce new functionalities and properties while maintaining the crystallinity and porosity of the MOF.²²⁷
- In PS Deprotection (PSD), the protective functional group in the organic linker is removed after its synthesis to uncover an underlying chemical group.²²⁸
- PS Polymerization (PSP) can be carried out by multiple organic reactions to connect the ligands within each other²²⁹ or by growing the polymer on the surface or within the channels of the MOF.²³⁰
- In PS Insertion (PSI)^{231,232} and PS Exchange (PSE),^{233,234} formation of dative bonds such as metal-ligand bonds is produced. In particular, the Solvent-Assisted Linker Exchange (SALE) or Incorporation (SALI)²³⁵ refers to the replacement or introduction

of the ligand with a new functional group, while in the case of anionic frameworks, cation exchange or transmetallation refers to the replacement of a metal.²³⁶ However, the process is strongly influenced by diffusion and size effects because the exchange occurs especially in the pores. The exchange of anions is more difficult, and sometimes the use of acids is needed.

Cation exchange, based on the replacement of the extra-framework cations connected to the anionic framework²³⁷ or inside the pores,²³⁸ has been long studied in zeolites,²³⁹ molecular cages,²⁴⁰ and more recently in PCPs.^{241,242} The metal exchange reactions often follow the Irving–Williams series, and especially, with bivalent transition metal ions, the stability increases across the period (Mn(II) < Fe(II) < Co(II) < Ni(II) < Cu(II) > Zn(II)).^{243,244} In addition, it is important to consider the Jahn–Teller effect for Cu²⁺ octahedral or square-planar coordination.²⁴⁵

Transmetallation is based on the partial or full replacement of the SBU or metal nodes with a metal precursor. Ions with higher charge or smaller size form stronger bonds²⁴⁶ and are easily incorporated.²⁴⁷⁻²⁵⁰ However, this process is not only influenced by the liability of the exchanged metal ion but also by the valence and coordination of the incoming metal ion, the flexibility of the framework,²⁵¹ and the nature of the solvents.^{252,253}

It is worth noting that the simultaneous exchange of the inorganic and organic components in a MOF represents the highest level of complexity among PSMs. However, there are relatively few examples of this degree of complexity.²⁵⁴

1.1.7. Characterization

To gain insight into the behavior of reticular materials, it is crucial to characterize their physical and chemical properties using a combination of various techniques. Accurate evaluations require the

1. INTRODUCTION

analysis of properly activated samples, taking into account the porous nature of these materials.^{255,256}

Next, we will describe the techniques that are commonly employed, many of which form the basis of the characterization techniques used in this thesis.

Scanning and Transmission Electron Microscopy (SEM and TEM) are commonly used to study crystal size, morphology, and elemental composition.^{257,258} However, it should be noted that these techniques are not quantitatively accurate for elemental analysis, as it is obtained from the detection of characteristic X-rays from the surface of the sample (Energy-Dispersive X-ray analysis (EDX)). Consequently, for a more accurate characterization of the weight percent of metal, carbon, hydrogen, nitrogen, and sulfur, Inductively Coupled Plasma-Optical Emission Spectroscopy (ICP-OES) or Mass Spectrometry (ICP-MS) and Elemental Analysis (EA) are required.

Nuclear Magnetic Resonance (NMR) spectroscopy is typically used to determine bulk purity, linker ratios, and detect/quantify impurities. However, often the previous digestion of the material is required since many MOFs are not soluble in NMR solvents.²⁵⁹ Solid-State NMR (SS-NMR) spectroscopy^{260,261} can also be used not only to study the chemical state of a specific functional group inside a MOF^{262,263} but also to understand the supramolecular interactions and kinetics of guest molecules inside a MOF.²⁶⁴

Thermogravimetric Analysis (TGA) is used to quantitatively determine the water content and thermal stability of a sample by measuring the mass loss over time when it is heated at a constant rate.^{265,266} There are two characteristic steps: one at low temperatures (*ca.* < 300 °C) corresponding to the desorption of trapped solvent (near the solvent boiling point), and the other at a higher temperature, which indicates framework degradation.

1. INTRODUCTION

Atomic Force Microscopy (AFM) allows for monitoring the evolution of a single crystal during its growth.²⁶⁷ Dynamic Light Scattering (DLS) and Fluorescence Correlation Spectroscopy (FCS)²⁶⁸ are typically used to determine the size distribution, while Small Angle and Wide Angle X-ray Scattering (SAXS/WAXS)²⁶⁹ are used to study anisotropy.

According to the classic postulate of crystallography, “only one single chemically sound crystal structure exists that is compatible with the observed diffraction data”.²⁷⁰ Therefore, the crystal structure is considered the most important information for a general description of materials at the atomic level. In this regard, since the beginnings of reticular chemistry, crystal structure analysis has relied on Single-Crystal X-Ray Diffraction (SCXRD). SCXRD also allows the study of host-guest interactions resulting from sorption processes.^{271,272} However, the limiting factor is the size and the quality of the crystal. Synchrotron radiation is used when the crystals are too small or intergrown.²⁷³ Later on, the development of Low-Dose Electron Diffraction (LD-ED) revolutionized the field of single-crystal diffraction since crystal size was no longer a problem.²⁷⁴ However, despite its great potential, this technique is not yet widely accessible and, consequently, cannot be applied routinely like SCXRD.

Powder X-Ray Diffraction (PXRD) is a useful technique for studying MOFs when it is difficult to obtain single crystals. PXRD provides information about crystal size, crystallinity, and phase purity of the material. The experimental diffraction pattern should match with the calculated pattern, and all reflections that do not match should be assigned to identify contaminants, unreacted starting compounds, or byproducts (ideally). Variable Temperature PXRD (VT-PXRD)²⁷⁵ is also used in the study of dynamic reticular structures and phase change.²⁷⁶ Additionally, it is interesting to note that the interpenetration of MOFs can make crystallographic characterization very challenging, although interpenetrated MOFs often exhibit better diffraction since they are denser and have less void space.²⁷⁷

Since MOF structures are composed of crystalline networks with voids, they were expected to possess the inherent capability to be permanently porous. In this regard, architectural stability is an important feature of the framework, as flexibility allows for reversible structural transformation, providing unique properties to MOFs over other conventional porous materials (such as zeolites and active carbons). However, the more reversibility the less chemical robustness.²⁷⁸ Although thermal stability is lower than that of zeolites and active carbons, weak bonds such as hydrogen bonds, π - π stacking, or Van der Waals interactions make it easier for the repeatable uptake and release of guests without stressing the backbone structure. Reversible sorption measurements²⁷⁹⁻²⁸¹ are used to confirm the permanent porosity and to calculate the surface area and pore volume. For this purpose, monatomic gases (such as He, Ne, Ar, Kr, Xe, and Rn), diatomic gases (such as N₂, O₂, and H₂), or polyatomic gases (such as CO₂, H₂S, H₂O, and hydrocarbons), can be used, with nitrogen (N₂) being the most commonly employed. The pore size and its distribution are experimentally determined from the isotherm profile. Sometimes, the observation of hysteresis in the isotherm behavior is indicative of the framework's flexibility, which has great potential for gas separation applications.²⁸²

However, sorption measurements are strongly influenced by theoretical models, approximations, and the accuracy of the parameters, such as pore shape, size, and the main interactions between adsorbent and adsorbate.²⁸³ Therefore, many other complementary techniques are used for studying porosity, such as SAXS analysis,²⁸⁴ porosimetry measurements by mercury intrusion-extrusion cycles,²⁸⁵ and Positron Annihilation Lifetime Spectroscopy (PALS),²⁸⁶ among others.

1.2. Previous Work

MOFs have garnered significant attention in recent decades due to their high crystallinity, exceptional porosity, high modularity, and diverse functionality.^{287,288}

The chemistry of MOFs has traditionally been associated with carboxylate-based ligands, as evidenced by the large number of reported MOFs with such linkers.²⁸⁹⁻²⁹¹ This is mainly due to the fact that metal-carboxylate bonds are stronger than the traditional coordination bonds with pyridine-based ligands commonly used in first coordination polymers. However, in recent years, different types of ligands have emerged as viable and competitive alternatives for building robust and functional MOFs. This has been exemplified by research conducted with oxamato and oxamidato derivatives in the group where I have performed my PhD thesis.

1.2.1. Oxamato and Oxamidato-Based MOFs

The oxamato- and oxamidato-based proligands exhibit interesting characteristics. Firstly, they can adopt bidentate and bis-(bidentate) coordination modes to form mono-, bi-, or polynuclear^{292,293} metal complexes in either *cis* or *trans* conformation (Figure 10).²⁹⁴ The multiple coordinating sites, including both carbonyl and amide groups, allow for very versatile chemistry.

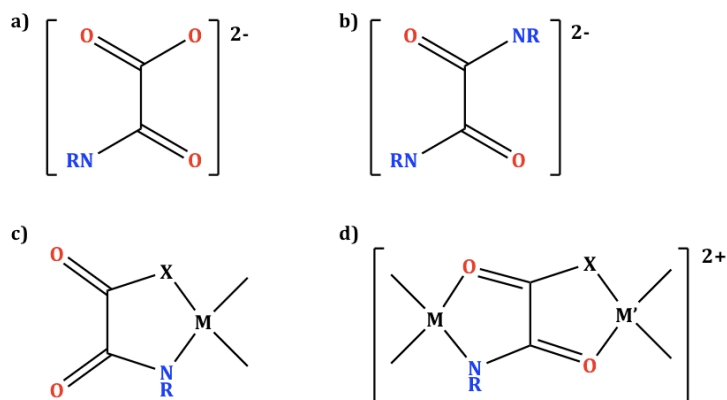


Figure 10. Top: Oxamate (a) and oxamidate (b) dianions. Bottom: Mono- (c) and dinuclear complexes (d). R = aromatic or aliphatic substituents, X = O or NR, and M, M' = divalent metal ions.

1. INTRODUCTION

Secondly, they exhibit strong electron-donating capacity and excellent coordination affinity towards divalent first-row transition metal ions, such as Cu^{II}, Ni^{II}, Co^{II}, and Mn^{II}, forming highly stable complexes in solution. In addition, the free carbonyl-oxygen atoms can bind other divalent transition or alkaline earth metal ions (Sr^{II}, Ca^{II}, and Ba^{II}), forming heterobimetallic MOFs. Thirdly, the bis(bidentate) oxamate and oxamidate bridges mediate magnetic interactions between the neighboring paramagnetic metal ions, allowing for long-range magnetic ordering,²⁹⁵ Single-Molecule Magnet (SMM)²⁹⁶ or Single Chain Magnet (SCM)^{297,298} behaviors. Notably, oxamidate bridges allow stronger magnetic interactions between metal centers than oxalate, due to the lower electronegativity of nitrogen atoms compared to oxygen ones. Finally, they are chiral molecules and their chirality can be transferred to their derivate structures to build chiral MOFs.

Going back to the origins, the exciting properties of oxamato-based linkers in molecular-based magnetism, when acting as bridging ligands between transition metal ions, provoked significant interest and development in the field.²⁹⁹ Since then, a wide variety of oxamato-based compounds, including both discrete complexes (0D) and extended nD (n = 1-3) structures with different interesting properties, have been reported.³⁰⁰ Also, Journaux's and Lloret's groups extended this knowledge to oxamidato analogs, using aliphatic or aromatic bis(oxamidato)-copper(II) complexes as metalloligands toward other metal ions,^{301,302} demonstrating that the structure and function of bis(oxamato)/bis(oxamidato) complexes can be controlled by the steric and/or electronic effects of simple alkyl or aromatic substituents attached to the nitrogen donor atom and/or variation donor-atom of the ligands. Initially, 1D compounds³⁰³ were obtained, and later, they focused on the preparation of 2D and 3D structures to increase *T_c* towards higher temperatures.³⁰⁴

1. INTRODUCTION

It is worth noting that the use of *N, N'*-bis(substituted)oxamides improves their solubility since oxamide is insoluble in common solvents, and avoids the hydrolytic reaction that occurs under deprotonation, producing oxalato. Therefore, in the last few decades, the *N, N'*-bis(substituted) oxamate/oxamide ligands have played an important role in the rational design of a wide variety of mono-, di-, and trinuclear complexes.^{292,305}

For instance, heterobimetallic 1D chains with SCM behavior were obtained by using dianionic oxamate-containing mononuclear copper(II) complexes, $[\text{CuL}_2]^{2-}$, as bis(bidentate) metalloligands.^{297,298} Furthermore, the influence of the length of the alkyl-substituents in the aromatic ring of the oxamate ligands and the use of different divalent ions were studied, resulting in high dimensionality compounds (2D and 3D CPs) with long-range magnetic ordering (Figure 11).²⁹⁵

1. INTRODUCTION

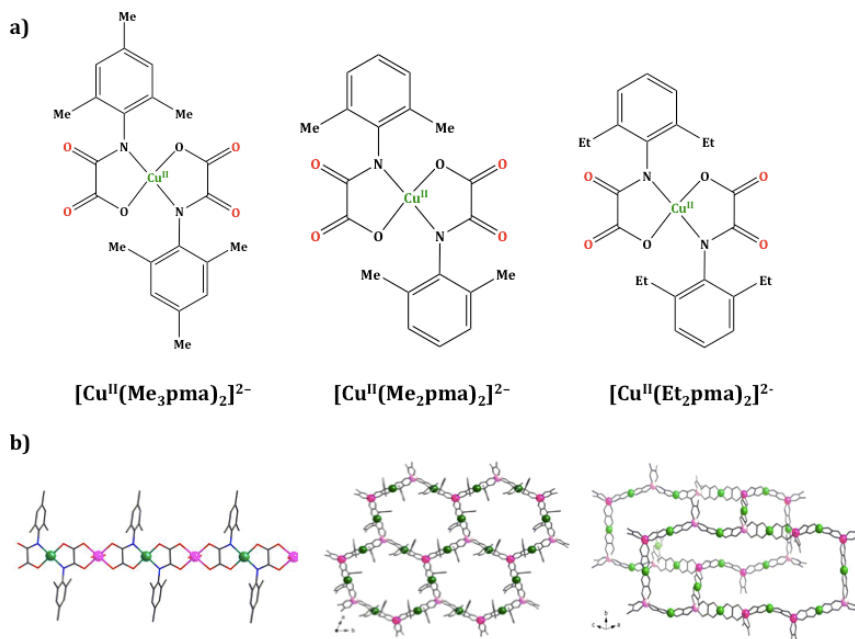


Figure 11. Mononuclear copper(II) complexes $[\text{Cu}^{\text{II}}\text{L}_2]^{2-}$ (a) and perspective view of a fragment of 1D ($\{[\text{Co}^{\text{II}}\text{Cu}^{\text{II}}(\text{Me}_3\text{pma})_2(\text{H}_2\text{O})_2] \cdot 4\text{H}_2\text{O}\}_n$), 2D ($(\text{n-Bu}_4\text{N})_4[\text{Mn}^{\text{II}}_4\text{Cu}^{\text{II}}_6(\text{Me}_2\text{pma})_{12}] \cdot 2\text{dmsO}$), and 3D ($(\text{n-Bu}_4\text{N})_4[\text{Mn}^{\text{II}}_4\text{Cu}^{\text{II}}_6(\text{Et}_2\text{pma})_{12}]$) CPs obtained (b). Me_3pma = *N*-2, 4, 6- trimethylphenyloxamate, Me_2pma = *N*-2, 6- dimethylphenyloxamate, Et_2pma = *N*-2, 6- diethylphenyloxamate and $\text{n-Bu}_4\text{N}^+$ = tetra-*n*-butylammonium cation. Cu and Mn atoms are represented by green and purple, respectively.

In the case of anionic dinuclear copper(II) complexes, $[\text{Cu}_2\text{L}_2]^{4-}$, with π -conjugated phenylene spacers, as tetrakis(bidentate) metalloligands towards M(II) ions, high dimensionality magnetic MOFs were obtained in 1D, 2D, or 3D (Figure 12).³⁰⁶⁻³⁰⁸

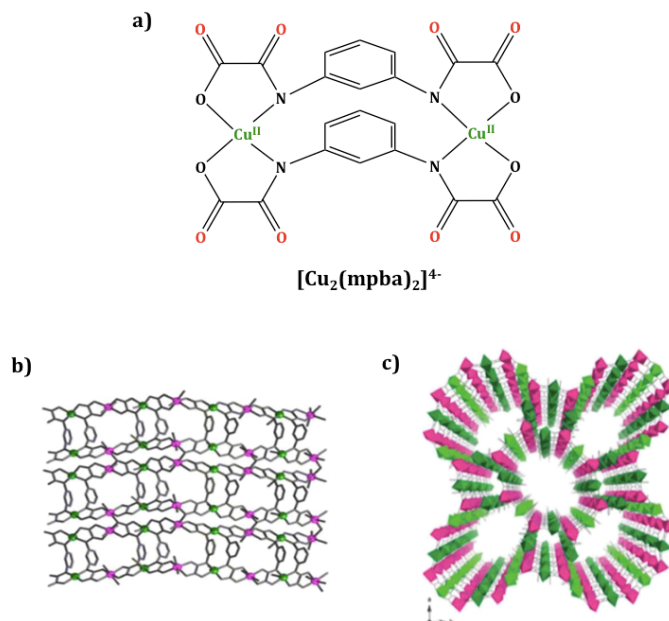


Figure 12. Dinuclear copper(II) complex $[\text{Cu}^{\text{II}}_2\text{L}_2]^{4-}$ (a) and perspective view of a fragment of 2D $[\text{Mn}_4\text{Cu}_4(\text{mpba})_4(\text{H}_2\text{O})_9] \cdot 14\text{H}_2\text{O}$ (b) and 3D $[\text{Na}(\text{H}_2\text{O})_4]_4\{\text{Mn}_4[\text{Cu}_2(\text{mpba})_2(\text{H}_2\text{O})_4]_3\} \cdot 56.5\text{H}_2\text{O}$ (c) CPs obtained. mpba = *N, N'*-1, 3-phenylenebis(oxamate). Cu atoms are represented by green spheres, while Mn or Co atoms are represented by purple spheres.

Another powerful approach to introduce or enhance physical properties in a preformed MOF is the use of PSMs, such as metal substitution (transmetallation) or the exchange of guest molecules hosted in the pores. Metal exchange may involve metal nodes and/or countercations residing within the MOF cavity. In the case of the anionic MOF $\text{Na}^+_4\{\text{Mn}^{\text{II}}_4[\text{Cu}^{\text{II}}_2(\text{Me}_3\text{mpba})_2]_3\} \cdot 60\text{H}_2\text{O}$ [$\text{Me}_3\text{mpba}^{2-} = N, N'$ -2, 4, 6-trimethyl-1, 3-phenylene-bis(oxamate)], the replacement of the Na^+ ions hosted in the channels by Li^+ or K^+ ions through SC to SC process improved both the gas adsorption and magnetic properties (Figure 13).³⁰⁹ Moreover, the possibility to perform PS ion exchange is one of the interesting properties of anionic or cationic MOFs that do not have neutral frameworks.

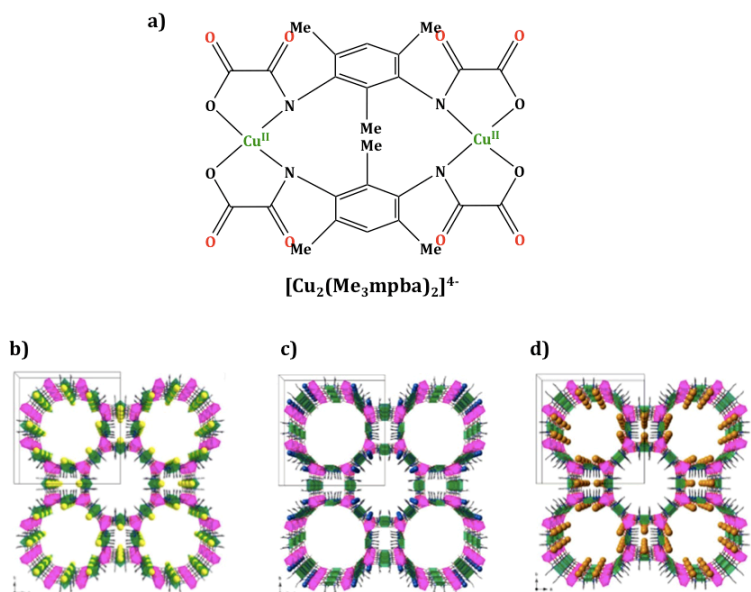


Figure 13. Dinuclear copper(II) complex $[\text{Cu}^{\text{II}}_2\text{L}_2]^{4-}$ (a) and perspective view of the 3D anionic networks along the crystallographic c axes, illustrating the cation exchange process of the Na(I) ions in $\text{Na}^4_4\{\text{Mn}^{\text{II}}_4[\text{Cu}^{\text{II}}_2(\text{Me}_3\text{mpba})_2]_3\} \cdot 60\text{H}_2\text{O}$ (b) with Li(I) or K(I) cations to obtain $\text{Li}^4_4\{\text{Mn}^{\text{II}}_4[\text{Cu}^{\text{II}}_2(\text{Me}_3\text{mpba})_2]_3\} \cdot 68\text{H}_2\text{O}$ (c) and $\text{K}^4_4\{\text{Mn}^{\text{II}}_4[\text{Cu}^{\text{II}}_2(\text{Me}_3\text{mpba})_2]_3\} \cdot 69\text{H}_2\text{O}$ (d). $\text{Me}_3\text{mpba}^{2-} = N, N'-2, 4, 6$ -trimethyl-1, 3-phenylenebis (oxamate). The pink and green spheres represent the Mn(II) and Cu(II) atoms from the covalent framework respectively, while the yellow, blue, and orange spheres stand for the Na(I), Li(I), and K(I) counterions, respectively.

Another example is the anionic MOF $\text{Ni}^{\text{II}}_2\{\text{Ni}^{\text{II}}_4[\text{Cu}^{\text{II}}_2(\text{Me}_3\text{mpba})_2]_3\} \cdot 54\text{H}_2\text{O}$ [$\text{Me}_3\text{mpba}^{4-} = N, N'-2, 4, 6$ -trimethyl-1, 3-phenylene-bis (oxamate)] obtained by transmetallation of Mg(II) ions with Ni(II) on $\text{Mg}^{\text{II}}_2\{\text{Mg}^{\text{II}}_4[\text{Cu}^{\text{II}}_2(\text{Me}_3\text{mpba})_2]_3\} \cdot 45\text{H}_2\text{O}$, to encapsulate and stabilize Fe(III) and Ru(III) species in the pores through strong interactions, and therefore, enable its use in catalysis. Firstly, the transmetallation of the Mg(II) ions with Ni(II) ions improved the robustness of the MOF.³¹⁰ Secondly, Fe(III) and Ru(III) species were incorporated by SC to SC through solid-state PSE of the Ni(II) atoms hosted in the pores, resulting in improved structural stability, crystallinity, and porosity,

1. INTRODUCTION

as well as long-range magnetic ordering due to the substitution of diamagnetic Mg(II) ions by paramagnetic Ni(II) ions.

The same anionic MOF $\text{Mg}^{\text{II}}_2\{\text{Mg}^{\text{II}}_4[\text{Cu}^{\text{II}}_2(\text{Me}_3\text{mpba})_2]_3\} \cdot 45\text{H}_2\text{O}$ was used as a template for the synthesis of sub-Nanometric Pd₄ Clusters (sMCs)⁹³ with mixed-valence oxidation states, stabilized and homogeneously organized within the MOF structure, for catalytic applications. For this purpose, three consecutive PS steps were carried out: transmetallation of the Mg(II) ions with Ni(II) ions, cation exchange of the Ni(II) cations of the pores by $[\text{Pd}^{\text{II}}(\text{NH}_3)_4]^{2+}$, and reduction. This approach demonstrated that the confinement of metal ions within MOF channels enables control over the formation of these small metallic species, which have potential in catalytic applications (Figure 14).

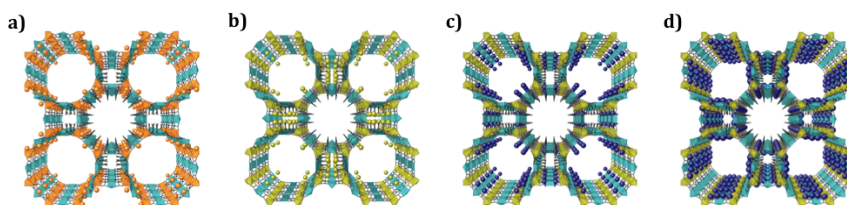


Figure 14. Perspective views of the 3D anionic $\text{M}^{\text{II}}_4\text{Cu}^{\text{II}}_6$ structures transitioning from transmetallation (a) to (b), followed by the exchange of the Ni^{II} cations in the pores with $[\text{Pd}^{\text{II}}(\text{NH}_3)_4]^{2+}$ (c) and the final reduction process (d). The green, orange, and purple polyhedra represent the Cu, Mg, and Ni atoms in the coordination network and the orange and purple spheres stand for the Mg and Ni atoms occupying the channels.

Taking advantage of the opportunities provided by oxamato chemistry, our research group has obtained a wide variety of high-dimensional magnetic³¹¹ and multifunctional³¹² oxamato and oxamidato-based MOFs. These materials have demonstrated remarkable resistance to various solvents and conditions, while maintaining their structure integrity and crystallinity. As a result, it is easy to insert and stabilize active catalytic species within their channels using PSM processes.³¹³

In this context, our group has recently focused on preparing new multifunctional materials that are environmentally sustainable and have potential for bio-applications. To this end, we have been working on synthesizing oxamidato-based MOFs from enantiopure amino acids.³¹⁴⁻³¹⁶

1.2.2. Amino Acid-Derived Oxamidato-Based MOFs

As mentioned earlier, the amino group in amino acids makes them excellent precursors for synthesizing oxamato or oxamidato-based ligands that are promising linkers for forming water-stable MOFs (Figure 15).³¹⁷

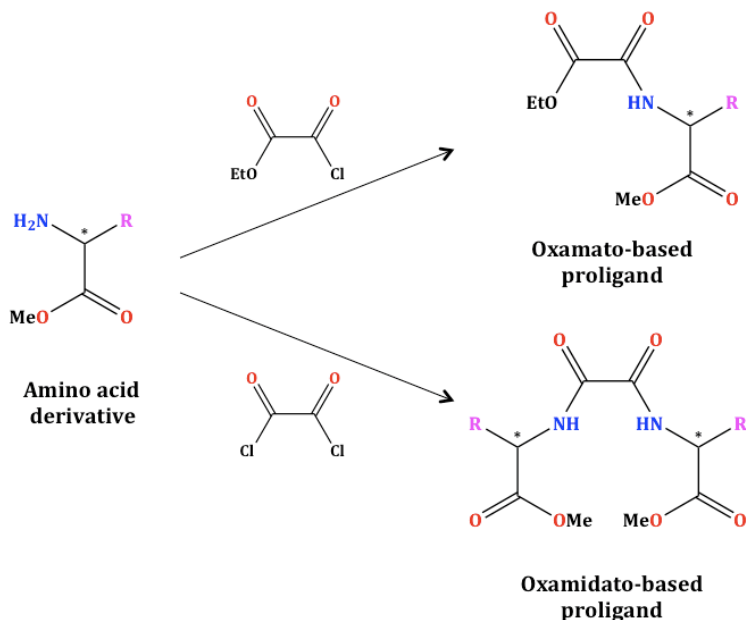


Figure 15. Schematic route for the synthesis of proligands derived from amino acids, where R refers to the amino acid residue, and (*) indicates the asymmetric α -carbon atom. The red (O) and blue (N) atoms represent the coordination sites.

1. INTRODUCTION

They offer the possibility of forming chiral materials due to the presence of asymmetric α -carbon atoms in their structures and exhibit other properties. It has been observed that they can be easily prepared, and just by selecting a desirable amine precursor, the specific side chain/R group can provide MOFs with functional arms. This results in decorated channels and varying pores sizes, offering a wide range of possibilities for various relevant applications, such as catalysis and water remediation.³¹⁸⁻³²²

Previous work by Lloret *et al.*^{140,141,294} has revealed that the oxamidato-based proligand usually exhibits a *trans* configuration, as the *cis* configuration is less stable due to steric hindrance between the substituents. This leads to dinuclear copper(II) complexes that act as bis(tridentate) bridging ligands towards alkaline-earth (Sr^{II} , Ca^{II} or Ba^{II}) and lanthanide ions, which are used to construct chiral MOFs. These MOFs have demonstrated water stability and permanent microporosity, showcasing the potential of MOFs derived from enantiopure amino acids.

One example is the S-C to S-C cations metathesis of the Ca^{2+} counterions of the chiral MOF $\text{Ca}^{\text{II}}_6 \{ \text{Cu}^{\text{II}}_{24} [(\text{S}, \text{S})\text{-hismox}]_{12} (\text{OH}_2)_3 \} \cdot 212\text{H}_2\text{O}$ (where hismox = bis [(*S*)- histidine] oxalyl diamide) with a molecule having a strong dipole moment (CH_3NH_3^+) (Figure 16). This process leads to the development of ferroelectricity while preserving the polar space *via* the efficient transmission of the chiral information from the organic ligands to the final network.³²³

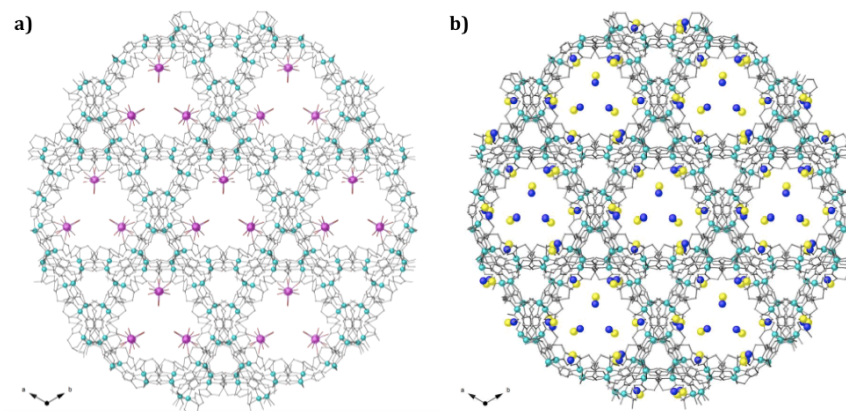


Figure 16. View along the c crystallographic axis of the 3D MOF structures hosting hydrated Ca^{2+} ions (a) and methylammonium cations (b). Cyan spheres represent copper atoms, while organic ligands are depicted as grey sticks. The Ca^{2+} ions are shown as purple spheres. The nitrogen and carbon atoms of the methylammonium cations are represented as blue and yellow spheres, respectively.

Alternatively, it has been demonstrated that 3D homometallic MOFs can be obtained by modifying the pH of the copper precursor solution until precipitation occurs, as in the case of the MOF Cu^{II}_2 (*S, S*)-hismox $\cdot 5\text{H}_2\text{O}$, with only copper nodes and histidine-base proligand. This MOF is an interesting example of a MOF with a continuous and reversible breathing behavior, capable of efficiently adsorbing CO_2 , N_2 , Ar, and C_3H_6 and separating mixtures of CO_2/N_2 , CO_2/CH_4 , and $\text{C}_3\text{H}_8/\text{C}_3\text{H}_6$.³²⁴

Furthermore, derivatives of alanine, leucine, and valine, with hexagonal channels decorated with hydrophobic aliphatic arms of varying lengths, have allowed the study of the effect of the size of the amino acid residue on the final 3D structure (Figure 17).^{325,145}

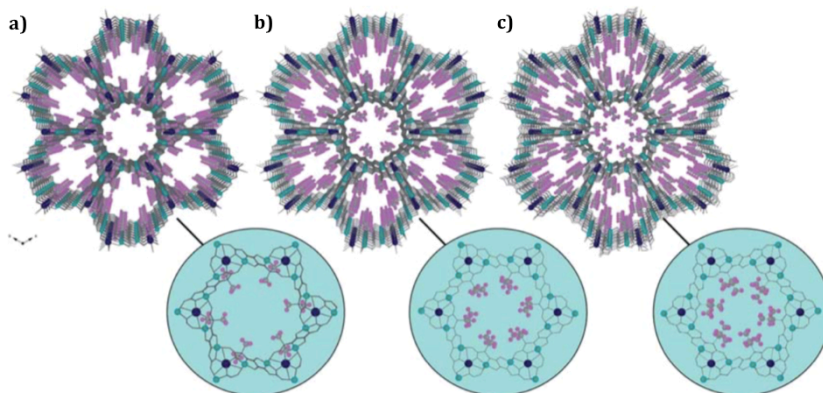


Figure 17. Perspective views along the crystallographic c axis of the MOF structures, highlighting the different alkyl groups from the amino acid residues of alanine (a), leucine (b), and valine (c).

The flexible and highly crystalline MOFs, derived from the natural amino acids *L*-serine and *L*-threonine, featuring hexagonal channels decorated with hydroxyl (-OH) groups, were studied for lanthanide discrimination *via* Solid-Phase Extraction (SPE).³²⁶ They were able to discriminate and separate a mixture of selected lanthanide salts based on the flexibility and disposition of the amino acid residues, the radius of the lanthanide, and its affinity/interactions with O atoms from the pores. In addition, a different trend was observed for each compound due to the different locations of the hydroxyl groups, and subsequently, steric complementarity between the substrate and receptor (Figure 18).

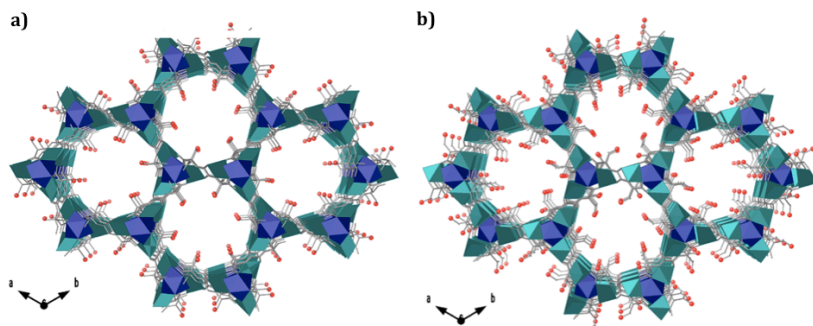


Figure 18. Perspectives views along the *c* axis of the MOF structures synthesized from the amino acids *L*-methionine (a) and *L*-threonine (b). Cu and Ca/Sr are represented by cyan and blue polyhedra, respectively, while the ligands are depicted as sticks. The sulfur and oxygen atoms are shown as yellow and red spheres, respectively.

Of particular interest in this thesis are MOFs based on methionine and methionine, which contain methylated thionyl groups that can strongly interact with soft metals. Our group has exploited this property for the capture of metal contaminants and insertion of catalytically active metals.

One example is the study of the Pd insertion in a MOF based on the modified amino acid methionine $\{\text{Sr}^{\text{II}}\text{Cu}^{\text{II}}_6 [(\text{S}, \text{S})\text{-Mecysmox}]_3 (\text{OH})_2 (\text{H}_2\text{O})\} \cdot 15\text{H}_2\text{O}$ (where Mecysmox = bis [(*S*)-methyl-(*L*)-cysteine] oxalyl diamide). This MOF allows the sequential formation and stabilization of Pd₁ Single-Atom Catalysts (SACs) along their functional hexagonal channels.³¹² The intrinsic flexibility of the chains, combined with the size of the pores, confine the Pd₁ SACs more effectively than in the Me₃mpba-based MOF (Figure 19).

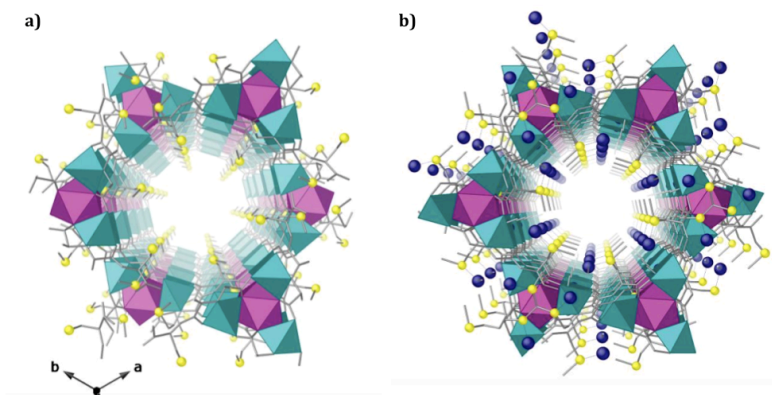


Figure 19. Perspective view along the c axis with the polyhedral model of a single channel of the MOF derived from methionine before (a) and after (b) the insertion of Pd^{2+} ions. The network's copper and strontium atoms are represented by cyan and purple polyhedra, respectively, while the organic ligands are depicted as grey sticks. The sulfur and palladium atoms are shown as yellow and blue spheres.

In addition, it was reported a family of MOFs prepared from *L*-serine and *L*-methionine with channels decorated with flexible and functional arms. The MOFs derived from *L*-methionine $\{\text{Ca}^{\text{II}}\text{Cu}^{\text{II}}_6 [(\text{S}, \text{S})\text{-methiomox}]_3 (\text{OH})_2 (\text{H}_2\text{O})\} \cdot 16\text{H}_2\text{O}$ (where methiomox = bis-[(*S*)-methionine] oxalyl diamide) have channels decorated with thioether arms that strongly interact with gold salts³²⁷ and other noble metals (*i.e.* silver, platinum), making them materials with interesting catalytic properties. They can also efficiently remove hazardous mercury species (Hg^{2+} and CH_3Hg^+) from drinking water. On the other hand, the MOFs derived from *L*-serine $\{\text{Ca}^{\text{II}}\text{Cu}^{\text{II}}_6 [(\text{S}, \text{S})\text{-serimox}]_3 (\text{OH})_2 (\text{H}_2\text{O})\} \cdot 39\text{H}_2\text{O}$ (where serimox = bis[(*S*)-serine] oxalyl diamide), have pores decorated with hydroxyl groups that enable the efficient removal of various organic dyes and drugs (vitamins, anti-depressants, and hormones) due to specific host-guest interactions with these organic molecules.³²⁸

1. INTRODUCTION

It has also been studied the simultaneous and efficient removal of both inorganic (heavy metals such as Hg^{2+} , Pb^{2+} , and Tl^+) and organic (dyes such as Pyronin Y (PY), Auramine O (AO), Brilliant Green (BG) and Methylene Blue (MB)) contaminants from water using a MTV-MOF $\{\text{Ca}^{\text{II}}\text{Cu}^{\text{II}}_6 [(\text{S}, \text{S})\text{-methiomox}]_{1.5} [(\text{S}, \text{S})\text{-serimox}]_{1.5} (\text{OH})_2 (\text{H}_2\text{O})\} \cdot 30\text{H}_2\text{O}$ composed of the aforementioned single-component MOFs. The results showed that the MTV-MOF exhibited improved performance, in terms of kinetics and amount removed, compared to the related single-component MOFs, revealing the synergistic behavior of both types of functional groups decorating the channels.³²⁹ Crystallographic analysis evidenced that the thioether groups participated cooperatively with hydroxyl residues in the capture process. Remarkably, the removal of mixtures of organic contaminants was more efficient than in separate solutions (Figure 20).

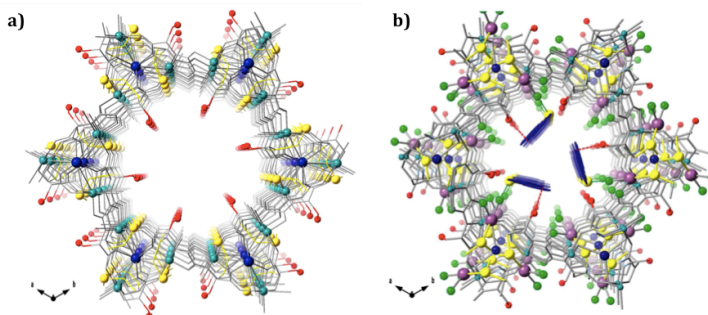


Figure 20. Perspective view along the c axis of the MTV-MOF structures (a) showing the synergistic interaction of the arms with MB molecules (b). Ligands and metal atoms from the network are depicted as grey sticks, except for the residues of the *L*-Serine and *L*-methionine, which are represented as red and yellow sticks, respectively.

Nevertheless, only a few examples of MTV-MOFs with environmental applications have been reported to date, and there is still much work to be done to understand the host-guest interactions, especially at very low concentrations (parts per million) typical of non-accidental industrial discharges.

1.3. Aim of the Thesis

On this basis and to obtain new high dimensional multifunctional materials, we have used pre-synthesized oxamidate proligands derived from various enantiopure natural amino acids to obtain oxamidato-based MOFs through the metalloligand approach. Furthermore, we have expanded this strategy to obtain MTV-MOFs and investigated their potential applications in catalysis and environmental remediation.

In the metalloligand approach, transition metal complexes (in our case, dinuclear Cu(II) SBUs) act as metalloligands towards alkaline earth metal ions (such as Ca(II), Ba(II), or Sr(II)) to assemble heterobimetallic 3D MOFs with functional pores decorated with amino acid residues (Figure 21).

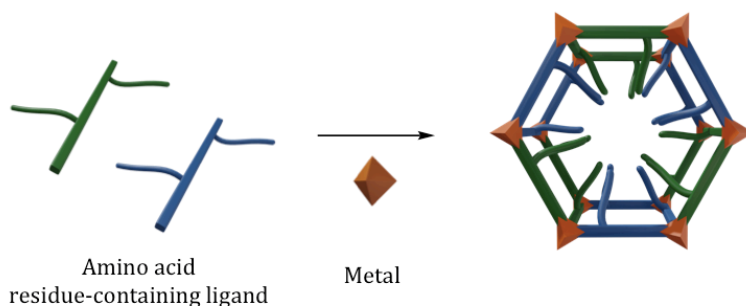


Figure 21. Schematic representation showing the design strategy proposed to prepare MTV-MOFs. Each different metalloligand has been depicted as using different color sticks (green and blue).

We chose larger alkaline earth metal ions over first-row metal ions to allow for the easy accommodation of more SBUs into their coordination environment. We selected methyl cysteine and methionine-based MOFs because they possess methylated thionyl groups as a side chain, which have a strong affinity towards soft metals. Therefore, we exploited this sulfur atom-soft metal affinity for the capture of contaminants and the insertion of catalytically

1. INTRODUCTION

active metals. Additionally, serine and threonine have hydroxyl groups as a side chain, making them hydrophilic and creating a suitable environment for hosting polar molecules.

The first step involved preparing the oxamidato-based proligands. All of them were prepared using the same synthetic procedure: oxalyl chloride was condensed with the methyl ester derivative of the corresponding enantiopure amino acid in the presence of NEt_3 and DCM as the base and solvent respectively, at room temperature. The products were isolated as methyloxamidato-derivatives with good yields (ranging from 80 to 90 %). In the case of cysteine, a prior esterification step was necessary to obtain the proligand. This procedure involved slowly adding an excess of thionyl chloride (SOCl_2) dropwise, under agitation and N_2 atmosphere, to a solution of *S*-Methyl-*L*-cysteine in MeOH at 0 °C in an ice bath, and then refluxing the resulting mixture at 80 °C for 6 hours. Afterwards, the excess thionyl chloride was distilled off using the same solvent, and the remaining solution was concentrated under reduced pressure to obtain the methyl ester derivative of the amino acid *S*-Methyl-*L*-cysteine, which was used to obtain the proligand.

Table 1. Methyl derivative proligands and dinuclear Cu(II) complexes synthesized.

Amino acid	-R group	Proligand	Cu(II) Metalloligand
<i>L</i> -Serine	Hydroxyl -CH ₂ OH	H ₂ Me ₂ -(<i>S</i> , <i>S</i>)- serimox	(Me ₄ N) ₂ {Cu ₂ [(<i>S</i> , <i>S</i>)- serimox](OH) ₂ } · 5H ₂ O
<i>L</i> -Threonine	Hydroxyl -CH(CH ₃)OH	H ₂ Me ₂ -(<i>S</i> , <i>S</i>)- threomox	(Me ₄ N) ₂ {Cu ₂ [(<i>S</i> , <i>S</i>)- threomox](OH) ₂ } · 4H ₂ O
<i>L</i> -Methionine	Thioether -CH ₂ CH ₂ SCH ₃	H ₂ Me ₂ -(<i>S</i> , <i>S</i>)- methiomox	(Me ₄ N) ₂ {Cu ₂ [(<i>S</i> , <i>S</i>)- methiomox](OH) ₂ } · 4H ₂ O
<i>S</i> -Methyl- <i>L</i> - Cysteine	Thioether -CH ₂ SCH ₃	H ₂ Me ₂ -(<i>S</i> , <i>S</i>)- Mecysmox	(Me ₄ N) ₂ {Cu ₂ [(<i>S</i> , <i>S</i>)- Mecysmox](OH) ₂ } · 4H ₂ O

1. INTRODUCTION

The second step involved synthesizing the metal complexes from these oxamidato-based proligands by reacting stoichiometric amounts of $\text{CuCl}_2 \cdot 6\text{H}_2\text{O}$ and the enantiopure proligands (in a 2:1 metal to ligand molar ratio) with Me_4NOH in an aqueous solution. The resulting dinuclear Cu(II) complexes were isolated as tetramethylammonium salts with a general formula of $(\text{Me}_4\text{N})_2 [\text{Cu}^{\text{II}}_2\text{L}(\text{OH})_2] \cdot n\text{H}_2\text{O}$ (Table 1).

Finally, the Cu(II) precursors were used as metalloligands through the free coordination sites towards a second metal cation, alkaline earth (in particular Ca(II) and Sr(II)).

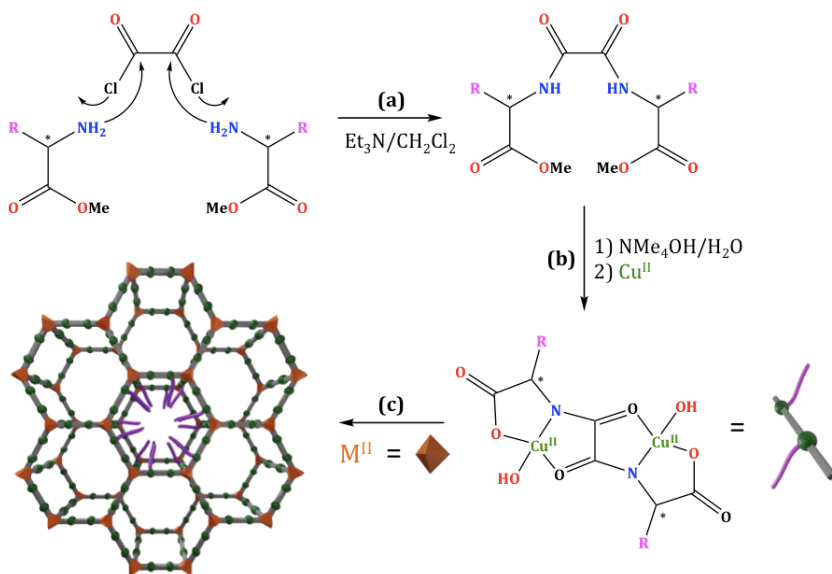


Figure 22. Scheme of the synthetic route used in this thesis to obtain the oxamidato-based proligands (a), dinuclear Cu(II) complexes (b), and heterobimetallic metal(II)/ Cu(II) 3D MOFs (c).

In particular, six hexanuclear Cu(II) structures were obtained; four MOFs derived from a single amino acid (methionine, serine, threonine, and methionine) and two MTV-MOFs, prepared using equimolar amounts of the corresponding precursors.

1. INTRODUCTION

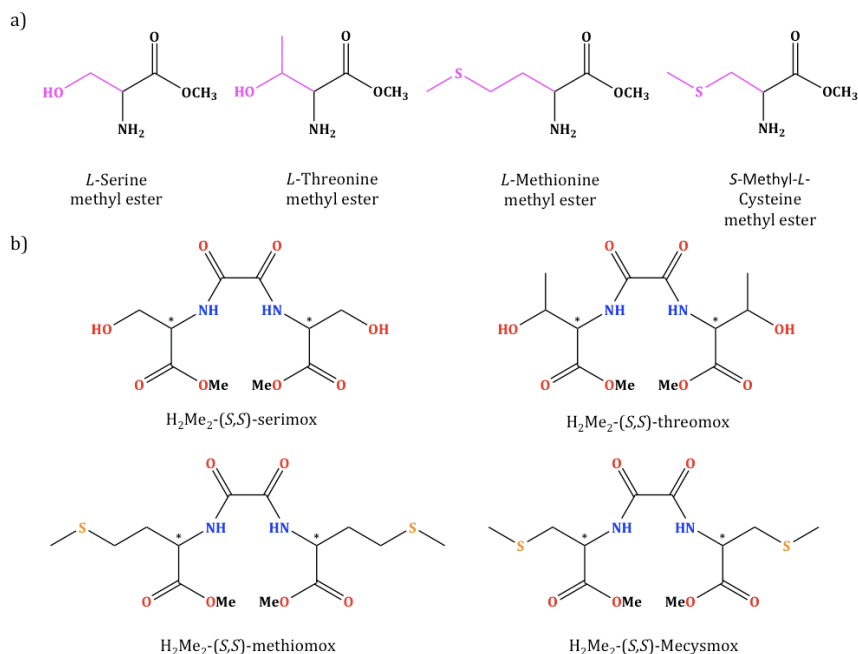


Figure 23. Derivatives of amino acids used (a) to synthesize methyl derivative prolignands (b).

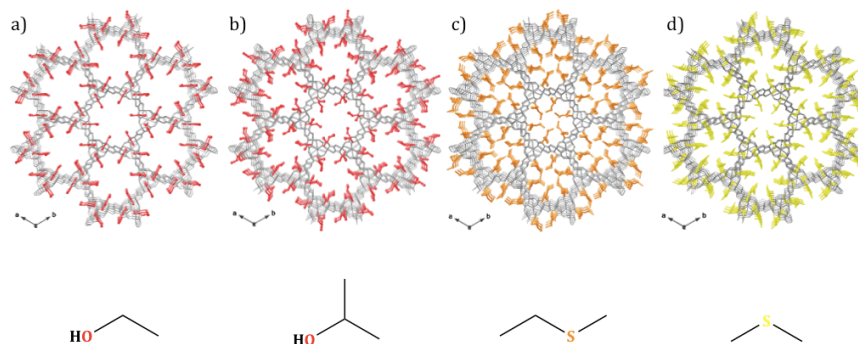


Figure 24. Perspective view along the crystallographic *c* axis of the synthesized oxamidato-based MOFs containing the following amino acids: *L*-serine (a), *L*-threonine (b), *L*-methionine (c), and *S*-Methyl-*L*-cysteine (d). Metals and organic ligands are depicted as grey sticks, whereas the amino acid residues are represented with the following color code: -CH₂OH (a)/-CH(CH₃)OH (b) in red, -CH₂CH₂SCH₃ (c) in orange, and -CH₂SCH₃ (d) in yellow.

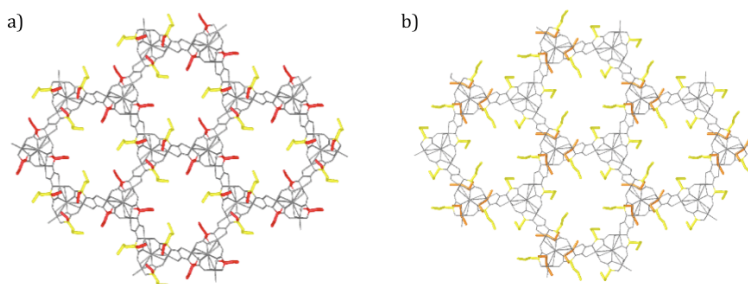


Figure 25. Perspective view along the crystallographic *c* axis of the synthesized oxamidato-based MTV-MOF containing the following amino acids: *S*-Methyl-*L*-cysteine/*L*-serine (a) and *S*-Methyl-*L*-cysteine/*L*-methionine (b). Metals and organic ligands are depicted as grey sticks, whereas the amino acid residues are represented with the following color code: -CH₂OH (a)/-CH(CH₃)OH (b) in red, -CH₂CH₂SCH₃ (c) in orange, and -CH₂SCH₃ (d) in yellow.

The family of structures obtained was determined by SCXRD. Overall, these 3D networks exhibit a honeycomb-like architecture with relatively large hexagonal channels along the crystallographic *c* axis. Their structures consist of chiral 3D Sr(II) or Ca(II)-Cu(II) networks where the corresponding Cu(II) oxamidato units, [Cu^{II}₂L(OH)₂], act as linkers between the Sr(II) or Ca(II) ions through their carboxylate groups. The Sr(II) or Ca(II) ions occupy the vertices of each hexagonal channel, and the dicopper(II) oxamidato units are located along the edges of the channels. Further aqua/hydroxo groups (1:2 statistical distribution), acting as additional bridges between two neighboring dicopper(II) units and a Ca(II) or Sr(II) ion, coordinated in a μ₃ fashion, support the whole system, unfolding an uni-nodal six-connected net of (4⁹·6⁶) Schläfli symbol.

The family of MOFs studied in this thesis is highly versatile, exhibits chirality and excellent water stability. These MOFs feature functional pores with varying sizes and reactivity, making them ideal platforms for a wide range of applications. Specifically, we have focused on their potential applications in heterogeneous catalysis and water remediation, as their unique properties position them as exceptionally promising candidates.

1.4. References

1. Werner, A. *Z. Anorg. Allg. Chem.* **1893**, 3, 267-330.
2. Hofmann, K. A.; Küspert, F. *Z. Anorg. Allg. Chem.* **1897**, 15, 204-207.
3. Büttner, H. G.; Kearley, G. J.; Howard, C. J.; Fillaux, F. *Acta Cryst.* **1994**, B50, 431-435.
4. Lewis, G. N. *J. Am. Chem. Soc.* **1916**, 38, 762-786.
5. Shibata, Y. *J. Coll. Sci., Imperial Univ. Tokyo* **1916**, 37, 1-31.
6. Powell, H. M.; Rayner, J. H. *Nature* **1949**, 163, 566-567.
7. Freund, R.; Canossa, S.; Cohen, S. M.; Yan, W.; Deng, H.; Guillerm, V.; Eddaoudi, M.; Madden, D. G.; Fairen-Jimenez, D.; Lyu, H.; Macreadie, L. K.; Ji, Z.; Zhang, Y.; Wang, B.; Haase, F.; Wöll, C.; Zaremba, O.; Andreo, J.; Wuttke, S.; Diercks, C. S. *Angew. Chem. Int. Ed.* **2021**, 60, 23946-23974.
8. Yaghi, O. M. *ACS Cent. Sci.* **2019**, 5, 1295-1300.
9. Wells, A. F. *Acta Cryst.* **1954**, 7, 535-544.
10. Kinoshita, Y.; Matsubara, I.; Saito, Y. *Bull. Chem. Soc. Jpn.* **1959**, 32, 741-747.
11. Kinoshita, Y.; Matsubara, I.; Higuchi, T.; Saito, Y. *Bull. Chem. Soc. Jpn.* **1959**, 32, 1216-1226.
12. Hoskins, B. F.; Robson, R. *J. Am. Chem. Soc.* **1989**, 111, 596.
13. Hoskins, B. F.; Robson, R. *J. Am. Chem. Soc.* **1990**, 112, 1546-1554.
14. Abrahams, B. F.; Hoskins, B. F.; Michail, D. M.; Robson, R. *Nature* **1994**, 369, 727-729.
15. O'Keeffe, M.; Yaghi, O. M. *Chem. Rev.* **2012**, 112, 675-702.
16. Gropp, C.; Canossa, S.; Wuttke, S.; Gándara, F.; Li, Q.; Gagliardi, L.; Yaghi, O. M. *ACS Cent. Sci.* **2020**, 6, 1255-1273.
17. Yaghi, O. M.; Li, H. *J. Am. Chem. Soc.* **1995**, 117, 10401-10402.
18. Riou, D.; Férey, G. *J. Mater. Chem.* **1998**, 8, 2733-2735.
19. Kitagawa, S.; Matsuyama, S.; Munakata, M.; Emori, T. *J. Chem. Soc., Dalton Trans.* **1991**, 0, 2869-2874.
20. MacGillivray, L. R.; Subramanian, S.; Zaworotko, M. J. *J. Chem. Soc., Chem. Commun.* **1994**, 0, 1325-1326.
21. Kondo, M.; Yoshitomi, T.; Seki, K.; Matsuzaka, H.; Kitagawa, S. *Angew. Chem. Int. Ed. Engl.* **1997**, 36, 1725-1727.

22. Yaghi, O. M.; Li, G.; Li, H. *Nature* **1995**, 378, 703-706.
23. Li, H.; Eddaoudi, M.; Groy, T. L.; Yaghi, O. M. *J. Am. Chem. Soc.* **1998**, 120, 8571-8572.
24. Kitagawa, S.; Kitaura, R.; Noro, S. I. *Angew. Chem. Int. Ed.* **2004**, 43, 2334-2375.
25. Li, H.; Eddaoudi, M.; O'Keeffe, M.; Yaghi, O. M. *Nature* **1999**, 402, 276-279.
26. Eddaoudi, M.; Kim, J.; Rosi, N.; Vodak, D.; Wachter, J.; O'Keeffe, M.; Yaghi, O. M. *Science* **2002**, 295, 469-472.
27. Diercks, C. S.; Yaghi, O. M. *Science* **2017**, 355, eaal1585.
28. Li, M.; Li, D.; O'Keeffe, M.; Yaghi, O. M. *Chem. Rev.* **2014**, 114, 1343-1370.
29. Kaszynski, P.; Friedli, A. C.; Michl, J. *J. Am. Chem. Soc.* **1992**, 114, 601-620.
30. Gardner, G. B.; Venkataraman, D.; Moore, J. S.; Lee, S. *Nature* **1995**, 374, 792-795.
31. Eddaoudi, M.; Moler, D. B.; Li, H.; Chen, B.; Reineke, T. M.; O'Keeffe, M.; Yaghi, O. M. *Acc. Chem. Res.* **2001**, 34, 319-330.
32. Furukawa, H.; Cordova, K. E.; O'Keeffe, M.; Yaghi, O. M. *Science* **2013**, 341, 1230444.
33. Tan, J.; Tao, Y.; Zhang, X.; Wang, Q.; Zeng, T.; Shi, Z.; Cordova, K. E.; Lee, Y.; Liu, H.; Zhang, Y. B. *J. Mater. Chem. A* **2021**, 9, 24857-24862.
34. O'Nolan, D.; Madden, D. G.; Kumar, A.; Chen, K. J.; Pham, T.; Forrest, K. A.; Patyk-Kazmierczak, E.; Yang, Q. Y.; Murray, C. A.; Tang, C. C.; Space, B.; Zaworotko, M. J. *Chem. Commun.* **2018**, 54, 3488-3491.
35. Gupta, M.; Vittal, J. J. *Coord. Chem. Rev.* **2021**, 435, 213789.
36. Deshpande, R. K.; Waterhouse, G. I. N.; Jameson, G. B.; Telfer, S. G. *Chem. Commun.* **2012**, 48, 1574-1576.
37. Sun, D.; Ma, S.; Ke, Y.; Collins, D. J.; Zhou, H. C. *J. Am. Chem. Soc.* **2006**, 128, 3896-3897.
38. Cheon, Y. E.; Suh, M. P. *Chem. Eur. J.* **2008**, 14, 3961-3967.
39. Song, F.; Wang, C.; Falkowski, J. M.; Ma, L.; Lin, W. *J. Am. Chem. Soc.* **2010**, 132, 15390-15398.

1. INTRODUCTION

40. Xue, D. X.; Belmabkhout, Y.; Shekhah, O.; Jiang, H.; Adil, K.; Cairns, A. J.; Eddaoudi, M. *J. Am. Chem. Soc.* **2015**, 137, 5034-5040.
41. Lehn, J.- M. *Supramolecular Chemistry: Concepts and Perspectives*; VCH: Weinheim, **1995**; pp 1-10.
42. Yaghi, O. M.; Kalmutzki, M. J.; Diercks, C. S. *Angew. Chem. Int. Ed.* **2019**, 58, 40 14024-14024.
43. Gropp, C.; Ma, T.; Hanikel, N.; Yaghi, O. M. *Science* **2020**, 370, 23.
44. Mon, M.; Bruno, R.; Ferrando-Soria, J.; Bartella, L.; Di Donna, L.; Talia, M.; Lappano, R.; Maggiolini, M.; Armentano, D.; Pardo, E. *Mater. Horiz.* **2018**, 5, 683-690.
45. Kitagawa, S.; Kondo, M. *Bull. Chem. Soc. Jpn.* **1998**, 71, 1739-1753.
46. Rowsell, J. L. C.; Yaghi, O. M. *Micropor. Mesopor. Mater.* **2004**, 73, 3-14.
47. Wang, X.; Fan, M.; Guan, Y.; Liu, Y.; Liu, M.; Karsili, T. N. V.; Yi, J.; Zhou, X. D.; Zhang, J. *J. Mater. Chem. A* **2021**, 9, 22710-22728.
48. Murray, L. J.; Dincă, M.; Long, J. R. *Chem. Soc. Rev.* **2009**, 38, 1294.
49. Makal, T. A.; Li, J.-R.; Lu, W.; Zhou, H.-C. *Chem. Soc. Rev.* **2012**, 41, 7761.
50. Li, J.-R.; Sculley, J.; Zhou, H.-C. *Chem. Rev.* **2012**, 112, 869.
51. Lee, J.; Farha, O. K.; Roberts, J.; Scheidt, K. A.; Nguyen, S. T.; Hupp, J. T. *Chem. Soc. Rev.* **2009**, 38, 1450.
52. Ma, L.; Abney, C.; Lin, W. *Chem. Soc. Rev.* **2009**, 38, 1248.
53. Quartapelle Procopio, E.; Linares, F.; Montoro, C.; Colombo, V.; Maspero, A.; Barea, E.; Navarro, J. A. R. *Angew. Chem. Int. Ed.* **2010**, 49, 7308-7311.
54. Kreno, L. E.; Leong, K.; Farha, O. K.; Allendorf, M.; Van Duyne, R. P.; Hupp, J. T. *Chem. Rev.* **2012**, 112, 1105.
55. Min, K. S.; Suh, M. P. *J. Am. Chem. Soc.* **2000**, 122, 6834-6835.
56. Horike, S.; Umeyama, D.; Kitagawa, S. *Acc. Chem. Res.* **2013**, 46, 2376-2384.
57. Horcajada, P.; Gref, R.; Baati, T.; Allan, P. K.; Maurin, G.; Couvreur, P.; Férey, G.; Morris, R. E.; Serre, C. *Chem. Rev.* **2012**, 112, 1232-1268.
58. Kent, C. A.; Mehl, B. P.; Ma, L.; Papanikolas, J. M.; Meyer, T. J.; Lin, W. *J. Am. Chem. Soc.* **2010**, 132, 12767-12769.

59. Kim, H.; Yang, S.; Rao, S. R.; Narayanan, S.; Kapustin, E. A.; Furukawa, H.; Umans, A. S.; Yaghi, O. M.; Wang, E. N. *Science* **2017**, 356, 430-434.
60. Agarwal, X. R. A.; Gupta, N. K. *RSC Adv.* **2017**, 7, 3870-3878.
61. Ma, Y.; Sun, Y. *J. Appl. Phys.* **2020**, 127, 080901.
62. Fathieh, F.; Kalmutzki, M. J.; Kapustin, E. A.; Waller, P. J.; Yang, J.; Yaghi, O. M. *Sci. Adv.* **2018**, 4, 3198.
63. Smith, J. K. History of catalysis. In *Encyclopedia of Catalysis*; Horváth, I., Ed.; John Wiley & Sons, Inc.: Hoboken, NJ, **2010**.
64. Pilgrim, B. S.; Champness, N. R. *ChemPlusChem* **2020**, 85, 1842-1856.
65. Rothenberg, G. *Catalysis: Concepts and Green Applications*; Wiley-VCH: Weinheim, Germany, **2008**.
66. Pei, G. X.; Liu, X. Y.; Yang, X.; Zhang, L.; Wang, A.; Li, L.; Wang, H.; Wang, X.; Zhang, T. *ACS Catal.* **2017**, 7, 1491-1498.
67. Sorribes, I.; Liu, L.; Corma, A. *ACS Catal.* **2017**, 7, 2698-2706.
68. Bhaduri, S.; Mukesh, D., Eds. *Homogeneous Catalysis*; John Wiley & Sons, Inc.: New York, **2000**.
69. Copéret, C.; Comas-Vives, A.; Conley, M. P.; Estes, D. P.; Fedorov, A.; Mougel, V.; Nagae, H.; Núñez-Zarur, F.; Zhizhko, P. A. *Chem. Rev.* **2016**, 116, 323-421.
70. Thomas, J. M.; Thomas, W. J. *Principles and Practice of Heterogeneous Catalysis*; Wiley-VCH Verlag GmbH & Co. KGaA: Weinheim, Germany, **2015**.
71. Jong, K. P. *Synthesis of Solid Catalysts*; Wiley-VCH Verlag GmbH & Co. KGaA: Weinheim, Germany, **2009**.
72. Li, J.-R.; Kuppler, R. J.; Zhou, H.-C. *Chem. Soc. Rev.* **2009**, 38, 1477.
73. Rogge, S. M. J.; Bavykina, A.; Hajek, J.; Garcia, H.; Olivos-Suarez, A. I.; Sepúlveda-Escribano, A.; Vimont, A.; Clet, G.; Bazin, P.; Kapteijn, F.; Daturi, M.; Ramos-Fernandez, E. V.; Llabrés i Xamena, F. X.; Van Speybroeck, V.; Gascon, J. *Chem. Soc. Rev.* **2017**, 46, 3134-3138.
74. Fujita, M.; Kwon, Y. J.; Washizu, S.; Ogura, K. *J. Am. Chem. Soc.* **1994**, 116, 1151-1152.
75. Valvekens, P.; Vermoortele, F.; De Vos, D. *Catal. Sci. Technol.* **2013**, 3, 1435.

76. Juan-Alcañiz, J.; Gascon, J.; Kapteijn, F. *J. Mater. Chem.* **2012**, *22*, 10102-10118.
77. Jiao, L.; Wang, Y.; Jiang, H. L.; Xu, Q. *Adv. Mater.* **2018**, *30*, e1703663.
78. Hasegawa, S.; Horike, S.; Matsuda, R.; Furukawa, S.; Mochizuki, K.; Kinoshita, Y.; Kitagawa, S. *J. Am. Chem. Soc.* **2007**, *129*, 2607-2614.
79. Lee, J.; Farha, O. K.; Roberts, J.; Scheidt, K. A.; Nguyen, S. T.; Hupp, J. T. *Chem. Soc. Rev.* **2009**, *38*, 1450-1459.
80. Kang, Y.-S.; Lu, Y.; Chen, K.; Zhao, Y.; Wang, P.; Sun, W.-Y. *Coord. Chem. Rev.* **2019**, *378*, 262-280.
81. Gulati, S. *Metal-Organic Frameworks (MOFs) as Catalysts*; Springer Verlag: Singapore, **2022**; pp 789.
82. Chen, B.; Eddaoudi, M.; Reineke, T. M.; Kampf, J. W.; O'Keeffe, M.; Yaghi, O. M. *J. Am. Chem. Soc.* **2000**, *122*, 11559-11560.
83. Schlichte, K.; Kratzke, T.; Kaskel, S. *Micropor. Mesopor. Mater.* **2004**, *73*, 81-88.
84. Alaerts, L.; Séguin, E.; Poelman, H.; Thibault-Starzyk, F.; Jacobs, P. A.; De Vos, D. E. *Chem. Eur. J.* **2006**, *12*, 7353-7363.
85. Vimont, A.; Goupil, J.-M.; Lavalley, J.-C.; Daturi, M.; Surblé, S.; Serre, C.; Millange, F.; Férey, G.; Audebrand, N. *J. Am. Chem. Soc.* **2006**, *128*, 3218-3227.
86. Henschel, A.; Gedrich, K.; Kraehnert, R.; Kaskel, S. *Chem. Commun.* **2008**, *0*, 4192-4194.
87. Juan-Alcañiz, J.; Gielisse, R.; Lago, A. B.; Ramos-Fernandez, E. V.; Serra-Crespo, P.; Devic, T.; Guillou, N.; Serre, C.; Kapteijn, F.; Gascon, J. *Catal. Sci. Technol.* **2013**, *3*, 2311-2318.
88. Valenzano, L.; Civalleri, B.; Chavan, S.; Bordiga, S.; Nilsen, M. H.; Jakobsen, S.; Lillerud, K. P.; Lamberti, C. *Chem. Mater.* **2011**, *23*, 1700-1718.
89. Li, X.; Sun, Y.; Yao, Q.; Wang, Y.; Zheng, H.; Cao, R. *ACS Catal.* **2016**, *6*, 3461-3468.
90. Yoon, M.; Srirambalaji, R.; Kim, K. *Chem. Rev.* **2012**, *112*, 1196-1231.
91. Genna, D. T.; Wong-Foy, A. G.; Matzger, A. J.; Sanford, M. S. *J. Am. Chem. Soc.* **2013**, *135*, 10586.

1. INTRODUCTION

92. Abherve, A.; Grancha, T.; Ferrando-Soria, J.; Clemente-Leon, M.; Coronado, E.; Waerenborgh, J. C.; Lloret, F.; Pardo, E. *Chem. Commun.* **2016**, 52, 7360-7363.
93. Fortea-Peñez, F. R.; Mon, M.; Ferrando-Soria, J.; Boronat, M.; Leyva-Pérez, A.; Corma, A.; Herrera, J. M.; Osadchii, D.; Gascon, J.; Armentano, D.; Pardo, E. *Nat. Mater.* **2017**, 16, 760-766.
94. Liang, W.; Xu, H.; Carraro, F.; Maddigan, N. K.; Li, Q.; Bell, S. G.; Huang, D. M.; Tarzia, A.; Solomon, M. B.; Amenitsch, H.; Vaccari, L.; Sumbly, C. J.; Falcaro, P.; Doonan, C. J. *J. Am. Chem. Soc.* **2019**, 141, 2348-2355.
95. Li, Y. M.; Yuan, J.; Ren, H.; Ji, C. Y.; Tao, Y.; Wu, Y.; Chou, L. Y.; Zhang, Y. B.; Cheng, L. *J. Am. Chem. Soc.* **2021**, 143, 15378-15390.
96. Moon, H. R.; Limb, D.-W.; Suh, M. P. *Chem. Soc. Rev.* **2013**, 42, 1807-1824.
97. Richardson, S. D.; Kimura, S. Y. *Anal. Chem.* **2016**, 88, 546-582.
98. Suffet, I. H.; Malaiyandi, M., Eds. *Organic Pollutants in Water: Sampling, Analysis and Toxicity Testing*; American Chemical Society: Washington, **1987**.
99. Seckler, D.; Barker, R.; Amarasinghe, U. *Int. J. Water Resour. Dev.* **1999**, 15, 29-42.
100. United Nations. Resolution Adopted by the General Assembly on 25 September **2015**. A/RES/70/1.
101. Giusti, L. *Waste Manag.* **2009**, 29, 2227-2239.
102. Bhattacharya, S.; Gupta, A. B.; Gupta, A.; Pandey, A. In *Water Remediation. Energy, Environment and Sustainability*; Springer: Singapore, **2018**; pp 3-8.
103. Xu, Y.; Liu, T.; Zhang, Y.; Ge, F.; Steel, R. M.; Sun, L. *J. Mater. Chem. A* **2017**, 5, 12001-12014.
104. Gupta, V. K.; Ali, I.; Saleh, T. A.; Nayak, A.; Agarwal, S. *RSC Adv.* **2012**, 2, 6380.
105. Alcamo, J.; Henrichs, T.; Rösch, T. *World Water in 2025: Global Modeling and Scenario Analysis for the World Commission on Water for the 21st Century*; Centre for Environmental Systems Research, University of Kassel: Germany, **2000**.
106. Dias, E. M.; Petit, C. J. *Mater. Chem. A* **2015**, 3, 22484-22506.
107. Palmer, M. *Science* **2004**, 304, 1251-1252.

1. INTRODUCTION

108. Galal-Gorchev, H. *Food Addit. Contam.* **1993**, 10, 115-128.
109. World Health Organization. Guidelines for Drinking-water Quality: Fourth Edition Incorporating the First Addendum. Geneva, Switzerland, **2017**.
110. Yuan, S.; Qin, J.-S.; Zou, L.; Chen, Y.-P.; Wang, X.; Zhang, Q.; Zhou, H.-C. *J. Am. Chem. Soc.* **2016**, 138, 6636-6642.
111. Oak Ridge National Lab. Materials for Separation Technologies: Energy and Emission Reduction Opportunities; Oak Ridge National Lab.: Oak Ridge, **2005**.
112. Wang, C.; Liu, X.; Keser, N.; Demir; Chen, J. P.; Li, K. *Chem. Soc. Rev.* **2016**, 45, 5107-5134.
113. Rojas, S.; Horcajada, P. *Chem. Rev.* **2020**, 120, 8378-8415.
114. Li, J.; Wang, X.; Zhao, G.; Chen, C.; Chai, Z.; Alsaedi, A.; Hayat, T.; Wang, X. *Chem. Soc. Rev.* **2018**, 47, 2322-2356.
115. Mon, M.; Bruno, R.; Ferrando-Soria, J.; Armentano, D.; Pardo, E. *J. Mater. Chem. A* **2018**, 6, 4912-4947.
116. Kobielska, P. A.; Howarth, A. J.; Farha, O. K.; Nayak, S. *Coord. Chem. Rev.* **2018**, 358, 92-107.
117. Tchounwou, P. B.; Yedjou, C. G.; Patlolla, A. K.; Sutton, D. J. Environmental Toxicology. In *Molecular, Clinical and Environmental Toxicology*, Volume 3; Luch, A., Ed.; Springer Basel AG: Basel, **2012**; pp 133-164.
118. Yu, C.; Shao, Z.; Hou, H. *Chem. Sci.* **2017**, 8, 7611-7619.
119. Desai, A. V.; Manna, B.; Karmakar, A.; Sahu, A.; Ghosh, S. K. *Angew. Chem. Int. Ed.* **2016**, 55, 7811-7815.
120. World Health Organization. Persistent Organic Pollutants: Impact on Child Health; WHO Press: Geneva, Switzerland, **2010**.
121. Li, T. T.; Liu, Y. M.; Wang, T.; Wu, Y. L.; He, Y. L.; Yang, R.; Zheng, S. R. *Microporous Mesoporous Mater.* **2018**, 272, 101-108.
122. Wang, B.; Lv, X.-L.; Feng, D.; Xie, L.-H.; Zhang, J.; Li, M.; Xie, Y.; Li, J.-R.; Zhou, H.-C. *J. Am. Chem. Soc.* **2016**, 138, 6204-6216.
123. Singha, D. K.; Majee, P.; Mondal, S. K.; Mahata, P. *Polyhedron* **2019**, 158, 277-282.
124. Wang, C.-C.; Li, J.-R.; Lv, X.-L.; Zhang, Y.-Q.; Guo, G. *Energy Environ. Sci.* **2014**, 7, 2831-2867.
125. Yang, J.; Yang, Y.-W. *Small* **2020**, 16, e1906847.

1. INTRODUCTION

126. Della Rocca, J.; Liu, D.; Lin, W. *Acc. Chem. Res.* **2011**, 44, 957.
127. Horcajada, P.; Serre, C.; Vallet-Regí, M.; Sebban, M.; Taulelle, F.; Férey, G. *Angew. Chem. Int. Ed.* **2006**, 45, 5974-5978.
128. Xu, J.; Wu, L.; Guo, T.; Zhang, G.; Wang, C.; Li, H.; Li, X.; Singh, V.; Chen, W.; Gref, R.; Zhang, J. *Int. J. Pharm.* **2019**, 556, 89-96.
129. Miller, S. R.; Heurtaux, D.; Baati, T.; Horcajada, P.; Grenèche, J.-M.; Serre, C. *Chem. Commun.* **2010**, 46, 4526-4528.
130. Rojas, S.; Baati, T.; Njim, L.; Manchego, L.; Neffati, F.; Abdeljelil, N.; Saguem, S.; Serre, C.; Najjar, M. F.; Zakhama, A.; Horcajada, P. *J. Am. Chem. Soc.* **2018**, 140, 9581-9586.
131. Lipinski, C. A.; Lombardo, F.; Dominy, B. W.; Feeney, P. J. *Adv. Drug Deliv. Rev.* **1997**, 23, 3-25.
132. Rojas, S.; Devic, T.; Horcajada, P. *J. Mater. Chem. B* **2017**, 5, 2560-2573.
133. Zhong, G.; Liu, D.; Zhang, J. *Cryst. Growth Des.* **2018**, 18, 7730-7744.
134. Yaghi, O. M.; O'Keeffe, M.; Ockwig, N. W.; Chae, H. K.; Eddaoudi, M.; Kim, J. *Nature* **2003**, 423, 705-714.
135. Kong, D.; Zoñ, J.; McBee, J.; Clearfield, A. *Inorg. Chem.* **2006**, 45, 977-986.
136. Chandler, B. D.; Yu, J. O.; Cramb, D. T.; Shimizu, G. K. H. *Chem. Mater.* **2007**, 19, 4467-4473.
137. Suryawanshi, P. L.; Sonawane, S. H.; Bhanvase, B. A.; Ashokkumar, M.; Pimplapure, M. S.; Gogate, P. R. *Green Process Synth.* **2018**, 7, 1-11.
138. Liu, Y.; Xi, X.; Ye, C.; Gong, T.; Yang, Z.; Cui, Y. *Angew. Chem. Int. Ed.* **2014**, 53, 13821-13825.
139. Ferguson, A.; Liu, L.; Tapperwijn, S. J.; Perl, D.; Coudert, F.-X.; Van Cleuvenbergen, S.; Verbiest, T.; van der Veen, M. A.; Telfer, S. G. *Nat. Chem.* **2016**, 8, 250-257.
140. Lloret, F.; Julve, M.; Faus, J.; Ruiz, R.; Castro, I.; Mollar, M.; Philoche-Levisalles, M. *Inorg. Chem.* **1992**, 31, 784-791.
141. Lloret, F.; Julve, M.; Real, J. A.; Faus, J.; Ruiz, R.; Mollar, M.; Castro, I.; Bois, C. *Inorg. Chem.* **1992**, 31, 2956-2961.
142. Zhou, Z.; He, C.; Xiu, J.; Yang, L.; Duan, C. *J. Am. Chem. Soc.* **2015**, 137, 15066-15069.

1. INTRODUCTION

143. Zhang, S.-Y.; Li, D.; Guo, D.; Zhang, H.; Shi, W.; Cheng, P.; Wojtas, L.; Zaworotko, M. J. *J. Am. Chem. Soc.* **2015**, 137, 15406-15409.
144. Newar, R.; Akhtar, N.; Antil, N.; Kumar, A.; Shukla, S.; Begum, W.; Manna, K. *Angew. Chem. Int. Ed.* **2021**, 60, 10964-10971.
145. Grancha, T.; Mon, M.; Ferrando-Soria, J.; Armentano, D.; Pardo, E. *Cryst. Growth Des.* **2016**, 16, 5571-5578.
146. Chen, L.; Bu, X. *Chem. Mater.* **2006**, 18, 1857-1860.
147. Luo, T.; Hsu, L.; Su, C.; Ueng, C.; Tsai, T.; Lu, K. *Inorg. Chem.* **2007**, 46, 1532-1534.
148. Anokhina, E. V.; Go, Y. B.; Lee, Y.; Vogt, T.; Jacobson, A. J. *J. Am. Chem. Soc.* **2006**, 128, 9957-9962.
149. Zhu, P.; Gu, W.; Cheng, F.-Y.; Liu, X.; Chen, J.; Yan, S.-P.; Liao, D.-Z. *CrystEngComm.* **2008**, 10, 963-967.
150. Ma, B.; Zhang, D.; Gao, S.; Jin, T. *Angew. Chem. Int. Ed.* **2000**, 39, 3644-3646.
151. Gramaccioli, C. M. *Acta Crystallogr.* **1966**, 21, 600-605.
152. Zhang, Y.; Saha, M. K.; Bernal, I. *CrystEngComm.* **2003**, 5, 34-37.
153. Wang, R.; Liu, H.; Carducci, M. D.; Jin, T.; Zheng, C.; Zheng, Z. *Inorg. Chem.* **2001**, 40, 2743-2750.
154. Kathalikkattil, A. C.; Babu, R.; Roshan, R. K.; Lee, H.; Kim, H.; Tharun, J.; Suresh, E.; Park, D.-W. *J. Mater. Chem. A* **2015**, 3, 22636-22647.
155. Vaidhyanathan, R.; Bradshaw, D.; Rebilly, J.-N.; Barrio, J. P.; Gould, J. A.; Berry, N. G.; Rosseinsky, M. J. *Angew. Chem. Int. Ed.* **2006**, 45, 6495-6499.
156. Barrio, J. P.; Rebilly, J. N.; Carter, B.; Bradshaw, D.; Bacsá, J.; Ganin, A. Y.; Park, H.; Trewin, A.; Vaidhyanathan, R.; Cooper, A. I.; Warren, J. E.; Rosseinsky, M. J. *Chem. A Eur. J.* **2008**, 14, 4521-4532.
157. Qu, Z.-R.; Zhao, H.; Wang, X.-S.; Li, Y.-H.; Song, Y.-M.; Liu, Y.-j.; Ye, Q.; Xiong, R.-G.; Abrahams, B. F.; Xue, Z.-L.; You, X.-Z. *Inorg. Chem.* **2003**, 42, 7710-7712.
158. Imaz, I.; Rubio-Martinez, M.; An, J.; Sole-Font, I.; Rosi, N. L.; MasPOCH, D. *Chem. Commun.* **2011**, 47, 7287-7302.
159. Kundu, T.; Sahoo, S. C.; Banerjee, R. *CrystEngComm* **2013**, 15, 9634-9640.

160. Farha, O. K.; Eryazici, I.; Jeong, N. C.; Hauser, B. G.; Wilmer, C. E.; Sarjeant, A. A.; Snurr, R. Q.; Nguyen, S. T.; Yazydin, O.; Hupp, J. T. *J. Am. Chem. Soc.* **2012**, 134, 15016.
161. Viciano-Chumillas, M.; Liu, X.; Leyva-Pérez, A.; Armentano, D.; Ferrando-Soria, J.; Pardo, E. *Coord. Chem. Rev.* **2022**, 451, 214273.
162. Bunck, D. N.; Dichtel, W. R. *Chem. Eur. J.* **2013**, 19, 818-827.
163. Doonan, C. J.; Morris, W.; Furukawa, H.; Yaghi, O. M. *J. Am. Chem. Soc.* **2009**, 131, 9492-9493.
164. Karagiari, O.; Lalonde, M. B.; Bury, W.; Sarjeant, A. A.; Farha, O. K.; Hupp, J. T. *J. Am. Chem. Soc.* **2012**, 134, 18790-18796.
165. Kleist, W.; Jutz, F.; Maciejewski, M.; Baiker, A. *Eur. J. Inorg. Chem.* **2009**, 24, 3552-3561.
166. Burrows, A. D. *CrystEngComm* **2011**, 13, 3623.
167. Masoomi, M. Y.; Morsali, A.; Dhakshinamoorthy, A.; Garcia, H. *Angew. Chem. Int. Ed.* **2019**, 58, 15188-15205.
168. Deng, H.; Doonan, C. J.; Furukawa, H.; Ferreira, R. B.; Towne, J.; Knobler, C. B.; Wang, B.; Yaghi, O. M. *Science* **2010**, 327, 846-850.
169. Jiao, J.; Gong, W.; Wu, X.; Yang, S.; Cui, Y. *Coord. Chem. Rev.* **2019**, 385, 174-190.
170. Pang, Q.; Tu, B.; Li, Q. *Coord. Chem. Rev.* **2019**, 388, 107-125.
171. Koh, K.; Wong-Foy, A. G.; Matzger, A. J. *J. Am. Chem. Soc.* **2010**, 132, 15005-15010.
172. Ji, Z.; Wang, H.; Canossa, S.; Wuttke, S.; Yaghi, O. M. *Adv. Funct. Mater.* **2020**, 30, 2000238.
173. Kalaj, M.; Cohen, S. M. *ACS Cent. Sci.* **2020**, 6, 1046-1057.
174. Yuan, S.; Qin, J. S.; Li, J.; Huang, L.; Feng, L.; Fang, Y.; Lollar, C.; Pang, J.; Zhang, L.; Sun, D.; Alsalmeh, A.; Cagin, T.; Zhou, H. C. *Nat. Commun.* **2018**, 9, 808.
175. Park, T.-H.; Koh, K.; Wong-Foy, A. G.; Matzger, A. J. *Cryst. Growth Des.* **2011**, 11, 2059-2063.
176. Cliffe, M. J.; Wan, W.; Zou, X.; Chater, P. A.; Kleppe, A. K.; Tucker, M. G.; Wilhelm, H.; Funnell, N. P.; Coudert, F. X.; Goodwin, A. L. *Nat. Commun.* **2014**, 5, 4176.
177. Katzenmeyer, A. M.; Canivet, J.; Holland, G.; Farrusseng, D.; Centrone, A. *Angew. Chem., Int. Ed.* **2014**, 53, 2852-2856.

178. Tu, B.; Pang, Q.; Ning, E.; Yan, W.; Qi, Y.; Wu, D.; Li, Q. *J. Am. Chem. Soc.* **2015**, 137, 13456-13459.
179. Liu, L.; Telfer, S. G. *J. Am. Chem. Soc.* **2015**, 137, 3901-3909.
180. Tu, B.; Diestel, L.; Shi, Z.; Bandara, W. R. L. N.; Chen, Y.; Lin, W.; Zhang, Y.; Telfer, S. G.; Li, Q. *Angew. Chem., Int. Ed.* **2019**, 58, 5348-5353.
181. Feng, L.; Wang, K. Y.; Day, G. S.; Zhou, H. C. *Chem. Soc. Rev.* **2019**, 48, 4823-4853.
182. Lee, S. J.; Doussot, C.; Baux, A.; Liu, L.; Jameson, G. B.; Richardson, C.; Pak, J. J.; Trouselet, F.; Coudert, F.-X.; Telfer, S. G. *Chem. Mater.* **2016**, 28, 368-375.
183. Fang, Z.; Bueken, B.; De Vos, D. E.; Fischer, R. A. *Angew. Chem. Int. Ed.* **2015**, 54, 7234-7254.
184. Tu, B.; Pang, Q.; Wu, D.; Song, Y.; Weng, L.; Li, Q. *J. Am. Chem. Soc.* **2014**, 136, 14465-14471.
185. Koh, K.; Wong-Foy, A. G.; Matzger, A. J. *Angew. Chem. Int. Ed.* **2008**, 47, 677-680.
186. Kong, X.; Deng, H.; Yan, F.; Kim, J.; Swisher, J. A.; Smit, B.; Yaghi, O. M.; Reimer, J. A. *Science* **2013**, 341, 882-885.
187. Schrimpf, W.; Jiang, J.; Ji, Z.; Hirschle, P.; Lamb, D. C.; Yaghi, O. M.; Wuttke, S. *Nat. Commun.* **2018**, 9, 1647.
188. Furukawa, H.; Müller, U.; Yaghi, O. M. *Angew. Chem. Int. Ed.* **2015**, 54, 3417-3430.
189. Zhang, Y.-B.; Furukawa, H.; Ko, N.; Nie, W.; Park, H. J.; Okajima, S.; Cordova, K. E.; Deng, H.; Kim, J.; Yaghi, O. M. *J. Am. Chem. Soc.* **2015**, 137, 2641-2650.
190. Wang, L.-J.; Deng, H.; Furukawa, H.; Gándara, F.; Cordova, K. E.; Peri, D.; Yaghi, O. M. *Inorg. Chem.* **2014**, 53, 5881-5883.
191. Xu, W.; Tu, B.; Liu, Q.; Shu, Y.; Liang, C. C.; Diercks, C. S.; Yaghi, O. M.; Zhang, Y. B.; Deng, H.; Li, Q. *Nat. Rev. Mater.* **2020**, 5, 764-779.
192. Liu, L.; Konstas, K.; Hill, M. R.; Telfer, S. G. *J. Am. Chem. Soc.* **2013**, 135, 17731-17734.
193. Meek, S. T.; Greathouse, J. A.; Allendorf, M. D. *Adv. Mater.* **2011**, 23, 249-267.
194. Mueller, U.; Schubert, M.; Teich, F.; Puetter, H.; Schierle-Arndt, K.; Pastré, J. *J. Mater. Chem.* **2006**, 16, 626-636.

195. Stock, N.; Biswas, S. *Chem. Rev.* **2012**, 112, 933-969.
196. Schaate, A.; Roy, P.; Godt, A.; Lippke, J.; Waltz, F.; Wiebcke, M.; Behrens, P. *Chem. Eur. J.* **2011**, 17, 6643-6651.
197. Sun, Y.; Zhou, H.-C. *Sci. Technol. Adv. Mater.* **2015**, 16, 054202.
198. Uzarevic, K.; Wang, T. C.; Moon, S. Y.; Fidelli, A. M.; Hupp, J. T.; Farha, O. K.; Friscic, T. *Chem. Commun.* **2016**, 52, 2133-2136.
199. Diring, S. P.; Furukawa, S.; Takashima, Y.; Tsuruoka, T.; Kitagawa, S. *Chem. Mater.* **2010**, 22, 4531-4538.
200. Venna, S. R.; Jasinski, J. B.; Carreon, M. A. *J. Am. Chem. Soc.* **2010**, 132, 18030-18033.
201. Liang, P.; Xia, W.-X.; Tian, W.-M.; Yin, X.-H. *Molecules* **2013**, 18, 14826-14839.
202. Al-Kutubi, H.; Gascon, J.; Sudhölter, E. J. R.; Rassaei, L. *ChemElectroChem* **2015**, 2, 462-474.
203. Li, M.; Dincă, M. *J. Am. Chem. Soc.* **2011**, 133, 12926-12929.
204. Khan, N. A.; Jhung, S. H. *Coord. Chem. Rev.* **2015**, 285, 11-23.
205. Klinowski, J.; Paz, F. A.; Silva, P.; Rocha, J. *Dalton Trans.* **2011**, 40, 321-330.
206. Klimakow, M.; Klobes, P.; Thünemann, A. F.; Rademann, K.; Emmerling, F. *Chem. Mater.* **2010**, 22, 5216-5221.
207. James, S. L.; Adams, C. J.; Bolm, C.; Braga, D.; Collier, P.; Friscic, T.; Grepioni, F.; Harris, K. D.; Hyett, G.; Jones, W.; Krebs, A.; Mack, J.; Maini, L.; Orpen, A. G.; Parkin, I. P.; Shearouse, W. C.; Steed, J. W.; Waddell, D. C. *Chem. Soc. Rev.* **2012**, 41, 413-47.
208. Israr, F.; Chun, D.; Kim, Y.; Kim, D. K. *Ultrason. Sonochem.* **2016**, 31, 93-101.
209. Safarifard, V.; Morsali, A. *Coord. Chem. Rev.* **2015**, 292, 1-14.
210. Yang, H. M.; Song, X. L.; Yang, T. L.; Liang, Z. H.; Fan, C. M.; Hao, X. *G. RSC Adv.* **2014**, 4, 15720-15726.
211. Friscic, T.; Reid, D. G.; Halasz, I.; Stein, R. S.; Dinnebier, R. E.; Duer, M. J. *Angew. Chem. Int. Ed.* **2010**, 49, 712-715.
212. Ma, T.-Y.; Li, H.; Deng, Q.-F.; Liu, L.; Ren, T.-Z.; Yuan, Z.-Y. *Chem. Mater.* **2012**, 24, 2253-2255.
213. Baerlocher, C.; McCusker, L. B.; Olson, D. H. *Atlas of Zeolite Framework Types*, 6th rev. ed.; Elsevier Science: Amsterdam, **2007**.

214. García, H.; Navalón, S. *Metal-Organic Frameworks: Applications in Separations and Catalysis*; Wiley-VCH: Weinheim, **2018**.
215. McKinstry, C.; Cussen, E. J.; Fletcher, A. J.; Patwardhan, S. V.; Sefcik, J. *Chem. Eng. J.* **2017**, 326, 570-577.
216. Millange, F.; Serre, C.; Férey, G. *Chem. Commun.* **2002**, 822-823.
217. Férey, G.; Serre, C.; Mello-Draznieks, C.; Millange, F.; Surblé, S.; Dutour, J.; Margiolaki, I. *Angew. Chem. Int. Ed.* **2004**, 43, 6296-6301.
218. Ryu, U.; Jee, S.; Rao, P. C.; Shin, J.; Ko, C.; Yoon, M.; Park, K. S.; Choi, K. M. *Coord. Chem. Rev.* **2021**, 426, 213544.
219. Blay, V.; Bobadilla, L. F.; Cabrera García, A. (Eds.) *Zeolites and Metal-Organic Frameworks: From Lab to Industry*; Amsterdam University Press: Amsterdam, **2018**.
220. Mandal, S.; Natarajan, S.; Mani, P.; Pankajakshan, A. *Adv. Funct. Mater.* **2021**, 31, 2006291.
221. Cohen, S. M. *Chem. Rev.* **2012**, 112, 970-1000.
222. Cohen, S. M. *J. Am. Chem. Soc.* **2017**, 139, 2855-2863.
223. Islamoglu, T.; Goswami, S.; Li, Z.; Howarth, A. J.; Farha, O. K.; Hupp, J. T. *Acc. Chem. Res.* **2017**, 50, 805-813.
224. Evans, J. D.; Sumbly, C. J.; Doonan, C. J. *Chem. Soc. Rev.* **2014**, 43, 5933-5951.
225. Tanabe, K. K.; Cohen, S. M. *Chem. Soc. Rev.* **2011**, 40, 498-519.
226. Du Bois, D. R.; Matzger, A. J. *J. Am. Chem. Soc.* **2021**, 143, 671-674.
227. Fracaroli, A. M.; Siman, P.; Nagib, D. A.; Suzuki, M.; Furukawa, H.; Toste, F. D.; Yaghi, O. M. *J. Am. Chem. Soc.* **2016**, 138, 8352-8355.
228. Deshpande, R. K.; Minnaar, J. L.; Telfer, S. G. *Angew. Chem. Int. Ed.* **2010**, 49, 4598-4602.
229. Ishiwata, T.; Furukawa, Y.; Sugikawa, K.; Kokado, K.; Sada, K. *J. Am. Chem. Soc.* **2013**, 135, 5427-5432.
230. McDonald, K. A.; Feldblyum, J. I.; Koh, K.; Wong-Foy, A. G.; Matzger, A. J. *Chem. Commun.* **2015**, 51, 11994-11996.
231. Park, H. J.; Cheon, Y. E.; Suh, M. P. *Chem. Eur. J.* **2010**, 16, 11662-11669.
232. Zhang, X.; Frey, B. L.; Chen, Y.-S.; Zhang, J. *J. Am. Chem. Soc.* **2018**, 140, 7710-7715.
233. Brozek, C. K.; Dinca, M. *Chem. Soc. Rev.* **2014**, 43, 5456-5467.

234. Fei, H.; Cahill, J. F.; Prather, K. A.; Cohen, S. M. *Inorg. Chem.* **2013**, 52, 4011-4016.
235. Karagiari, O.; Bury, W.; Mondloch, J. E.; Hupp, J. T.; Farha, O. K. *Angew. Chem. Int. Ed.* **2014**, 53, 4530-4540.
236. Lalonde, M.; Bury, W.; Karagiari, O.; Brown, Z.; Hupp, J. T.; Farha, O. K. *J. Mater. Chem. A* **2013**, 1, 5453-5468.
237. Dinca, M.; Long, J. R. *J. Am. Chem. Soc.* **2007**, 129, 11172-11176.
238. Huang, M.; Adnot, A.; Kaliaguine, S. *J. Am. Chem. Soc.* **1992**, 114, 10005-10010.
239. Yaghi, O. M.; Sun, Z.; Richardson, D. A.; Groy, T. L. *J. Am. Chem. Soc.* **1994**, 116, 807-808.
240. Yaghi, O. M.; Li, H.; Davis, C.; Richardson, D.; Groy, T. L. *Acc. Chem. Res.* **1998**, 31, 474-484.
241. Liu, Y.; Kravtsov, V. C.; Larsen, R.; Eddaoudi, M. *Chem. Commun.* **2006**, 1488-1490.
242. Housecroft, C.; Sharpe, A. G. *Inorganic Chemistry*, 2nd ed.; Prentice Hall: New Jersey, **2007**.
243. Deria, P.; Mondloch, J. E.; Karagiari, O.; Bury, W.; Hupp, J. T.; Farha, O. K. *Chem. Soc. Rev.* **2014**, 43, 5896.
244. Lv, L. L.; Yang, J.; Zhang, H. M.; Liu, Y. Y.; Ma, J. F. *Inorg. Chem.* **2015**, 54, 1744.
245. Irving, H.; Williams, R. J. P. *J. Chem. Soc.* **1953**, 3192-3210.
246. Prasad, T. K.; Hong, D. H.; Suh, M. P. *Chem. Eur. J.* **2010**, 16, 14043-14050.
247. Zhang, Z.-J.; Shi, W.; Niu, Z.; Li, H.-H.; Zhao, B.; Cheng, P.; Liao, D.-Z.; Yan, S.-P. *Chem. Commun.* **2011**, 47, 6425-6427.
248. Wang, X.-J.; Li, P.-Z.; Liu, L.; Zhang, Q.; Borah, P.; Wong, J. D.; Chan, X. X.; Rakesh, G.; Li, Y.; Zhao, Y. *Chem. Commun.* **2012**, 48, 10286-10288.
249. Yao, Q.; Sun, J.; Li, K.; Su, J.; Peskov, M. V.; Zou, X. *Dalton Trans.* **2012**, 41, 3953-3955.
250. Song, X.; Jeong, S.; Kim, D.; Lah, M. S. *CrystEngComm* **2012**, 14, 5753-5756.
251. Wang, J.-H.; Zhang, Y.; Li, M.; Yan, S.; Li, D.; Zhang, X.-M. *Angew. Chem. Int. Ed.* **2017**, 56, 6478-6482.

252. Brozek, C. K.; Bellarosa, L.; Soejima, T.; Clark, T. V.; López, N.; Dincă, M. *Chem. Eur. J.* **2014**, *20*, 6871-6874.
253. Tu, B.; Pang, Q.; Wu, D.; Song, Y.; Weng, L.; Li, Q. *J. Am. Chem. Soc.* **2014**, *136*, 14465-14468.
254. Guo, M.; Cai, H.-L.; Xiong, R.-G. *Inorg. Chem. Commun.* **2010**, *13*, 1590-1598.
255. Howarth, A. J.; Peters, A. W.; Vermeulen, N. A.; Wang, T. C.; Hupp, J. T.; Farha, O. K. *Chem. Mater.* **2017**, *29*, 26-39.
256. Mondloch, J. E.; Karagiari, O.; Farha, O. K.; Hupp, J. T. *CrystEngComm* **2013**, *15*, 9258-9264.
257. Suga, M.; Asahina, S.; Sakuda, Y.; Kazumori, H.; Nishiyama, H.; Nokuo, T.; Alfredsson, V.; Kjellman, T.; Stevens, S. M.; Cho, H. S.; Cho, M.; Han, L.; Che, S.; Anderson, M. W.; Schüth, F.; Deng, H.; Yaghi, O. M.; Liu, Z.; Jeong, H. Y.; Stein, A.; Sakamoto, K.; Ryoo, R.; Terasaki, O. *Prog. Solid State Chem.* **2014**, *42*, 1-2.
258. Wiktor, C.; Meledina, M.; Turner, S.; Lebedev, O. I.; Fischer, R. A. *J. Mater. Chem. A* **2017**, *5*, 14969-14989.
259. Wang, T. C.; Vermeulen, N. A.; Kim, I. S.; Martinson, A. B. F.; Stoddart, J. F.; Hupp, J. T.; Farha, O. K. *Nat. Protoc.* **2016**, *11*, 149-162.
260. Hoffmann, H.; Debowski, M.; Müller, P.; Paasch, S.; Senkowska, I.; Kaskel, S.; Brunner, E. *Materials* **2012**, *5*, 2537-2572.
261. Huang, A.; Huang, Y. *Solid State Nucl. Magn. Reson.* **2013**, 49-50.
262. Gul-E-Noor, F.; Mendt, M.; Michel, D.; Pöppel, A.; Krautscheid, H.; Haase, J.; Bertmer, M. *J. Phys. Chem. C* **2013**, *117*, 7703-7712.
263. Rimoldi, M.; Nakamura, A.; Vermeulen, N. A.; Henkelis, J. J.; Blackburn, A. K.; Hupp, J. T.; Stoddart, J. F.; Farha, O. K. *Chem. Sci.* **2016**, *7*, 4980-4984.
264. Li, Q.; Zhang, W.; Miljanic, O. S.; Sue, C. H.; Zhao, Y. L.; Liu, L.; Knobler, C. B.; Stoddart, J. F.; Yaghi, O. M. *Science* **2009**, *325*, 855-859.
265. Virmani, E.; Beyer, O.; Luning, U.; Ruschewitz, U.; Wuttke, S. *Mater. Chem. Front.* **2017**, *1*, 1965-1974.
266. Lippke, J.; Brosent, B.; von Zons, T.; Virmani, E.; Lilienthal, S.; Preuß, T.; Hulsmann, M.; Schneider, A. M.; Wuttke, S.; Behrens, P.; Godt, A. *Inorg. Chem.* **2017**, *56*, 748-761.

267. Cubillas, P.; Anderson, M. W.; Attfield, M. P. *Chem. Eur. J.* **2012**, *18*, 15406-15415.
268. Hirschle, P.; Preiß, T.; Auras, F.; Pick, A.; Vçlkner, J.; Valdepørez, D.; Witte, G.; Parak, W. J.; Rädler, J. O.; Wuttke, S. *CrystEngComm* **2016**, *18*, 4359-4368.
269. Maia, R. A.; Carneiro, L. S. D. A.; Cifuentes, J. M. C.; Buarque, C. D.; Esteves, P. M.; Percebom, A. M. J. *Appl. Crystallogr.* **2020**, *53*, 1376-1386.
270. Giacovazzo, C. *Fundamentals of Crystallography*, 3rd ed.; Oxford University Press: Oxford, **2014**.
271. Rowsell, J. L. C.; Spencer, E. C.; Eckert, J.; Howard, J. A. K.; Yaghi, O. M. *Science* **2005**, *309*, 1350-1354.
272. Furukawa, H.; Gañdara, F.; Zhang, Y.-B.; Jiang, J.; Queen, W. L.; Hudson, M. R.; Yaghi, O. M. *J. Am. Chem. Soc.* **2014**, *136*, 4369-4381.
273. Julien, P. A.; Uzarević, K.; Katsenis, A. D.; Kimber, S. A. J.; Wang, T.; Farha, O. K.; Zhang, Y.; Casaban, J.; Germann, L. S.; Etter, M.; Dinnebier, R. E.; James, S. L.; Halasz, I.; Frisčić, T. *J. Am. Chem. Soc.* **2016**, *138*, 2929-2932.
274. Huang, Z.; Grape, E. S.; Li, J.; Inge, A. K.; Zou, X. *Coord. Chem. Rev.* **2021**, *427*, 213583.
275. Mason, J. A.; Sumida, K.; Herm, Z. R.; Krishna, R.; Long, J. R. *Energy Environ. Sci.* **2011**, *4*, 3030-3040.
276. Gándara, F.; Bennett, T. D. *IUCrJ* **2014**, *1*, 563-570.
277. Wu, H.; Yang, J.; Su, Z.-M.; Batten, S. R.; Ma, J.-F. *J. Am. Chem. Soc.* **2011**, *133*, 11406-11409.
278. McHugh, L. N.; McPherson, M. J.; McCormick, L. J.; Morris, S. A.; Wheatley, P. S.; Teat, S. J.; McKay, D.; Dawson, D. M.; Sansome, C. E. F.; Ashbrook, S. E.; Stone, C. A.; Smith, M. W.; Morris, R. E. *Nat. Chem.* **2018**, *10*, 1096-1102.
279. Zhang, X.; Chen, Z.; Liu, X.; Hanna, S. L.; Wang, X.; Taheri-Ledari, R.; Maleki, A.; Li, P.; Farha, O. K. *Chem. Soc. Rev.* **2020**, *49*, 7406-7427.
280. Thommes, M.; Kaneko, K.; Neimark, A. V.; Olivier, J. P.; Rodriguez-Reinoso, F.; Rouquerol, J.; Sing, K. S. W. *Pure Appl. Chem.* **2015**, *87*, 1051-1069.

281. Thommes, M. *Chem. Ing. Tech.* **2010**, 82, 1059-1073.
282. Carrington, E. J.; McAnally, C. A.; Fletcher, A. J.; Thompson, S. P.; Warren, M.; Brammer, L. *Nat. Chem.* **2017**, 9, 882-889.
283. Möllmer, J.; Celer, E. B.; Luebke, R.; Cairns, A. J.; Staudt, R.; Eddaoudi, M.; Thommes, M. *Microporous Mesoporous Mater.* **2010**, 129, 345-353.
284. Tsao, C. S.; Yu, M. S.; Chung, T. Y.; Wu, H. C.; Wang, C. Y.; Chang, K. S.; Chen, H. L. *J. Am. Chem. Soc.* **2007**, 129, 15997-16004.
285. Beurroies, I.; Boulhout, M.; Llewellyn, P. L.; Kuchta, B.; FØrey, G.; Serre, C.; Denoyel, R. *Angew. Chem. Int. Ed.* **2010**, 49, 7526-7529
286. Song, Q.; Nataraj, S. K.; Roussenova, M. V.; Tan, J. C.; Hughes, D. J.; Li, W.; Bourgoïn, P.; Alam, M. A.; Cheetham, A. K.; Al-Muhtaseb, S. A.; Sivaniah, E. *Energy Environ. Sci.* **2012**, 5, 8359-8369.
287. Kitagawa, S.; Kitaura, R.; Noro, S.-I. *Angew. Chem. Int. Ed.* **2004**, 43, 2334-2375.
288. Janiak, C. *Dalton Trans.* **2003**, 2781-2804.
289. Kahn, O.; Pei, Y.; Verdaguer, M.; Renard, J. P.; Sletten, J. *J. Am. Chem. Soc.* **1988**, 110, 782-789.
290. Pei, Y.; Verdaguer, M.; Kahn, O.; Sletten, J.; Renard, J. P. *J. Am. Chem. Soc.* **1986**, 108, 7428-7430.
291. Pei, Y.; Verdaguer, M.; Kahn, O.; Sletten, J.; Renard, J.-P. *Inorg. Chem.* **1987**, 26, 138-143.
292. Pardo, E.; Ruiz-García, R.; Cano, J.; Ottenwaelder, X.; Lescouëzec, R.; Journaux, Y.; Lloret, F.; Julve, M. *Dalton Trans.* **2008**, 0, 2780-2805.
293. Dul, M.-C.; Pardo, E.; Lescouëzec, R.; Journaux, Y.; Ferrando-Soria, J.; Ruiz-García, R.; Cano, J.; Julve, M.; Lloret, F.; Cangussu, D.; Pereira, C. L. M.; Stumpf, H. O.; Pasán, J.; Ruiz-Pérez, C. *Coord. Chem. Rev.* **2010**, 254, 2281-2296.
294. Ruiz, R.; Faus, J.; Lloret, F.; Julve, M.; Journaux, Y. *Coord. Chem. Rev.* **1999**, 193-195, 1069-1117.
295. Ferrando-Soria, J.; Grancha, T.; Julve, M.; Cano, J.; Lloret, F.; Journaux, Y.; Pasán, J.; Ruiz-Pérez, C.; Pardo, E. *Chem. Commun.* **2012**, 48, 3539-3541.

296. Pardo, E.; Morales-Osorio, I.; Julve, M.; Lloret, F.; Cano, J.; Ruiz-García, R.; Pasán, J.; Ruiz-Pérez, C.; Ottenwaelder, X.; Journaux, Y. *Inorg. Chem.* **2004**, 43, 7594-7596.
297. Ferrando-Soria, J.; Pardo, E.; Ruiz-García, R.; Cano, J.; Lloret, F.; Julve, M.; Journaux, Y.; Pasán, J.; Ruiz-Pérez, C. *Chem. Eur. J.* **2011**, 17, 2176-2188.
298. Pardo, E.; Ruiz-García, R.; Lloret, F.; Faus, J.; Julve, M.; Journaux, Y.; Novak, M. A.; Delgado, F. S.; Ruiz-Pérez, C. *Chem. Eur. J.* **2007**, 13, 2054-2066.
299. Kahn, O. *Molecular Magnetism*; VCH Publishers: New York, NY, **1993**.
300. Ojima, H.; Nonoyama, K. *Coord. Chem. Rev.* **1988**, 92, 85-111.
301. Ferrando-Soria, J.; Pasán, J.; Ruiz-Pérez, C.; Journaux, Y.; Julve, M.; Lloret, F.; Cano, J.; Pardo, E. *Inorg. Chem.* **2011**, 50, 8694-8696.
302. Grancha, T.; Mon, M.; Lloret, F.; Ferrando-Soria, J.; Journaux, Y.; Pasán, J.; Pardo, E. *Inorg. Chem.* **2015**, 54, 8890-8892.
303. Nakatani, K.; Carriat, J. Y.; Journaux, Y.; Kahn, O.; Floret, F.; Renard, J. P.; Pei, Y.; Sletten, J.; Verdagner, M. *J. Am. Chem. Soc.* **1989**, 111, 5739-5748.
304. Journaux, Y.; Ruiz, R.; Aukauloo, A.; Pei, Y. *Mol. Cryst. Liq. Cryst.* **1997**, 305, 193-202.
305. Grancha, T.; Ferrando-Soria, J.; Castellano, M.; Julve, M.; Pasán, J.; Armentano, D.; Pardo, E. *Chem. Commun.* **2014**, 50, 7569-7585.
306. Ferrando-Soria, J.; Grancha, T.; Pasán, J.; Ruiz-Pérez, C.; Cañadillas-Delgado, L.; Journaux, Y.; Julve, M.; Cano, J.; Lloret, F.; Pardo, E. *Inorg. Chem.* **2012**, 51, 7019-7021.
307. Pereira, C. L. M.; Pedroso, E. F.; Stumpf, H. O.; Novak, M. A.; Ricard, L.; Ruiz-García, R.; Rivière, E.; Journaux, Y. *Angew. Chem. Int. Ed.* **2004**, 43, 956-958.
308. Ferrando-Soria, J.; Ruiz-García, R.; Cano, J.; Stiriba, S.-E.; Vallejo, J.; Castro, I.; Julve, M.; Lloret, F.; Amorós, P.; Pasán, J.; Ruiz-Pérez, C.; Journaux, Y.; Pardo, E. *Chem. Eur. J.* **2012**, 18, 1608-1617.
309. Grancha, T.; Acosta, A.; Cano, J.; Ferrando-Soria, J.; Seoane, B.; Gascon, J.; Pasán, J.; Armentano, D.; Pardo, E. *Inorg. Chem.* **2015**, 54, 10834-10840.

310. Grancha, T.; Ferrando-Soria, J.; Zhou, H.-C.; Gascon, J.; Seoane, B.; Pasán, J.; Fabelo, O.; Julve, M.; Pardo, E. *Angew. Chem. Int. Ed.* **2015**, 54, 6521-6525.
311. Ferrando-Soria, J.; Serra-Crespo, P.; de Lange, M.; Gascon, J.; Kapteijn, F.; Julve, M.; Cano, J.; Lloret, F.; Pasán, J.; Ruiz-Pérez, C.; Journaux, Y.; Pardo, E. *J. Am. Chem. Soc.* **2012**, 134, 15301-15304.
312. Tiburcio, E.; Greco, R.; Mon, M.; Ballesteros-Soberanas, J.; Ferrando-Soria, J.; López-Haro, M.; Hernández-Garrido, J. C.; Oliver-Meseguer, J.; Marini, C.; Boronat, M.; Armentano, D.; Leyva-Pérez, A.; Pardo, E. *J. Am. Chem. Soc.* **2021**, 143, 6, 2581-2592.
313. Greco, R.; Tiburcio-Fortes, E.; Fernandez, A.; Marini, C.; Vidal-Moya, A.; Oliver-Meseguer, J.; Armentano, D.; Pardo, E.; Ferrando-Soria, J.; Leyva-Pérez, A. *Chem. Eur. J.* **2022**, 28, e202103781.
314. Grancha, T.; Qu, X.; Julve, M.; Ferrando-Soria, J.; Armentano, D.; Pardo, E. *Inorg. Chem.* **2017**, 56, 6551-6557.
315. Grancha, T.; Ferrando-Soria, J.; Cano, J.; Amorós, P.; Seoane, B.; Gascon, J.; Bazaga-García, M.; Losilla, E. R.; Cabeza, A.; Armentano, D.; Pardo, E. *Chem. Mater.* **2016**, 28, 4608-4615.
316. Grancha, T.; Ferrando-Soria, J.; Cano, J.; Lloret, F.; Julve, M.; De Munno, G.; Armentano, D.; Pardo, E. *Chem. Commun.* **2013**, 49, 5942-5944.
317. Ferrando-Soria, J.; Castellano, M.; Ruiz-García, R.; Cano, J.; Julve, M.; Lloret, F.; Pasán, J.; Ruiz-Pérez, C.; Cañadillas-Delgado, L.; Li, Y.; Journaux, Y.; Pardo, E. *Chem. Commun.* **2012**, 48, 8401-8403.
318. Castellano, M.; Ruiz-García, R.; Cano, J.; Julve, M.; Lloret, F.; Journaux, Y.; De Munno, G.; Armentano, D. *Chem. Commun.* **2013**, 49, 3534-3536.
319. Castellano, M.; Ferrando-Soria, J.; Pardo, E.; Julve, M.; Lloret, F.; Mathonière, C.; Pasán, J.; Ruiz-Pérez, C.; Cañadillas-Delgado, L.; Ruiz-García, R.; Cano, J. *Chem. Commun.* **2011**, 47, 11035-11037.
320. Fortea-Pérez, F. R.; Schlegel, I.; Julve, M.; Armentano, D.; De Munno, G.; Stiriba, S.-E. *J. Organomet. Chem.* **2013**, 743, 102-108.
321. Pim, W. D. do; Oliveira, W. X. C.; Ribeiro, M. a; Faria, E. N. de; Teixeira, I. F.; Stumpf, H. O.; Lago, R. M.; Pereira, C. L. M.; Pinheiro, C. B.; Figueiredo-Júnior, J. C. D.; Nunes, W. C.; Souza, P. P. de;

- Pedroso, E. F.; Castellano, M.; Cano, J.; Julve, M. *Chem. Commun.* **2013**, 49, 10778-10780.
322. Mon, M.; Lloret, F.; Ferrando-Soria, J.; Martí-Gastaldo, C.; Armentano, D.; Pardo, E. *Angew. Chem. Int. Ed.* **2016**, 55, 11167-11172.
323. Mon, M.; Ferrando-Soria, J.; Verdaguer, M.; Train, C.; Paillard, C.; Dkhil, B.; Versace, C.; Bruno, R.; Armentano, D.; Pardo, E. *J. Am. Chem. Soc.* **2017**, 139, 8098-8101.
324. Mon, M.; Bruno, R.; Tiburcio, E.; Grau-Atienza, A.; Sepúlveda-Escribano, A.; Ramos-Fernández, E. V.; Fuoco, A.; Esposito, E.; Monteleone, M.; Jansen, J. C.; Cano, J.; Ferrando-Soria, J.; Armentano, D.; Pardo, E. *Chem. Mater.* **2019**, 31, 5856–5866.
325. Grancha, T.; Mon, M.; Ferrando-Soria, J.; Gascon, J.; Seoane, B.; Ramos-Fernández, E. V.; Armentano, D.; Pardo, E. *J. Mater. Chem. A* **2017**, 5, 11032–11039.
326. Mon, M.; Bruno, R.; Elliani, R.; Tagarelli, A.; Qu, X.; Chen, S.; Ferrando-Soria, J.; Armentano, D.; Pardo, E. *Inorg. Chem.* **2018**, 57, 13895–13900.
327. Mon, M.; Ferrando-Soria, J.; Grancha, T.; Fortea-Pérez, F. R.; Gascon, J.; Leyva-Pérez, A.; Armentano, D.; Pardo, E. *J. Am. Chem. Soc.* **2016**, 138, 7864–7867.
328. Mon, M.; Bruno, R.; Tiburcio, E.; Casteran, P. E.; Ferrando-Soria, J.; Armentano, D.; Pardo, E. *Chem. Eur. J.* **2018**, 24, 17712–17718.
329. Mon, M.; Bruno, R.; Tiburcio, E.; Viciano-Chumillas, M.; Kalinke, L. H. G.; Ferrando-Soria, J.; Armentano, D.; Pardo, E. *J. Am. Chem. Soc.* **2019**, 141, 13601–13609.



2. MOFs AND MTV-MOFs FOR CATALYSIS

2.1. Introduction

Overall, this chapter pursued two main objectives. Firstly, we aimed to investigate the nature of catalytically active species and reaction mechanisms by taking advantage of the steric constraint effects induced by the MOF network to examine changes in reactivity of organometallic catalysts. Secondly, inspired by the active centers of enzymes, where different organic functionalities can act synergetically, we explored the effects on catalytic reactions of industrial relevance, of the presence of functional channels decorated with more than one distinct amino acid residues in a family of isorecticular 3D MOFs.

The development of catalytic and selective methods for oxidation reactions is crucial in organic synthesis. Among several oxidizing systems,¹ metal-catalyzed methodologies² have experienced tremendous growth and application over the years. One of the most notable examples is the VO(acac)₂/TBHP (vanadyl acetylacetonate/tert-butyl hydroperoxide) system,³ developed by Sharpless and Michaelson, for the highly regio- and stereoselective epoxidation of allylic alcohols.⁴ However, to the best of our knowledge, this system has not yet been precisely atomically characterized, which limits our understanding of the rationalization of structure-property relationships.⁵

In this context, we present the PSI of the vanadyl acetylacetonate complex VO(acac)₂ within a preformed MOF of formula {Ca^{II}Cu^{II}}_6 [(S, S)-methiomox]₃(OH)₂(H₂O)} · 16H₂O, to obtain a hybrid material as a heterogeneous catalyst for the epoxidation and dehydrogenation of allylic alcohols.⁶ (**Publication 1.** Epoxidation vs dehydrogenation of allylic alcohols: heterogenization of the VO(acac)₂ catalyst in a Metal-Organic Framework).

On the other hand, the addition of alcohols to the carbonyl group of aldehydes and ketones is an important reaction in both nature⁷ and industrial synthesis,⁸ since it can alter the electronic density of the

carbonyl group from electron-rich to electron-poor. Hemiketalization and ketalization reactions are commonly used in organic synthesis to protect aldehyde and ketone groups during other reactions.⁹ However, the acid-catalyzed conditions required for these reactions are not always compatible with other functional groups, which must be previously protected by alternative methods.¹⁰ In nature, this issue is resolved by using non-acid enzymes, such as glycosidases, which catalyze hemiketalization and ketalization reactions through the cooperative action of two different pocketed base groups, *i.e.* carboxylates.¹¹

In this study, we introduce a family of isorecticular MOFs, derived from amino acids, and investigate the impact of the number and nature of functional groups decorating the channels on the catalytic activity of (hemi)-ketalization reactions of various simple carbonyl compounds. (**Publication 2.** Exploring the role of amino acid-derived Multivariate-Metal-Organic Frameworks as catalyst in (hemi)-ketalization reactions).

2.2. References

1. Trost, B. M.; Fleming, I. *Comprehensive Organic Synthesis: Selectivity, Strategy, and Efficiency in Modern Organic Chemistry*, 7th ed.; Pergamon Press: Oxford, **1991**.
2. Mijs, W. J.; de Jonge, C. R. H. I. *Organic Syntheses by Oxidation with Metal Compounds*; Mijs, W. J., de Jonge, C. R. H. I., Eds.; Plenum Press: New York, **1986**.
3. Hirao, T. *Chem. Rev.* **1997**, 97, 2707–2724.
4. Sharpless, K. B.; Michaelson, R. C. *J. Am. Chem. Soc.* **1973**, 95, 6136–6137.
5. Lattanzi, A.; Leadbeater, N. E. *Org. Lett.* **2002**, 4, 1519–1521.
6. Jeoung, S.; Kim, S.; Kim, M.; Moon, H. R. *Coord. Chem. Rev.* **2020**, 420, 213377.
7. Sinnott, M. L. *Chem. Rev.* **1990**, 90, 1171–1202.
8. Ruiz, V. R.; Velty, A.; Santos, L. L.; Leyva-Pérez, A.; Sabater, M. J.; Iborra, S.; Corma, A. *J. Catal.* **2010**, 271, 351–357.
9. Ley, S. V.; Polara, A. J. *Org. Chem.* **2007**, 72, 5943–5959.
10. Veitch, G. E.; Beckmann, E.; Burke, B. J.; Boyer, A.; Maslen, S. L.; Ley, S. V. *Angew. Chem. Int. Ed.* **2007**, 46, 7629–7632.
11. Davies, G.; Henrissat, B. *Structure* **1995**, 3, 853–859.

2.3. Epoxidation vs Dehydrogenation of Allylic Alcohols: Heterogenization of the VO(acac)₂ Catalyst in a Metal-Organic Framework (Publication 1)

Allylic alcohol epoxidation and dehydrogenation reactivity is distinguished when VO(acac)₂ is used in solution or anchored in a Metal-Organic Framework (MOF). The chemical mechanism depends on the electronic profile of alkene substituents when the vanadyl complex is used in homogenous phase. However, confinement effects imparted by MOF channels allow to gain control on the chemoselectivity toward the dehydrogenation product.

2.3.1. Introduction

The development of catalytic and selective methods for oxidation reactions is extremely important in organic synthesis. Among several oxidizing systems,¹ metal-catalysed methodologies² have experienced ever increasing growth and application over the years. One of the best examples reported so far is the VO(acac)₂/TBHP system,³ developed by Sharpless and Michaelson, for the highly regio- and stereoselective epoxidation of allylic alcohols.⁴ This catalytic system has been also extensively employed in a wide plethora of reactions,⁵ such as the chemoselective dehydrogenation of acyclic and cyclic secondary alcohols to the corresponding ketones,⁶ or the oxidation of *o*-alkenyl phenols to *o*-hydroxybenzyl ketones.⁷ However, to the best of our knowledge, it has not been clearly specified yet the exact conditions where the corresponding epoxidation or alcohol dehydrogenation takes place.

Metal-Organic Frameworks⁸ (MOFs) have blossomed in recent years in catalysis as a direct consequence of their unique characteristics,⁹ such as a fascinating host-guest chemistry¹⁰ and the possibility to use single-crystal X-ray diffraction (SC-XRD)¹¹ to unveil the nature of

catalytically active species and reaction mechanisms.¹² MOFs catalytic activity can be originated intrinsically -arising from open metal sites and/or the organic linkers constituting the coordination network-, extrinsically -emerging from guest active species hosted in their channels^{11,13-} and a synergic combination of both of them.¹² Dealing with guest active species, different examples showing the encapsulation of active metal-based species of different chemical nature and nuclearity have been reported recently.¹²⁻¹⁵ This matrix-isolation strategy^{11,13} offers clear benefits over homogenous solution, such as structural characterisation and higher reusability.¹⁵ However, much work needs to be done to understand how chemical and steric environment offered by the host matrix affects the chemical nature of guest species and the concomitant effects on their catalytic activity.

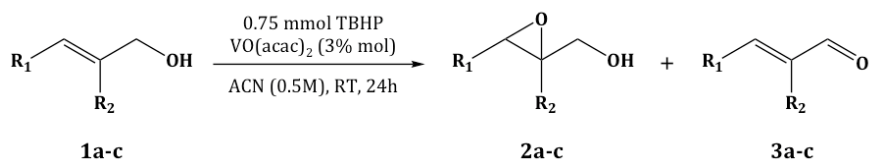
Here, we aim to shed light on both open questions. Thus, firstly, we demonstrate that when VO(acac)₂ is in solution, the selection of the reaction pathway of allylic alcohols with TBHP -underpinned by activation energy evaluations- depends on the electronic profile (electron donating/withdrawing groups) of alkene substituents, which set the preference toward either the corresponding epoxide or aldehyde product. Then, we present the post-synthetic insertion of VO(acac)₂ within a preformed MOF of formula {Ca^{II}Cu^{II}₆ [(*S,S*)-methox]₃(OH)₂(H₂O)} · 16H₂O (**4**) (methox = (*S,S*)- oxaloyl- bis (*N*-methioninate)),^{16,17} to lead to the hybrid material [V^{IV}O (acac) (H₂O)]@ {Ca^{II}Cu^{II}₆ [(*S,S*)-methox]₃(OH)₃} · 8H₂O (**VO(acac)(H₂O)@4**), whose crystal structure is unveiled by single-crystal X-ray crystallography. The confinement effect of MOFs channels in **VO(acac)(H₂O)@4** plays a key role, considerably reducing the substrate-dependence and imparting a preference toward the less-sterically demanding dehydrogenation reaction.

2.3.2. Results and Discussion

VO(acac)₂ is able to catalyse the epoxidation and the dehydrogenation of allylic alcohols.¹⁸ However, as far as we know, a structure-activity relationship has not been clearly specified in the open literature. A plausible reaction mechanisms for both reactions, could indicate that the coordination either of the alkene or final alcohol functionalities to the vanadyl site dictates the final reaction (Figure S1, ESI†).¹⁹ In order to confirm the absence of one of the acac ligands in the active species, we performed the reaction using 1 equivalent of extra acac⁻ ligand (Figure S2a, ESI†). The low conversion obtained can be attributed to the saturated positions of the VO(acac)⁺, blocking the position to the allylic alcohol. Moreover, acac ligand signals were observed by NMR in the reaction solution (Figure S2b, ESI†). With these mechanisms in hand, electron donating groups (EDG) on the alkene (R) should favour coordination of the alkene to the vanadyl and epoxidation, while electron withdrawing groups (EWG) should favour alcohol coordination and dehydrogenation.

Figure 1 shows the results obtained for the reaction of different allyl alcohols with TBHP in the presence of VO(acac)₂, under typical reaction conditions.⁴ We observe that the product obtained for allyl alcohol **1a** with an aliphatic substituent, is epoxide **2a** (Figure 1). On the contrary, the major product for allyl alcohol **1b** with an aromatic substituent is aldehyde **3b** (Figure 1). Interestingly, when an additional CH₃ group substituent is present in the allylic alcohol, the selectivity of **1c** reverts back to the epoxidation product **2c**, although in very low yield (Figure 1). Blank experiments for compound **1b**, without catalyst and with **4**, showed reaction conversions below 8 % and 15 %, respectively (Table S1, ESI†).

2. MOFs AND MTV-MOFs FOR CATALYSIS



	R ¹	R ²	Conversion %	Selectivity 2 %	Selectivity 3 %
1a	Propyl	H	90.3	97.9	2.1
1b	Ph	H	87.7	22.9	77.1
1c	Ph	Me	8.6	51.3	48.7

Figure 1. Reaction scheme for allylic alcohol epoxidation/dehydrogenation of aliphatic **1a**, aromatic **1b**, and both aliphatic and aromatic allylic alcohol **1c**. ACN: acetonitrile.

With the aim to rationalize these results, we have evaluated the activation energy for both reactions in substrates containing either an aliphatic (EDG) or aromatic (EWG) substituent (Figures S3-S5, ESI† for complete calculations). We obtained that the epoxidation was favoured by almost 60 KJ mol⁻¹ respect to the dehydrogenation for 2-hexenol (**1a**) (Figures S3a and S4, ESI†), 28.9 and 88.6 KJ·mol⁻¹, respectively. However, this was inverted for cinnamyl alcohol **1b**, where the dehydrogenation showed an activation energy of 50.3 KJ mol⁻¹ while the epoxidation was less favoured (53.9 KJ mol⁻¹, Figures S3b and S5, ESI† for complete calculations). Thus, these energetic differences explain why changing the benzene by an alkyl substituent (**1a**), or just adding a methyl substituent in the other carbon atom of the alkene (**1c**), the reactivity can be reversed so easily from the dehydrogenation to the epoxidation.

Considering these findings, we have extended our study to different starting materials with modulated electronics of substituents (Figure S6, ESI†), where we further confirm the observed trend. Thus, with these results in hand, it seems that the epoxidation vs dehydrogenation reaction of allylic alcohols catalysed by VO(acac)₂, in solution, is natively controlled by the substrate, which leave little room for improvement.

Heterogenization of metal Schiff base catalyst has attracted great interest in recent years,²⁰ being mostly used to improve the performance of hydrogen peroxide as an oxidant for alkene epoxidation.^{21,22} Among them, expanded research has been performed on vanadium Schiff base complexes, owing to its amazing structural features and catalytic purpose.²³ However, as far as we know, despite the interest, the ultimate catalyst after VO(acac)₂ heterogenization in MOFs have not been atomically-precisely well-characterised, which limit the knowledge on the real active catalyst and difficult the rationalization of structure-properties relationships.²⁴

In this work, we report the postsynthetic²⁵ insertion of the vanadyl acetylacetonate complex VO(acac)₂¹⁸ within the preformed MOF **4**^{16,17} (Figure 2). MOF **4** present functional hexagonal channels decorated by the highly flexible ethylenethiomethyl chains of the methionine amino acid (Figure 2a), which are prone for a high loading of vanadyl complexes. This results in a homogenous distribution of them along the pores, anchored to these functional thioalkyl groups, as confirmed by SC-XRD, to lead to [V^{IV}O(acac)(H₂O)] @ {Ca^{II}Cu^{II}₆ [(S, S)-methox]₃(OH)₃} · 8H₂O (**VO(acac)(H₂O)**@**4**). **VO(acac)(H₂O)**@**4** was synthesised by soaking crystals of **4** in an acetonitrile solution of the VO(acac)₂ complex during three days in open air (see Experimental Section, ESI†). This insertion process was followed through ICP-MS and SEM-EDX (Table S2, ESI†).

VO(acac)(H₂O)@**4** was crystallized in the chiral *P*6₃ space group of the hexagonal system (Table S3, ESI†) like the precursor **4** (Figure 2). The crystal structure of **VO(acac)(H₂O)**@**4** allowed to confirm the presence of VO(acac)(H₂O)⁺ moieties, being recognized by the flexible²⁶ thioether arms of the methionine residues and confined into the channels through S··vanadyl interactions (Figures 2b-d). In this complex vanadium is penta-coordinated (Figure 2d), linked by one acac ligand, a terminal solvent molecule and being grasped by sulfur atom from methionine amino acid residues (Figures S6-S10,

ESI†). The vanadium environment is highly distorted, resembling a trigonal bipyramidal geometry with a very bent apical position occupied by water molecule. This is likely because of the steric constraints imposed by the network (Figure S9, ESI†). The values of VO-acac bond lengths [2.00(3) and 2.01(3) Å] are in agreement with previously reported ones.²⁷ On the contrary, the vanadium...S [2.83(10) Å] and vanadyl...O_{water} [2.69(14) Å] bond distances are longer than those reported so far.^{28,29} A second water molecule reside close to the VO(acac)(H₂O) moiety at a distance of 2.96(3) Å, longer than expected, but still low than sum of van der Waals radius (Figure S10, ESI†).

Complementary to the above described structural characterization, the chemical nature of the final host-guest adsorbate **VO(acac)(H₂O)@4** was also determined by different characterization techniques. The atom composition was established by elemental (C, H, S, N) analysis, SEM-EDX and ICP-MS (ESI†). The integrity of the framework and solvent contents were established by PXRD and TGA (Figures S12 and S13, ESI†). The oxidation state of vanadium atoms was definitively established by XPS (Figure S14, ESI†). N₂ adsorption isotherm at 77 K revealed the permanent microporosity of **VO(acac)(H₂O)@4** (Figure S15, ESI†).

The XPS spectra of **VO(acac)(H₂O)@4** and VO(acac)₂ (Figure S14, ESI†), showed identical binding energy (BE) of 516.6 eV (V2p_{3/2} line) in both cases, which confirms the V(IV)-valence state in **VO(acac)(H₂O)@4**, as previously reported.³⁰ This can be extended to V2p_{1/2} and O1s bands (Figure S14, ESI†), exhibiting similar BEs, further confirming the proposed oxidation state (IV).

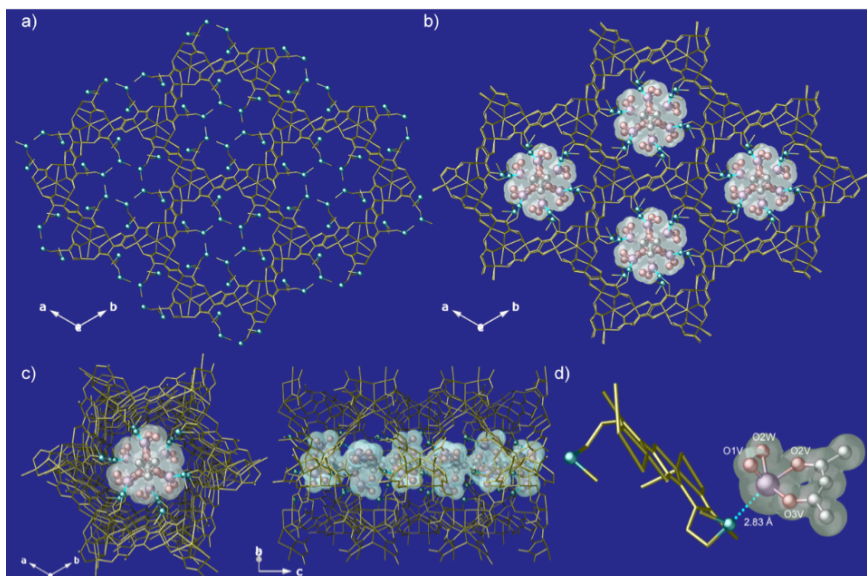


Figure 2. Views of the 3D open-framework of **4** (a) and **VO(acac)(H₂O)@4** (b) along the *c*-axis (crystallization water molecules are omitted for clarity). The 3D network is depicted as gold sticks, with the only exception of sulphur atoms, which are represented as blue spheres. For the guest **VO(acac)(H₂O)⁺** species hosted in the channels (b), vanadium, carbon and oxygen atoms are represented as purple, grey and red spheres, respectively. Surfaces are used to highlight these guest species. c) Top (left) and side (right) perspective views of a single channel of **VO(acac)(H₂O)@4**. (d) Fragment of **VO(acac)(H₂O)@4** emphasising the host-guest interactions. Dashed blue lines represent the S...V interaction.

VO(acac)(H₂O)@4 can be seen as a pre-activated catalyst, which has already released the unnecessary acac⁻ ligand, but influenced by the constraints of MOF channels. Thus, it could be expected that the less sterically-demanding dehydrogenation reaction takes preferentially. Indeed, Figure 3 shows an increase in the selectivity towards the dehydrogenation of allylic alcohols not only with EWG substituents (products **3b** and **3f**) but also with EDG (products **3a** and **3e**). Thus, it can be said that the MOF structure allows for control the chemoselectivity of the reaction beyond the native structure of the reactant allylic alcohol toward the dehydrogenation product. This selectivity is not total, and some substrate-control persists and, for instance, the methyl substituent in **1c** is still enough to increase the selectivity towards the epoxide. But, when the substituent is larger (**1i**), the EWG benzene is sufficient to reverse the selectivity to the dehydrogenation (see Figure S16, ESI† for comparison between VO(acac)₂ and **VO(acac)(H₂O)@4**). The better reactivity of **1c** and **1g** with **VO(acac)(H₂O)@4** may be explained by any sort of favoured *p*-interactions between the aromatic part of substrates and the catalytic site within the MOF channels. However, compounds **1b** and **1f** does not react so efficiently. Thus, it is difficult at this point to explain the different reactivity on the basis of selective adsorptions on the catalytic site.

No leaching processes were observed during reaction (Figure S17, ESI†). **VO(acac)(H₂O)@4** could be reused up to seven times for the epoxidation of **1c** without depletion in the final yield, while retaining the crystallinity as PXRD supported (Figure S12c, ESI†). The presence of the active species within the MOF and the stability of **VO(acac)(H₂O)@4** during the reaction was checked by FT-IR (Figures S18 and S19, ESI†). We observed an oxidation of the sulphur groups when the reaction proceeds in low yields. In the reaction of **1i** appear new peaks at 1207 and 1440 cm⁻¹, corresponding to S=O bands, while the intensity of these new peaks is very low for **1h**, maintaining also the peaks of the original S at 1287 and 1370 cm⁻¹.

Moreover, when we just impregnated a solution of $\text{VO}(\text{acac})_2$ either in neat **4** or in a second isostructural MOF with hydroxyl-residues decorating the channels instead of the thioether-arms ($\{\text{Ca}^{\text{II}}\text{Cu}^{\text{II}}_6[(S, S)\text{-serimox}]_3(\text{OH})_2(\text{H}_2\text{O})\}_3\cdot 39\text{H}_2\text{O}(\mathbf{5})$, where serimox = (*S, S*)-oxalyl-bis(*N*-serineninate)),³¹ we also observed high catalytic activities (Figure S20, ESI[†]). However, the vanadyl active species leached out from the structure (Figure S21, ESI[†]), being the material only active for 2 uses. Even when the $\text{VO}(\text{acac})_2$ was impregnated on SiO_2 , we could observe the leaching of the active species (Figure S22, ESI[†]). These results confirm the requisite of encapsulating, not impregnating, the $\text{VO}(\text{acac})_2$ inside **4** for obtaining a robust solid catalyst.

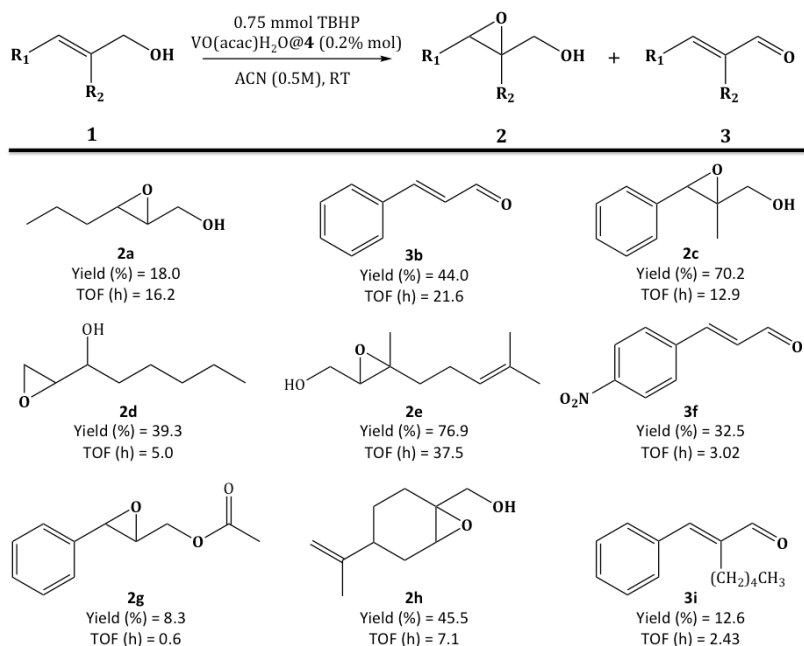


Figure 3. Scope of the reaction using $\text{VO}(\text{acac})\text{H}_2\text{O}@4$ as a catalyst.

2.3.3. Conclusions

Overall, we have observed in homogenous phase (VO(acac)₂/TBHP) the selectivity of allylic alcohols towards the epoxidation or dehydrogenation reactions is subtly controlled by the substituents around the allylic alcohol functionalities. A MOF encapsulating VO(acac)(H₂O) species has been synthesized and atomically-resolved by SC-XRD. **VO(acac)(H₂O)@4** as a heterogeneous catalyst, taking advantage of the steric constraints induced by the solid network on the catalyst, allow to gain some control on the chemoselectivity of the reaction toward the dehydrogenation product.³² These studies are representative of the change in reactivity imparted by a well-defined structured solid in organometallic catalysts, and expand the study of vanadium catalyst within MOFs channels.^{33,34}

2.3.4. References

1. Trost, B. M.; Fleming, I. *Comprehensive Organic Synthesis: Selectivity, Strategy, and Efficiency in Modern Organic Chemistry*, 7th ed.; Pergamon Press: Oxford, **1991**.
2. Mijs, W. J.; de Jonge, C. R. H. I. *Organic Syntheses by Oxidation with Metal Compounds*; Mijs, W. J.; de Jonge, C. R. H. I., Eds.; Plenum Press: New York, **1986**.
3. Hirao, T. *Chem. Rev.* **1997**, 97, 2707–2724.
4. Sharpless, K. B.; Michaelson, R. C. *J. Am. Chem. Soc.* **1973**, 95, 6136–6137.
5. Tanaka, S.; Yamamoto, H.; Nozaki, H.; Sharpless, K. B.; Michaelson, R. C.; Cutting, J. D. *J. Am. Chem. Soc.* **1974**, 96, 5254–5255.
6. Kaneda, K.; Kawanishi, Y.; Jitsukawa, K.; Teranishi, S. *Tetrahedron Lett.* **1983**, 24, 5009–5010.
7. Lattanzi, A.; Senatore, A.; Massa, A.; Scettri, A. J. *Org. Chem.* **2003**, 68, 3691–3694.
8. Furukawa, H.; Cordova, K. E.; O’Keeffe, M.; Yaghi, O. M. *Science* **2013**, 341, 974.

- Freund, R.; Zaremba, O.; Arnauts, G.; Ameloot, R.; Skorupskii, G.; Dinča, M.; Bavykina, A.; Gascon, J.; Ejsmont, A.; Goscianska, J.; Kalmutzki, M.; L'achelt, U.; Ploetz, E.; Diercks, C. S.; Wuttke, S. *Angew. Chem., Int. Ed.* **2021**, 60, 23975–24001.
- Kitagawa, S.; Matsuda, R. *Coord. Chem. Rev.* **2007**, 251, 2490–2509.
- Young, R. J.; Huxley, M. T.; Pardo, E.; Champness, N. R.; Sumbly, C. J.; Doonan, C. J. *Chem. Sci.* **2020**, 11, 4031–4050.
- Yang, D.; Gates, B. C. *ACS Catal.* **2019**, 9, 1779–1798.
- Viciano-Chumillas, M.; Mon, M.; Ferrando-Soria, J.; Corma, A.; Leyva-Pérez, A.; Armentano, D.; Pardo, E. *Acc. Chem. Res.* **2020**, 53, 520–531.
- Adam, R.; Mon, M.; Greco, R.; Kalinke, L. H. G.; Vidal-Moya, A.; Fernandez, A.; Winpenny, R. E. P.; Doménech-Carbó, A.; Leyva-Pérez, A.; Armentano, D.; Pardo, E.; Ferrando-Soria, J. *J. Am. Chem. Soc.* **2019**, 141, 10350–10360.
- Fortea-Pérez, F. R.; Mon, M.; Ferrando-Soria, J.; Boronat, M.; Leyva-Pérez, A.; Corma, A.; Herrera, J. M.; Osadchii, D.; Gascon, J.; Armentano, D.; Pardo, E. *Nat. Mater.* **2017**, 16, 760–766.
- Mon, M.; Ferrando-Soria, J.; Grancha, T.; Fortea-Pérez, F. R.; Gascon, J.; Leyva-Pérez, A.; Armentano, D.; Pardo, E. *J. Am. Chem. Soc.* **2016**, 138, 7864–7867.
- Mon, M.; Lloret, F.; Ferrando-Soria, J.; Martí-Gastaldo, C.; Armentano, D.; Pardo, E. *Angew. Chem. Int. Ed.* **2016**, 55, 11167–11172.
- Lattanzi, A.; Leadbeater, N. E. *Org. Lett.* **2002**, 4, 1519–1521.
- Vandichel, M.; Leus, K.; Van Der Voort, P.; Waroquier, M.; Van Speybroeck, V. *J. Catal.* **2012**, 294, 1–18.
- Barbaro, P.; Liguori, F., Eds. *Heterogenized Homogeneous Catalysts for Fine Chemicals Production*, 1st ed.; Springer: Netherlands, **2010**.
- Wang, X.; Wu, S.; Li, Z.; Yang, X.; Su, H.; Hu, J.; Huo, Q.; Guan, J.; Kan, Q. *Microporous Mesoporous Mater.* **2016**, 221, 58–66.

22. Yang, Y.; Guan, J.; Qiu, P.; Kan, Q. *Appl. Surf. Sci.* **2010**, 256, 3346–3351.
23. Rayati, S.; Torabi, N.; Ghaemi, A.; Mohebbi, S.; Wojtczak, A.; Kozakiewicz, A. *Inorg. Chim. Acta* **2008**, 361, 1239–1245.
24. Jeoung, S.; Kim, S.; Kim, M.; Moon, H. R. *Coord. Chem. Rev.* **2020**, 420, 213377.
25. Cohen, S. M. *Chem. Rev.* **2012**, 112, 970–1000.
26. Bradshaw, D.; Claridge, J. B.; Cussen, E. J.; Prior, T. J.; Rosseinsky, M. J. *Acc. Chem. Res.* **2005**, 38, 273–282.
27. Mikuriya, M.; Kotera, T.; Adachi, F.; Bandow, S. *Chem. Lett.* **1993**, 945–948.
28. Jenkins, R. M.; Pinder, T. A.; Hatley, M. L.; Reibenspies, J. H.; Darensbourg, M. Y. *Inorg. Chem.* **2011**, 50, 1849–1855.
29. Saatchi, K.; Thompson, K. H.; Patrick, B. O.; Pink, M.; Yuen, V. G.; McNeill, J. H.; Orvig, C. *Inorg. Chem.* **2005**, 44, 2689–2697.
30. Ageeva, T. A.; Golubev, D. V.; Gorshkova, A. S.; Ionov, A. M.; Kopylova, E. V.; Koifman, O. I.; Mozhchil, R. N.; Rozhkova, E. P.; Rummyantseva, V. D.; Sigov, A. S.; Fomichev, V. V. *Macroheterocycles* **2019**, 12, 148–153.
31. Mon, M.; Bruno, R.; Ferrando-Soria, J.; Bartella, L.; Di Donna, L.; Talia, M.; Lappano, R.; Maggolini, M.; Armentano, D.; Pardo, E. *Mater. Horiz.* **2018**, 5, 683–690.
32. For GC-MS of some products, see Fig. S23 (ESI[†]).
33. Otake, K.; Cui, Y.; Buru, C. T.; Li, Z.; Hupp, J. T.; Farha, O. K. *J. Am. Chem. Soc.* **2018**, 140, 8652–8656.
34. Ingleson, M. J.; Perez Barrios, J.; Guilbaud, J.-B.; Khimyak, Y. Z.; Rosseinsky, M. J. *Chem. Commun.* **2008**, 2680–2682.

2.4. Exploring the Role of Amino Acid-Derived Multivariate Metal-Organic Frameworks as Catalyst in (Hemi)-Ketalization Reactions (Publication 2)

Understanding the host-guest chemistry in MOFs represent a research field with an outstanding potential to develop in a rational manner novel porous materials with improved performances in fields as heterogeneous catalysis. Herein, we report a family of three isorecticular MOFs, derived from amino acids, and study the influence of the number and nature of functional groups decorating the channels as catalyst on (hemi)-ketalization reactions. In particular, MTV-MOF **3**, prepared by using equal percentages of amino acids *L*-serine and *L*-Mecysteine, in comparison to single-component (“traditional”) MOFs, derived from either *L*-serine or *L*-Mecysteine – MOFs **1** and **2**–, exhibits the most efficient catalytic conversions for the hemiketalization of different aldehydes and ketalization of cyclohexanone. On the basis of the experimental data reported, the nice catalytic performance of the MTV-MOF **3** was attributed to the intrinsic heterogeneity of MTV-MOFs. These results highlight the potential of MTV-MOFs as strong candidates to mimic natural non-acidic enzymes, such as glycosidases, and to unveil novel catalytic mechanism not so easily accessible with other microporous materials.

2.4.1. Introduction

Multivariate-Metal-Organic Frameworks (MTV-MOFs)¹⁻⁷ represent a novel generation of porous crystalline materials within MOFs, constituted of linkers with identical backbones but different functionalities decorating the ligand, where heterogeneity and complexity of composition have opened the way to synergetic behaviors, and thus, to novel and/or enhanced properties respect single-component (“traditional”) MOFs.⁸⁻¹⁰

Despite still it is difficult to get precise atomic information of the location and distribution of the different functionalities decorating the MTV-MOF channels, and further work adapting/improving existing characterization techniques or implementing new ones will be needed,¹¹⁻¹³ the exciting exhibited properties by MTV-MOFs in different applications pay off this uncertainty and it has not been a limitation for the growing interest in develop novel MTV-MOFs.¹⁴⁻¹⁹

Elegant application examples of taking advantage of the heterogeneity of MTV-MOFs have been reported for heterogenous catalysis.²⁰⁻²³ Indeed, such complex porous platforms represent a step-closer to engender materials that mimic the existing complexity and functionality of enzymes.^{24,25}

A beautiful example was the seminal work reported by Fracalori *et al.*,²⁰ where in a MTV-MOF performed up to seven post-synthetic modifications to lead to more complex MTV-MOFs with channels decorated with a tripeptide. In particular, the one with H₂N-Cys-His-Asp-CONHL sequence (Cys = cysteine, His = histidine, Asp = aspartic acid and L = organic backbone) of the endopeptidase enzyme tobacco etch virus (TEV) was investigated as mimic of this enzyme for the sequence-specific bond-cleavage of a pentapeptide. Despite the low conversion achieved, this work illustrated that is possible to transfer the compositional heterogeneity of MTV-MOFs into a complex target application.

One of our main research lines have been devoted to explore the development of MTV-MOFs with oxamidato-based ligands derived from amino acids, with the main aim to take advantage of the heterogeneity of composition and the intrinsic flexibility of the residues decorating the MTV-MOFs channels toward more complex applications. So far, we have observed a successful transfer from complexity of composition to improvement of performance in water remediation.^{14,18,26,27} In particular, a MTV-MOF {Ca^{II}Cu^{II}₆ [(S, S)-methox]_{1.43-1.46} [(S, S)-serimox]_{1.57-1.54} (OH)₂ (H₂O)} · 30H₂O (where methox = bis [(S)-methionine] oxalyl diamide and serimox = bis [(S)-

serine] oxalyl diamide) with functional channels decorated with approximately 50 % of hydroxyl-groups and 50 % thioalkyl ones derived from natural amino acids *L*-serine and *L*-methionine, respectively, have proven very efficient in the simultaneous capture of contaminants with inorganic and organic nature.¹⁴ Also, this has been further validated with a isorecticular MTV-MOF $\{\text{Sr}^{\text{II}}\text{Cu}^{\text{II}}_6 [([S, S]\text{-methox})_{1.50} [(S, S)\text{-Mecysmox}]_{1.50} (\text{OH})_2 (\text{H}_2\text{O})]\} \cdot 36 \text{ H}_2\text{O}$ (where methox = bis $[(S)\text{-methylcysteine}]$ oxalyl diamide), which outperform single-component MOFs in the removal of emergent neonicotinoids contaminants from water.¹⁸

On this basis, and with the background inspiration of the active centers of enzymes -where different organic functionalities are able to act synergistically to interact, adapt and efficiently catalyze the transformation of specific substrates-, the aim of this investigation has been to explore within a family of isorecticular MOFs the role and influence of having or not functional channels decorated with more than one distinct amino acid residue in catalysis. To this end, we have focused on the use of two previously reported MOFs, with formulas $\{\text{Sr}^{\text{II}}\text{Cu}^{\text{II}}_6 [([S, S]\text{-serimox})_3 (\text{OH})_2 (\text{H}_2\text{O})]\} \cdot 38\text{H}_2\text{O}$ (**1**)^{28,29} and $\{\text{Sr}^{\text{II}}\text{Cu}^{\text{II}}_6 [([S, S]\text{-Mecysmox})_3 (\text{OH})_2 (\text{H}_2\text{O})]\} \cdot 15\text{H}_2\text{O}$ (**2**),³⁰ and a novel MTV-MOF of formula $\{\text{Sr}^{\text{II}}\text{Cu}^{\text{II}}_6 [([S, S]\text{-serimox})_{1.50} [(S, S)\text{-Mecysmox}]_{1.50} (\text{OH})_2 (\text{H}_2\text{O})]\} \cdot 12\text{H}_2\text{O}$ (**3**) (Scheme S1 and Figure S1) as catalyst for hemiketalization and ketalization reactions.

The addition of alcohols to the carbonyl group of aldehydes and ketones is an essential reaction in Nature³¹ and industrial synthesis,³² since the electronic density of the carbonyl group is completely switched from electron rich to electron poor. Hemiketalization and ketalization reactions have been traditionally used in organic synthesis to protect the aldehyde and ketone groups during other reactions, which are regenerated after simple water acidic treatment.³³ However, the acid-catalyzed conditions required for the hemiketalization and ketalization reactions are not always compatible with other groups. Indeed, it is not surprising to find in the literature synthetic routes where a functional group is previously

protected by other methodology before the carbonyl group is protected under acid-catalyzed conditions.³⁴ Thus, any catalytic method for hemiketalization and ketalization reactions based under non-acidic conditions is of interest.

Nature makes use of non-acid enzymes, such as glycosidases, to catalyze hemiketalization and ketalization reactions, by the cooperative action of two different pocketed base groups, *i.e.* carboxylates.³⁵ In this context, we have recently reported that MOF **1** is able to selectively hydrolyze ketal groups in complex organic molecules under non-acid conditions, by the combined action of the alcohol groups from the serine residues within the MOF's channels in the presence of water.³⁶ Since ketalization reactions are reversible, we hypothesized that the same MOF **1** could catalyze the formation of the ketal under anhydrous conditions. Unfortunately, this reaction only occurred in a very minor extent.³⁵ Thus, at this point, on the basis of the efficient σ -hole interactions observed on MOFs containing thioether residues on the recognition and capture of organic contaminants¹⁸ as well as the fact that cyclic thiols in stoichiometric amounts, after forming dithianes, have been traditionally used to protect carbonyl groups,³⁷ we turned our attention to MOF **2**. However, despite these *a priori* optimal conditions, **2** has not revealed as very efficient catalyst.

Intrigued by these results, we aimed to take advantage of the heterogenization and synergistic effect observed in MTV-MOFs, to explore the possibility that the MTV-MOF **3** could be active for hemiketalization and ketalization reactions, since the combination of $-\text{CH}_2\text{OH}$ and $-\text{CH}_2\text{SCH}_3$ groups in **3** could help to the carbonyl group activation. Thus, the amino acid residues containing alcohol and thioether groups in MTV-MOF **3** will not form permanent bonds, but could co-operatively activate the carbonyl group in the presence of an external alcohol, in a similar way as glycosidases do. The catalytic mechanism of this microporous bifunctional solid will significantly differ from previous examples with microporous solids - *i.e.*

zeolites^{38,39} and MOFs⁴⁰⁻, based on amine/acid and other functional groups.

We will present below that this strategy works, and that MTV-MOF **3** catalyzes the hemiketalization and ketalization reactions within its confined space more efficiently than MOFs **1** and **2**.

2.4.2. Results and Discussion

In this work, we show an expansion of the application of the metalloligand design strategy, to synthesize a novel water-stable 3D MTV-MOF, with formula $\{\text{Sr}^{\text{II}}\text{Cu}^{\text{II}}_6 [(\text{S}, \text{S})\text{-serimox}]_{1.50} [(\text{S}, \text{S})\text{-Mecysmox}]_{1.50} (\text{OH})_2 (\text{H}_2\text{O})\} \cdot 12\text{H}_2\text{O}$ (**3**), obtained as green prisms by slow diffusion in H-shaped tubes at room temperature of aqueous solutions containing stoichiometric amounts of an equimolar mixture of $(\text{Me}_4\text{N})_2 \{\text{Cu}_2 [(\text{S}, \text{S})\text{-serimox}] (\text{OH})_2\} \cdot 5\text{H}_2\text{O}$ and $(\text{Me}_4\text{N})_2 \{\text{Cu}_2 [(\text{S}, \text{S})\text{-Mecysmox}] (\text{OH})_2\} \cdot 5\text{H}_2\text{O}$ in one arm and $\text{Sr}(\text{NO}_3)_2$ in the other.

The crystal structure of **3** determined by SCXRD consists of a chiral honeycomb-like 3D strontium(II)/copper(II) network featuring functional hexagonal channels of approximately 0.4 nm, developing along the *c* crystallographic axis, where the methylenethiomethyl chains of the methylcysteine derivatives are located (Figures 1). It is an **acs** uninodal sixfold-connected net (4⁹.6⁶), built from *trans*-oxamidato-bridged dicopper(II) units of $\{\text{Cu}^{\text{II}}_2 [(\text{S}, \text{S})\text{-serimox}]\}$ and $\{\text{Cu}^{\text{II}}_2 [(\text{S}, \text{S})\text{-mecysmox}]\}$ (Scheme S1 and Figure 1 and S1-S3), which are expected to be statistically disordered in the crystal structure. They act as linkers between the Sr^{II} ions through the carboxylate groups (Figure 1a and 1b). Neighboring Cu²⁺ and Cu²⁺/Sr²⁺ ions are auxiliary interconnected, in a μ_3 fashion, by aqua/hydroxo groups (in a 1:2 statistical distribution) (inset Figure 1a). As previously tested for the refinement of best model in crystal structure of the isorecticular MTV-MOF $\{\text{Ca}^{\text{II}}\text{Cu}^{\text{II}}_6 [(\text{S}, \text{S})\text{-methox}]_{1.43-1.46} [(\text{S}, \text{S})\text{-serimox}]_{1.57-1.54} (\text{OH})_2 (\text{H}_2\text{O})\} \cdot 30 \text{H}_2\text{O}$,¹⁴ the similar percentage of mixed serimox and mecysmox (confirmed by the composition analysis, *vide infra* C, H, S, N in Experimental Section and Supporting

Information) lead to superimposed snapshots of mixed $\{\text{Cu}^{\text{II}}[(\text{S}, \text{S})\text{-mecysmox}/\text{serimox}]\}$ metalloligands. Thus, once more, the disorder in **3** has been modelled as an averaged view of the crystal structure, which is the spatial average of all molecules/fragments structures in the crystal *via* only one unit cell (see crystallographic details in the Supporting Information). This, even if could seem counterintuitive, is the better description to the real situation, where pure copper(II) metalloligands of each amino acid-derived ligand are randomly distributed (with 1:1 ratio) within the net (see crystallographic details in the Supporting Information). Looking at such modelled crystal structure of **3**, the two “arms” decorated with serine and methylcysteine derivatives, respectively, show different orientations, with the methylcysteine one more distended, within the largest octagonal pores, and the serine one bent and confined in smallest channels developing along *a* crystallographic axis (Figure 1b-c and S3).

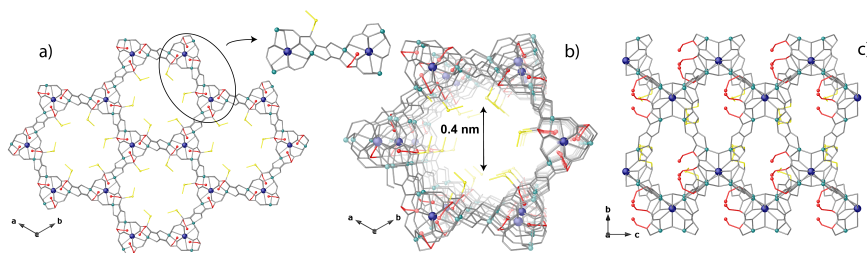


Figure 1. (a) View of porous structure of **3** along *c* crystallographic axes (inset emphasizes the dianionic bis(hydroxo) dicopper(II) building blocks). (b) and (c) Views of a single channel for the porous structure of the MTV-MOF **3** along the *c* (b) and *a* (c) axes (the crystallization water molecules are omitted for clarity). Copper(II) and strontium(II) ions from the network are represented as cyan and blue spheres, respectively. Oxygen and sulfur atoms from the residues are shown as red and yellow spheres, respectively. The organic ligands are represented as gray sticks, with the exception of *L*-serine ($-\text{CH}_2\text{OH}$) and *L*-methylcysteine ($-\text{CH}_2\text{SCH}_3$) residues, which are represented as red and yellow sticks, respectively.

Here, it is worth to note that MTV-MOFs, as already underlined in our previous works,^{14,18,26,27} show as trilling feature an impressive

flexibility of the functional arms confined within the pores, exhibiting different conformations depending on the target molecules captured in pores. Thus, loaded reactants of a given catalytic reaction might have an effect on the final conformation adopted by the flexible aminoacidic arms decorating the pores. Indeed, it depends on host-guest interactions, which are at the origin of the stabilization of such species within confined spaces. Finally, the estimated empty volume for **3**, without the crystallization water molecules, is 1764.7 (1) Å³, value which represent 48.3 %, of potential void per unit cell volume [$V = 3653.9 \text{ Å}^3$].

In addition to the structural characterization and elemental analysis, the nature and identity of MTV-MOF **3** was also established by PXRD, N₂ adsorption isotherm at 77 K and TGAs (see the Supporting Information). The experimental PXRD pattern of **3** is consistent with the theoretical one, extracted from SCXRD (Figure S4), which confirm the homogeneity and purity of the powder sample. The permanent porosity of **3** was supported by measuring the N₂ adsorption isotherm at 77 K and compared to those adsorption isotherms of traditional MOFs **1** and **2** (Figure S5). They confirm the permanent porosity for all three materials, with N₂ adsorbed amounts for **3** between the ones of **1** and **2**, but closer to **2**, which is consistent with the accessible void spaces shown in the crystal structures. The solvent content of **3** was established by TGA (Figure S6), with a calculated percentage weight loss value of 85 % at 388 K, which corresponds to 12 water molecules. **3** is stable up to 200 °C, when decomposition starts.

Figure 2 shows the catalytic results for the hemiketalization reaction of benzaldehyde **4** with methanol. After screening some reaction conditions, the best results were obtained at 60 °C after 8 h reaction time. Under these reaction conditions, it can be seen that MOF **1** is completely inactive for the reaction (entries 1-2), as observed before,³⁶ and that MOF **2** shows some activity, to give a 45 % yield of hemiacetal **5** (entry 3). In contrast, MTV-MOF **3** catalyzes the reaction much more efficiently to give product **5** in 75 % yield (entry

4). The selectivity of the reaction is complete since other products are not observed, and the fact that the transformation does not advance further is probably due to reaching the equilibrium. Magnesium sulfate was added to the reaction media, in order to adsorb the water formed during reaction, further shifting the equilibrium towards the hemiketal product **5**. However, the addition of MgSO_4 did not improve the yield of **5**, since the generated water is probably retained in the highly polar MOF's pores and reacts back with **5** at high conversions of **4**.

In order to confirm the retention of the structural integrity of **1-3** under catalytic conditions, also ruling out the possibility of partial/total structural collapse in **1** and **2**, N_2 adsorption isotherms at 77 K and PXRD were also performed after catalytic experiments (Figures S5b and S7). From PXRD, it can be concluded that all materials are robust enough to maintain their structural integrity under reaction conditions. In an analogous way, the similarity of Brunauer-Emmett-Teller (BET)⁴¹ surface areas before [791(**1**), 633(**2**) and 682(**3**) m^2/g] and after [763(**1**), 609(**2**) and 670(**3**) m^2/g] catalysis, support the retention of porosity and further reflect the stability of **1-3**. The stability of MTV-MOF **3** in aqueous and nonaqueous solvents was further validated by PXRD (Figure S8) of polycrystalline samples of **3** immersed during 24 hours in hot water, dimethylformamide, methanol and acetonitrile.

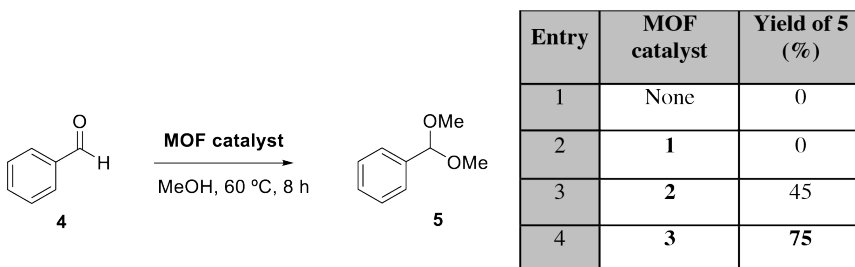


Figure 2. Results for the MOF-catalyzed hemiketalization reaction of benzaldehyde **4** with methanol. Selectivity to **5** is 100 % (conversion equals yield). GC yields.

Figure 3 (left) shows the hot filtration test for the reaction catalyzed by the MTV-MOF **3**, where it can be seen that hemiketalization reaction of benzaldehyde **4** stops after the solid catalyst is filtered off. In accordance, Figure 3 (right) shows that MTV-MOF **3** could be reused up to 3 times without appreciable depletion of the final yield of **5**.

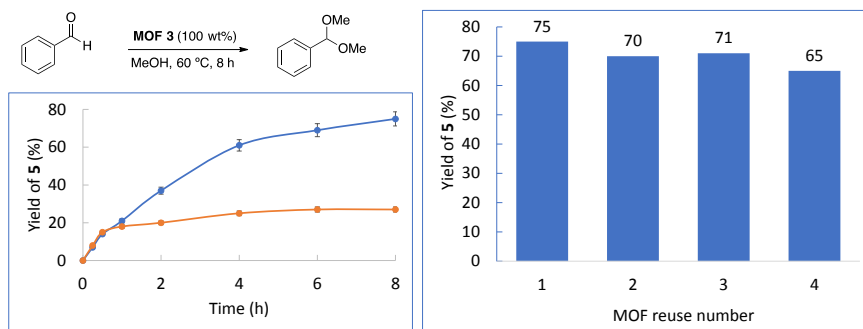


Figure 3. (left) Hot filtration test for MTV-MOF **3** during the hemiketalization reaction of benzaldehyde **4** with MeOH under the reaction conditions shown in Table 1. Error bars account for a 5 % uncertainty. (right) Reuses of MOF **3** under the same reaction conditions. GC yields.

The scope of aldehydes was then assessed for the hemiketalization reaction catalyzed by MTV-MOF **3**, under the optimized reaction conditions. The results are shown in Figure 4. It can be seen that aromatic aldehydes with halide and methoxy substituents in different positions of the aryl ring can be obtained in good yields (products **5b-g**), and that alkyl aldehydes are even better reactive (products **5h-i**), including acid-sensitive propargyl aldehydes (**5j**). These results support the ability of MTV-MOF **3** to catalyze the hemiketalization reaction of aldehydes with disparate electronics.

2. MOFs AND MTV-MOFs FOR CATALYSIS

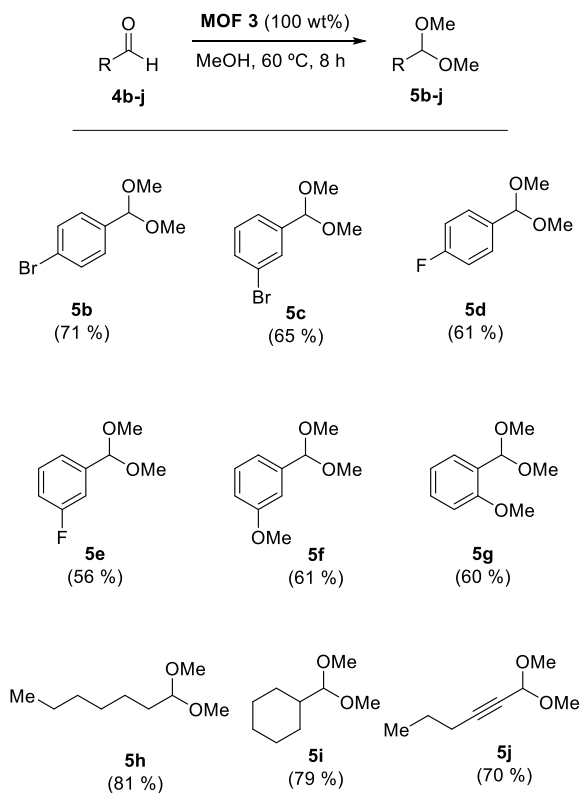
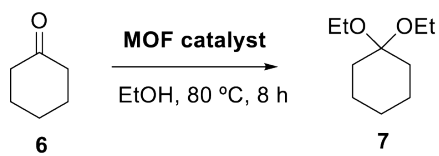


Figure 4. Scope of aldehydes for the hemiketalization reaction catalyzed by MTV-MOF 3. GC yields.

Ketones are more unreactive than aldehydes in ketalization reactions, however, they were also tested with the MOF catalysts. Figure 5 shows the catalytic results for cyclohexanone **6**. In accordance with the lower reactivity of ketones, a higher reaction temperature (80 °C) was needed to get significant conversions, and EtOH instead of MeOH was used as nucleophile to avoid overpressure in the reaction. The results show that, again, MTV-MOF 3 was the best catalyst, although with just a slight difference with MOF 2 (compare entries 3 and 4), to give 50 % of product **7** with complete selectivity. Thus, MTV-MOF 3 can be considered as a general catalyst for the (hemi)-ketalization reaction of simple carbonyl compounds (aldehydes and ketones).



Entry	MOF catalyst	Yield of 7 (%)
1	None	5
2	1	10
3	2	40
4	3	50

Figure 5. Results for the MOF-catalyzed hemiketalization reaction of cyclohexanone **6** with ethanol. Selectivity to **7** is 100 % (conversion equals yield). GC yields.

2.4.3. Conclusions

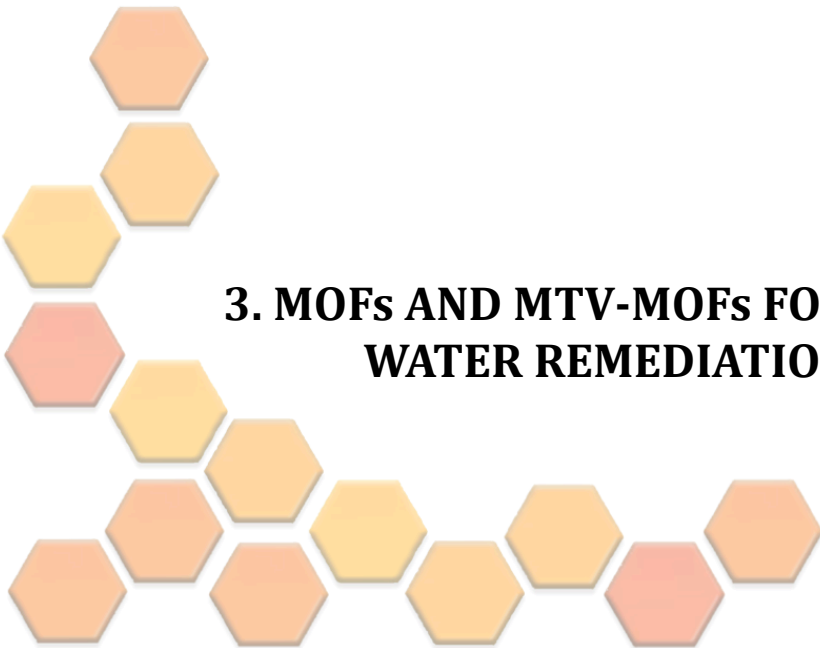
Herein we have presented the synthesis and crystal structure of a novel component of the oxamidato-based derived from amino acid 3D MTV-MOFs family, and we have reported the influence of the functionalization of the channels -with one or two types of distinct functional groups decorating the channels- on the (hemi)-ketalization reaction of different simple carbonyl compounds. On the basis of the obtained results, we can confirm that the heterogeneity present in MTV-MOF **3** is nicely translated in a more efficient catalytic behavior on the reactions under study. Thus, these results also illustrate the potential of MTV-MOFs to somehow mimic nature non-acidic enzymes and to uncover novel catalytic mechanisms not accessible with traditional microporous materials or single-component MOFs. Nevertheless, further work will be needed to fully uncover the key role that the distinct functional groups play on MTV-MOFs, and how the subtle modification of their proportions and/or spatial arrangement have a massive influence on their functionality, in a similar manner as it occurs in natural enzymes.

2.4.4. References

1. Deng, H.; Doonan, C. J.; Furukawa, H.; Ferreira, R. B.; Towne, J.; Knobler, C. B.; Wang, B.; Yaghi, O. M. *Science* **2010**, 327, 846–850.
2. Furukawa, H.; Müller, U.; Yaghi, O. M. *Angew. Chem. Int. Ed.* **2015**, 54, 3417–3430.
3. Helal, A.; Yamani, Z. H.; Cordova, K. E.; Yaghi, O. M. *Natl. Sci. Rev.* **2017**, 4, 296–298.
4. Osborn Popp, T. M.; Yaghi, O. M. *Acc. Chem. Res.* **2017**, 50, 532–534.
5. Jiao, J.; Gong, W.; Wu, X.; Yang, S.; Cui, Y. *Coord. Chem. Rev.* **2019**, 385, 174–190.
6. Feng, L.; Wang, K.-Y.; Day, G. S.; Zhou, H.-C. *Chem. Soc. Rev.* **2019**, 48, 4823–4853.
7. Viciano-Chumillas, M.; Liu, X.; Leyva-Pérez, A.; Armentano, D.; Ferrando-Soria, J.; Pardo, E. *Coord. Chem. Rev.* **2022**, 451, 214273.
8. Furukawa, H.; Cordova, K. E.; O’Keeffe, M.; Yaghi, O. M. *Science* **2013**, 341, 974.
9. Maurin, G.; Serre, C.; Cooper, A.; Férey, G. *Chem. Soc. Rev.* **2017**, 46, 3104–3107.
10. Zhang, X.; Wang, B.; Alsalme, A.; Xiang, S.; Zhang, Z.; Chen, B. *Coord. Chem. Rev.* **2020**, 423, 213507.
11. Castillo-Blas, C.; de la Peña-O’Shea, V. A.; Puente-Orench, I.; de Paz, J. R.; Sáez-Puche, R.; Gutiérrez-Puebla, E.; Gándara, F.; Monge, A. *Sci. Adv.* **2017**, 3, e1700773.
12. Schrimpf, W.; Jiang, J.; Ji, Z.; Hirschle, P.; Lamb, D. C.; Yaghi, O. M.; Wuttke, S. *Nat. Commun.* **2018**, 9, 1647.
13. Ji, Z.; Li, T.; Yaghi, O. M. *Science* **2020**, 369, 674–680.
14. Mon, M.; Bruno, R.; Tiburcio, E.; Viciano-Chumillas, M.; Kalinke, L. H. G.; Ferrando-Soria, J.; Armentano, D.; Pardo, E. *J. Am. Chem. Soc.* **2019**, 141, 13601–13609.

15. Fan, W.; Yuan, S.; Wang, W.; Feng, L.; Liu, X.; Zhang, X.; Wang, X.; Kang, Z.; Dai, F.; Yuan, D.; Sun, D.; Zhou, H.-C. *J. Am. Chem. Soc.* **2020**, *142*, 8728–8737.
16. Ma, R.; Jiang, H.; Wang, C.; Zhao, C.; Deng, H. *Chem. Commun.* **2020**, *56*, 2715–2718.
17. Nandi, F. S.; Wang, S.; Wahiduzzaman, M.; Yadav, V.; Taksande, K.; Maurin, G.; Serre, C.; Devautour-Vinot, S. *ACS Appl. Mater. Interfaces* **2021**, *13*, 20194–20200.
18. Negro, C.; Martínez Pérez-Cejuela, H.; Simó-Alfonso, E. F.; Herrero-Martínez, J. M.; Bruno, R.; Armentano, D.; Ferrando-Soria, J.; Pardo, E. *ACS Appl. Mater. Interfaces* **2021**, *13*, 28424–28432.
19. Canossa, S.; Ji, Z.; Gropp, C.; Rong, Z.; Ploetz, E.; Wuttke, S.; Yaghi, O. M. *Nat. Rev. Mater.* **2022**, DOI: 10.1038/s41578-022-00482-5.
20. Fracaroli, M.; Siman, P.; Nagib, D. A.; Suzuki, M.; Furukawa, H.; Toste, F. D.; Yaghi, O. M. *J. Am. Chem. Soc.* **2016**, *138*, 8352–8355.
21. Xia, Q.; Li, Z.; Tan, C.; Liu, Y.; Gong, W.; Cui, Y. *J. Am. Chem. Soc.* **2017**, *139*, 8259–8266.
22. Liang, J.; Xie, Y.-Q.; Wu, Q.; Wang, X.-Y.; Liu, T.-T.; Li, H.-F.; Huang, Y.-B.; Cao, R. *Inorg. Chem.* **2018**, *57*, 2584–2593.
23. Liu, T.-T.; Liang, J.; Xu, R.; Huang, Y.-B.; Cao, R. *Chem. Commun.* **2019**, *55*, 4063–4066.
24. Okamoto, Y.; Ward, T. R. *Supramolecular Enzyme Mimics*. In *Comprehensive Supramolecular Chemistry II*; Atwood, J., Ed.; Elsevier: Oxford, UK, **2017**, vol. 4, pp 459-510.
25. Schramm, V. L. *Chem. Rev.* **2006**, *106*, 3029–3030.
26. Baratta, M.; Mastropietro, T. F.; Bruno, R.; Tursi, A.; Negro, C.; Ferrando-Soria, J.; Mashin, A. I.; Nezhdanov, A.; Nicoletta, F. P.; De Filpo, G.; Pardo, E.; Armentano, D. *ACS Appl. Nano Mater.* **2022**, *5*, 5223–5233.
27. Negro, C.; Martínez Pérez-Cejuela, H.; Simó-Alfonso, E. F.; Iqbal, W.; Herrero-Martínez, J. M.; Armentano, D.; Ferrando-Soria, J.; Pardo, E. *ACS Appl. Mater. Interfaces* **2023**, *15*, 3069–3076.

28. Mon, M.; Bruno, R.; Ferrando-Soria, J.; Bartella, L.; Di Donna, L.; Talia, M.; Lappano, R.; Maggiolini, M.; Armentano, D.; Pardo, E. *Mater. Horizons* **2018**, *5*, 683–690.
29. Mon, M.; Bruno, R.; Elliani, R.; Tagarelli, A.; Qu, X.; Chen, S.; Ferrando-Soria, J.; Armentano, D.; Pardo, E. *Inorg. Chem.* **2018**, *57*, 13895–13900.
30. Tiburcio, E.; Greco, R.; Mon, M.; Ballesteros-Soberanas, J.; Ferrando-Soria, J.; López-Haro, M.; Hernández-Garrido, J. C.; Oliver-Meseguer, J.; Marini, C.; Boronat, M.; Armentano, D.; Leyva-Pérez, A.; Pardo, E. *J. Am. Chem. Soc.* **2021**, *143*, 2581–2592.
31. Sinnott, M. L. *Chem. Rev.* **1990**, *90*, 1171–1202.
32. Ruiz, V. R.; Velty, A.; Santos, L. L.; Leyva-Pérez, A.; Sabater, M. J.; Iborra, S.; Corma, A. *J. Catal.* **2010**, *271*, 351–357.
33. Ley, S. V.; Polara, A. *J. Org. Chem.* **2007**, *72*, 5943–5959.
34. Veitch, G. E.; Beckmann, E.; Burke, B. J.; Boyer, A.; Maslen, S. L.; Ley, S. V. *Angew. Chem. Int. Ed.* **2007**, *46*, 7629–7632.
35. Davies, G.; Henrissat, B. *Structure* **1995**, *3*, 853–859.
36. Mon, M.; Bruno, R.; Sanz-Navarro, S.; Negro, C.; Ferrando-Soria, J.; Bartella, L.; Di Donna, L.; Prejanò, M.; Marino, T.; Leyva-Pérez, A.; Armentano, D.; Pardo, E. *Nat. Commun.* **2020**, *11*, 3080.
37. Gaunt, M. J.; Sneddon, H. F.; Hewitt, P. R.; Orsini, P.; Hook, D. F.; Ley, S. V. *Org. Biomol. Chem.* **2003**, *1*, 15–16.
38. Lewis, J. D.; Van de Vyver, S.; Román-Leshkov, Y. *Angew. Chem. Int. Ed.* **2015**, *54*, 9835–9838.
39. Corma, A.; Díaz, U.; García, T.; Sastre, G.; Velty, A. *J. Am. Chem. Soc.* **2010**, *132*, 15011–15021.
40. Zhou, G.; Wang, B.; Cao, R. *J. Am. Chem. Soc.* **2020**, *142*, 14848–14853.
41. Rouquerol, J.; Avnir, D.; Fairbridge, C. W.; Everett, D. H.; Haynes, J. H.; Pernicone, N.; Ramsay, J. D. F.; Sing, K. S. W.; Unger, K. K. *Pure Appl. Chem.* **1994**, *66*, 1739–1758.



3. MOFs AND MTV-MOFs FOR WATER REMEDIATION

3.1. Introduction

We have taken advantage of our knowledge about oxamidato-based MOFs, which have already proven their efficiency in capturing and/or encapsulating heavy metals,^{1,2} complexes,^{3,4} and even to construct small metal clusters⁵ *via* PSMs, to evaluate the importance of functionalizing the channels of MOFs to achieve efficient water remediation. Specifically, we have focused our efforts on removing the following organic contaminants from aquatic ecosystems.

Firstly, organic dyes are widely used in many industrial applications, including textile, leather, plastic, cosmetic, paper, and food processing. It is estimated that more than 70.000 tons of 100.000 commercially available dyes are produced annually, and around 2-10 % of total production is discharged into aquatic systems,⁶ causing undesirable color in water even at low concentrations, and severely reducing sunlight penetration, affecting the photoactivity in aquatic life. Moreover, the presence of metals makes them extremely toxic for fish, as they have teratogenic, mutagenic, and carcinogenic properties, which ultimately poses a risk to human life.⁷

Secondly, the transition from traditional farming to intensive agricultural practices has led to an accumulation of increasing amounts of insecticides, herbicides, pesticides, and fertilizers in our ecosystems. Their considerable water solubility and toxicity provide many advantages in pest control but also make them a significant threat to living beings. In particular, neonicotinoids (NEOs),⁸ the most extensively used type of insecticides in the world, present a long life and accumulate in soils. Therefore, their removal is a crucial issue for maintaining the ecological balance in our ecosystems.⁹

This chapter of the thesis introduces a family of eco-friendly, water-stable 3D isoreticular MOFs, prepared from amino acids, and demonstrated their rational application for the efficient capture of some of the most common organic contaminants from water, as mentioned before, thereby reducing the presence of these pollutants

in aquatic environments. It is noteworthy to mention that all the studies were carried out on spiked solutions of the contaminants on real water samples from Turia River and Albufera natural park (Valencia, Spain), where the presence of other ions could interfere with the adsorption process.

Sulfur σ -hole interactions are known to play a key role in the biological activity of living beings, as well as in relevant molecular recognition processes, but they have been barely explored so far. Herein, we present one of the first studies on the rational exploitation of these underestimated interactions for efficient water remediation. The neutral 3D MOF, with the formula $\{\text{Sr}^{\text{II}}\text{Cu}_6^{\text{II}}[(\text{S}, \text{S})\text{-methiomox}]_3(\text{OH})_2(\text{H}_2\text{O})\} \cdot 16\text{H}_2\text{O}$ (methiomox = bis [(S)-methionine] oxalyl diamide), derived from *L*-methionine, has narrow channels decorated with $-\text{CH}_2\text{SCH}_3$ thioalkyl chains and can efficiently capture a family of organic dyes (such as AO, PY, MB, and BG) at very low concentrations (10 ppm) -similar to those found in industrial wastewaters- from environmental matrices. (**Publication 3. Metal-Organic Frameworks as unique platforms to gain insight of σ -hole interactions for the removal of organic dyes from aquatic ecosystems**).

When considering the contamination of aquatic environments by insecticides, NEOs are of significant concern due to their long life and moderate water solubility, which make them easily applicable to soils and plants, contributing to the contamination of aquatic environments. Therefore, it is crucial to effectively capture this type of pollutants. To this end, we have explored the efficiency of MOFs as adsorbents under dynamic SPE conditions for the removal of NEOs (such as thiamethoxam, clothianidin, imidacloprid, acetamiprid, and thiacloprid). Our findings indicate that this family of MOFs exhibits notable removal efficiency in a single step, making them an efficient means of removing NEOs from aquatic environments (**Publication 4. Highly efficient removal of neonicotinoid insecticides by thioether-based (Multivariate) Metal-Organic Frameworks**).

3.2. References

1. Mon, M.; Ferrando-Soria, J.; Grancha, T.; Fortea-Perez, F. R.; Gascon, J.; Leyva-Perez, A.; Armentano, D.; Pardo, E. *J. Am. Chem. Soc.* 2016, 138, 7864–7867.
2. Mon, M.; Lloret, F.; Ferrando-Soria, J.; Marti-Gastaldo, C.; Armentano, D.; Pardo, E. *Angew. Chem. Int. Ed.* 2016, 55, 11167–11172.
3. Mon, M.; Pascual-Alvarez, A.; Grancha, T.; Cano, J.; Ferrando-Soria, J.; Lloret, F.; Gascon, J.; Pasan, J.; Armentano, D.; Pardo, E. *Chem. Eur. J.* 2016, 22, 539–545.
4. Abherve, T.; Grancha, T.; Ferrando-Soria, J.; Clemente-Leon, M.; Coronado, E.; Waerenborgh, J. C.; Lloret, F.; Pardo, E. *Chem. Commun.* 2016, 52, 7360–7363.
5. Fortea-Perez, F. R.; Mon, M.; Ferrando-Soria, J.; Boronat, M.; Leyva-Perez, A.; Corma, A.; Herrera, J. M.; Osadchii, D.; Gascon, J.; Armentano, D.; Pardo, E. *Nat. Mater.* 2017, 16, 760–766.
6. Yagub, M. T.; Sen, T. K.; Afroze, S.; Ang, H. M. *Adv. Colloid Interface Sci.* 2014, 209, 172–184.
7. Hao, O.; Kim, H.; Chiang, P. *Crit. Rev. Env. Sci. Tec.* 2000, 30, 449–505.
8. Goulson, D. *J. Appl. Ecol.* 2013, 50, 977–987.
9. Tilman, D.; Cassman, K. G.; Matson, P. A.; Naylor, R.; Polasky, S. *Nature*, 2002, 418, 671–677.

3.3. Metal-Organic Frameworks as Unique Platforms to Gain Insight of σ -Hole Interactions for the Removal of Organic Dyes from Aquatic Ecosystems (Publication 3)

The combination of high crystallinity and rich host-guest chemistry in MOFs, have situated them in an advantageous position with respect to traditional porous materials, to gain insight on specific weak noncovalent supramolecular interactions. In particular, sulfur σ -hole interactions are known to play a key role in the biological activity of living beings as well as on relevant molecular recognitions processes. However, they have been barely explored so far. Here we describe how the combination of the intrinsic features of MOFs, especially the possibility of using single-crystal X-ray crystallography can be an extremely valuable tool to gain insight on sulfur σ -hole interactions, and how their rational exploitation can be enormously useful in the efficient removal of harmful organic molecules from aquatic ecosystems. Thus, we have used a MOF, prepared from the amino acid *L*-methionine and possessing channels decorated with $-\text{CH}_2\text{CH}_2\text{SCH}_3$ thioalkyl chains, to remove a family of organic dyes at very low concentrations (10 ppm) from water. This MOF is able to efficiently capture the four dyes in a very fast manner, reaching within five minutes nearly the maximum removal. Remarkably, the crystal structure of the different organic dyes within MOFs channels could be determined by SCXRD. This have enabled us to directly visualize the important role sulfur σ -hole interactions play on the removal of organic dyes from aqueous solutions, representing one of the first studies on the rational exploitation of σ -hole interactions for water remediation.

3.3.1. Introduction

Weak non-covalent interactions are ubiquitous in many relevant processes occurring in living beings, and represent one of the most important tools in Supramolecular Chemistry to mimic/emulate such processes.¹⁻⁴ Among them, σ -hole interactions are of particular interest. A σ -hole is the region of electron deficiency that appears in the outer lobe of an orbital, when an atom from the group V-VII (with half-filled p orbitals), participate in a covalent bond.⁵⁻⁷ This σ -hole can create a region of positive electrostatic potential if the rest of the molecule presents a relatively sufficient electron-withdrawing nature with respect to the group V-VII atom, and this one is sufficiently polarizable to interact with electron donors, such as nitrogen and oxygen, and even, π -systems. Despite this interaction is present in key supramolecular recognitions processes and is very relevant in biological activity, its importance has been somehow underestimated in comparison to hydrogen-bonds, with the exception of halogen ones.⁷ For example, this is the case of sulfur σ -hole interaction, which has been mainly described in post-analysis of close contacts in protein data bank or as stabilizing agent of desired conformations of drugs for interacting with receptors.⁸⁻¹² Indeed, the rational use of such interaction for specific applications has been barely explored.¹³⁻²⁰

Metal-organic frameworks (MOFs)²¹⁻²⁸ are a class of crystalline porous inorganic-organic materials, whose rich host-guest chemistry²⁹⁻³⁵ and high crystallinity,³⁶⁻³⁸ together with the possibility to have - to a certain extent - a control of their dimensionality, topology and functionality by chemical design,³⁹⁻⁴⁵ have situated them in an advantageous position among other porous materials. This has been clearly exemplified by the continuous growth of novel aesthetically pleasant crystal structures,⁴⁶⁻⁴⁹ as well as by the wide range of applications where they have shown successful, *e.g.* gas storage and separation, catalysis, drug delivery, conductivity, molecular recognition of small molecules, encapsulation of functional moieties, magnetism, chemical nanoreactors and water

remediation.⁵⁰⁻⁶² Indeed, relevant advances performed in MOFs' chemistry have been, mainly, consequence of the combined possibility to tailor the functionalities decorating MOFs channels by chemical design and the application of SCXRD as basic characterization tool.⁶³⁻⁶⁸ This has demonstrated as a powerful approach to understand/rationalize host-guest interactions and, eventually, to find, structure-properties relationships that have enabled positive feedback of knowledge to develop more performant MOFs.⁶⁹ Thus, MOFs are, *a priori*, excellent playgrounds to gain insight on specific molecular recognitions interactions, such as sulfur σ -hole, in order to exploit them towards a targeted application.

Contamination of aquatic ecosystems with organic dyes represents a severe environmental problem, having a negative impact on the quality of aquatic ecosystems - *i.e.* inhibiting plants and algae photoactivity and representing a health threat for fish as a consequence of their teratogenic, mutagenic and carcinogenic character - and consequently on human life.⁷⁰

Different technologies have been studied for the removal of organic dyes from wastewater streams.⁷¹⁻⁷³ Among them, the use of water-resistant highly stable MOFs^{74,75} for their capture and/or photodegradation has revealed as a very promising approach.^{71,76-79} This is mainly due to the intrinsic characteristic properties of MOFs highlighted above. However, despite the great structural, compositional and functional diversity of MOFs, its potential has been poorly explored and somehow underdeveloped so far in this field, and consequently more research efforts are needed to fully unleash them.

One of our research lines is focused on exploiting the differentiating features of MOFs toward catalytic and water remediation applications.^{52,71} Along the development of our investigations, we have found that sulfur σ -hole interactions¹³⁻²⁰ may have a more prominent role in the capture process than previously thought.

In this context, we intend to expand our knowledge on these interactions, through the rational application of suitable MOFs for the removal of organic dyes from aquatic ecosystems. To this end, we have prepared a neutral 3D MOF, with formula $\{\text{Sr}^{\text{II}}\text{Cu}_6^{\text{II}} [(\text{S}, \text{S})\text{-methox}]_3 (\text{OH})_2 (\text{H}_2\text{O})\} \cdot 16\text{H}_2\text{O}$ (**1**; methox = bis [(*S*)-methionine] oxalyl diamide), constructed with oxamate ligands derived from the natural amino acid *L*-methionine (see Experimental Section, Supporting Information).^{13,14,18,19} The selection of **1** was not accidental. This was based on our previous work with an isorecticular MOF to **1** - with calcium instead of strontium.^{13,14} This MOF exhibited functional channels decorated with flexible $-\text{CH}_2\text{CH}_2\text{SCH}_3$ thioalkyl chains with outstanding molecular recognition properties - for a variety of heavy metals and organic contaminants like neonicotinoid insecticides - and high crystallinity - which have enabled to unveil the crystal structure of diverse and unique host-guest assemblies.^{15,18} In this work, we have observed that **1** is capable to remove, efficiently, four organic dyes -that are commonly used as antiseptics in hospitals or in textile industries (Auramine O (AO), Brilliant Green (BG), Methylene Blue (MB) and Pyronin Y (PY))- at very low concentrations (10 ppm) from water (Scheme S1). Indeed, this process takes place with a very fast kinetics, improving, notably, the performance of a related reported MOF with serine hydroxyl-residues functionalizing the pores,⁸⁰ which, *a priori*, would be expected to interact more efficiently with organic molecules through hydrogen-bonds. Thanks to the high degree of crystallinity of **1** and the application of cutting-edge single-crystal X-ray crystallography techniques, we have been able to get unique snapshots of the assembled host-guest systems, which have allowed to rationalize the nice removal efficiency of **1**, and more importantly, improve our knowledge on sulfur σ -hole interaction.

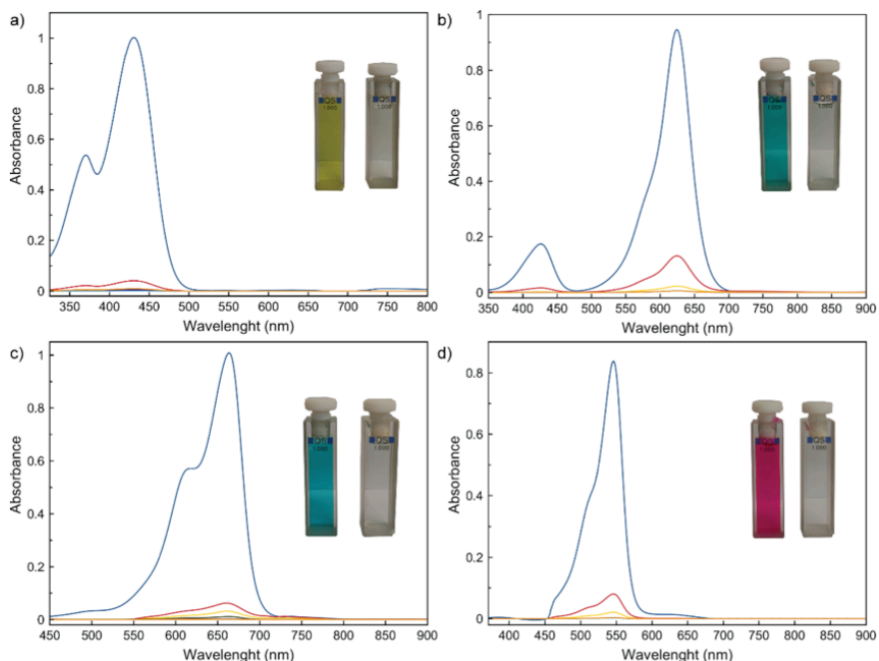


Figure 1. Evolution with time of the UV-Vis absorption spectra of 10 ppm solutions of AO (a), BG (b), MB (c) and PY (d) in real water samples from Turia river when using 50 mg of pellets of **1** as adsorbent. Colors code: Blue: $t = 0$; Red: $t = 1$ min.; Yellow: $t = 5$ min.; Orange $t = 30$ min.; Light blue $t = 360$ min.; Green: $t = 720$ minutes. The inset shows the photographs of the solutions at $t = 0$ (left) and after only five minutes of the dye removal experiments (right).

3.3.2. Results and Discussion

Removal experiments of organic dyes

In order to evaluate the removal efficiency of **1** toward the four selected organic dyes - Auramine O (AO), Brilliant Green (BG), Methylene Blue (MB) and Pyronin Y (PY) - we processed **1** in the form of extruded pellets, by mixing polycrystalline powders of **1** with commercial Matrimid in 80:20 ratios (Experimental Section, Supporting Information).

3. MOFs AND MTV-MOFs FOR WATER REMEDIATION

The structuration of MOFs is a very interesting and necessary topic of research, which allows to prepare materials with improved applicability as a direct consequence of their better handling and longer lifetime.⁸¹ However, in some cases it is difficult to retain the chemical/physical properties of the selected MOF. To preclude this option, we have performed PXRD pattern of the prepared pellets of **1**, which evidence that is isostructural to polycrystalline powders of **1** (Figure S1a,b).

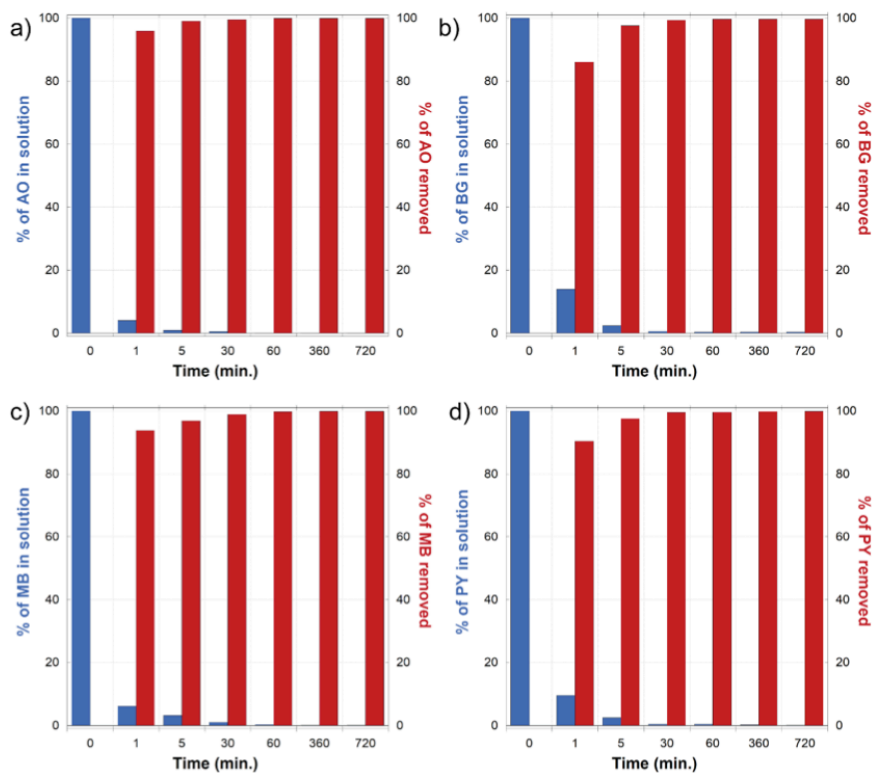


Figure 2. Evolution with time of the adsorption of AO (a), BG (b), MB (c) and PY (d) in 10 ppm solutions using real water samples from Turia river (50 mg of pellets of **1** as adsorbent). Blue bars represent the % of each dye within the solution and red bars represent the % of the dye removed from the solution.

Then, using the prepared pellets of **1** (50 mg), we have studied its efficiency for the removal of organic dyes using individual spiked solutions of each of them (10 mL, 10 ppm) in real water samples from Turia river (Valencia, Spain). These processes were followed with UV-vis spectroscopy (Figures 1 and 2), measuring the decrease in the intensity of the respective characteristic/principal absorption band in the visible region at different times (1, 5, 30, 60, 360 and 720 min). The kinetic profile obtained (Figure 2 and Table S2) evidenced the efficient and fast adsorption of all four tested dyes, reaching nearly 90 % of removal after only 5 min. This contrast with the serine-based MOF, which need nearly 24 hours to reach the same capture efficiency.⁸⁰ This removal efficiency and kinetics of adsorption was even maintained when using a multi-dye mixture solution, 10 ppm of each of all four dyes (Figure S2, Table S3 and Experimental Section, Supporting Information). Here, it is noteworthy to remark the relevance of the observed results by **1**, which not only is capable to capture these organic contaminants at very low concentration –similar to the ones found in industrial wastewaters– in a very efficient and fast manner, but also in samples where the presence of other ions could interfere the adsorption process.

The pH-dependence of the capture properties of **1** has been also evaluated. Thus, the same capture experiments above described were repeated using the same water samples from Turia river whose pH was adjusted at 5 and 11, with HCl and NaOH, respectively (Figures S3-S6). Overall, the capture efficiency in both acid and basic media are almost identical to that observed with real water samples, suggesting that **1** is equally effective under moderate changes in pH.

Recyclability, maximum uptake and scale-up

The reusability and structural and physical integrity of any adsorbent are parameters of main relevance in order to fully characterize them and think toward real-world applications. We observed **1** could be easily regenerated by immersing the extruded pellets in a methanol solution for 15 min, while retaining the crystallinity -as PXRD in Figure S1c evidenced- and maintaining the removal efficiency in the next capture experiment (Table S4). The crystallinity is also retained for **1**, after capture experiments at pH = 5 and 11 and the same regeneration treatment with methanol, as PXRD shows (Figure S1d, e). Further evidence of the robustness of the extruded pellets of **1** was assessed by SEM. Figure S7 shows the final appearance of pellets of **1** before and after the capture/regeneration process.

Aiming at evaluating the maximum loading capacity of **1** for each organic dye, we prepared aqueous saturated solutions of each dye and soaked **1** for two weeks while replacing the saturated solution every 12 hours. Maximum uptakes of 598.9, 786.8, 554.0 and 542.6 mg g⁻¹ were obtained for AO, BG, MB and PY, respectively (see Experimental Section for characterization details). These values were obtained from the CHSN analyses that are collected in Table S5. Overall, these features together with the easiness to produce **1** at multigram-scale (see Experimental Section, Supporting Information) and environmentally benign nature of its components, makes **1** an attracting candidate to be tested in pilot plants or structured in mixed-matrix membranes.

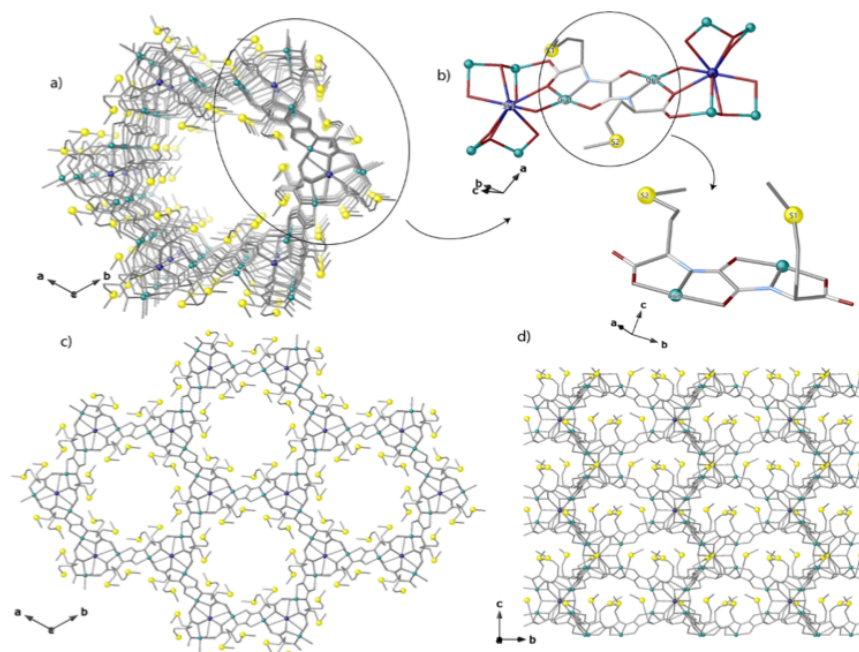
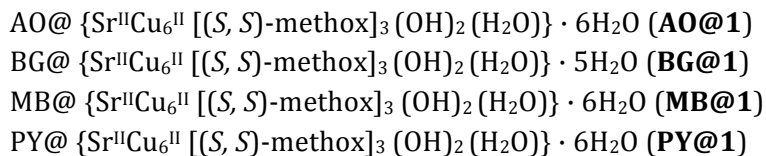


Figure 3. Crystal structure of **1**. (a) Perspective view along *c* crystallographic axis of a single channel in crystal structure of **1**. (b) Fragments of **1** showing the dianionic bis (hydroxo) dicopper(II) building blocks. Views of a fragment of **1** in the *ab* (c) and *bc* (d) planes, respectively. Copper, strontium and sulfur atoms are represented by cyan, blue and yellow spheres, respectively, whereas the ligands (except sulfur) are depicted as sticks (carbon: gray, oxygen: red and nitrogen: blue).

X-ray crystal structure

In order to elucidate the host-guest interactions established between **1** (structure shown in Figure 3) and the captured organic dyes - playing special attention to sulfur σ -hole ones-, crystals of **1** were soaked in saturated acetonitrile solutions of each organic dye for one week. After that period, crystals of enough quality to solve the crystal structure of four host-guest systems by means of SCXRD could be obtained (Table S1). Their formula, supported by CHSN EA, ICP-MS and TGA (see Experimental Section, Supporting Information), are:



The resolution of the crystal structure of adsorbates allowed the atomically-precise visualization of the main host-guest interactions, likely at the origin of the efficient captures of pollutant dyes by the thio-alkyl residues decorating the framework (Figures 4, 5 and S8-S14).

The four compounds **AO@1**, **BG@1**, **MB@1** and **PY@1** are isomorphous to **1**, crystallizing in the $P6_3$ chiral space group of the hexagonal system. This behavior confirms the robustness of **1** as hosting matrix. They are built by uni-nodal **acs** six-connected 3D strontium(II)-copper(II) porous networks, decorated by highly flexible $\text{CH}_2\text{CH}_2\text{SCH}_3$ thioalkyl chains, which are capable to act as receptors towards guest dyes (Figures 3-5, S9, S11 and S13). The four crystal structures undoubtedly evidence that AO, BG, MB and PY guest molecules are encapsulated in the nanopores of **1**, where they are recognized by the thioether arms of the methionine residues. As expected for loaded-porous structures, the dye molecules displayed a severe disorder in pores, both dynamical and statistic (see Experimental Section, Supporting Information). All the crystal structures exhibit different allocations of guests with a 1:3 statistical distribution (Figures S8, S10, S12 and S14) strictly dependent on the size and chemical nature of the dye. The main host-guest interactions are assured by sulfur atoms directly interacting either with Cl^- anions in **AO@1**, **MB@1** and **PY@1** or with aromatic rings *via* the low-lying σ^* orbitals of the c-s bond (σ -hole), available for interaction with electron donors such as the four dyes π -systems.

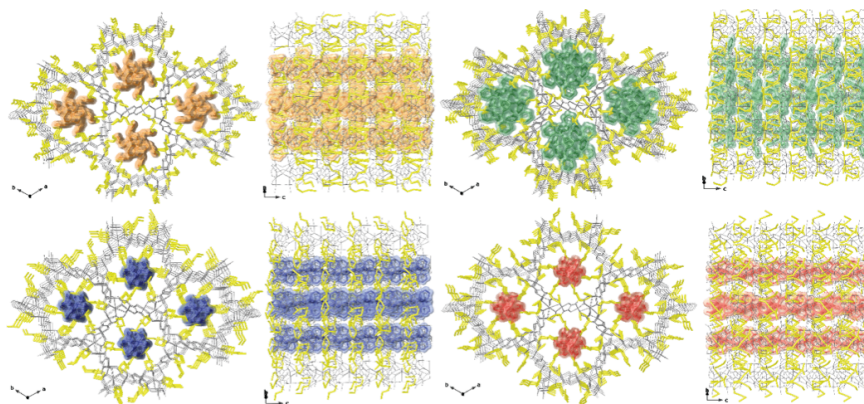


Figure 4. Perspective views in the *ab* (left) and *bc* (right) planes of the host-guest assemblies of **AO@1** (a), **BG@1** (b), **MB@1** (c) and **PY@1** (d). The networks are represented as light gray sticks with $-\text{CH}_2\text{CH}_2\text{SCH}_3$ ethylthiomethyl residues as yellow sticks and guest organic dyes as orange (AO), green (BG), blue (MB) and red (PY) solid surfaces. Free water molecules have been omitted for clarity.

As far as **AO@1**, **MB@1** and **PY@1** is concerned, the capture of Cl^- anions, nicely blocked in the most hindered voids of the MOF by directly $\text{S}\cdots\text{Cl}$ interaction [2.43(3), 2.20(2) and 2.87(2) Å, for **AO@1**, **MB@1** and **PY@1**, respectively], can be seen as a driving force to the further insertion of cationic dye molecules, which are captured thanks to $\text{S}\cdots\pi$ interactions, supported also by those electrostatic interactions (Figures 5, S11 and S13).

In **AO@1** and **PY@1** the network host displayed a more open structure when compared with **MB@1** and especially with **BG@1**. The bigger size and/or less efficient packing of the latter dyes likely accounting for that. Indeed, in **PY@1** methionine arms are distended to interact through $\text{S}\cdots\text{H}-\text{C}$ weak interactions [shortest $\text{S}\cdots\text{H}-\text{C}$ distances of 2.88(3) and 3.16(3) Å], which anchor external aromatic rings to the walls of the MOF. The severe statistic and thermal disorder did not allow us to model terminal $-\text{N}(\text{CH}_3)_2$ (see Experimental Section for details). However, the defined orientations gave clues on potential $\text{C}-\text{H}\cdots\text{N}$ intermolecular interactions involving adjacent molecules.

Indeed, supramolecular chains of Pyronin Y molecules evidence a propagation along the direction of channels, as imposed by the hosting matrix, which not only host but also align guests.

More evident σ -hole interactions are detected in **AO@1** crystal structure, where $-\text{CH}_2\text{CH}_2\text{SCH}_3$ methionine arms point toward the $-\text{NH}_2^+$ group of the Auramine O organic dye [$\text{S}\cdots\text{N}$ distance of 4.44(3) Å] (Figure 5). Further stabilizing host-guest interactions occur between $-\text{CH}_2\text{CH}_2\text{SCH}_3$ ethylthiomethyl chains and aromatic rings of AO dye molecule [centroid $\cdots\text{C}$ distances of 3.40(2), 3.56(2) and 3.72(2) Å] (Figure 5). Despite the unresolved disorder -that does not allow to spot any further details and neither defining the messy $-\text{N}(\text{CH}_3)_2$ terminal group of the organic dye and a lattice water molecule-, it can be inferred implications of the free rotation of the two phenyl rings in reducing the strength of the interactions, which, even if detected, it appears weak when looking at distances, although they must be imagined as averaged in the crystal.

In **BG@1** and **MB@1** crystal structures, the size of BG and MB and/or their worst self-packing impose a more contracted conformation of the methionine derivatives arms. BG crystal structure, exhibits a very nice interlock between BG molecules and hosting matrix, based on $\text{S}\cdots\pi$ interactions [centroid $\cdots\text{C}$ distance of 3.14(3) Å] (Figure S9). As far as for **MB@1** is concerned, we have to underline a direct bond involving methionine-sulfur and nitrogen atoms belonging to the MB molecule at a distance of 1.79(2) Å, in agreement with similar bonds reported in literature,¹⁵ which packed dye molecules confining sulfur atoms of the dye molecule at the center of the pores (Figure S11). Also in these cases, due to dynamic disorder, terminal $-\text{N}(\text{CH}_2\text{CH}_3)_2$ groups present in **BG@1** and $-\text{N}(\text{CH}_3)_2$ in **MB@1** have not been modelled (see Experimental Section for details). However, the core of the dye molecules, although with disorder, has been defined, suggesting the main interactions with terminal $-\text{N}(\text{CH}_2\text{CH}_3)_2$ and $-\text{N}(\text{CH}_3)_2$ groups likely involve dye intermolecular ones. Surprisingly, for all dyes, the high degree of loading in the confined space is the same. Each dye molecule does

displace almost all water molecules from pores in order to reach the observed close packing. The totally fill of the channels makes the adsorbates very stable at air and room temperature for months.

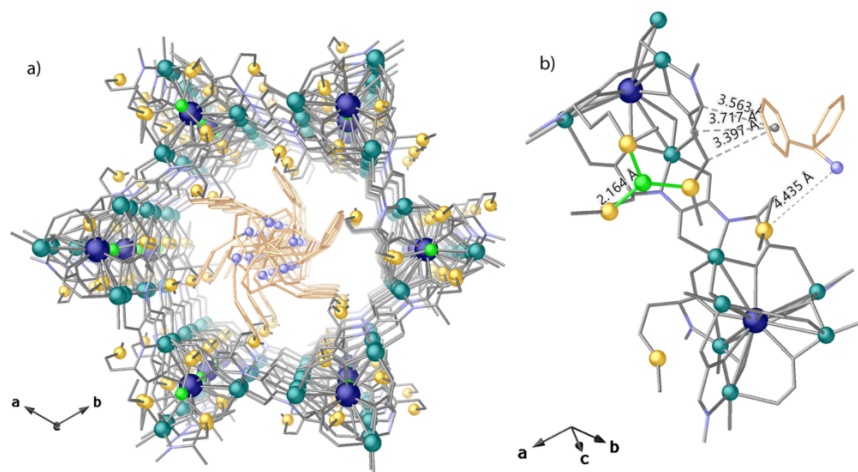


Figure 5. Details of host-guest interactions in **AO@1**: (a) Perspective view of a single channel of X-ray crystal structure of **AO@1** along *c* crystallographic axis emphasizing pores filled by Auramine O and (b) details of host-guest interactions ($S\cdots Cl$ and $AO\cdots S$ represented as green and grey dashed lines, respectively). Copper and calcium are represented by cyan and blue spheres respectively, whereas the ligands and guest molecules are depicted as grey and gold sticks except for sulfur atoms of methox moieties and nitrogen atoms of guest' molecule, which are represented by yellow and blue-sky spheres, respectively. Free water molecules are omitted for clarity.

The good performance of **1** for chosen dye capture could be understood analyzing non-covalent interactions within the final aggregates with the help of X-ray crystallography. As stated above, it is known that σ -hole bonding plays a pivotal role in the 3D organization of crystalline structures and in various molecular scaffolds. Indeed, these interactions, frequently unnoticed or identified as secondary contacts, can be highly predictable and generally present. In this work we considered and used them as a novel and efficient tool to reach high performance in capture of pollutant dyes.

Studies on this subject have worked dramatically to interpret and rationalize properties of **1**. In fact, the importance of such interactions is clearly manifested in a multitude of biological phenomena.⁸² In all the four adsorbates **AO@1**, **BG@1**, **MB@1** and **PY@1** a kind of S $\cdots\pi$ interactions, together with S \cdots Cl interactions in **AO@1**, **MB@1** and **PY@1**, have been detected. Certainly, although an aromatic π -system can be electron-rich or electron-deficient, it can be non-covalently bonded to a σ -hole-containing molecule, as in the cases reported here containing molecule $\cdots\pi$ -system interactions. The σ -hole term is assigned to the area of positive or less negative electrostatic potential emerging on the outer surface of the covalently bonded sulfur atom. In this scenario, σ -hole interactions found in **AO@1**, **BG@1**, **MB@1** and **PY@1**, even if different in nature and discussed in the context of other electrostatic interactions, are the main forces at the origin of efficient capture of dyes in **1**. Their density of propagation, through the confined space ensured by **1**, represent the power of encapsulation of the system, being reminiscent of peptide-based methionine. In such supramolecular aggregates, these bonds rely to a large extent also on polarization and charge transfer effects, accompanied by dispersive forces –even if the precise mix of these different components varies from one bond to another. Thus, it is clear that a particular sort of hole does not have to be present in the isolated monomer, but it will be active when cooperative and polarizing forces can occur.

Thermogravimetric analysis, N₂ isotherm adsorption and X-ray powder diffraction

The water content of **1**, **AO@1**, **BG@1**, **MB@1** and **PY@1** was determined by TGA under a dry N₂ atmosphere. All of them show a small loss of solvent from room temperature, in comparison with **1**, which agrees with the fact that the channels are filled with organic dyes. In particular, they showed a weight loss of 15.86 (**1**), 5.30 (**AO@1**), 4.35 (**BG@1**), 5.25 (**MB@1**) and 5.22 % (**PY@1**), that correspond with 16, 6, 5, 6 and 6 water molecules, respectively, which is in line with CHSN analyses (Figure S15).

The N₂ adsorption at 77 K of **AO@1**, **BG@1**, **MB@1** and **PY@1** showed a considerable reduction with respect to **1**, which further support that the channels are occupied by organic dyes molecules (Figure S16). The experimental PXRD patterns of polycrystalline sample of **1**, **AO@1**, **BG@1**, **MB@1** and **PY@1** confirm the purity and homogeneity of the bulk samples (Figure S17). As it was previously observed, the slight increase in relative intensity at the higher-angle peaks of dyes@**1**, with respect to **1**, are most likely consequence of the increase of the electronic density in the channels filled with organic dyes.

3.3.3. Conclusions

Here we have presented our recent advances on the relevance of σ -hole interactions toward applications. In particular, we have gained insight by means of single-crystal X-ray crystallography of the importance of such poorly investigated interactions for the removal of four organic dyes from real river waters. In doing so, we have precisely characterized four host-guest adsorbates, where the main interactions between the organic dyes and the framework allowed us to rationalize the appealing removal properties of **1**. Indeed, **1** has revealed as one of the best performing MOFs –in terms of both speed and removal efficiency–for the capture of organic dyes.⁷¹ In an indirect manner, we have taken this MOF one step closer to real world applications by both its structuration as extruded pellets and the scale-up synthesis. This work represents an interesting beginning of a research line, which currently we are developing to integrate **1** in a decontamination pilot plant.

3.3.4. References

1. Lehn, J.-M. *Supramolecular Chemistry*; Wiley: **1995**.
2. Vantomme, G.; Meijer, E. W. *Science* **2019**, 363, 1396–1397.
3. Amabilino, D. B.; Gale, P. A. *Chem. Soc. Rev.* **2017**, 46, 2376–2377.

4. Liu, W.; Stoddart, J. F. *Chem* **2021**, 7, 919–947.
5. Murray, J. S.; Lane, P.; Politzer, P. *Int. J. Quantum Chem.* 2008, 108, 2770–2781.
6. Scheiner, S.; Adhikari, U. *J. Phys. Chem. A* **2011**, 115, 11101–11110.
7. Politzer, P.; Murray, J. S.; Clark, T. *Phys. Chem. Chem. Phys.* **2013**, 15, 11178.
8. Obata, A.; Kawazura, H.; Miyamae, H. *Acta Crystallogr. Sect. C Cryst. Struct. Commun.* **1984**, 40, 45–48.
9. Nagao, Y.; Hirata, T.; Goto, S.; Sano, S.; Kakehi, A.; Iizuka, K.; Shiro, M. *J. Am. Chem. Soc.* **1998**, 120, 3104–3110.
10. Iwaoka, M.; Takemoto, S.; Tomoda, S. *J. Am. Chem. Soc.* **2002**, 124, 10613–10620.
11. Hudson, B. M.; Nguyen, E.; Tantillo, D. J. *Org. Biomol. Chem.* **2016**, 14, 3975–3980.
12. Thomas, S. P.; Jayatilaka, D.; Guru Row, T. N. *Phys. Chem. Chem. Phys.* **2015**, 17, 25411–25420.
13. Mon, M.; Ferrando-Soria, J.; Grancha, T.; Fortea-Pérez, F. R.; Gascon, J.; Leyva-Pérez, A.; Armentano, D.; Pardo, E. *J. Am. Chem. Soc.* **2016**, 138, 7864–7867.
14. Mon, M.; Lloret, F.; Ferrando-Soria, J.; Martí-Gastaldo, C.; Armentano, D.; Pardo, E. *Angew. Chem. Int. Ed.* **2016**, 55, 11167–11172.
15. Mon, M.; Bruno, R.; Tiburcio, E.; Viciano-Chumillas, M.; Kalinke, L. H. G.; Ferrando-Soria, J.; Armentano, D.; Pardo, E. *J. Am. Chem. Soc.* **2019**, 141, 13601–13609.
16. Mon, M.; Qu, X.; Ferrando-Soria, J.; Pellicer-Carreño, I.; Sepúlveda-Escribano, A.; Ramos-Fernandez, E. V.; Jansen, J. C.; Armentano, D.; Pardo, E. *J. Mater. Chem. A* **2017**, 5, 20120–20125.
17. Mon, M.; Rivero-Crespo, M. A.; Ferrando-Soria, J.; Vidal-Moya, A.; Boronat, M.; Leyva-Pérez, A.; Corma, A.; Hernández-Garrido, J. C.; López-Haro, M.; Calvino, J. J.; Ragazzon, G.; Credi, A.; Armentano, D.; Pardo, E. *Angew. Chem. Int. Ed.* **2018**, 57, 6186–6191.

18. Negro, C.; Martínez Pérez-Cejuela, H.; Simó-Alfonso, E. F.; Herrero-Martínez, J. M.; Bruno, R.; Armentano, D.; Ferrando-Soria, J.; Pardo, E. *ACS Appl. Mater. Interfaces* **2021**, 13, 28424–28432.
19. Bruno, R.; Mon, M.; Escamilla, P.; Ferrando-Soria, J.; Esposito, E.; Fuoco, A.; Monteleone, M.; Jansen, J. C.; Elliani, R.; Tagarelli, A.; Armentano, D.; Pardo, E. *Adv. Funct. Mater.* **2021**, 31, 2008499.
20. Tiburcio, E.; Greco, R.; Mon, M.; Ballesteros-Soberanas, J.; Ferrando-Soria, J.; López-Haro, M.; Hernández-Garrido, J. C.; Oliver-Meseguer, J.; Marini, C.; Boronat, M.; Armentano, D.; Leyva-Pérez, A.; Pardo, E. *J. Am. Chem. Soc.* **2021**, 143, 2581–2592.
21. Furukawa, H.; Cordova, K. E.; O’Keeffe, M.; Yaghi, O. M. *Science* **2013**, 341, 974.
22. Zhou, H.-C.; Kitagawa, S. *Chem. Soc. Rev.* **2014**, 43, 5415–5418.
23. Seoane, B.; Castellanos, S.; Dikhtiarenko, A.; Kapteijn, F.; Gascon, J. *Coord. Chem. Rev.* **2016**, 307, 147–187.
24. Maurin, G.; Serre, C.; Cooper, A.; Férey, G. *Chem. Soc. Rev.* **2017**, 46, 3104–3107.
25. Yaghi, O. M.; Kalmutzki, M. J.; Diercks, C. S. *Introduction to Reticular Chemistry*; Wiley-VCH: Weinheim, Germany, **2019**.
26. Zhang, X.; Wang, B.; Alsalme, A.; Xiang, S.; Zhang, Z.; Chen, B. *Coord. Chem. Rev.* **2020**, 423, 213507.
27. Xu, W.; Tu, B.; Liu, Q.; Shu, Y.; Liang, C.-C.; Diercks, C. S.; Yaghi, O. M.; Zhang, Y.-B.; Deng, H.; Li, Q. *Nat. Rev. Mater.* **2020**, 5, 764–779.
28. Freund, R.; Zaremba, O.; Arnauts, G.; Ameloot, R.; Skorupskii, G.; Dincă, M.; Bavykina, A.; Gascon, J.; Ejsmont, A.; Goscianska, J.; Kalmutzki, M.; Lächelt, U.; Ploetz, E.; Diercks, C. S.; Wuttke, S. *Angew. Chem. Int. Ed.* **2021**, 60, 23975–24001.
29. Deng, H.; Grunder, S.; Cordova, K. E.; Valente, C.; Furukawa, H.; Hmadeh, M.; Gandara, F.; Whalley, A. C.; Liu, Z.; Asahina, S.; Kazumori, H.; O’Keeffe, M.; Terasakij, O.; Stoddart, F.; Yaghi, O. M. *Science* **2012**, 336, 1018–1023.

30. Antypov, D.; Shkurenko, A.; Bhatt, P. M.; Belmabkhout, Y.; Adil, K.; Cadiau, A.; Suyetin, M.; Eddaoudi, M.; Rosseinsky, M. J.; Dyer, M. S. *Nat. Commun.* **2020**, *11*, 6099.
31. Ji, Z.; Wang, H.; Canossa, S.; Wuttke, S.; Yaghi, O. M. *Adv. Funct. Mater.* **2020**, *30*, 2000238.
32. Wang, H.; Shi, Z.; Yang, J.; Sun, T.; Rungtaweivoranit, B.; Lyu, H.; Zhang, Y.; Yaghi, O. M. *Angew. Chem. Int. Ed.* **2021**, *60*, 3417–3421.
33. Mon, M.; Bruno, R.; Sanz-Navarro, S.; Negro, C.; Ferrando-Soria, J.; Bartella, L.; Di Donna, L.; Prejanò, M.; Marino, T.; Leyva-Pérez, A.; Armentano, D.; Pardo, E. *Nat. Commun.* **2020**, *11*, 3080.
34. Mon, M.; Bruno, R.; Tiburcio, E.; Grau-Atienza, A.; Sepúlveda-Escribano, A.; Ramos-Fernandez, E. V.; Fuoco, A.; Esposito, E.; Monteleone, M.; Jansen, J. C.; Cano, J.; Ferrando-Soria, J.; Armentano, D.; Pardo, E. *Chem. Mater.* **2019**, *31*, 5856–5866.
35. Mon, M.; Bruno, R.; Ferrando-Soria, J.; Bartella, L.; Di Donna, L.; Talia, M.; Lappano, R.; Maggiolini, M.; Armentano, D.; Pardo, E. *Mater. Horiz.* **2018**, *5*, 683–690.
36. Inokuma, Y.; Arai, T.; Fujita, M. *Nat. Chem.* **2010**, *2*, 780–783.
37. Inokuma, Y.; Yoshioka, S.; Ariyoshi, J.; Arai, T.; Fujita, M. *Nat. Protoc.* **2014**, *9*, 246–252.
38. Zigon, N.; Hoshino, M.; Yoshioka, S.; Inokuma, Y.; Fujita, M. *Angew. Chem. Int. Ed.* **2015**, *54*, 9033–9037.
39. Guillerm, V.; Eddaoudi, M. *Acc. Chem. Res.* **2021**, *54*, 3298–3312.
40. Jiang, H.; Alezi, D.; Eddaoudi, M. *Nat. Rev. Mater.* **2021**, *6*, 466–487.
41. Freund, R.; Canossa, S.; Cohen, S. M.; Yan, W.; Deng, H.; Guillerm, V.; Eddaoudi, M.; Madden, D. G.; Fairen-Jimenez, D.; Lyu, H.; Macreadie, L. K.; Ji, Z.; Zhang, Y.; Wang, B.; Haase, F.; Wöll, C.; Zaremba, O.; Andreo, J.; Wuttke, S.; Diercks, C. S. *Angew. Chem. Int. Ed.* **2021**, *60*, 23946–23974.
42. Feng, L.; Day, G. S.; Wang, K.-Y.; Yuan, S.; Zhou, H.-C. *Chem.* **2020**, *6*, 2902–2923.

43. Chen, Z.; Jiang, H.; Li, M.; O’Keeffe, M.; Eddaoudi, M. *Chem. Rev.* **2020**, 120, 8039–8065.
44. Li, M.; Li, D.; O’Keeffe, M.; Yaghi, O. M. *Chem. Rev.* **2014**, 114, 1343–1370.
45. O’Keeffe, M.; Yaghi, O. M. *Chem. Rev.* **2012**, 112, 675–702.
46. Isaka, Y.; Kawase, Y.; Kuwahara, Y.; Mori, K.; Yamashita, H. *Angew. Chem. Int. Ed.* **2019**, 58, 5402–5406.
47. Jiang, H.; Jia, J.; Shkurenko, A.; Chen, Z.; Adil, K.; Belmabkhout, Y.; Weselinski, L. J.; Assen, A. H.; Xue, D.-X.; O’Keeffe, M.; Eddaoudi, M. *J. Am. Chem. Soc.* **2018**, 140, 8858–8867.
48. Li, P.; Vermeulen, N. A.; Malliakas, C. D.; Gómez-Gualdrón, D. A.; Howarth, A. J.; Mehdi, B. L.; Dohnalkova, A.; Browning, N. D.; O’Keeffe, M.; Farha, O. K. *Science* **2017**, 356, 624–627.
49. Fortea-Pérez, F. R.; Mon, M.; Ferrando-Soria, J.; Boronat, M.; Leyva-Pérez, A.; Corma, A.; Herrera, J. M.; Osadchii, D.; Gascon, J.; Armentano, D.; Pardo, E. *Nat. Mater.* **2017**, 16, 760–766.
50. Li, R.; Alomari, S.; Islamoglu, T.; Farha, O. K.; Fernando, S.; Thagard, S. M.; Holsen, T. M.; Wriedt, M. *Environ. Sci. Technol.* **2021**, 55, 15162–15171.
51. Jiang, Z.; Xu, X.; Ma, Y.; Cho, H. S.; Ding, D.; Wang, C.; Wu, J.; Oleynikov, P.; Jia, M.; Cheng, J.; Zhou, Y.; Terasaki, O.; Peng, T.; Zan, L.; Deng, H. *Nature* **2020**, 586, 549–554.
52. Viciano-Chumillas, M.; Mon, M.; Ferrando-Soria, J.; Corma, A.; Leyva-Pérez, A.; Armentano, D.; Pardo, E. *Acc. Chem. Res.* **2020**, 53, 520–531.
53. Young, R. J.; Huxley, M. T.; Pardo, E.; Champness, N. R.; Sumbly, C. J.; Doonan, C. J. *J. Chem. Sci.* **2020**, 11, 4031–4050.
54. Wang, B.; Lv, X.-L.; Feng, D.; Xie, L.-H.; Zhang, J.; Li, M.; Xie, Y.; Li, J.-R.; Zhou, H.-C. *J. Am. Chem. Soc.* **2016**, 138, 6204–6216.
55. Gonzalez, M. I.; Turkiewicz, A. B.; Darago, L. E.; Oktawiec, J.; Bustillo, K.; Grandjean, F.; Long, G. J.; Long, J. R. *Nature* **2020**, 577, 64–68.

56. Hanikel, N.; Prévot, M. S.; Yaghi, O. M. *Nat. Nanotechnol.* **2020**, *15*, 348–355.
57. Bavykina, A.; Kolobov, N.; Khan, I. S.; Bau, J. A.; Ramirez, A.; Gascon, J. *Chem. Rev.* **2020**, *120*, 8468–8535.
58. Chen, Z.; Li, P.; Anderson, R.; Wang, X.; Zhang, X.; Robison, L.; Redfern, L. R.; Moribe, S.; Islamoglu, T.; Gómez-Gualdrón, D. A.; Yildirimj, T.; Stoddart, F.; Farha, O. K. *Science* **2020**, *368*, 297–303.
59. Lin, R.-B.; Xiang, S.; Zhou, W.; Chen, B. *Chem.* **2020**, *6*, 337–363.
60. Xie, L. S.; Skorupskii, G.; Dincă, M. *Chem. Rev.* **2020**, *120*, 8536–8580.
61. Hu, Q.; Yu, J.; Liu, M.; Liu, A.; Dou, Z.; Yang, Y. *J. Med. Chem.* **2014**, *57*, 5679–5685.
62. Viciano-Chumillas, M.; Liu, X.; Leyva-Pérez, A.; Armentano, D.; Ferrando-Soria, J.; Pardo, E. *Coord. Chem. Rev.* **2022**, *451*, 214273.
63. Bloch, W. M.; Burgun, A.; Coghlan, C. J.; Lee, R.; Coote, M. L.; Doonan, C. J.; Sumbly, C. J. *Nat. Chem.* **2014**, *6*, 906–912.
64. Bloch, W. M.; Champness, N. R.; Doonan, C. J. *Angew. Chem. Int. Ed.* **2015**, *54*, 12860–12867.
65. Burgun, A.; Coghlan, C. J.; Huang, D. M.; Chen, W.; Horike, S.; Kitagawa, S.; Alvino, J. F.; Metha, G. F.; Sumbly, C. J.; Doonan, C. J. *Angew. Chem. Int. Ed.* **2017**, *56*, 8412–8416.
66. Huang, R.-W.; Wei, Y.-S.; Dong, X.-Y.; Wu, X.-H.; Du, C.-X.; Zang, S.-Q.; Mak, T. C. W. *Nat. Chem.* **2017**, *9*, 689–697.
67. Rissanen, K. *Chem. Soc. Rev.* **2017**, *46*, 2638–2648.
68. Adam, R.; Mon, M.; Greco, R.; Kalinke, L. H. G.; Vidal-Moya, A.; Fernandez, A.; Winpenny, R. E. P.; Doménech-Carbó, A.; Leyva-Pérez, A.; Armentano, D.; Pardo, E.; Ferrando-Soria, J. *J. Am. Chem. Soc.* **2019**, *141*, 10350–10360.
69. Hanikel, N.; Pei, X.; Chheda, S.; Lyu, H.; Jeong, W.; Sauer, J.; Gagliardi, L.; Yaghi, O. M. *Science* **2021**, *374*, 454–459.
70. Tkaczyk, A.; Mitrowska, K.; Posyniak, A. *Sci. Total Environ.* **2020**, *717*, 137222.

71. Mon, M.; Bruno, R.; Ferrando-Soria, J.; Armentano, D.; Pardo, E. *J. Mater. Chem. A* **2018**, *6*, 4912–4947.
72. Ahmad, A.; Mohd-Setapar, S. H.; Chuong, C. S.; Khatoon, A.; Wani, W. A.; Kumar, R.; Rafatullah, M. *RSC Adv.* **2015**, *5*, 30801–30818.
73. Brillas, E.; Martínez-Huitle, C. A. *Appl. Catal. B Environ.* **2015**, *166–167*, 603–643.
74. He, T.; Kong, X.-J.; Li, J.-R. *Acc. Chem. Res.* **2021**, *54*, 3083–3094.
75. Kong, X.-J.; Li, J.-R. *Engineering* **2021**, *7*, 1115–1139.
76. Wang, C.-C.; Li, J.-R.; Lv, X.-L.; Zhang, Y.-Q.; Guo, G. *Energy Environ. Sci.* **2014**, *7*, 2831–2867.
77. Jiang, D.; Chen, M.; Wang, H.; Zeng, G.; Huang, D.; Cheng, M.; Liu, Y.; Xue, W.; Wang, Z. *Coord. Chem. Rev.* **2019**, *380*, 471–483.
78. Dias, E. M.; Petit, C. *J. Mater. Chem. A* **2015**, *3*, 22484–22506.
79. Wen, Y.; Zhang, P.; Sharma, V. K.; Ma, X.; Zhou, H.-C. *Cell Reports Phys. Sci.* **2021**, *2*, 100348.
80. Mon, M.; Bruno, R.; Tiburcio, E.; Casteran, P.-E.; Ferrando-Soria, J.; Armentano, D.; Pardo, E. *Chem. Eur. J.* **2018**, *24*, 17712–17718.
81. Knebel, A.; Bavykina, A.; Datta, S. J.; Sundermann, L.; Garzon-Tovar, L.; Lebedev, Y.; Durini, S.; Ahmad, R.; Kozlov, S. M.; Shterk, G.; Karunakaran, M.; Carja, I. D.; Simic, D.; Weilert, I.; Klüppel, M.; Giese, U.; Cavallo, L.; Rueping, M.; Eddaoudi, M.; Caro, J.; Gascon, J. *Nat. Mater.* **2020**, *19*, 1346–1353.
82. Smith, M. S.; Lawrence, E. E. K.; Billings, W. M.; Larsen, K. S.; Bécar, N. A.; Price, J. L. *ACS Chem. Biol.* **2017**, *12*, 2535–2537.

3.4. Highly Efficient Removal of Neonicotinoid Insecticides by Thioether-Based (Multivariate) Metal-Organic Frameworks (Publication 4)

Circumventing the impact of agrochemicals on aquatic environments has become a necessity for health and ecological reasons. Herein, we report the use of a family of five eco-friendly water-stable isoreticular MOFs, prepared from amino acids, as adsorbents for the removal of neonicotinoid insecticides (thiamethoxam, clothianidin, imidacloprid, acetamiprid and thiacloprid) from water. Among them, the three MOFs containing thioether-based residues show remarkable removal efficiency. In particular, the novel multivariate MOF $\{Sr^{II}Cu^{II}_6 [(S, S)\text{-methox}]_{1.5} [(S, S)\text{-MecysmoX}]_{1.50} (OH)_2 (H_2O)\} \cdot 36H_2O$ (**5**), featuring narrow functional channels decorated with both $-CH_2SCH_3$ and $-CH_2CH_2SCH_3$ thioalkyl chains (from *L*-methionine and *L*-methylcysteine amino acids derived ligands, respectively), stands out and exhibits the higher removal efficiency, being capable to capture 100 % of acetamiprid and thiacloprid in a single capture step under dynamic solid-phase extraction conditions -less than 30 seconds. Such unusual combination of outstanding efficiency, high stability in environmental conditions and low-cost straightforward synthesis in **5**, places this material among the most attractive adsorbents reported for the removal of this type of contaminants.

3.4.1. Introduction

Neonicotinoids¹ (NEOs) -so-called because of their chemical resemblance to nicotine alkaloid- are a widely used type of insecticides that, despite some recent restrictions,² have extensively spread throughout the world in the past decades, due to their high efficiency in controlling insect pests. However, such efficiency also lies at the origin of important environmental concerns.¹ Thus, despite low-toxicity for beneficial insects was reported initially, subsequent studies demonstrated potential toxicity to beneficial

insects,³ such as honey-bee colonies as well as an alarming impact on avian species biodiversity, especially on grassland and insectivorous bird populations.⁴ In this context, another feature of NEOs insecticides, that explain to a certain extent their popularity, is their moderate water solubility, which facilitates their application to soils and plant adsorptions.¹ This point, also constitutes a problem, from an environmental point of view, due to the concomitant contamination of aquatic environments.⁵ As a consequence, it is clear that, as long as NEOs are not definitely banned, efficient capture technologies are needed.

Different technologies have been proposed for the removal/degradation of pesticides and insecticides.^{6,7} These include precipitation, coagulation/flocculation, membrane technologies, use of biological processes, advanced oxidation processes (AOPs) or adsorption by porous sorbents.^{5,8-10} Among them, the removal of these contaminants by a porous material offers potential advantages over other technologies, such as, for example, preventing the formation of secondary contaminants and offering the possibility to implement economically-viable decontamination protocols worldwide, which is of main relevance, especially in developing countries, giving a global application character to such potent technology.¹¹

Metal-organic frameworks¹²⁻¹⁶ (MOFs) are porous crystalline materials, that, among many other properties, have already demonstrated highly performant in the removal of both, organic and inorganic contaminants.^{6,11,17-25} Main reasons for such efficiency are high water and structural stability,^{26,27} microporosity that can be functionalized pre- or post-synthetically,²⁸ to increase affinity for contaminants, and a certain degree of flexibility and/or adaptability that may play a key role capturing and accommodating the guest target contaminant.^{29,30} Moreover, unlike other porous materials, such thrilling host-guest chemistry can be visualized with the precious help of SCXRD^{31,32}, given the high crystallinity of these porous materials.^{33,34}

This last point has demonstrated extremely useful to unveil host-guest interaction governing the mechanism of the capture processes. More recently, a particular type of MOFs, the so called multivariate MOFs³⁵⁻³⁷ (MTV-MOFs), which combine organic linkers with different functional groups decorating their channels, have emerged strongly in different fields, that include water remediation.¹¹ However, despite all these remarkable features, the use of MOFs for the sensing³⁸⁻⁴¹ and/or removal of pesticides/insecticides has been only barely explored.⁴²⁻⁴⁸

In this work, we explore the performance of a family of five water-stable highly crystalline 3D isorecticular MOFs (one of them MTV-MOFs) in the removal of different neonicotinoids of environmental concern from water. In particular, we have focused on the use of four previously reported MOFs, with formulas $\{\text{Ca}^{\text{II}}\text{Cu}^{\text{II}}_6 [(\text{S}, \text{S})\text{-serimox}]_3 (\text{OH})_2 (\text{H}_2\text{O})\} \cdot 39\text{H}_2\text{O}$ ⁴⁹ (**1**), $\{\text{Sr}^{\text{II}}\text{Cu}^{\text{II}}_6 [(\text{S}, \text{S})\text{-threomox}]_3 (\text{OH})_2 (\text{H}_2\text{O})\} \cdot 36\text{H}_2\text{O}$ ⁵⁰ (**2**), $\{\text{Ca}^{\text{II}}\text{Cu}^{\text{II}}_6 [(\text{S}, \text{S})\text{-methox}]_3 (\text{OH})_2 (\text{H}_2\text{O})\} \cdot 16\text{H}_2\text{O}$ ^{29,30} (**3**) and $\{\text{Ca}^{\text{II}}\text{Cu}^{\text{II}}_6 [(\text{S}, \text{S})\text{-Mecysmox}]_3 (\text{OH})_2 (\text{H}_2\text{O})\} \cdot 16\text{H}_2\text{O}$ ^{51,52} (**4**) (where serimox = bis [(*S*)-serine] oxalyl diamide; threomox = bis [(*S*)-threonine] oxalyl diamide; methox = bis [(*S*)-methionine] oxalyl diamide and Mecysmox = bis [(*S*)-methylcysteine] oxalyl diamide) and a novel MTV-MOF of formula $\{\text{Sr}^{\text{II}}\text{Cu}^{\text{II}}_6 [(\text{S}, \text{S})\text{-methox}]_{1.5} [(\text{S}, \text{S})\text{-Mecysmox}]_{1.50} (\text{OH})_2 (\text{H}_2\text{O})\} \cdot 36\text{H}_2\text{O}$ (**5**) (Scheme S1 and Figure 1). The election of this family of MOFs is not accidental. This is based on their good mechanical properties, which have already permitted their processability as pellets²⁹ or mixed matrix membranes⁵¹ (MMM-MOFs), their proven air and water stability⁵³ (neutral and basic media), and their excellent performances in the removal of both inorganic^{29,51} (Hg^{2+}) and organic contaminants (dyes⁵⁴ or vitamins^{49,55}), recently reported for **1-4**, in the presence of other metal cations and inorganic anions usually present in potable drinking water.^{29,30,35,54} The main reasons that lie at the origin of such remarkable capture properties are two-fold: (i) These MOFs feature channels decorated with different functional groups, which can be tuned depending on the nature of the chosen amino acid residue ($-\text{CH}_2\text{OH}$, $-\text{CH}(\text{CH}_3)\text{OH}$, $-\text{CH}_2\text{SCH}_3$ and/or $-\text{CH}_2\text{CH}_2\text{SCH}_3$), and (ii) these

amino acid residues exhibit a high degree of adaptability,⁵⁶ being capable to accommodate and adjust to guest molecules by maximizing host-guest interactions with the contaminant.

3.4.2. Results and Discussion

We report here the efficiency of the whole family of MOFs, as SPE sorbents, towards five well-known NEOs like thiamethoxam, clothianidin, imidacloprid, acetamiprid and thiacloprid (Scheme S2 and Table S1).¹ Overall, the three thioether-derived isorecticular MOFs (**3-5**) are capable to capture, very efficiently, NEOs in a single loading step –within 30 seconds. In particular, the novel MTV-MOF **5**, featuring functional pores tailored with, approximately, a 50 % of $-\text{CH}_2\text{CH}_2\text{SCH}_3$ groups and another 50 % of the $-\text{CH}_2\text{SCH}_3$ residues from the amino acids *L*-methionine and *S*-Methyl-*L*-cysteine (Figure 1f), respectively, shows the best performance for all the NEOs, being capable to capture 99-100 % of acetamiprid and thiacloprid in a single capture process. In addition, it has been possible to solve the crystal structures of the resulting host-guest adsorbates with acetamiprid and thiacloprid that help to unveil the mechanism of the capture process of MTV-MOF **5**.

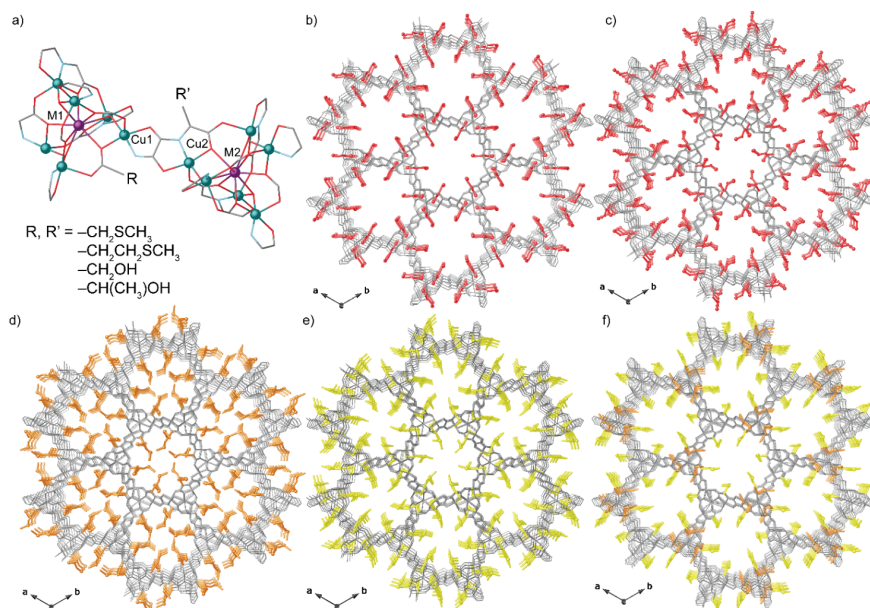


Figure 1. Fragment of the structure of MOFs **1-5** emphasizing the common dicopper(II) building block (a). Copper and calcium/strontium (M) atoms from the network are represented by cyan and purple spheres, respectively, whereas organic ligands are depicted as gray (C), blue (N) and red (O) sticks. Perspective views of MOFs **1** (b), **2** (c), **3** (d), **4** (e) and **5** (f) along the *c* axes. Metals and organic ligands are depicted as gray sticks, whereas the amino acid residues are represented with the following color code: -CH₂OH (1)/-CH(CH₃)OH (2) (red), -CH₂CH₂SCH₃ (3 and 5) (orange) and -CH₂SCH₃ (4 and 5) (yellow).

Figure 1 shows the crystal structures of **1-5**. They all are isomorphous, crystallizing in the chiral $P6_3$ space group of the hexagonal system, and exhibit chiral 3D calcium(II)/strontium(II)-copper(II) networks featuring hexagonal channels where the different adaptable amino acid residues are depicted in different colors (see color code in Figure 1). The crystal structure of the novel material reported here $\{\text{Sr}^{\text{II}}\text{Cu}^{\text{II}}_6 [(\text{S}, \text{S})\text{-methox}]_{1.5} [(\text{S}, \text{S})\text{-Mecysmox}]_{1.50} (\text{OH})_2 (\text{H}_2\text{O})\} \cdot 36\text{H}_2\text{O}$ (**5**) has been determined by SCXRD measurements using synchrotron radiation at the I19 beamline of the Diamond Light Source (Table S2). Well-shaped crystals of **5** were grown with a slow diffusion technique (see Supporting Information details).

5 presents an uni-nodal **acs** six-connected 3D strontium(II)-copper(II) network with functional hexagonal channels (virtual diameters of *ca.* 1 nm) decorated by the two types of flexible amino acid residues (the ethylene (-CH₂CH₂SCH₃) and the methylene-thiomethyl (-CH₂SCH₃), belonging to methionine and methyl cysteine amino acids, respectively (Figures 1 and S1).

Similarly to single-ligand parent compounds **3** and **4**, MTV-MOF **5** shows also a highly stable 3D porous network, with flexibility confined only in pores, where highly bendable arms are prone to adopt different conformations of the thioether chains depending on the different chemical environments determined by guest' s nature (Figure S1c-s1d). In particular, the crystal structure of **5** shows methionine arms more bent than methyl-cysteine ones (Figures 1 and S1a-S1b), featuring available sulfur groups for interaction (mainly based on σ -hole-with electron donors including oxygen and nitrogen atoms⁵⁷⁻⁶¹ and π -systems (*vide infra*)).⁶² Thus, they encapsulate the targeted guest molecules assuming the favorite conformation, in each case, to maximize the host-guest interactions. The channels size in **5** (Figure S1b) is similar to that of **3** and **4**, with the added value of chemical diversity confined in the same pores, guaranteed by diverse length and electron density for -CH₂CH₂SCH₃ and -CH₂SCH₃ groups. The crystal structure of the chiral network **5** unveils statistically disordered *trans* oxamidato-bridged dicopper(II) units of {Cu^{II}₂[(*S*, *S*)-mecysmox]} and {Cu^{II}₂[(*S*, *S*)-methox]} (Figure S1 inset, and Figure S1c), which build the 3D motif. As stated above, SCXRD measurements on **5** have been performed using synchrotron radiation. This was done with the aim to safeguard the desirable high quality of data set in case of such statistical disordered. At this respect, the best final model found for the crystal structure is based on the most realistic assumption that there is a random distribution of methyl-cysteine and methionine moieties (with 1:1 ratio) within the net (see crystallographic details in Supporting Information), as previously reported by us for an analogue MTV-MOF.³⁵ In so doing, the spatial average, of all fragments and all their possible orientations averaged in the crystal *via* only one unit-cell (see

3. MOFs AND MTV-MOFs FOR WATER REMEDIATION

crystallographic details in the Supporting Information), discloses basically the crystal structure of **5**, which results assembled by copper(II) dimers acting as linkers between the Sr^{II} ions by means of the carboxylate groups (Figure S1). Aqua/hydroxo groups (in a 1:2 statistical distribution) contribute to further connect neighboring Cu²⁺ and Cu²⁺/Sr²⁺ ions finally linked in a μ_3 fashion (Figures S1c and S1d). Indeed, it must be the comparable percentage of mecysmox and methox that gives back to superimposed snapshot of mixed {Cu^{II}₂ [(*S,S*)-methox/Mecysmox]} dimers, which is also supported by the experimental results of composition analysis (*vide infra* C, H, S, N and Supporting Information).

Table 1. Removal values (%) for NEOs from different aqueous samples (at three levels of concentration) using MOFs 3-5 (n=3).

NEOs	Conc. (mg L ⁻¹)	MOF		
		3	4	5
Thiamethoxam	0.1	66	45	71
	10	30	28	33
	100	33	25	30
Clothianidin	0.1	60	48	86
	10	64	48	74
	100	47	43	61
Imidacloprid	0.1	65	50	86
	10	50	42	57
	100	38	41	60
Acetamiprid	0.1	95	91	99
	10	96	91	99
	100	86	94	100
Thiacloprid	0.1	93	96	100
	10	91	96	100
	100	87	98	100

Besides the structural characterization and elemental analysis, the chemical identity of **5** was further established by PXRD, electronic microscopy and TGA (see Supporting Information).

Figure S2 shows the experimental PXRD pattern of **5**. It is identical to the theoretical one, which confirms that the bulk sample is pure and homogeneous. Moreover, the structural stability of **5** was tested after being soaked, for 48 h, in neutral (Figure S3b) basic (Figure S3c, pH = 12) and acid (Figure S3d, pH = 5 and Figure S3e, pH = 2) aqueous media (Figure S3). This test confirmed that **5** is stable in basic and moderately acid media. The permanent porosity of **5** was verified by measuring their N₂ adsorption isotherm at 77 K, which is also compared to those adsorption isotherms of related MOFs **3** and **4** (Figure S4). Overall, they confirm permanent porosity for **3-5**, with larger N₂ adsorbed amounts for **4** and **5**, which is consistent with higher accessible void spaces, as suggested by the crystal structures (Figure 1). The solvent content of **5** was, on the other hand, definitively established by TGA (see Figure S5, Supporting Information), which also confirms that **5** is stable up to 250 °C, when decomposition starts. The reported analyses performed both on the bulk and crystal sample of MTV-MOF **5** unveils similar composition to that used in the reaction mixture, validating the hypothesis that there were no significant ligand preferences giving nature and stability of both **3** and **4** parent MOFs. These results, together with previously reported ones,³⁵ confirm a successful protocol, which proposes that the composition can be controlled through the relative reactant concentrations in this family of materials.

For the evaluation of the NEO capture properties, SPE devices were prepared by packing 25 mg of the corresponding MOF (**1-5**) between two frits into 1 mL empty propylene cartridges. First of all, activation and equilibration of the sorbent was done with 1 mL of MeOH and 1 mL of H₂O, consecutively. Then, 1 mL of aqueous mixtures of thiamethoxam, clothianidin, imidacloprid, acetamiprid and thiacloprid at four levels of concentrations (0.1, 1, 10 and 100 mg L⁻¹) were percolated through the SPE cartridges. Then, a washing step

was carried out with 1 mL of H₂O. After that, elution of the retained analytes was accomplished with MeOH (5 mL). All SPE fractions were collected and filtered (membrane with pore size 0.22 μm) prior to their injection in HPLC system and the NEO content was established (see also Experimental Section).

Following this procedure, the efficiency of the NEO capture was, initially, evaluated for **1-5** using a mixture of the five NEOs (at 1 mg L⁻¹ each), and the results are collected in Table S3. Overall, the five MOFs showed distinct behaviors, and they can be classified in two clearly distinct groups. The serine- (**1**) and threonine-derived (**2**) MOFs -for which a high capture efficiency of organic dyes was reported previously- exhibit, by far, much worse capture properties than the thio-alkyl MOFs (**3-5**) (Table S3). **1** and **2** do not surpass 20 % of removal efficiency for any of the NEOs. In turn, **3**, **4** and, especially, the MTV-MOF **5**, show much higher efficiencies. On this basis, MOFs **3-5** were subjected to further capture experiments using different contents of the five NEOs (0.1, 10 and 100 mg L⁻¹). In so doing, it was observed that, overall, the three MOFs capture, very efficiently, thiacloprid and acetamiprid and, moderately well, clothianidin, imidacloprid and thiamethoxam (Table 1). In particular, MTV-MOF **5** exhibits outstanding capture properties, especially at very diluted conditions. Thus, **5** captures, in a single step, 100 % of thiacloprid and acetamiprid in any condition and 71-86 %, at the most diluted conditions, of clothianidin, imidacloprid and thiamethoxam.

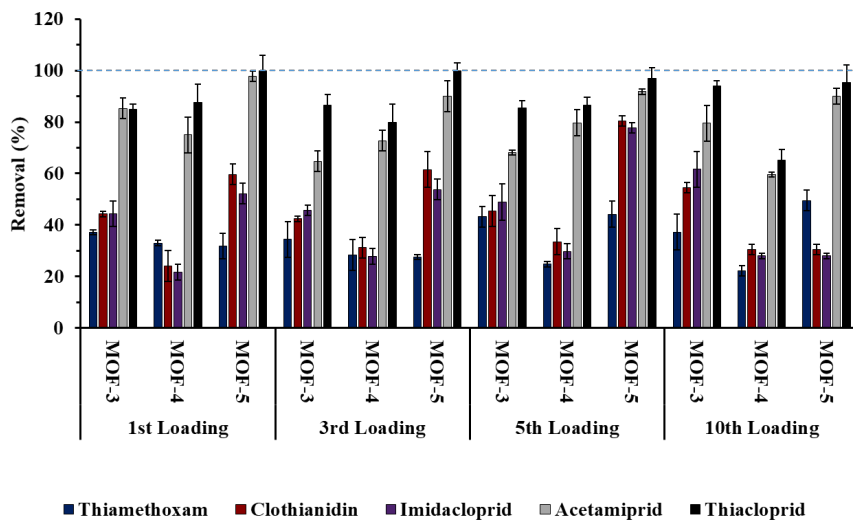


Figure 2. Reuses of 3-5 for the removal (%) of thiamethoxam, clothianidin, imidacloprid, acetamiprid and thiacloprid using a 1 mg L^{-1} mixture of NEOs.

To further confirm the applicability of the developed method removing NEOs from environmental matrices with possible competing species, a real water samples from river (Turia river; 39.504095, -0.473712; Valencia) were analyzed. For real sample analysis (river water), the same SPE protocol described above was used. None of the target pollutants were found in the samples using the optimized protocol (see Experimental section). Therefore, the river water was spiked at 5 mg L^{-1} with each of the five NEOs. As it can be seen in Figure S6, a significant decrease of the signal was observed after SPE treatment with MOFs 3-5 as sorbents, indicating the suitable removal efficiency of these MOFs for organic pollutants in environmental waters (Table S4). Furthermore, the reproducibility of these sorbents was evaluated, as relative standard deviation (RSD), showing values lower than 9 % for all the analytes (Table S5).

In order to evaluate the reusability of the MOFs, up to 10 capture cycles -using a mixture of the five NEOs (at 1 mg L⁻¹ level)- were performed for **3-5** (Figure 2). For this purpose, the same SPE optimized protocol, used before (see Experimental section) was followed using an aqueous standard mixture of the five NEOs, at 1 µg mL⁻¹. It can be observed that, at least for 10 cycles, the three MOFs maintain the efficiency for the removal of the five NEOs, showing a similar capture performance. Figure S7 shows the PXRD patterns, after 10 consecutive NEOs sorption/desorption cycles, which confirm that **3-5** maintain the structural integrity. Moreover, no metal leaching could be observed in any of the sorption/desorption cycles.

Finally, we evaluated the maximum loading capacity of the best performing materials (**3-5**) towards each of the selected NEOs. Thus, polycrystalline samples of **3-5** were soaked in saturated water:acetonitrile (1:1) solutions of thiamethoxam, clothianidin, imidacloprid, acetamiprid and thiacloprid for one week, replacing each saturated solution every 24 h (see Experimental section). In so doing, maximum uptakes of 275, 312, 356, 426 and 411 (**3**), 402, 321, 399, 423 and 415 (**4**) and 447, 379, 402, 445 and 499 (**5**) mg g⁻¹ were determined for thiamethoxan, clothianidin, imidacloprid, acetamiprid and thiacloprid, respectively. Maximum loadings observed for **5** closely corresponds to up to 3 guest molecules per SrCu₆ formula unit.

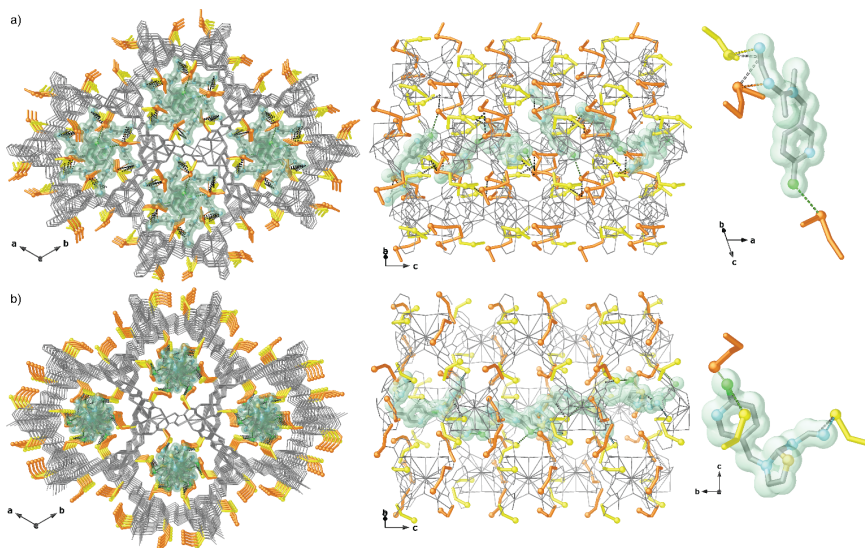


Figure 3. Perspective views in the *ab* (left) and *bc* (middle) planes of the porous structures of **acetamidrid@5** (a) and **thiacloprid@5** (b). Metals and organic ligands from the network are represented as in Figure 1, whereas the guest NEOs molecules are represented as light blue (nitrogen), green (chloride), pale yellow (sulfur) ball-and-stick and gray (carbon) sticks. Guest molecules are also represented as green solid surfaces with the same color code for atoms. The guest molecule structures are shown in detail in the right side of the porous structures.

On the basis of these results and aiming at elucidating the mechanisms involved in the capture processes of the best performing material, insertion experiments were also carried out on single crystals of MTV-MOF **5** (see Supporting Information, experimental section). Remarkably, suitable samples of host-guest aggregates of **5** with acetamidrid and thiacloprid for SCXRD were obtained, and the crystal structure of **acetamidrid@5** and **thiacloprid@5** could be determined (Table S2), which allowed the atomically-precise visualization on the interaction of the two most efficiently captured NEOs pollutants with the thio-alkyl residues decorating the framework.

The chemical formulas were finally established with the help of CHNS and SEM/EDX analyses (see Experimental Section and Supporting Information) and the solvent contents were estimated by TGA (Figure 3 and S5):

Acetamidrid@ {Sr^{II}Cu^{II}}_6 [(*S,S*)-methox]_{1.5} [(*S,S*)-Mecysmox]_{1.50} (OH)₂ (H₂O)} · 9H₂O (**acetamidrid@5**)

Thiacloprid@ {Sr^{II}Cu^{II}}_6 [(*S,S*)-methox]_{1.5} [(*S,S*)-Mecysmox]_{1.50} (OH)₂ (H₂O)} · 18H₂O (**thiacloprid@5**)

Compounds **acetamidrid@5** and **thiacloprid@5** are isomorphous to **5** and crystallize in the *P*6₃ chiral space group of the hexagonal system, confirming the preservation of the 3D network of the hosting matrix **5** even after guests' capture. The crystal structures clearly evidence that acetamidrid and thiacloprid guest molecules are encapsulated in the nanopores of **5**, where they are simultaneously recognized by the thioether arms of the methyl-cysteine and methionine residues. The most stabilizing forces are assured by sulfur atoms interacting either with nitrile groups or with Cl atoms as electron donors. Despite the different chemical nature of acetamidrid and thiacloprid -featuring nitrile groups-, among the whole family of tested NEOs, seems *a priori* to be discriminant, it is not supported by host-guest interactions visualized by SCXRD. Indeed, it is pretty interesting to observe that in **acetamidrid@5** both methyl-cysteine and methionine arms distend their conformation within pores pointing towards nitrile groups, while in **thiacloprid@5** it is observed the S...Cl interaction as prominent, with molecules orienting in such a way to confine the -CN moieties towards the hidden center of the pores (Figures 2 and S8-S11). Although both acetamidrid and thiacloprid molecules were disordered in the pores, we succeeded to get their possible configurations and locations (see SI for structural details), as well as details on their interaction sites with the hosting matrix MTV-MOF **5** (Figure S8-S13).

Details of **acetamiprid@5** crystal structure show molecules statistically disordered on three configuration sets, (see Figures S8 and S12) residing in the pores, packed *via* straight S...N-CN (involving only methionine residues) [S...N distances of 3.18(1) Å] and S...nitrile interactions (involving both kind of arms), which block acetamiprid terminal moieties at almost identical distance [S...CN_{Centroid} distances of 3.67(1) and 3.82(1) Å, for methyl-cysteine and methionine residues, respectively] (Figure S9). On the contrary, in **thiacloprid@5** crystal structure (Figure S10) the two kind of amino acid residues are involved in different contacts. Thiacloprid molecules, statistically disordered as well on three configuration sets (Figure S13), are captured either *via* methionine residues, which involve sulfur atoms to interact with Cl [S...Cl distance of 3.10 (1) Å], or *via* methyl-cysteine residues, which contribute with interactions of the type S...S held with thiazolidine ring of pollutants molecules [S...S distance of 2.76(1) Å] (Figure S11). Both contact distances fall in the range of those found in the literature for similar S interactions,⁶¹ although the last distance, exhibiting a value lower than the sum of van der Waals radii, has been rarely observed.⁶³ The arrangement of the two NEOs molecules is also governed by pore's size, which impose preferential configurations (despite the structural similarity, is surprisingly different the molecular orientation found in the nanoconfined space for acetamiprid and thiacloprid), and the high degree of loading for guests, which displace almost all water molecules from pores and it is at the origin of the close-packing observed. In fact, **acetamiprid@5** and **thiacloprid@5** almost totally fill channels (Figure S8 and S10) making extremely robust the adsorbates being stable at air and room temperature for four weeks. This, indeed, represents an added value for a more safely storage and handling of a *scavenger* material like that, for which only the regeneration process, based on the use of appropriate solvent, will cause the release of captured pollutants.

The high performance of **5** for some NEOs capture could be understood with the help of X-ray crystallography. Interactions found in **acetamiprid@5** and **thiacloprid@5**, discussed in the

context of both sulfur-containing ligands, have a prominent role due to their extensive propagation in the nanoconfined space ensured by **5**, exactly as observed for peptide-based methionine, cysteine, and cystine moieties –where associations extend beyond that of simple hydrophobic interactions. Both, intra- and intermolecular interactions (involving low-lying sulfur σ^* orbitals), are known to be implicated in chemical reactivity, with electronic characteristics of chemical systems responsible, in part, for specific kinetic, regiochemical, or even stereochemical outcomes. Indeed, it is also known that electron deficient bivalent sulfur atoms have two areas of positive electrostatic potential, as consequence of the low-lying σ^* orbitals of the C–S bond (the so called σ -hole),^{62,64} which are available for interaction with electron donors such as nitrogen atoms or, as in the present case, nitrile groups and, even, π -systems. The present results, together with the previously reported by us,^{20,25-27} represent the first examples of a judicious exploitation of these sulfur-based interactions. Intramolecular interactions are by far the most common manifestation of this effect, which offers a means of modulating the conformational preferences of a molecule. Although it is a well-documented phenomenon, *a priori* applications in rational capture are relatively sparse, and this interaction, which is often isosteric with an intramolecular hydrogen-bonding interaction, appears to be underappreciated by the applied chemistry community. The majority of the examples of this kind of sulfur interaction have been noted in *post facto* analyses of crystallographic or other structural information, and there are relatively few examples reported in the literature where this interaction has been exploited in a prospective fashion.⁶⁵

3.4.3. Conclusions

In summary, we report the one-step efficient capture of neonicotinoid insecticides by a family of isoreticular thioether-based MOFs derived from amino acids *L*-methionine and *S*-Methyl-*L*-cysteine. In particular, the novel MTV-MOF **5**, combining both amino acids in equal proportions, exhibits outstanding capture properties,

being capable to remove, in a single step, 100 % of acetamiprid and thiacloprid at different conditions and 71-86 %, at the most diluted conditions, of clothianidin, imidacloprid and thiamethoxam.

In addition, the capture properties are maintained during, at least 10 cycles. Remarkably, the crystal structures of the two host-guest aggregates of **5** with acetamiprid and thiacloprid could be resolved, which allowed to visualize how both NEOs are encapsulated and immobilized. Also, it enables to unveil the synergistic interactions of both types of thioether groups with the guest molecules, which are the ultimate responsible for such capture efficiency. This family of thioether-containing MOFs arise as alternative of more traditional materials, such as activated carbons,⁶⁶⁻⁶⁸ for the capture of this type of emerging contaminants.

3.4.4. References

1. Goulson, D. *J. Appl. Ecol.* **2013**, 50, 977–987.
2. European Food Safety Authority Journal. Conclusion on the Peer Review of the Pesticide Risk Assessment for Bees for the Active Substance Clothianidin. *EFSA J.* **2013**, 11, 3066.
3. Schmuck, R.; Lewis, G. *Ecotoxicology* **2016**, 25, 1617–1629.
4. Li, Y.; Miao, R.; Khanna, M. *Nat. Sustain.* **2020**, 3, 1027–1035.
5. Castillo, M. D. P.; Torstensson, L.; Stenström, J. *J. Agric. Food Chem.* **2008**, 56, 6206–6219.
6. Bolisetty, S.; Peydayesh, M.; Mezzenga, R. *Sustainable Chem. Soc. Rev.* **2019**, 48, 463–487.
7. Patel, M.; Kumar, R.; Kishor, K.; Mlsna, T.; Pittman, C. U.; Mohan, D. *Chem. Rev.* **2019**, 119, 3510–3673.
8. Vagi, M. C.; Petsas, A. S.; Kostopoulou, M. N.; Lekkas, T. D. *Int. J. Environ. Anal. Chem.* **2010**, 90, 369–389.
9. Rodríguez-Castillo, G.; Molina-Rodríguez, M.; Cambronero-Heinrichs, J. C.; Quirós-Fournier, J. P.; Lizano-Fallas, V.; Jiménez-

- Rojas, C.; Masís-Mora, M.; Castro-Gutiérrez, V.; Mata-Araya, I.; Rodríguez-Rodríguez, C. E. *Chemosphere* **2019**, 235, 1097–1106.
10. González, T.; Dominguez, J. R.; Correia, S. J. *Environ. Manage.* **2020**, 261, 110156.
 11. Mon, M.; Bruno, R.; Ferrando-Soria, J.; Armentano, D.; Pardo, E. J. *Mater. Chem. A* **2018**, 6, 4912–4947.
 12. Kitagawa, S.; Matsuda, R. *Coord. Chem. Rev.* **2007**, 251, 2490–2509.
 13. Férey, G. *Chem. Soc. Rev.* **2008**, 37, 191–214.
 14. Long, J. R.; Yaghi, O. M. *Chem. Soc. Rev.* **2009**, 38, 1213–1214.
 15. Farha, O. K.; Hupp, J. T. *Acc. Chem. Res.* **2010**, 43, 1166–1175.
 16. Furukawa, H.; Cordova, K. E.; O’Keeffe, M.; Yaghi, O. M. *Science* **2013**, 341, 1230444.
 17. Li, J.; Wang, X.; Zhao, G.; Chen, C.; Chai, Z.; Alsaedi, A.; Hayat, T.; Wang, X. *Chem. Soc. Rev.* **2018**, 47, 2322–2356.
 18. Feng, M.; Zhang, P.; Zhou, H.-C.; Sharma, V. K. *Chemosphere* **2018**, 209, 783–800.
 19. Kobielska, P. A.; Howarth, A. J.; Farha, O. K.; Nayak, S. *Coord. Chem. Rev.* **2018**, 358, 92–107.
 20. Rojas, S.; Horcajada, P. *Chem. Rev.* **2020**, 120, 8378–8415.
 21. Dias, E. M.; Petit, C. *J. Mater. Chem. A* **2015**, 3, 22484–22506.
 22. Martínez-Pérez-Cejuela, H.; Mompó-Roselló, Ó.; Crespí-Sánchez, N.; Palomino Cabello, C.; Catalá-Icardo, M.; Simó-Alfonso, E. F.; Herrero-Martínez, J. M. *J. Chromatogr. A* **2020**, 1631, 461580.
 23. Martínez-Pérez-Cejuela, H.; Guíñez, M.; Simó-Alfonso, E. F.; Amorós, P.; El Haskouri, J.; Herrero-Martínez, J. M. *Microchim. Acta* **2020**, 187, 301.
 24. Ghosh, S. K. *Metal-Organic Frameworks (MOFs) for Environmental Applications*; Elsevier: Amsterdam, **2019**.
 25. Yoo, D. K.; Bhadra, B. N.; Jhung, S. H. *J. Hazard. Mater.* **2021**, 403, 123655.
 26. Ding, M.; Cai, X.; Jiang, H.-L. *Chem. Sci.* **2019**, 10, 10209–10230.

27. Burtch, N. C.; Jasuja, H.; Walton, K. S. *Chem. Rev.* **2014**, 114, 10575–10612.
28. Cohen, S. M. *J. Am. Chem. Soc.* **2017**, 139, 2855–2863.
29. Mon, M.; Lloret, F.; Ferrando-Soria, J.; Martí-Gastaldo, C.; Armentano, D.; Pardo, E. *Angew. Chem. Int. Ed.* **2016**, 55, 11167–11172.
30. Mon, M.; Ferrando-Soria, J.; Grancha, T.; Fortea-Pérez, F. R.; Gascon, J.; Leyva-Pérez, A.; Armentano, D.; Pardo, E. *J. Am. Chem. Soc.* **2016**, 138, 7864–7867.
31. Inokuma, Y.; Kawano, M.; Fujita, M. *Nat. Chem.* **2011**, 3, 349–358.
32. Bloch, W. M.; Champness, N. R.; Doonan, C. J. *Angew. Chem. Int. Ed.* **2015**, 54, 12860–12867.
33. Young, R. J.; Huxley, M. T.; Pardo, E.; Champness, N. R.; Sumbly, C. J.; Doonan, C. J. *Chem. Sci.* **2020**, 11, 4031–4050.
34. Viciano-Chumillas, M.; Mon, M.; Ferrando-Soria, J.; Corma, A.; Leyva-Pérez, A.; Armentano, D.; Pardo, E. *Acc. Chem. Res.* **2020**, 53, 520–531.
35. Mon, M.; Bruno, R.; Tiburcio, E.; Viciano-Chumillas, M.; Kalinke, L. H. G.; Ferrando-Soria, J.; Armentano, D.; Pardo, E. *J. Am. Chem. Soc.* **2019**, 141, 13601–13609.
36. Kong, X.; Deng, H.; Yan, F.; Kim, J.; Swisher, J. A.; Smit, B.; Yaghi, O. M.; Reimer, J. A. *Science* **2013**, 341, 882–885.
37. Deng, H.; Doonan, C. J.; Furukawa, H.; Ferreira, R. B.; Towne, J.; Knobler, C. B.; Wang, B.; Yaghi, O. M. *Science* **2010**, 327, 846–850.
38. Yang, Q.; Wang, J.; Chen, X.; Yang, W.; Pei, H.; Hu, N.; Li, Z.; Suo, Y.; Li, T.; Wang, J. *J. Mater. Chem. A* **2018**, 6, 2184–2192.
39. Kumar, P.; Paul, A. K.; Deep, A. *Microporous Mesoporous Mater.* **2014**, 195, 60–66.
40. Wang, G.-D.; Li, Y.-Z.; Shi, W.-J.; Zhang, B.; Hou, L.; Wang, Y.-Y. *Sensors Actuators B Chem.* **2021**, 331, 129377.
41. Liu, G.; Li, L.; Huang, X.; Zheng, S.; Xu, D.; Xu, X.; Zhang, Y.; Lin, H. *Microporous Mesoporous Mater.* **2018**, 270, 258–264.
42. Jung, B. K.; Hasan, Z.; Jhung, S. H. *Chem. Eng. J.* **2013**, 234, 99–105.

43. Cao, X.; Liu, G.; She, Y.; Jiang, Z.; Jin, F.; Jin, M.; Du, P.; Zhao, F.; Zhang, Y.; Wang, J. *RSC Adv.* **2016**, 6, 113144–113151.
44. Liu, G.; Li, L.; Xu, D.; Huang, X.; Xu, X.; Zheng, S.; Zhang, Y.; Lin, H. *Carbohydr. Polym.* **2017**, 175, 584–591.
45. Zhu, X.; Li, B.; Yang, J.; Li, Y.; Zhao, W.; Shi, J.; Gu, J. *ACS Appl. Mater. Interfaces* **2015**, 7, 223–231.
46. Seo, Y. S.; Khan, N. A.; Jhung, S. H. *Chem. Eng. J.* **2015**, 270, 22–27.
47. Fu, Q.; Wen, L.; Zhang, L.; Chen, X.; Pun, D.; Ahmed, A.; Yang, Y.; Zhang, H. *ACS Appl. Mater. Interfaces* **2017**, 9, 33979–33988.
48. Yang, J.; Trickett, C. A.; Alahmadi, S. B.; Alshammari, A. S.; Yaghi, O. M. J. *Am. Chem. Soc.* **2017**, 139, 8118–8121.
49. Mon, M.; Bruno, R.; Ferrando-Soria, J.; Bartella, L.; Di Donna, L.; Talia, M.; Lappano, R.; Maggiolini, M.; Armentano, D.; Pardo, E. *Mater. Horizons* **2018**, 5, 683–690.
50. Mon, M.; Bruno, R.; Elliani, R.; Tagarelli, A.; Qu, X.; Chen, S.; Ferrando-Soria, J.; Armentano, D.; Pardo, E. *Inorg. Chem.* **2018**, 57, 13895–13900.
51. Bruno, R.; Mon, M.; Escamilla, P.; Ferrando-Soria, J.; Esposito, E.; Fuoco, A.; Monteleone, M.; Jansen, J. C.; Elliani, R.; Tagarelli, A.; Armentano, D.; Pardo, E. *Adv. Funct. Mater.* **2021**, 31, 2008499.
52. Tiburcio, E.; Greco, R.; Mon, M.; Ballesteros-Soberanas, J.; Ferrando-Soria, J.; López-Haro, M.; Hernández-Garrido, J. C.; Oliver-Meseguer, J.; Marini, C.; Boronat, M.; Armentano, D.; Leyva-Pérez, A.; Pardo, E. *J. Am. Chem. Soc.* **2021**, 143, 2581–2592.
53. Grancha, T.; Ferrando-Soria, J.; Cano, J.; Amorós, P.; Seoane, B.; Gascon, J.; Bazaga-García, M.; Losilla, E. R.; Cabeza, A.; Armentano, D.; Pardo, E. *Chem. Mater.* **2016**, 28, 4608–4615.
54. Mon, M.; Bruno, R.; Tiburcio, E.; Casteran, P.-E.; Ferrando-Soria, J.; Armentano, D.; Pardo, E. *Chem. Eur. J.* **2018**, 24, 17712–17718.
55. Pérez-Cejuela, H. M.; Mon, M.; Ferrando-Soria, J.; Pardo, E.; Armentano, D.; Simó-Alfonso, E. F.; Herrero-Martínez, J. M. *Microchim. Acta* **2020**, 187, 201.

56. Yan, Y.; Carrington, E. J.; Pétuya, R.; Whitehead, G. F. S.; Verma, A.; Hylton, R. K.; Tang, C. C.; Berry, N. G.; Darling, G. R.; Dyer, Antypov, D.; Katsoulidis, A. P.; Rosseinsky, M. J. *J. Am. Chem. Soc.* **2020**, *142*, 14903–14913.
57. Nagao, Y.; Hirata, T.; Goto, S.; Sano, S.; Kakehi, A.; Iizuka, K.; Shiro, M. *J. Am. Chem. Soc.* **1998**, *120*, 3104–3110.
58. Iwaoka, M.; Takemoto, S.; Tomoda, S. *J. Am. Chem. Soc.* **2002**, *124*, 10613–10620.
59. Adhikari, U.; Scheiner, S. *J. Phys. Chem. A* **2012**, *116*, 3487–3497.
60. Thomas, S. P.; Jayatilaka, D.; Guru Row, T. N. *Phys. Chem. Chem. Phys.* **2015**, *17*, 25411–25420.
61. Hudson, B. M.; Nguyen, E.; Tantillo, D. *J. Org. Biomol. Chem.* **2016**, *14*, 3975–3980.
62. Politzer, P.; Murray, J. S.; Clark, T. *Phys. Chem. Chem. Phys.* **2013**, *15*, 11178.
63. Obata, A.; Kawazura, H.; Miyamae, H. *Acta Crystallogr. Sect. C Cryst. Struct. Commun.* **1984**, *40*, 45–48.
64. Murray, J. S.; Lane, P.; Politzer, P. *Int. J. Quantum Chem.* **2008**, *108*, 2770–2781.
65. Lin, S.; Wroblewski, S. T.; Hynes, J.; Pitt, S.; Zhang, R.; Fan, Y.; Doweyko, A. M.; Kish, K. F.; Sack, J. S.; Malley, M. F.; Kiefer, S. E.; Newitt, J. A.; McKinnon, M.; Trzaskos, J.; Barrish, J. C.; Dodd, J. H.; Schieven, G. L.; Leftheris, K. *Bioorg. Med. Chem. Lett.* **2010**, *20*, 5864–5868.
66. Nawaz, A.; Niaz, A.; Ilyas, M.; Shah, S. S. H.; Asi, M. R.; Ahmad, Z. A. *Int. J. Food Allied Sci.* **2015**, *1*, 63–66.
67. Webb, D. T.; Nagorzanski, M. R.; Powers, M. M.; Cwiertny, D. M.; Hladik, M. L.; LeFevre, G. H. *Environ. Sci. Technol.* **2020**, *54*, 14694–14705.
68. Mohammad, S. G.; Ahmed, S. M.; Amr, A. E.-G. E.; Kamel, A. H. *Molecules* **2020**, *25*, 2339.



**4. CONCLUDING REMARKS
AND PERSPECTIVES**

In this thesis, we successfully applied the metalloligand approach to design and develop novel water-stable metal-organic frameworks (MOFs) and multivariate metal-organic frameworks (MTV-MOFs) for catalysis and water remediation. We used oxamidato-based proligands derived from enantiopure natural amino acids to construct dinuclear Cu(II) SBUs, leading to the development of oxamidato-based MOFs with functional pores decorated with amino acid residues. The amino acid chains provided significant framework flexibility, which affected the properties and applications of these materials, and the chiral information was efficiently transferred from the starting amino acids to the final structure.

We synthesized a family of six oxamidato-based MOFs from various amino acid derivatives, such as *L*-methionine, *S*-Methyl-*L*-cysteine, *L*-serine, and *L*-threonine. The MOFs derived from the amino acids *L*-methionine and *S*-Methyl-*L*-cysteine had pores decorated with flexible and accessible thioether groups, exhibiting a strong affinity for soft metals. On the other hand, MOFs derived from *L*-serine and *L*-threonine had pores decorated with hydroxyl groups, that could capture different organic molecules such as dyes or drugs due to their ability to establish specific host-guest interactions. In particular, we obtained four MOFs derived from a single amino acid and two MTV-MOFs, prepared using equimolar amounts of the corresponding precursors.

The study's results have been divided into two chapters, which have been further subdivided based on the number of publications. In

chapter 2, we demonstrated the essential role played by the steric constraint effects induced by the MOF network in catalysis, providing valuable insights into the nature of catalytically active species and reaction mechanisms. In chapter 3, we showed that MOFs are highly effective for the selective and efficient capture of emerging organic contaminants from water, which could lead to significant benefits for aquatic environments.

In **Publication 1**, titled “Epoxidation vs dehydrogenation of allylic alcohols: heterogenization of the VO(acac)₂ catalyst in a Metal-Organic Framework”, it was observed that the chemical reaction mechanism in the homogeneous phase (VO(acac)₂/TBHP) depends on the electronic profile of the alkene substituents: Electron-Donating Groups (EDGs) promote alkene coordination to the vanadyl and epoxidation, while Electron-Withdrawing Groups (EWGs) promote alcohol coordination and dehydrogenation. However, our work has demonstrated that the confinement effect displayed by MOFs plays a key role in reducing the substrate dependence and gaining control over the chemoselectivity of the reaction beyond the preference toward the less sterically demanding dehydrogenation reaction. We confirmed the homogenous distribution of vanadyl complexes along the pores, anchored to the functional thioether arms of the methionine residues, and confined into the channels through S⋯vanadyl interactions, by SC-XRD. Furthermore, our study has shown that PSMs represent a powerful tool for inserting new physical properties on a preformed PCP, enabling the preparation of materials that could not be synthesized through conventional synthetic routes.

Publication 2, titled “Exploring the role of amino acid-derived (multivariate) Metal-Organic Frameworks as catalyst in (hemi)-ketalization reactions”, investigated the potential of MOFs with functional channels decorated with more than one distinct amino acid residue as catalysts in (hemi)-ketalization reactions.

Inspired by the active centers of enzymes, where different organic functionalities can act synergistically, the study found that the presence of multiple functional groups in the MTV-MOF of formula $\{\text{Sr}^{\text{II}}\text{Cu}^{\text{II}}_6 [(\text{S}, \text{S})\text{-serimox}]_{1.50} [(\text{S}, \text{S})\text{-Mecysmox}]_{1.50} (\text{OH})_2 (\text{H}_2\text{O})\} \cdot 12\text{H}_2\text{O}$, prepared by using equal percentages of the amino acids *L*-serine and *L*-Mecysteine, improved catalytic conversions for the hemiketalization of different aldehydes and ketalization of cyclohexanone. The additional thioether groups in the MTV-MOF help to activate the carbonyl group, which cooperatively interacts with the amino acid residues containing alcohol and thioether groups. These findings demonstrate the potential of MTV-MOFs as promising candidates for mimicking natural non-acidic enzymes, such as glycosidases, and for uncovering novel catalytic mechanisms not readily accessible with other microporous materials or single-component MOFs.

In **Publication 3**, titled “Metal-Organic Frameworks as unique platforms to gain insight of σ -hole interactions for the removal of organic dyes from aquatic ecosystems”, we explored the potential of MOFs with electron-deficient bivalent sulfur atoms for the removal of organic dyes from aqueous solutions. These sulfur atoms have two areas of positive electrostatic potential, as a consequence of the low-lying σ^* orbitals of the C-S bond (the so-called σ -hole), which can interact with electron donors such as nitrogen atoms, nitrile groups, and even π -systems. The experimental results demonstrated that these MOFs efficiently capture a variety of organic dyes, including a multi-dye mixture, with nearly 90 % removal achieved after only 5 min. This is in stark contrast to the related serine-based MOF, which is decorated with hydroxyl groups and requires nearly 24 hours to reach the same capture efficiency through hydrogen-bonds. Furthermore, we were able to determine the crystal structure of the different organic dyes within the MOFs channels by using SCXRD, providing valuable insights into the key role played by sulfur σ -hole interactions in the removal of organic dyes from aqueous solutions.

In **Publication 4**, entitled “Highly efficient removal of neonicotinoid insecticides by thioether based (multivariate) Metal-Organic Frameworks”, we investigated the potential of three MOFs containing thioether-based residues for removing NEOs insecticides from aqueous solutions. Among the tested MOFs, the novel MTV-MOF, formulated as $\{Sr^{II}Cu_6^{II} [(S, S)\text{-methiomox}]_{1.5} [(S, S)\text{-Mecysmox}]_{1.5} (\text{OH})_2 (\text{H}_2\text{O})\} \cdot 36\text{H}_2\text{O}$ and prepared using equal percentages of amino acids *L*-methionine and *L*-methylcysteine, demonstrated exceptional removal efficiency by capturing 100 % of acetamiprid and thiacloprid in a single step under dynamic SPE conditions, in less than 30 seconds. Moreover, the MTV-MOF exhibited excellent reusability for at least 10 cycles. To understand the mechanisms involved in the efficient capture processes, we performed insertion experiments on single crystals of the MTV-MOF. The crystal structures of the MOF with acetamiprid and thiacloprid were resolved, revealing how both NEOs are encapsulated and immobilized within the MOF channels. The functional channels of the MTV-MOF, decorated with both $-\text{CH}_2\text{SCH}_3$ and $-\text{CH}_3\text{CH}_2\text{SCH}_3$ thioalkyl chains, play a crucial role in the synergistic interactions with the guest molecules. The sulfur σ^* orbitals of the thioether groups are responsible for the chemical reactivity, involving both intra- and intermolecular interactions, which propagate extensively in the nano-confined space ensured by the MOF.

In summary, these MOFs and MTV-MOFs serve as perfect platform for pollutant capture and the enhancement of catalytic activity. The stabilizing host-guest interactions, ensured by the confined spaces of the MOFs, guarantee the success of their use as porous systems for selectively capturing dangerous species and hosting reactants prior to catalytic reactions, thus acting as MOF-reactors. Moreover, the crystalline nature of the host matrices enables the use of X-ray crystallography as the gold standard for unequivocally characterizing their structures. These details provide insights into the synergistic host-guest interactions between the different functional groups of the MTV-MOF and the guest contaminants. They also elucidate the mechanisms underlying atomically precise

4. CONCLUDING REMARKS AND PERSPECTIVES

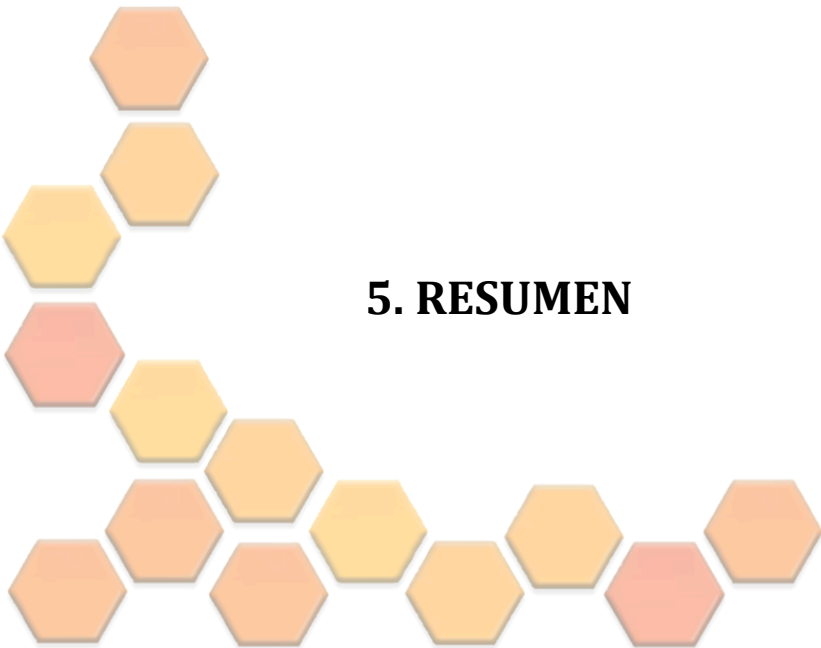
subnanometric clusters, revealing the nature of the metal species, their coordination environment, and the non-covalent interactions responsible for their stabilization.

The reported compounds represent a significant breakthrough in the applicability of MOFs in industrial catalysis, as some exhibit exceptional catalytic properties and can catalyze reactions that were previously unachievable. The heterogeneity of these MOFs translates into exceptional structural robustness, and they have also been demonstrated to be reusable adsorbents, making them attractive from both an environmental and industrial perspectives.

Additionally, these MOFs are not only highly efficient but also environmentally sustainable, cost-effective, and can be prepared on a large scale. This exceptional combination of properties makes these materials highly promising for future applications in water treatment and catalysis.

Based on the results of this study, we plan to develop practical devices, such as membranes, pellets, and films, among others, for the real-world application of these materials using the presented MOFs. Furthermore, we aim to synthesize new MTV-MOFs with functional groups distinct from those presented in this PhD thesis. Our ultimate goal is to gradually increase the degree of heterogeneity of the novel MTV-MOFs by decorating their pores with more than two distinct amino acid residues. This enhancement could potentially make them highly efficient catalyst and/or decontaminating agents, capable of removing both inorganic and organic pollutants from aquatic ecosystems in a single step.

The proposed initiatives will greatly expand the potential applications of these materials, while also contributing to the development of cleaner and more sustainable technologies, ultimately improving the well-being of our society.



5. RESUMEN

La presente tesis doctoral se ha realizado mediante compendio de publicaciones en cumplimiento con las normativas establecidas por la Universidad de Valencia, según lo dispuesto en el reglamento ACGUV 266/2011 referente al depósito, evaluación y defensa de tesis doctorales, con la última actualización correspondiente al 31 de Octubre de 2017.

El trabajo se encuentra estructurado en tres capítulos principales, seguidos de un capítulo final que engloba las conclusiones obtenidas a partir de los resultados de la investigación, así como los planes y perspectivas para trabajos futuros.

El capítulo 1 proporciona un contexto general sobre los materiales abordados en esta tesis: Metal-Organic Frameworks (MOFs) basados en oxamidato. Se presenta una breve revisión histórica que abarca desde los orígenes de la química de coordinación hasta los MOFs, destacando la importancia de la química reticular y el creciente interés en el campo de los MOFs. También se describen las metodologías sintéticas y de caracterización más comunes, junto con las propiedades físico-químicas más destacadas de los MOFs. Entre estas propiedades, destacan su alta porosidad y cristalinidad, lo que les permite presentar grandes áreas superficiales y volúmenes de poro, y ser caracterizados mediante técnicas de difracción de rayos X. Además, se resalta la interesante química host-guest de estos materiales, que puede ser controlada a través del tamaño, forma y reactividad de los poros. Esto los convierte en candidatos ideales para preparar materiales multifuncionales con aplicaciones en

diversas áreas tecnológicas, como se describe con ejemplos representativos en detalle. En este capítulo se enfatiza especialmente el papel clave de los MOFs Multivariantes (MTV-MOFs) debido a sus propiedades y aplicaciones únicas. Finalmente, se describe el trabajo previo relacionado realizado dentro de mi grupo de investigación, justificando la elección de la estrategia sintética utilizada y demostrando las ventajas que posee el uso de ligandos basados en oxamidato derivados de aminoácidos para obtener nuevos materiales quirales, estables en agua y con una rica diversidad estructural.

En los capítulos 2 y 3, se presentan los principales resultados obtenidos de esta tesis, los cuales han sido publicados en importantes revistas científicas. En el capítulo 2, se persiguieron dos objetivos. En primer lugar, se estudió el cambio en la reactividad de los catalizadores organometálicos con el fin de entender la naturaleza de las especies catalíticamente activas y los mecanismos de reacción, aprovechando los efectos de restricción estérica inducidos por el MOF. En segundo lugar, se exploraron los efectos de la funcionalización de los canales con más de un residuo de aminoácido distinto en reacciones catalíticas de relevancia industrial, inspirados en los centros activos de las enzimas, donde diferentes funcionalidades orgánicas pueden actuar sinérgicamente para mejorar la eficiencia catalítica. En el capítulo 3, se aprovechó la rica química *host-guest* de estos MOFs para la captura eficiente de algunos de los contaminantes orgánicos más comunes encontrados en ambientes acuáticos, como tintes orgánicos e insecticidas neonicotinoides (NEOs). En ambos capítulos se investigó el efecto de diferentes grupos funcionales para introducir nuevas o mejoradas propiedades físicas, así como su uso como catalizadores heterogéneos y para la captura de contaminantes en agua, respectivamente. Se destacó la importancia de la alta cristalinidad de este tipo de materiales para descubrir lo que sucede dentro de los poros a través de la difracción de rayos X de monocristal (SCXRD), ya que las estructuras cristalinas de los agregados *host-guest* proporcionaron evidencia de las interacciones sinérgicas entre los

diferentes grupos funcionales de los MOFs y los huéspedes, permitiendo comprender las propiedades excepcionales de estos materiales.

En general, se llevaron a cabo los siguientes pasos:

- Diseño y síntesis de prolígandos basados en oxamidato derivados de aminoácidos naturales enantiopuros capaces de coordinar Cu(II) y producir los precursores de dicobre(II) *trans*-oxamidato.
- Síntesis de MOFs y MTV-MOFs utilizando diferentes precursores de oxamidato, tanto en polvo como en monocristales.
- Estudio de las propiedades de los MOFs y MTV-MOFs obtenidos, analizando el efecto de la presencia de diferentes grupos funcionales para mejorar sus propiedades físicas o introducir nuevas funcionalidades.
- Estudio de su uso para la captura de contaminantes orgánicos en agua y como catalizadores heterogéneos, ya sea mediante la síntesis de MOFs catalíticamente activos que contienen complejos metálicos utilizando Métodos Post-Sintéticos (PSMs) o mediante su uso como plantillas para catalizar reacciones.

Los materiales obtenidos se caracterizaron mediante técnicas como espectroscopía infrarroja (IR), resonancia magnética nuclear (RMN), análisis termogravimétrico (TGA), difracción de rayos X de polvo (PXRD), adsorción de N₂ y CO₂ y microscopía electrónica de barrido (SEM). Sin embargo, la resolución de las estructuras cristalinas mediante SCXRD, así como los estudios de la actividad catalítica y los métodos analíticos de extracción en fase sólida (SPE) fueron realizados por el resto de coautores.

Metodología

La estrategia utilizada en esta tesis se basa en la síntesis inicial de prolígandos basados en oxamidato derivados de aminoácidos naturales enantiopuros, los cuales son relativamente sencillos de sintetizar y permiten la introducción de brazos funcionales en los MOFs. La selección cuidadosa del precursor de aminoácido de interés

5. RESUMEN

proporciona canales decorados con residuos de aminoácidos y tamaños de poro variables, lo que ofrece una amplia gama de posibilidades. Además, gracias a la presencia de átomos de α -carbono asimétricos en los aminoácidos, estos materiales pueden formar estructuras quirales.

Los proligandos basados en oxamidato presentan generalmente una configuración *trans*, ya que la configuración *cis* es menos estable debido al impedimento estérico entre los sustituyentes. Es importante destacar que estos proligandos tienen una alta afinidad hacia los iones metálicos de la primera serie de transición, lo que permite la formación de complejos metaloligandos extremadamente estables en disolución. Esto conduce a la formación de complejos dinucleares de cobre(II) que actúan como ligandos puente hacia iones alcalinotérreos y de lantánidos (Figura 1).

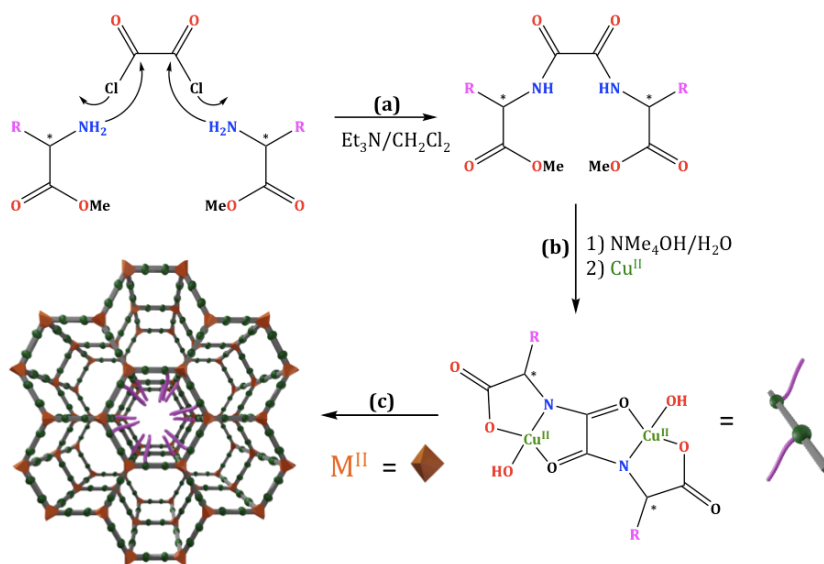


Figura 1. Esquema del procedimiento sintético seguido para la preparación de los proligandos de tipo bis-oxamidato (a), de los metaloligandos de cobre(II) derivados (b), y de los MOFs heterobimetálicos metal(II)/Cu(II) 3D correspondientes.

5. RESUMEN

En particular, se utilizaron los derivados metilados de *L*-metionina, *S*-metil-*L*-cisteína, *L*-serina y *L*-treonina (ver Tabla 1) para la síntesis de los proligandos. Todos los proligandos se prepararon utilizando el mismo procedimiento sintético (ver Figura 1a): el cloruro de oxalilo se condensó con el derivado de éster metílico del correspondiente aminoácido enantiopuro en presencia de trimetilamina y diclorometano como base y disolvente respectivamente, a temperatura ambiente. Los productos se aislaron como derivados metiloxamidato con rendimientos entre el 80 y el 90 % (Figura 2).

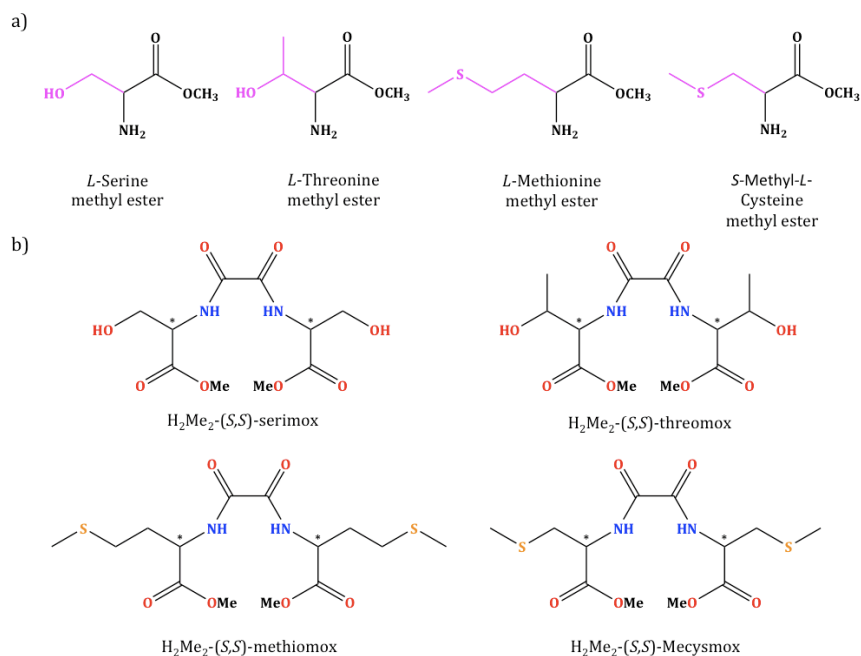


Figura 2. Derivados de aminoácidos utilizados (a) para sintetizar los proligandos metilados (b).

En el caso de la cisteína, fue necesario realizar una etapa previa de esterificación para obtener el proligando. Este procedimiento consistió en añadir gota a gota, bajo agitación y atmósfera de N_2 , un exceso de cloruro de tionilo ($SOCl_2$) a una solución de *S*-metil-*L*-cisteína en MeOH a 0 °C en un baño de hielo, y luego someter la mezcla resultante a reflujo a 80 °C durante 6 horas. Después, se

5. RESUMEN

destiló el exceso de cloruro de tionilo con el mismo disolvente y se concentró bajo presión reducida para obtener el derivado de éster metílico del aminoácido *S*-metil-*L*-cisteína, que se utilizó para obtener el proligando.

Tabla 1. Proligandos y metaloligandos sintetizados a partir de los correspondientes aminoácidos precursores.

Aminoácido	Proligando	Metaloligando
<i>L</i> -Serina	H ₂ Me ₂ -(<i>S</i> , <i>S</i>)-serimox	(Me ₄ N) ₂ {Cu ^{II} ₂ [(<i>S</i> , <i>S</i>)-serimox] (OH) ₂ } · 5H ₂ O
<i>L</i> -Treonina	H ₂ Me ₂ -(<i>S</i> , <i>S</i>)-treomox	(Me ₄ N) ₂ {Cu ^{II} ₂ [(<i>S</i> , <i>S</i>)-treomox] (OH) ₂ } · 4H ₂ O
<i>L</i> -Metionina	H ₂ Me ₂ -(<i>S</i> , <i>S</i>)-metiomox	(Me ₄ N) ₂ {Cu ^{II} ₂ [(<i>S</i> , <i>S</i>)-metiomox] (OH) ₂ } · 4H ₂ O
<i>S</i> -Metil- <i>L</i> -Cisteína	H ₂ Me ₂ -(<i>S</i> , <i>S</i>)-Mecismox	(Me ₄ N) ₂ {Cu ^{II} ₂ [(<i>S</i> , <i>S</i>)-Mecismox] (OH) ₂ } · 4H ₂ O

En el segundo paso, los proligandos de oxamidato se desprotonaron usando Me₄NOH como base y luego se hidrolizaron. Después se complejaron con CuCl₂ · 6H₂O en medio acuoso a temperatura ambiente, en una proporción molar de metal a ligando de 2:1 (ver Figura 1b). Los complejos de Cu(II) resultantes se aislaron como sales de tetrametilamonio y presentan una fórmula general de (Me₄N)₂ [Cu^{II}₂L(OH)₂] · nH₂O.

Por último, se utilizaron estos precursores de Cu(II) como metaloligandos, coordinando sus grupos carboxilato con un segundo ion metálico (en particular Ca(II) y Sr(II)), para formar MOFs quirales heterobimetálicos tridimensionales con poros funcionales decorados con residuos de aminoácidos (ver Figura 1c). Las cadenas de aminoácidos proporcionan una gran flexibilidad a la red, lo que influye en las propiedades y aplicaciones de estos materiales. Por lo tanto, las propiedades finales del material dependen de la naturaleza

del ligando orgánico, las propiedades de los diferentes iones metálicos utilizados, así como de la topología y estructura de la red tridimensional.

Resultados y Conclusiones

Se ha obtenido una familia de seis estructuras porosas isoestructurales con la fórmula general $\{M^{II}Cu^{II}_6 [(S, S)-L]_3 (OH)_2 (H_2O)\}_n \cdot xH_2O$ ($M = Ca$ o Sr , y $L =$ ligando derivado de oxamidato); cuatro de estas estructuras corresponden a derivados de un solo aminoácido, mientras que las otras dos son MTV-MOFs, preparados utilizando cantidades equimolares de los precursores correspondientes (ver Tabla 2).

Tabla 2. MOFs y MTV-MOFs heterobimetálicos obtenidos.

MOF
$\{Sr^{II}Cu^{II}_6 [(S, S)\text{-serimox}]_3 (OH)_2 (H_2O) \cdot 38H_2O\}$
$\{Sr^{II}Cu^{II}_6 [(S, S)\text{-treomox}]_3 (OH)_2 (H_2O) \cdot 36H_2O\}$
$\{Ca^{II}Cu^{II}_6 [(S, S)\text{-metiomox}]_3 (OH)_2 (H_2O) \cdot 16H_2O\}$
$\{Ca^{II}Cu^{II}_6 [(S, S)\text{-Mecismox}]_3 (OH)_2 (H_2O) \cdot 16H_2O\}$
$\{Sr^{II}Cu^{II}_6 [(S, S)\text{-serimox}]_{1.5} [(S, S)\text{-Mecismox}]_{1.5} (OH)_2 (H_2O) \cdot 12H_2O\}$
$\{Sr^{II}Cu^{II}_6 [(S, S)\text{-metiomox}]_{1.5} [(S, S)\text{-Mecismox}]_{1.5} (OH)_2 (H_2O) \cdot 36H_2O\}$

Esta nueva familia de MOFs presenta poros de diferentes tamaños, según el residuo de aminoácido utilizado en la síntesis. Además, las características de estos residuos, tales como su tamaño, forma e hidrofobicidad, influye en la topología y funcionalidad del MOF final. En el caso de serina y treonina, los poros tienen un tamaño de alrededor de 0.8-0.9 nm y están decorados con grupos hidroxilo que los hacen hidrofílicos, permitiéndoles alojar moléculas polares de forma efectiva. En los MOFs sintetizados a partir de cisteína los poros

tienen un tamaño entorno a 0.9 nm, mientras que en metionina son más pequeños, alrededor de 0.3 nm, y en ambos casos están decorados con grupos tioéter altamente flexibles y accesibles, lo que les confiere una fuerte afinidad por los metales blandos. Esta afinidad se ha utilizado con éxito en la captura de contaminantes y la inserción intencional de metales catalíticamente activos.

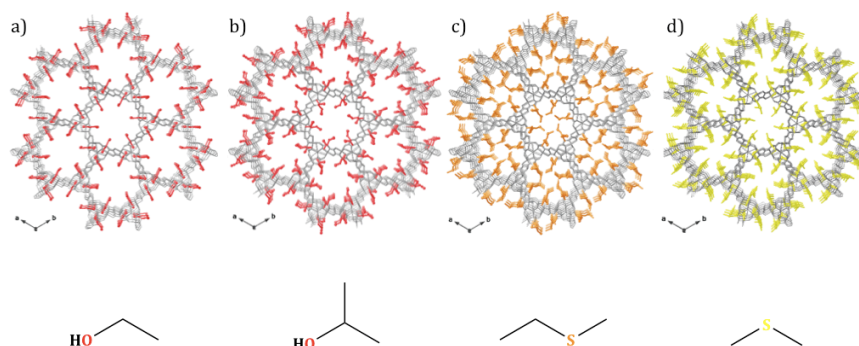


Figura 3. Vista en perspectiva a lo largo del eje cristalográfico *c* de los MOFs derivados de serina (a), treonina (b), metionina (c), y metilcisteina (d). Los metales y los ligandos orgánicos se representan como palos grises mientras que los residuos de los aminoácidos se representan como: $-\text{CH}_2\text{OH}$ (a)/ $-\text{CH}(\text{CH}_3)\text{OH}$ (b) en rojo, $-\text{CH}_2\text{CH}_2\text{SCH}_3$ (c) en naranja, y $-\text{CH}_2\text{SCH}_3$ (d) en amarillo.

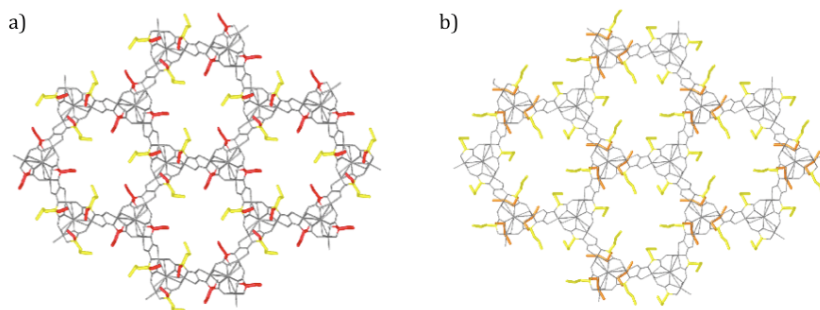


Figura 4. Vista en perspectiva a lo largo del eje cristalográfico *c* de los MTV-MOFs derivados de serina y metilcisteina (a), y metionina y metilcisteina (b). Los metales y los ligandos orgánicos se representan como palos grises mientras que los residuos de los aminoácidos se representan como: $-\text{CH}_2\text{OH}$ en rojo, $-\text{CH}_2\text{CH}_2\text{SCH}_3$ en naranja, y $-\text{CH}_2\text{SCH}_3$ en amarillo.

Las estructuras cristalinas de esta familia de MOFs fueron determinadas por SCXRD. En general, estas redes tridimensionales muestran una arquitectura similar a la de un panal de abejas con canales hexagonales funcionales relativamente grandes a lo largo del eje cristalográfico *c*. Estas estructuras consisten en redes tridimensionales Sr(II) o Ca(II)-Cu(II) donde las unidades de oxamidato de cobre(II) correspondientes $[\{\text{Cu}^{\text{II}}\text{L}(\text{OH})_2\}]$ actúan como conectores entre los iones Sr(II) o Ca(II) a través de sus grupos carboxilato. Los iones Sr(II) o Ca(II) ocupan los vértices de cada canal hexagonal, y las unidades de oxamidato de cobre(II) se encuentran a lo largo de los bordes de los canales. Moléculas adicionales de agua/hidróxido (en una distribución estadística de 1:2) que actúan como puentes adicionales entre dos unidades de oxamidato de cobre(II) y un ion Ca(II) o Sr(II), sostienen todo el sistema, revelando una topología de red con seis conexiones y un único nodo ($P6_3/\text{sistema hexagonal}$).

Los MOFs obtenidos en esta tesis han demostrado ser estables en agua y presentar microporosidad permanente, lo que confirma su potencial para diversas aplicaciones, como la catálisis y la remediación del agua. En particular, en el capítulo 2 se ha demostrado el papel crucial que juegan los efectos de restricción estérica inducidos por los MOFs en la catálisis, lo que proporciona información valiosa sobre la naturaleza de las especies catalíticamente activas y los mecanismos de reacción. En el capítulo 3, se ha aprovechado el conocimiento previo sobre MOFs basados en oxamidato, los cuales han demostrado ser eficaces en la captura y/o encapsulación de metales pesados e incluso para construir pequeños *clusters* metálicos mediante PSMs, para evaluar la importancia de la funcionalización de los canales de los MOFs en la captura eficiente de algunos de los contaminantes orgánicos más comunes en los ecosistemas acuáticos. Es importante destacar que todos los estudios en este capítulo se llevaron a cabo utilizando muestras reales de agua del río Turia y del parque natural de la Albufera (Valencia, España).

Epoxidation vs Dehydrogenation of Allylic Alcohols: Heterogenization of the VO(acac)₂ Catalyst in a Metal-Organic Framework (Publicación 1).

La búsqueda de métodos catalíticos y selectivos para las reacciones de oxidación es crucial en la síntesis orgánica, siendo uno de los ejemplos más notables el sistema VO(acac)₂/TBHP, que ha demostrado una alta selectividad y eficacia en la epoxidación de alcoholes alílicos, así como en otras reacciones como la deshidrogenación quimioselectiva de alcoholes secundarios acíclicos y cíclicos a las correspondientes cetonas y la oxidación de o-alquénil fenoles a o-hidroxibenzil cetonas. Sin embargo, a pesar de su amplio uso, todavía hay una falta de caracterización atómica precisa que limita nuestra comprensión de las relaciones estructura-propiedad en este sistema catalítico.

En general, hemos observado que en la fase homogénea (VO(acac)₂/TBHP) la selectividad de los alcoholes alílicos hacia las reacciones de epoxidación o deshidrogenación está sutilmente controlada por los sustituyentes alrededor de las funcionalidades de los alcoholes alílicos. En este estudio, se ha sintetizado un MOF que encapsula especies VO(acac)(H₂O) y se ha resuelto atómicamente mediante SC-XRD. Los complejos de vanadilo, anclados a los brazos tioéter de los residuos de metionina y confinados en los canales a través de interacciones S ... vanadilo, se distribuyen homogéneamente en los poros de {Ca^{II}Cu^{II}₆ [(S, S)-metiomox]₃ (OH)₂ (H₂O) · 16H₂O}. Se ha demostrado que el efecto de confinamiento de los MOFs juega un papel clave en la reducción de la dependencia del sustrato y en el control de la quimioselectividad de la reacción. Además, se demostró que los PSMs son herramientas poderosas para insertar nuevas propiedades físicas en un MOF preformado, lo que permite la preparación de materiales que no podrían obtenerse mediante rutas sintéticas convencionales.

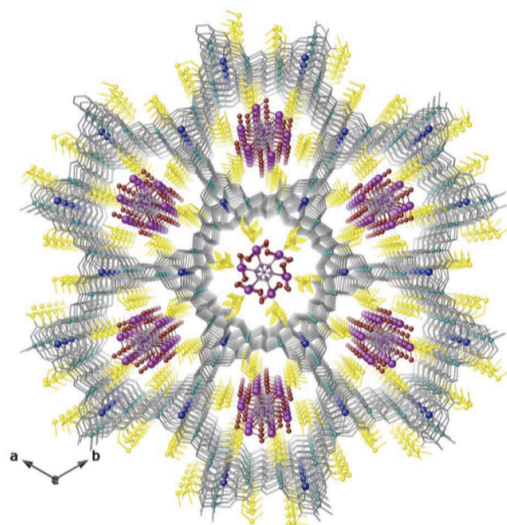


Figura 5. Vista en perspectiva de la estructura cristalina de $\{\text{Ca}^{\text{II}}\text{Cu}^{\text{II}}_6 [(\text{S}, \text{S})\text{-metiomox}]_3 (\text{OH})_2 (\text{H}_2\text{O}) \cdot 16\text{H}_2\text{O}\}$ a lo largo del eje cristalográfico c , mostrando los complejos $\text{VO}(\text{acac})(\text{H}_2\text{O})^+$ bien empaquetados dentro de los poros. La red tridimensional se representa como varillas grises, con la excepción del cobre y el calcio, representados como esferas cian y azules, y la cadena etílica y los átomos de azufre del residuo de metionina, representados como varillas amarillas (carbono) y esferas amarillas (azufre). Para las especies huésped $\text{VO}(\text{acac})(\text{H}_2\text{O})^+$ alojadas en los canales, los átomos de vanadio, carbono y oxígeno se representan como esferas moradas, grises y rojas, respectivamente. Las moléculas de agua de cristalización se han omitido por claridad.

Exploring the Role of Amino Acid-Derived Multivariate Metal-Organic Frameworks as Catalyst in (Hemi)-Ketalization Reactions (Publicación 2).

La adición de alcoholes al grupo carbonilo de aldehídos y cetonas es una reacción importante tanto en la naturaleza como en la síntesis industrial, ya que puede alterar la densidad electrónica del grupo carbonilo de rico en electrones a pobre en electrones. Las reacciones de hemi-cetalización y cetalización se utilizan comúnmente en la síntesis orgánica para proteger los grupos aldehído y cetona durante otras reacciones. Sin embargo, las condiciones ácido-catalizadas requeridas para estas reacciones no siempre son compatibles con

otros grupos funcionales, que deben protegerse previamente con métodos alternativos. En la naturaleza, este problema se resuelve mediante el uso de enzimas no ácidas, como las glicosidasas.

Tomando como inspiración los centros activos de las enzimas, donde diferentes funcionalidades orgánicas pueden actuar de manera sinérgica, investigamos los efectos de la presencia de canales funcionales decorados con más de un residuo de aminoácido distinto en reacciones catalíticas de relevancia industrial. En particular, el MTV-MOF de fórmula $\{\text{Sr}^{\text{II}}\text{Cu}^{\text{II}}_6 [(\text{S}, \text{S})\text{-serimox}]_{1.5} [(\text{S}, \text{S})\text{-Mecismox}]_{1.5} (\text{OH})_2 (\text{H}_2\text{O})\} \cdot 12\text{H}_2\text{O}$, preparado utilizando porcentajes iguales de los aminoácidos *L*-serina y *S*-Metil-*L*-cisteína, exhibe las conversiones catalíticas más eficientes para la hemi-cetalización de diferentes aldehídos y la cetalización de ciclohexanona en comparación con los dos MOFs de un solo componente (derivados de serina o cisteína), debido a que los grupos tioéter adicionales en el MTV-MOF pueden ayudar a la activación del grupo carbonilo. Por lo tanto, los residuos de aminoácidos que contienen grupos alcohol y tioéter no forman enlaces permanentes, pero podrían activar cooperativamente el grupo carbonilo en presencia de alcohol externo, de manera similar a como lo hacen las glicosidasas. La heterogeneidad en el MTV-MOF se traduce de manera excelente en un comportamiento catalítico mejorado en las reacciones estudiadas. Estos resultados resaltan el potencial del MTV-MOF como un candidato fuerte para imitar enzimas naturales no ácidas, como las glicosidasas, y para revelar nuevos mecanismos catalíticos no tan fácilmente accesibles con otros materiales microporosos o MOFs de un solo componente.

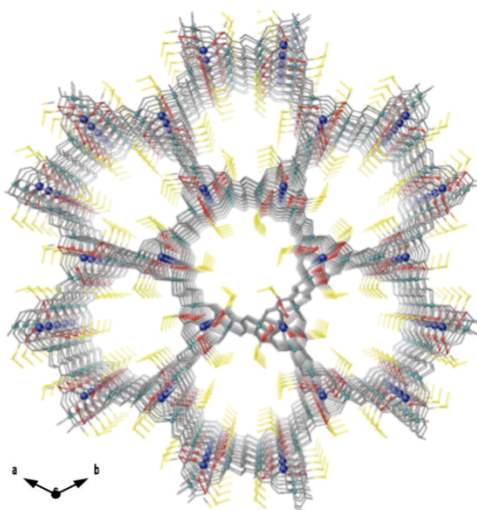


Figura 6. Vista en perspectiva de la estructura cristalina de $\{\text{Sr}^{\text{II}}\text{Cu}^{\text{II}}_6 [(\text{S}, \text{S})\text{-serimox}]_{1.5} [(\text{S}, \text{S})\text{-Mecismox}]_{1.5} (\text{OH})_2 (\text{H}_2\text{O})\} \cdot 12\text{H}_2\text{O}$ a lo largo del eje cristalográfico c . Los iones de cobre(II) y estroncio(II) de la red se representan como esferas cian y azules, respectivamente. Los átomos de oxígeno y azufre de los residuos se muestran como esferas rojas y amarillas, respectivamente. Los ligandos orgánicos se representan como varillas grises, con la excepción de los residuos de serina ($-\text{CH}_2\text{OH}$) y metilcisteína ($-\text{CH}_2\text{SCH}_3$), que se representan como varillas rojas y amarillas, respectivamente.

Metal-Organic Frameworks as Unique Platforms to Gain Insight of σ -Hole Interactions for the Removal of Organic Dyes from Aquatic Ecosystems (Publicación 3).

Los tintes orgánicos son ampliamente utilizados en muchas aplicaciones industriales, como el textil, cuero, plástico, cosmética, papel y la industria alimentaria, entre otras. Se estima que más de 100.000 tintes comerciales están disponibles en la actualidad, y se producen más de 70.000 toneladas anualmente para satisfacer la creciente demanda. Sin embargo, el uso indiscriminado de tintes orgánicos también puede tener un impacto negativo en el medio ambiente y la salud humana. El problema radica en que entre el 2 % y el 10 % del total de la producción de tintes se descarga en sistemas acuáticos, lo que provoca un color indeseable en el agua incluso a

bajas concentraciones, reduciendo severamente la penetración de la luz solar, y afectando la fotoactividad en la vida acuática. Además, la presencia de metales los hace extremadamente tóxicos para los peces, ya que pueden tener propiedades teratogénicas, mutagénicas y carcinogénicas, lo que en última instancia representa un riesgo para la vida humana.

En este trabajo se presenta uno de los primeros estudios sobre la explotación racional de las interacciones de σ -hueco de azufre para una eficiente captura de contaminantes orgánicos de agua. Se sabe que estas interacciones juegan un papel clave en la actividad biológica y en procesos relevantes de reconocimiento molecular, pero apenas han sido exploradas hasta ahora. Los átomos de azufre bivalentes deficientes en electrones tienen dos áreas de potencial electrostático positivo, como consecuencia de los orbitales σ^* de baja energía del enlace C-S (el llamado σ -hueco), que están disponibles para la interacción con donantes de electrones como átomos de nitrógeno o, como en el presente caso, grupos de nitrilo e incluso sistemas π . Por lo tanto el perfil cinético obtenido utilizando el MOF $\{Ca^{II}Cu^{II}_6 [(S, S)\text{-metiomox}]_3 (OH)_2 (H_2O) \cdot 16H_2O\}$ evidenció la eficiente y rápida adsorción de todos los colorantes probados (incluso usando una solución de mezcla de múltiples colorantes), alcanzando casi el 90 % de eliminación después de 5 minutos, en contraste con el MOF basado en serina relacionado, que muestra poros decorados con grupos hidroxilo y necesita casi 24 horas para alcanzar la misma eficiencia de captura a través de enlaces de hidrógeno. La estructura cristalina de los diferentes colorantes orgánicos dentro de los canales del MOF, caracterizados con precisión por SCXRD, nos permitió racionalizar y comprender el papel clave que juegan las interacciones σ -hueco de azufre en la eliminación de colorantes orgánicos de medios acuosos. De igual manera, hemos acercado indirectamente este MOF un paso más hacia aplicaciones del mundo real mediante su estructuración como *pellets* extruidos y su síntesis a gran escala. Cabe destacar que este trabajo representa el interesante comienzo de una línea de investigación que

actualmente estamos desarrollando para integrar este MOF en una planta piloto de descontaminación.

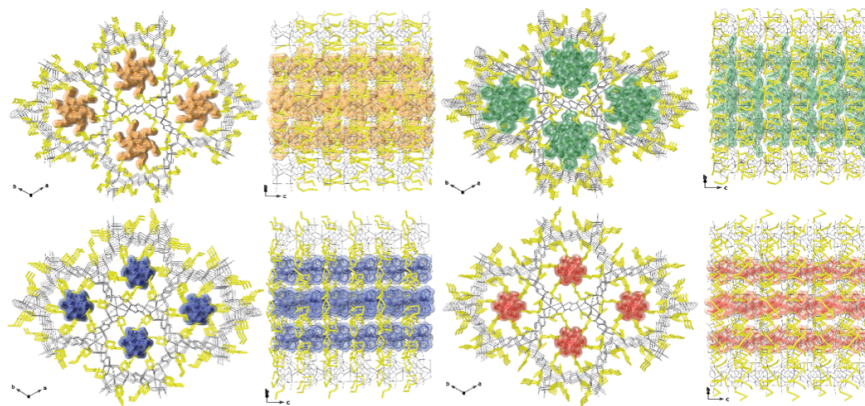


Figura 7. Vistas en perspectiva en los planos *ab* (izquierda) y *bc* (derecha) de los ensamblajes huésped-anfitrión de $\{Ca^{II}Cu^{II}_6 [(S, S)\text{-metiomox}]_3 (OH)_2 (H_2O) \cdot 16H_2O\}$ con AO (a), BG (b), MB (c) y PY (d). Las redes se representan como varillas de color gris claro con residuos etiltiometilo ($-CH_2CH_2SCH_3$) como varillas amarillas y los colorantes orgánicos huésped como superficies sólidas de color naranja (AO), verde (BG), azul (MB) y rojo (PY). Las moléculas de agua libres se han omitido por claridad.

Highly Efficient Removal of Neonicotinoid Insecticides by Thioether-Based (Multivariate) Metal–Organic Frameworks (Publicación 4).

El rápido crecimiento de la población mundial ha generado una mayor demanda de alimentos, lo que ha llevado a una transición de la agricultura tradicional a prácticas agrícolas intensivas en todo el mundo. Sin embargo, esta transición ha llevado a la acumulación de grandes cantidades de contaminantes en nuestros ecosistemas, incluyendo insecticidas, herbicidas, pesticidas y fertilizantes. Su considerable solubilidad en agua y toxicidad proporcionan muchas ventajas en el control de plagas, pero también los convierten en una amenaza significativa tanto para la salud humana como para el medio ambiente. En particular, los neonicotinoides (NEOs), el tipo de insecticida más ampliamente utilizado en el mundo, presentan una

larga vida útil y se acumulan en los suelos. Por lo tanto, su eliminación es un problema fundamental para mantener el equilibrio en nuestros ecosistemas.

En este trabajo, presentamos el uso de una familia de MOFs como adsorbentes para la eliminación de insecticidas neonicotinoides del agua, en particular, tiametoxam, clotianidina, imidacloprid, acetamiprid y tiacloprid. Se observó que los MOFs que contienen residuos basados en tioéter mostraron una notable eficiencia de captura. El nuevo MTV-MOF con la fórmula $\{\text{Sr}^{\text{II}}\text{Cu}^{\text{II}}\}_6 [(\text{S}, \text{S})\text{-metiomox}]_{1.5} [(\text{S}, \text{S})\text{-Mecismox}]_{1.5} (\text{OH})_2 (\text{H}_2\text{O})\} \cdot 36\text{H}_2\text{O}$, preparado utilizando porcentajes iguales de los aminoácidos *L*-metionina y *S*-Metil-*L*-cisteína, demostró una eficiencia de eliminación excepcional al capturar el 100 % de acetamiprid y tiacloprid en un solo paso bajo condiciones de SPE (en menos de 30 s). Además, las propiedades de captura se mantuvieron durante al menos 10 ciclos. Para comprender mejor los mecanismos involucrados en los procesos de captura, se realizaron experimentos de inserción en monocristales del MTV-MOF, y se resolvieron las estructuras cristalinas con acetamiprid y tiacloprid. De esta manera se observó cómo ambos compuestos están encapsulados e inmovilizados dentro de los canales del MOF gracias a las interacciones sinérgicas de ambos tipos de grupos tioéter con las moléculas huésped. Tanto las interacciones intramoleculares como las intermoleculares que involucran orbitales σ^* de azufre de baja energía juegan un papel destacado en la reactividad química, debido a su extensa propagación en el espacio nanoconfinado asegurado por el MOF.

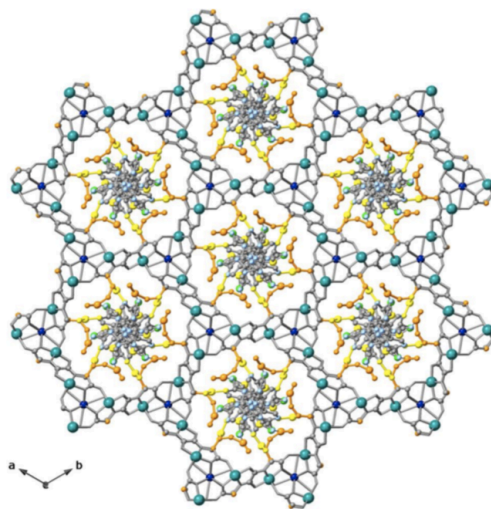


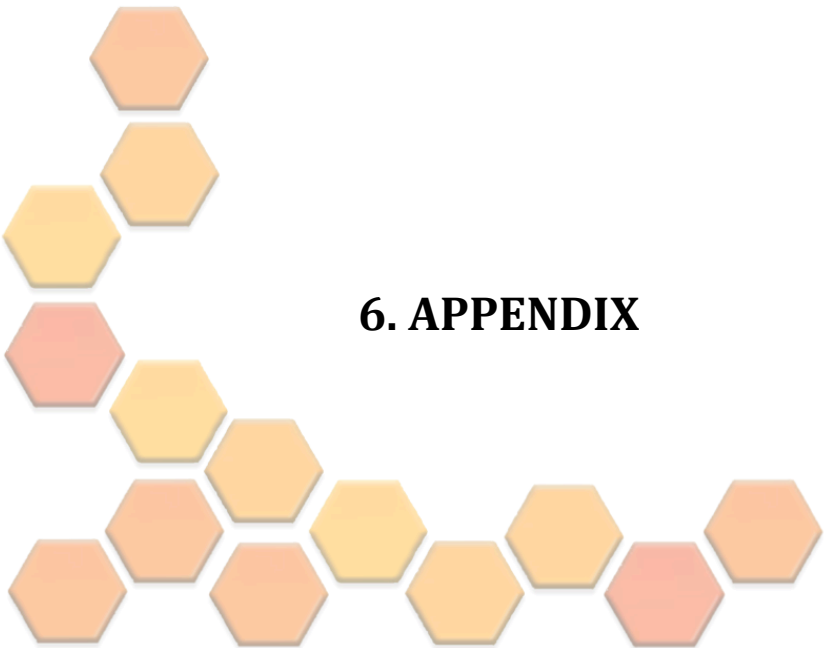
Figura 8. Vista de la estructura cristalina de $\{\text{Sr}^{\text{II}}\text{Cu}^{\text{II}}_6 [(\text{S}, \text{S})\text{-metiomox}]_{1.5} [(\text{S}, \text{S})\text{-Mecismox}]_{1.5} (\text{OH})_2 (\text{H}_2\text{O})\} \cdot 36\text{H}_2\text{O}$ a lo largo del eje c (las moléculas de agua de cristalización se han omitido por claridad), que muestra los poros llenos de moléculas huésped de thiacloprid. Los ligandos orgánicos de la red se representan como varillas grises, mientras que los residuos de aminoácidos se representan con el siguiente código de color: $-\text{CH}_2\text{SCH}_3$ (amarillo) y $-\text{CH}_2\text{CH}_2\text{SCH}_3$ (naranja). Las moléculas huésped se representan como bolas y varillas con carbono gris, nitrógeno azul claro y cloro verde. Los átomos de estroncio, cobre y azufre se muestran como esferas azules, cian y amarillas (para el fragmento de metilcisteína)/naranjas (para el fragmento de metionina), respectivamente.

En resumen, la investigación llevada a cabo en esta tesis ha demostrado que los MTV-MOF tienen un potencial enorme como materiales versátiles para la eliminación de contaminantes en medios acuosos y para llevar a cabo reacciones catalíticas. Los estudios de las estructuras cristalinas de los agregados *host-guest* obtenidos por medio de SCXRD permitieron analizar las interacciones sinérgicas entre los diferentes grupos funcionales del MTV-MOF y los contaminantes, proporcionando información valiosa sobre sus excelentes propiedades de captura. Además, los compuestos presentados suponen un avance significativo en la aplicación de los MOFs en la catálisis industrial, ya que algunos

exhiben propiedades catalíticas excepcionales y son capaces de catalizar reacciones que anteriormente se consideraban imposibles. La heterogeneidad de estos MOFs les confiere una robustez estructural excepcional y son reutilizables. Asimismo, estos MOF no solo son altamente eficientes, sino también sostenibles desde un punto de vista ambiental, rentables y pueden prepararse a gran escala. Esta combinación excepcional de propiedades hace que estos materiales sean altamente prometedores para futuras aplicaciones en el tratamiento de agua y en la catálisis.

En base a los resultados obtenidos en este estudio, nuestro próximo objetivo es llevar a cabo el desarrollo de dispositivos prácticos, tales como membranas, gránulos (*pellets*) y películas (*films*), entre otros, que permitan la aplicación real de los MOFs presentados. Además, pretendemos llevar a cabo la síntesis de nuevos MTV-MOF que contengan grupos funcionales diferentes a los presentados en esta tesis doctoral, buscando aumentar gradualmente el grado de heterogeneidad decorando los poros con más de dos residuos de aminoácidos distintos. Estas mejoras, que se proyectan en la línea de investigación que estamos desarrollando, podrían convertirlos en catalizadores altamente eficientes y/o agentes descontaminantes capaces de eliminar tanto contaminantes inorgánicos como orgánicos en un solo paso, mejorando significativamente la calidad de los ecosistemas acuáticos.

Las iniciativas propuestas tienen como objetivo ampliar significativamente el campo de aplicación de estos materiales y abordar de manera efectiva el problema de la contaminación en los ecosistemas acuáticos, contribuyendo así al desarrollo de tecnologías más limpias y sostenibles que favorezcan el bienestar de nuestra sociedad.



6. APPENDIX

6.1. Index of Abbreviations

0D	Zero-dimensional
1D	One-dimensional
2D	Two-dimensional
3D	Three-dimensional
4,4'-bipy	4,4'-bipyridine
AFM	Atomic Force Microscopy
Ala	Alanine
API	Active Pharmaceutical Ingredient
AO	Auramine O
AOP	Advanced Oxidation Processes
Asp	Aspartic acid
BE	Binding Energy
BET	Brunauer-Emmett-Teller
BG	Brilliant Green
BioMOF	Biocompatible MOF
CP	Coordination Polymer
CSD	Cambridge Structural Database
CUS	Coordinatively Unsaturated Site
Cys	Cysteine
DCM	Dichloromethane
DDS	Drug Delivery System
DEF	<i>N, N</i> -Diethylformamide
DLS	Dynamic Light Scattering
DMF	<i>N, N</i> -Dimethylformamide
DMSO	Dimethyl sulfoxide
EA	Elemental Analysis
EDG	Electron-Donating Group
EDX	Energy-Dispersive X-ray
EWG	Electron-Withdrawing Group
FCS	Fluorescence Correlation Spectroscopy
GC-MS	Gas chromatography mass spectrometry
Glu	Glutamic acid
His	Histidine
HKUST	Hong Kong University of Science and Technology
HPLC	High Performance Liquid Chromatography
ICP-MS	Inductively Coupled Plasma-Mass Spectroscopy

6. APPENDIX

ICP-OES	Inductively Coupled Plasma-Optical Emission Spectroscopy
IR	Infra Red
IRMOF	Isorecticular Metal-Organic Framework
LD-ED	Low-Dose Electron Diffraction
Leu	Leucine
MB	Methylene Blue
MBB	Molecular Building Block
Mecys	(<i>S</i>)-Methyl-(<i>L</i>)-cysteine
Me ₄ NOH	Tetramethylammonium hydroxide
MeOH	Methanol
Met	Methionine
MIL	Material of Institut Lavoisier
MMM-MOF	Mixed Matrix Membranes MOF
MOF	Metal-Organic Framework
MTG	Methanol To Gasoline
MTV	Multivariate
NEO	Neonicotinoid
NEt ₃	Triethylamine
NMR	Nuclear Magnetic Resonance
OMS	Open Metal Site
PALS	Positron Annihilation Lifetime Spectroscopy
PCP	Porous Coordination Polymer
Phe	Phenylalanine
PPCP	Pharmaceutical and Personal Care Product
PS	Post-Synthetic
PSD	Post-Synthetic Deprotection
PSE	Post-Synthetic Exchange
PSI	Post-Synthetic Insertion
PSM	Post-Synthetic Methodologies
PSP	Post-Synthetic Polymerization
PXRD	Powder X-Ray Diffraction
PY	Pyronin Y
RSD	Relative Standard Deviation
SAC	Single-Atom Catalyst
SALE	Solvent-Assisted Linker Exchange
SALI	Solvent-Assisted Linker Incorporation
SAXS	Small Angle X-ray Scattering
SBU	Secondary Building Unit
SC to SC	Single-Crystal to Single-Crystal

6. APPENDIX

SCM	Single-Chain magnet
SCXRD	Single-Crystal X-Ray Diffraction
SEM	Scanning Electron Microscopy
Ser	Serine
sMC	Sub-Nanometric Metal Cluster
SMM	Single-Molecule Magnet
SOCl ₂	Thionyl chloride
SPE	Solid-Phase Extraction
SSNMR	Solid-State Nuclear Magnetic Resonance
TBHP	Tert-butyl hidroperoxide
TEM	Transmission Electron Microscopy
TEV	Tobacco Etch Virus
TGA	Thermo-Gravimetric Analysis
Thr/Threo	Threonine
TON	Turn Over Number
TOF	Turn Over Frequency
UiO	Universitet i Oslo
UV-vis	Ultra Violet-visible
Val	Valine
VT-PXRD	Variable Temperatura Powder X-Ray Diffraction
WAXS	Wide Angle X-Ray Scattering
WHO	World Health Organization
XPS	X-ray Photoelectron Spectroscopy
ZIF	Zeolitic Imidazole Framework
ZSM	Zeolita Socony Mobil
ca.	circa (approximately)
i.e.	id est (that is)
e.g.	exempli gratia (for example)
et al.	et álíi (and others)

6.2. List of Publications

Author Contributions to this Thesis

Publication 1. Negro, C.; Bilanin, C.; Qu, X.; Oliver-Meseguer, J.; Ferrando-Soria, J.; Leyva-Pérez, A.; Armentano, D.; Pardo, E. Epoxidation vs dehydrogenation of allylic alcohols: heterogenization of the VO(acac)₂ catalyst in a Metal–Organic Framework. *Chem. Commun.* **2022**, 58, 5578-5581.

Publication 2. Negro, C.; Sanz-Navarro, S.; Leyva-Pérez, A.; Armentano, D.; Ferrando-Soria, J.; Pardo, E. Exploring the role of amino acid-derived (Multivariate) Metal–Organic Frameworks as catalyst in (hemi)-ketalization reactions. *Inorg. Chem.* **2023**, DOI: 10.1021/acs.inorgchem.3c00495.

Publication 3. Negro, C.; Escamilla, P.; Bruno, R.; Ferrando-Soria, J.; Armentano, D.; Pardo, E. Metal–Organic Frameworks as unique platforms to gain insight of σ -hole interactions for the removal of organic dyes from aquatic ecosystems. *Chem. Eur. J.* **2022**, 28, e202200034.

Publication 4. Negro, C.; Pérez-Cejuela, H. M.; Simó-Alfonso, E. F.; Herrero-Martínez, J. M.; Bruno, R.; Armentano, D.; Ferrando-Soria, J.; Pardo, E. Highly efficient removal of neonicotinoid insecticides by thioether-based (Multivariate) Metal–Organic Frameworks. *ACS Appl. Mater. Interfaces* **2021**, 13, 24, 28424–28432.

Other Contributions during this Thesis

Publication 5. Negro, C.; Pérez-Cejuela, H. M.; Simó-Alfonso, E. F.; Iqbal, W.; Herrero-Martínez, J. M.; Armentano, D.; Ferrando-Soria, J.; Pardo, E. (Multivariate) Metal–Organic Framework for highly efficient antibiotic capture from aquatic environmental matrices. *ACS Appl. Mater. Interfaces* **2023**, 15, 2, 3069–3076.

Publication 6. Baratta, M.; Mastropietro, T. F.; Bruno, R.; Tursi, A.; Negro, C.; Ferrando-Soria, J.; Mashin, A. I.; Nezhdanov, A.; Nicoletta, F. P.; De Filpo, G.; Pardo, E.; Armentano, D. (Multivariate) Metal–Organic Framework/Single-Walled Carbon Nanotube Buckypaper for selective lead decontamination. *ACS Appl. Nano Mater.* **2022**, 5, 4, 5223-5233.

Publication 7. Mon, M.; Bruno, R.; Sanz-Navarro, S.; Negro, C.; Ferrando-Soria, J.; Bartella, L.; Di Donna, L.; Prejanò, M.; Marino, T.; Leyva-Pérez, A.; Armentano, D.; Pardo, E. Hydrolase-like catalysis and structural resolution of natural products by a Metal–Organic Framework. *Nat. Commun.* **2020**, 11, 3080.

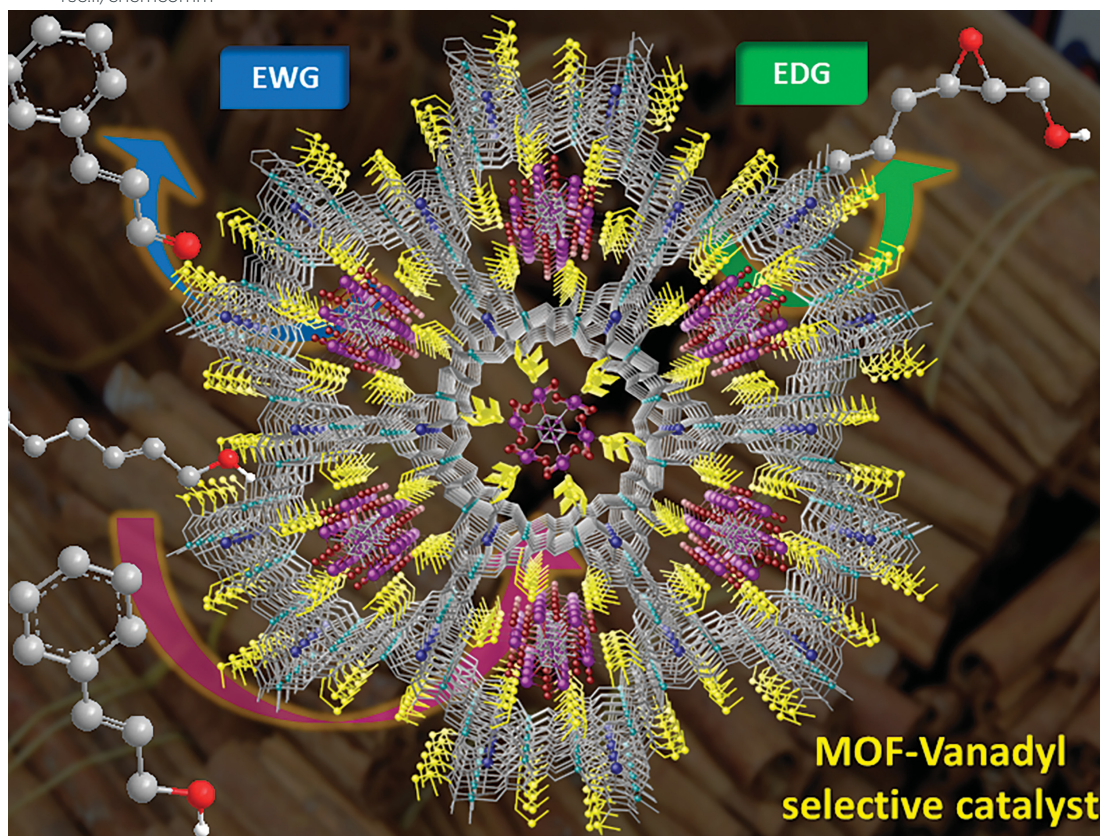


**PUBLICATION 1: Epoxidation vs Dehydrogenation
of Allylic Alcohols: Heterogenization of the
VO(acac)₂ Catalyst in a Metal-Organic Framework**



ChemComm

Chemical Communications

rsc.li/chemcomm

ISSN 1359-7345

ROYAL SOCIETY
OF CHEMISTRY**COMMUNICATION**Judit Oliver-Meseguer, Jesús Ferrando-Soria,
Antonio Leyva-Pérez, Donatella Armentano *et al.*
Epoxidation vs. dehydrogenation of allylic alcohols:
heterogenization of the VO(acac)₂ catalyst in a
metal-organic framework

Cite this: *Chem. Commun.*, 2022, 58, 5578Received 24th February 2022.
Accepted 6th April 2022

DOI: 10.1039/d2cc01137a

rsc.li/chemcomm

Epoxidation vs. dehydrogenation of allylic alcohols: heterogenization of the VO(acac)₂ catalyst in a metal–organic framework†

Cristina Negro,^{‡,a} Cristina Bilanin,^{‡,b} Xiaoni Qu,^{ac} Judit Oliver-Meseguer,^{*b} Jesús Ferrando-Soria,^{†b,*a} Antonio Leyva-Pérez,^{†b,*b} Donatella Armentano^{†b,*d} and Emilio Pardo^{†b,a}

Allylic alcohol epoxidation and dehydrogenation reactivity is distinguished when VO(acac)₂ is used in solution or anchored in a metal–organic framework (MOF). The chemical mechanism depends on the electronic profile of alkene substituents when the vanadyl complex is used in the homogenous phase. However, confinement effects imparted by MOF channels allow gaining control of the chemoselectivity toward the dehydrogenation product.

The development of catalytic and selective methods for oxidation reactions is extremely important in organic synthesis. Among several oxidizing systems,¹ metal-catalysed methodologies² have experienced ever-increasing growth and application over the years. One of the best examples reported so far is the VO(acac)₂/TBHP (vanadyl acetylacetonate/*tert*-butyl hydroperoxide) system,³ developed by Sharpless and Michaelson, for the highly regio- and stereoselective epoxidation of allylic alcohols.⁴ This catalytic system has been also extensively employed in a wide plethora of reactions,⁵ such as the chemoselective dehydrogenation of acyclic and cyclic secondary alcohols to the corresponding ketones,⁶ or the oxidation of *o*-alkenyl phenols to *o*-hydroxybenzyl ketones.⁷ However, to the best of our knowledge, it has not been clearly specified yet the exact conditions where the corresponding epoxidation or alcohol dehydrogenation takes place.

Metal–organic frameworks⁸ (MOFs) have blossomed in recent years in catalysis as a direct consequence of their unique characteristics,⁹ such as a fascinating host–guest chemistry¹⁰ and the possibility to use single-crystal X-ray diffraction (SC-XRD)¹¹ to unveil the nature of catalytically active species and reaction mechanisms.¹² MOFs' catalytic activity can be originated intrinsically, arising from open metal sites and/or the organic linkers constituting the coordination network, extrinsically, emerging from guest active species hosted in their channels,^{11,13} and a synergic combination of both of them.¹² Dealing with guest active species, different examples showing the encapsulation of active metal-based species of different chemical nature and nuclearity have been reported recently.^{12–15} This matrix-isolation strategy^{11,13} offers clear benefits over a homogenous solution, such as structural characterisation and higher reusability.¹⁵ However, much work needs to be done to understand how the chemical and steric environment offered by the host matrix affects the chemical nature of guest species and the concomitant effects on their catalytic activity.

Here, we aim to shed light on both open questions. Thus, firstly, we demonstrate that when VO(acac)₂ is in solution, the selection of the reaction pathway of allylic alcohols with TBHP, underpinned by activation energy evaluations, depends on the electronic profile (electron-donating/withdrawing groups) of alkene substituents, which sets the preference toward either the corresponding epoxide or aldehyde product. Then, we present the post-synthetic insertion of VO(acac)₂ within a preformed MOF of formula {Ca^{II}Cu^{II}[(S,S)-methox]₃(OH)₂(H₂O)}·16H₂O (**4**) (methox = (S,S)-oxaloyl-bis(*N*-methioninate))^{16,17} to lead to the hybrid material [V^{VO}O(acac)(H₂O)]@{Ca^{II}Cu^{II}[(S,S)-methox]₃(OH)₂·8H₂O} (VO(acac)(H₂O))@**4**, whose crystal structure is unveiled by single-crystal X-ray crystallography. The confinement effect of MOF channels in VO(acac)(H₂O))@**4** plays a key role, considerably reducing the substrate dependence and imparting a preference toward the less sterically demanding dehydrogenation reaction.

VO(acac)₂ is able to catalyse the epoxidation and the dehydrogenation of allylic alcohols.¹⁸ However, as far as we know, a structure–activity relationship has not been clearly specified in

^a Departament de Química Inorgànica, Institut de Ciència Molecular (ICMOL), Universitat de València, 46980 Paterna, València, Spain

^b Institut de Tecnologia Química (UPV-CSIC), Universitat Politècnica de València–Consejo Superior de Investigaciones Científicas, Avda. de los Naranjos s/n, 46022 Valencia, Spain

^c College of Chemistry and Materials Science, Northwest University, Xi'an 710069, China

^d Dipartimento di Chimica e Tecnologie Chimiche, Università della Calabria, 87036, Cosenza, Italy

† Electronic supplementary information (ESI) available: Preparation and physical characterization data. Crystallographic refinement details, Additional Fig. S1–S23 and Tables S1–S3. CCDC 2122007. For ESI and crystallographic data in CIF or other electronic format see DOI: <https://doi.org/10.1039/d2cc01137a>

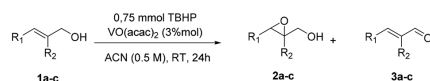
‡ These authors contributed equally to this work.

Communication

the open literature. A plausible reaction mechanism for both reactions could indicate that the coordination either of the alkene or the final alcohol functionalities to the vanadyl site dictates the final reaction (Fig. S1, ESI†).¹⁹ In order to confirm the absence of one of the acac ligands in the active species, we performed the reaction using 1 equivalent of extra acac⁻ ligand (Fig. S2a, ESI†). The low conversion obtained can be attributed to the saturated positions of the VO(acac)⁺, blocking the position of the allylic alcohol. Moreover, the acac ligand signals were observed by NMR spectroscopy in the reaction solution (Fig. S2b, ESI†). With these mechanisms in hand, electron-donating groups (EDGs) on the alkene (R) should favour coordination of the alkene to the vanadyl and epoxidation, while electron-withdrawing groups (EWG) should favour alcohol coordination and dehydrogenation.

Fig. 1 shows the results obtained for the reaction of different allyl alcohols with TBHP in the presence of VO(acac)₂, under typical reaction conditions.⁴ We observe that the product obtained for allyl alcohol **1a** with an aliphatic substituent is epoxide **2a**. On the contrary, the major product for allyl alcohol **1b** with an aromatic substituent is aldehyde **3b** (Fig. 1). Interestingly, when an additional CH₃ group substituent is present in the allylic alcohol, the selectivity of **1c** reverts back to the epoxidation product **2c**, though in very low yield (Fig. 1). Blank experiments for compound **1b**, without catalyst and with **4**, showed reaction conversions below 8 and 15%, respectively (Table S1, ESI†).

With the aim to rationalize these results, we have evaluated the activation energy for both reactions in substrates containing either an aliphatic (EDG) or aromatic (EWG) substituent (Fig. S3–S5, ESI† for complete calculations). We obtained that the epoxidation was favoured by almost 60 kJ mol⁻¹ with respect to the dehydrogenation for 2-hexenol (**1a**) (Fig. S3a and S4, ESI†), 28.9 and 88.6 kJ mol⁻¹, respectively. However, this was inverted for cinnamyl alcohol **1b**, where the dehydrogenation showed an activation energy of 50.3 kJ mol⁻¹ while the epoxidation was less favoured (53.9 kJ mol⁻¹, Fig. S3b and S5, ESI† for complete calculations). Thus, these energetic differences explain why changing the benzene with an alkyl substituent (**1a**), or just adding a methyl substituent in the other carbon atom of the alkene (**1c**), the reactivity can be reversed so easily from the dehydrogenation to the epoxidation.



	R ¹	R ²	Conversion %	Selectivity 2 %	Selectivity 3 %
1a	Propyl	H	90.3	97.9	2.1
1b	Ph	H	87.7	22.9	77.1
1c	Ph	Me	8.6	51.3	48.7

Fig. 1 Reaction scheme for allylic alcohol epoxidation/dehydrogenation of aliphatic **1a**, aromatic **1b**, and both aliphatic and aromatic allylic alcohol **1c**. ACN: acetonitrile.

Considering these findings, we have extended our study to different starting materials with modulated electronics of substituents (Fig. S6, ESI†), where we further confirm the observed trend. Thus, with these results in hand, it seems that the epoxidation vs. dehydrogenation reaction of allyl alcohols catalysed by VO(acac)₂, in solution, is natively controlled by the substrate, which leaves little room for improvement.

Heterogenization of the metal Schiff base catalyst has attracted great interest in recent years,²⁰ which is mostly used to improve the performance of hydrogen peroxide as an oxidant for alkene epoxidation.^{21,22} Among them, expanded research has been performed on vanadium Schiff base complexes, owing to their amazing structural features and catalytic purpose.²³ However, as far as we know, despite the interest, the ultimate catalyst after VO(acac)₂ heterogenization in MOFs has not been atomically precisely well-characterised, which limits the knowledge of the real active catalyst and difficulty of the rationalization of structure property relationships.²⁴

In this work, we report the postsynthetic²⁵ insertion of the vanadyl acetylacetonate complex VO(acac)₂¹⁸ within the preformed MOF **4**^{16,17} (Fig. 2). **4** presents functional hexagonal channels decorated by the highly flexible ethylenethiomethyl chains of the methionine amino acid (Fig. 2a), which are prone for high loading of vanadyl complexes. This results in a homogenous distribution of them along the pores, anchored to these functional thioalkyl groups, as confirmed by SC-XRD, to lead to [V^{VO}O(acac)(H₂O)]@{Ca^{II}Cu^{II}₆[(S,S)-methox]₃(OH)₃·8H₂O} (VO(acac)(H₂O)@**4**). Compound VO(acac)(H₂O)@**4** was synthesised by soaking crystals of **4** in an acetonitrile solution of the VO(acac)₂ complex for three days in the open air (see the Experimental Section, ESI†). This insertion process was followed through inductively coupled plasma mass spectrometry (ICP-MS) and scanning electron microscopy–energy dispersive X-ray spectroscopy (SEM–EDX) (Table S2, ESI†).

VO(acac)(H₂O)@**4** was crystallized in the chiral P6₃ space group of the hexagonal system (Table S3, ESI†) like the precursor **4** (Fig. 2). The crystal structure of VO(acac)(H₂O)@**4** allowed the confirmation of the presence of VO(acac)(H₂O)⁺ moieties, which is recognized by the flexible²⁶ thioether arms of the methionine residues and confined into the channels through S··vanadyl interactions (Fig. 2b–d). In this complex, vanadium is penta-coordinated (Fig. 2d), linked by one acac ligand, a terminal solvent molecule and being grasped by a sulfur atom from methionine amino acid residues (Fig. S6–S10, ESI†). The vanadium environment is highly distorted, resembling a trigonal bipyramidal geometry with a very bent apical position occupied by water molecules. This is likely because of the steric constraints imposed by the network (Fig. S9, ESI†). The values of VO–acac bond lengths [2.00(3) and 2.01(3) Å] are in agreement with previously reported ones.²⁷ On the contrary, the vanadium···S [2.83(10) Å] and vanadyl···O_{water} [2.69(14) Å] bond distances are longer than those reported so far.^{28,29} A second water molecule resides close to the VO(acac)(H₂O) moiety at a distance of 2.96(3) Å, longer than expected, but still lower than the sum of van der Waals radii (Fig. S10, ESI†).

Complementary to the above-described structural characterization, the chemical nature of the final host–guest adsorbate

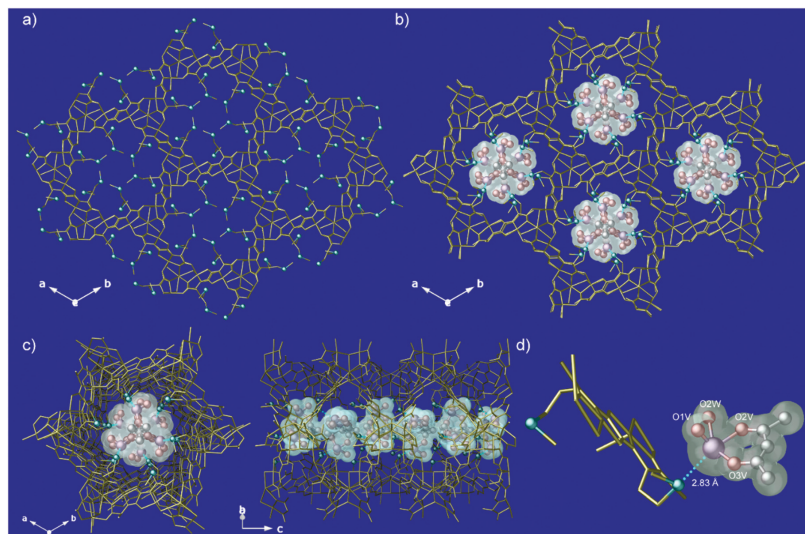


Fig. 2 Views of the 3D open-framework of **4** (a) and **VO(acac)(H₂O)@4** (b) along the *c*-axis (crystallization water molecules are omitted for clarity). The 3D network is depicted as gold sticks, with the only exception of sulphur atoms, which are represented as blue spheres. For the guest **VO(acac)(H₂O)⁺** species hosted in the channels (b), vanadium, carbon and oxygen atoms are represented as purple, grey and red spheres, respectively. Surfaces are used to highlight these guest species. (c) Top (left) and side (right) perspective views of a single channel of **VO(acac)(H₂O)@4**. (d) Fragment of **VO(acac)(H₂O)@4** emphasising the host-guest interactions. Dashed blue lines represent the S...V interaction.

VO(acac)(H₂O)@4 was also determined by different characterization techniques. The atom composition was established by elemental (C, H, S, N) analysis, SEM-EDX and ICP-MS (ESI[†]). The integrity of the framework and solvent contents were assessed using powder X-ray diffraction (PXRD) and thermogravimetric (TG) analyses (Fig. S12 and S13, ESI[†]). The oxidation state of vanadium atoms was definitively established by XPS (Fig. S14, ESI[†]). The N₂ adsorption isotherm at 77 K revealed the permanent microporosity of **VO(acac)(H₂O)@4** (Fig. S15, ESI[†]).

The XPS spectra of **VO(acac)(H₂O)@4** and **VO(acac)₂** (Fig. S14, ESI[†]) showed identical binding energy (BE) of 516.6 eV (V 2p_{3/2} line) in both cases, which confirms the V(IV)-valence state in **VO(acac)(H₂O)@4**, as previously reported.³⁰ This can be extended to V 2p_{1/2} and O 1s bands (Fig. S14, ESI[†]), exhibiting similar BEs, further confirming the proposed oxidation state (IV).

VO(acac)(H₂O)@4 can be seen as a pre-activated catalyst, which has already released the unnecessary acac⁻ ligands, but it is influenced by the constraints of the MOF channels. Thus, it could be expected that the less sterically demanding dehydrogenation reaction takes place preferentially. Indeed, Fig. 3 shows an increase in the selectivity towards the dehydrogenation of allyl alcohols not only with EWG substituents (products **3b** and **3f**) but also with EDGs (products **3a** and **3e**). Thus, it can be said that the MOF structure allows control of the chemoselectivity of the reaction beyond the native structure of the reactant allyl alcohol toward the

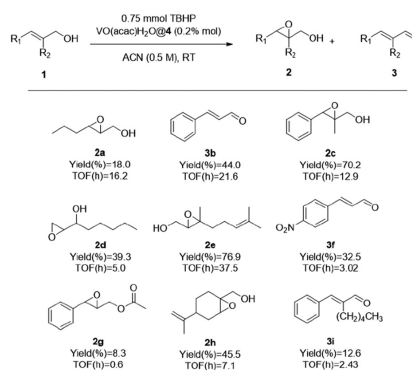


Fig. 3 Scope of the reaction using **VO(acac)(H₂O)@4** as a catalyst.

dehydrogenation product. This selectivity is not total, and some substrate-control persists, and, for instance, the methyl substituent in **1c** is still enough to increase the selectivity towards the epoxide. But, when the substituent is larger (**1h**), the EWG benzene is sufficient to reverse the selectivity to the dehydrogenation

Communication

(see Fig. S16, ESI† for comparison between VO(acac)₂ and VO(acac)(H₂O)@4). The better reactivity of **1c** and **1g** with VO(acac)(H₂O)@4 may be explained by any sort of favoured π -interaction between the aromatic part of the substrates and the catalytic site within the MOF channels. However, compounds **1b** and **1f** do not react so efficiently. Thus, it is difficult at this point to explain the different reactivity based on selective adsorptions on the catalytic site.

No leaching processes were observed during the reaction (Fig. S17, ESI†). VO(acac)(H₂O)@4 could be reused up to seven times for the epoxidation of **1c** without depletion in the final yield while retaining the crystallinity as PXRD supported (Fig. S12c, ESI†). The presence of the active species within the MOF and the stability of VO(acac)(H₂O)@4 during the reaction were screened by FT-IR spectroscopy (Fig. S18 and S19, ESI†). We observed oxidation of the sulphur groups when the reaction proceeds in low yields. New peaks appear at 1207 and 1440 cm⁻¹ for **1i**, corresponding to S=O bands, while the intensity of these new peaks is very low for **1h**, maintaining also the peaks of the original **5** at 1287 and 1370 cm⁻¹. Moreover, when we just impregnated a solution of VO(acac)₂ either in neat **4** or in a second isostructural MOF with hydroxyl-residues decorating the channels instead of the thioether-arms ((Ca^{II}-Cu^{II}[(S,S)-serimox]₃(OH)₂(H₂O))₃·39H₂O (**5**), where serimox = (S,S)-oxaloyl-bis(N-serineninate))³¹ we also observed high catalytic activities (Fig. S20, ESI†). However, the vanadyl active species leached out from the structure (Fig. S21, ESI†), the material only being active for 2 uses. Even when the VO(acac)₂ was impregnated on SiO₂, we could observe the leaching of the active species (Fig. S22, ESI†). These results confirm the requisite of encapsulating, not impregnating, the VO(acac)₂ inside **4** for obtaining a robust solid catalyst.

Overall, we have observed that in the homogenous phase (VO(acac)₂/TBHP), the selectivity of allylic alcohols towards the epoxidation or dehydrogenation reactions is subtly controlled by the substituents around the allylic alcohol functionalities. A MOF encapsulating VO(acac)(H₂O) species has been synthesized and atomically resolved by SC-XRD. VO(acac)(H₂O)@4 as a heterogeneous catalyst, taking advantage of the steric constraints induced by the solid network on the catalyst, allows gaining some control of the chemoselectivity in the reaction toward the dehydrogenation product.³² These studies are representative of the change in reactivity imparted by a well-defined structured solid in organometallic catalysts and expand the study of vanadium catalysts within MOF channels.^{33,34}

We acknowledge MCIN (PID2019-104778GB-I00, PID2020-115100GB-I00 and CEX2019-000919-M), the Generalitat Valenciana (SEJU/2020/034 and PROMETEO/2021/054), the Ministero dell'Istruzione, dell'Università e della Ricerca, the Fondazione CARIPLO (2019-2090) and the European Research Council (814804, MOF-reactors). J. O.-M. and C. B. thank the Juan de la Cierva program (IJC2018-036514-I) and ITCQ, respectively, for contracts. J. F.-S. thanks Ramón y Cajal program (RYC2019-027940-I).

Conflicts of interest

There are no conflicts to declare.

Notes and references

- B. M. Trost and I. Fleming, *Comprehensive Organic Synthesis: Selectivity, Strategy, and Efficiency in Modern Organic Chemistry*, Pergamon Press; Oxford, 7th edn, 1991.
- W. J. Mijs and C. R. H. I. de Jonge, *Organic syntheses by oxidation with metal compounds*, ed. W. J. Mijs and C. R. H. I. de Jonge, New York: Plenum Press, New York, 1986.
- T. Hirao, *Chem. Rev.*, 1997, **97**, 2707–2724.
- K. B. Sharpless and R. C. Michaelson, *J. Am. Chem. Soc.*, 1973, **95**, 6136–6137.
- S. Tanaka, H. Yamamoto, H. Nozaki, K. B. Sharpless, R. C. Michaelson and J. D. Cutting, *J. Am. Chem. Soc.*, 1974, **96**, 5234–5255.
- K. Kaneda, Y. Kawanishi, K. Jitsukawa and S. Teranishi, *Tetrahedron Lett.*, 1983, **24**, 5009–5010.
- A. Lattanzi, A. Senatore, A. Massa and A. Scettri, *J. Org. Chem.*, 2003, **68**, 3691–3694.
- H. Furukawa, K. E. Cordova, M. O'Keeffe and O. M. Yaghi, *Science*, 2013, **341**, 974.
- R. Freund, O. Zaremba, G. Arnauts, R. Ameloot, G. Skorupskii, M. Dincă, A. Bavykina, J. Gascon, A. Ejsmont, J. Goscińska, M. Kalmutzki, U. Lächelt, E. Ploetz, C. S. Diercks and S. Wuttke, *Angew. Chem., Int. Ed.*, 2021, **60**, 23975–24001.
- S. Kitagawa and R. Matsuda, *Coord. Chem. Rev.*, 2007, **251**, 2490–2509.
- R. J. Young, M. T. Hudley, E. Pardo, N. R. Champness, C. J. Sumbly and C. J. Doonan, *Chem. Sci.*, 2020, **11**, 4031–4050.
- D. Yang and B. C. Gates, *ACS Catal.*, 2019, **9**, 1779–1798.
- M. Viciano-Chumillas, M. Mon, J. Ferrando-Soria, A. Corma, A. Leyva-Pérez, D. Armentano and E. Pardo, *Acc. Chem. Res.*, 2020, **53**, 520–531.
- R. Adam, M. Mon, R. Greco, L. H. G. Kalinke, A. Vidal-Moya, A. Fernandez, R. E. P. Winpenney, A. Doménech-Carbó, A. Leyva-Pérez, D. Armentano, E. Pardo and J. Ferrando-Soria, *J. Am. Chem. Soc.*, 2019, **141**, 10350–10360.
- F. R. Fortea-Pérez, M. Mon, J. Ferrando-Soria, M. Boronat, A. Leyva-Pérez, A. Corma, J. M. Herrera, D. Osadchii, J. Gascon, D. Armentano and E. Pardo, *Nat. Mater.*, 2017, **16**, 760–766.
- M. Mon, J. Ferrando-Soria, T. Granchar, F. R. Fortea-Pérez, J. Gascon, A. Leyva-Pérez, D. Armentano and E. Pardo, *J. Am. Chem. Soc.*, 2016, **138**, 7864–7867.
- M. Mon, F. Lloret, J. Ferrando-Soria, C. Martí-Gastaldo, D. Armentano and E. Pardo, *Angew. Chem., Int. Ed.*, 2016, **55**, 11167–11172.
- A. Lattanzi and N. E. Leadbeater, *Org. Lett.*, 2002, **4**, 1519–1521.
- M. Vandichel, K. Leus, P. Van Der Voort, M. Waroquier and V. Van Speybroeck, *J. Catal.*, 2012, **294**, 1–18.
- P. Barbaro and F. Liguori, ed., *Heterogenized Homogeneous Catalysts for Fine Chemicals Production*, Springer; Netherlands, 1st edn, 2010.
- X. Wang, S. Wu, Z. Li, X. Yang, H. Su, J. Hu, Q. Huo, J. Guan and Q. Kan, *Microporous Mesoporous Mater.*, 2016, **221**, 58–66.
- Y. Yang, J. Guan, P. Qiu and Q. Kan, *Appl. Surf. Sci.*, 2010, **256**, 3346–3351.
- S. Rayati, N. Torabi, A. Ghaemi, S. Mohebbi, A. Wojtczak and A. Kozakiewicz, *Inorg. Chim. Acta*, 2008, **361**, 1239–1245.
- S. Jeoung, S. Kim, M. Kim and H. R. Moon, *Coord. Chem. Rev.*, 2020, **420**, 213377.
- S. M. Cohen, *Chem. Rev.*, 2012, **112**, 970–1000.
- D. Bradshaw, J. B. Claridge, E. J. Cussen, T. J. Prior and M. J. Rosseinsky, *Acc. Chem. Res.*, 2005, **38**, 273–282.
- M. Mikuriya, T. Kotera, F. Adachi and S. Bandow, *Chem. Lett.*, 1993, 945–948.
- R. M. Jenkins, T. A. Pinder, M. L. Hatley, J. H. Reibenspies and M. Y. Darensbourg, *Inorg. Chem.*, 2011, **50**, 1849–1855.
- K. Saatchi, K. H. Thompson, B. O. Patrick, M. Pink, V. G. Yuen, J. H. McNeill and C. Orvig, *Inorg. Chem.*, 2005, **44**, 2689–2697.
- T. A. Ageeva, D. V. Golubev, A. S. Gorshkova, A. M. Ionov, E. V. Kopylova, O. I. Koifman, R. N. Mozhschil, E. P. Rozhkova, V. D. Rumyantseva, A. S. Sigov and V. V. Fomichev, *Macrocyclics*, 2019, **12**, 148–153.
- M. Mon, R. Bruno, J. Ferrando-Soria, L. Bartella, L. Di Donna, M. Talia, R. Lappano, M. Maggolini, D. Armentano and E. Pardo, *Mater. Horiz.*, 2018, **5**, 683–690.
- For GC-MS of some products, see Fig. S23 (ESI†).
- K. Otake, Y. Cui, C. T. Buro, Z. Li, J. T. Hupp and O. K. Farha, *J. Am. Chem. Soc.*, 2018, **140**, 8652–8656.
- M. J. Ingleson, J. Perez Barrios, J.-B. Guibaud, Y. Z. Khimyak and M. J. Rosseinsky, *Chem. Commun.*, 2008, 2680–2682.

Electronic Supplementary Material (ESI) for ChemComm.
This journal is © The Royal Society of Chemistry 2022

ELECTRONIC SUPPLEMENTARY INFORMATION

Epoxidation vs. dehydrogenation of allylic alcohols: Heterogenization of the VO(acac)₂ catalyst in a metal-organic framework

Cristina Negro,^{‡a} Cristina Bilanin,^{‡b} Xiaoni Qu,^{ac} Judit Oliver-Meseguer,^{*b} Jesús Ferrando-Soria,^{*a} Antonio Leyva-Pérez,^{*b} Donatella Armentano^{*d} and Emilio Pardo^a

^a *Instituto de Ciencia Molecular (ICMol), Universidad de Valencia, 46980 Paterna, Valencia, Spain*

^b *Instituto de Tecnología Química, Universitat Politècnica de València – Consejo Superior de Investigaciones Científicas, Av .de los Naranjos, s/n, 46022 Valencia, Spain*

^c *College of Chemistry and Materials Science, Northwest University, Xi'an 710069, China*

^d *Dipartimento di Chimica e Tecnologie Chimiche, Università della Calabria, 87036, Cosenza, Italy*

Corresponding authors: joliverm@itq.upv.es, jesus.ferrando@uv.es anleyva@itq.upv.es, donatella.armentano@unical.it

Phone: +34963877812; Fax: +349638 77809.

TABLE OF CONTENTS:

- Experimental section:	S3
o General	S3
o Physical characterization techniques	S3
o Procedures for the synthesis of MOFs	S4
o Reaction procedures	S5
o Compounds characterization	S5
o X-Ray crystallographic section	S7
- Tables S1-S3	S10
- Figs. S1-S23	S13
- References	S36

Experimental Section.

General.

Reagents were obtained from commercial sources and used without further purification unless otherwise indicated. Anhydrous solvents were obtained from a resin-exchanger apparatus. Reactions were performed in conventional round-bottomed flasks or sealed vials equipped with a magnetic stirrer. All the products were characterized by gas chromatography-mass spectrometry (GC-MS), proton (^1H), carbon (^{13}C) and distortionless enhancement by polarization transfer (DEPT) nuclear magnetic resonance (NMR) spectroscopy. Gas chromatographic analyses were performed in an instrument equipped with a 25 m capillary column of 1 % phenylmethylsilicone using *n*-dodecane as an external standard. GC/MS analyses were performed on a spectrometer equipped with the same column as the GC and operated under the same conditions. ^1H -, ^{13}C and DEPT were recorded in a 300 MHz (or 400 MHz when available) instrument using CD_3CN as solvent unless otherwise indicated, containing TMS as internal standard. Infrared (IR) spectra of the compounds were recorded with a spectrophotometer by impregnating the windows with a dichloromethane solution of the compound and leaving evaporate before analysis. $\{\text{Ca}^{\text{II}}\text{Cu}^{\text{II}}_6[(S,S)\text{-methox}]_3(\text{OH})_2(\text{H}_2\text{O})\} \cdot 16\text{H}_2\text{O}$ (**4**) and $\{\text{Ca}^{\text{II}}\text{Cu}^{\text{II}}_6[(S,S)\text{-serimox}]_3(\text{OH})_2(\text{H}_2\text{O})\} \cdot 39\text{H}_2\text{O}$ (**5**) were prepared as earlier reported.^{1,2}

Elemental (C, H, S, N), and ICP-MS analyses were performed at the Microanalytical Service of the Universitat de València. FT-IR spectra were recorded on a Perkin-Elmer 882 spectrophotometer as KBr pellets. The thermogravimetric analysis was performed on crystalline samples under a dry N_2 atmosphere with a Mettler Toledo TGA/STDA 851° thermobalance operating at a heating rate of $10\text{ }^\circ\text{C min}^{-1}$.

Gas adsorption

The N_2 adsorption-desorption isotherms at 77 K, were carried out, on polycrystalline samples of **4** and **VO(acac)(H₂O)@4**, with a BELSORP-mini-X instrument. Samples were first activated with methanol and then evacuated at 348 K during 19 hours under 10^{-6} Torr prior to their analysis.

Microscopy measurements

Scanning Electron Microscopy (SEM) elemental analysis was carried out for all compounds, using a HITACHI S-4800 electron microscope coupled with an Energy Dispersive X-ray (EDX) detector. Data was analyzed with QUANTAX 400.

X-ray Powder Diffraction Measurements

Polycrystalline samples of **4** and **VO(acac)(H₂O)@4** were introduced into 0.5 mm borosilicate capillaries prior to being mounted and aligned on a Emyrean PANalytical powder diffractometer, using Cu K α radiation ($\lambda = 1.54056 \text{ \AA}$). For each sample, five repeated measurements were collected at room temperature ($2\theta = 2\text{--}60^\circ$) and merged in a single diffractogram. A polycrystalline sample of **VO(acac)(H₂O)@4** was also measured after catalysis following the same procedure.

X-ray photoelectron spectroscopy (XPS) measurements

Samples of VO(acac)₂ and **VO(acac)(H₂O)@4** were prepared by sticking, without sieving, the samples onto a molybdenum plate with scotch tape film, followed by air drying. Measurements were performed on a K-Alpha™ X-ray Photoelectron Spectrometer (XPS) System using a monochromatic Al K(alpha) source (1486.6 eV). As an internal reference for the peak positions in the XPS spectra, the C1s peak has been set at 284.8 eV.

Procedures for the synthesis of MOF catalyst.

[V^{IV}O(acac)(H₂O)]@{Ca^{II}Cu^{II}₆[(S,S)-methox]₃(OH)₃} · 8H₂O (VO(acac)(H₂O)@4): Well-formed hexagonal green prisms of **VO(acac)(H₂O)@4**, which were suitable for X-ray diffraction, were obtained by soaking crystals of **4** (5.0 mg) in a saturated acetonitrile solution of VO(acac)₂ for 72 hours. The crystals were washed with water, isolated by filtration on paper and air-dried (Table S3). Anal.: calcd for C₄₁Cu₆CaVH₇₇S₆N₆O₃₃ (1846.8): C, 26.67; H, 4.20; S, 10.42; N, 4.55%. Found: C, 26.93; H, 4.09; S, 10.36; N, 4.51%. IR (KBr): $\nu = 1613, 1605, 1591 \text{ cm}^{-1}$ (C=O). The same process can be followed, in a multigram-scale, using larger amounts of polycrystalline samples of **4**.³

Impregnation of VO(acac)₂ in **4 and **5**.**

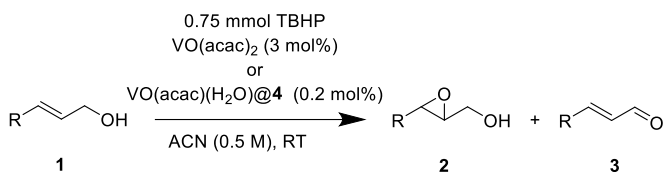
MOFs impregnation was carried out by suspending the corresponding MOF (100 mg) in a solution of 5 mL of acetonitrile with VO(acac)₂ (10 mg), in a beaker equipped with a

magnetic stirrer. After five hours, MOF is filtered, washed with acetonitrile and dried under vacuum.

Supporting VO(acac)₂ on SiO₂.

The catalyst was prepared by adding SiO₂ (530 mg), VO(acac)₂ (25.8 mg) and 50 mL of dry toluene in a round bottom flask equipped with a magnetic stirrer. This mixture was refluxed for 24 h. The material was vacuum-filtered, washed by reflux in dichloromethane (50 mL) and methanol (50 mL) and dried overnight in an oven at 120 °C. Then, the catalyst is obtained drying under vacuum. The content of vanadium obtained by ICP was 0.29%.

Reaction procedures.



The products **2** and **3** were prepared following the reaction scheme. Reagent **1** (0.5 mmol) was introduced in a sealed vial equipped with a magnetic stirrer and VO(acac)₂ (4 mg, 0.015 mmol) or VO(acac)(H₂O)@4 (2 mg) and 1 mL of acetonitrile, and allowed to react for the required time at room temperature. After reaction is complete, filtration is carried out to eliminate the catalyst, the resulting mixture is dried under vacuum and the products obtained are characterised by GC-MS, IR, and/or NMR.

Compound characterization of the major compounds.

2,3-Epoxyhexan-1-ol 2a.⁴ GC-MS (m/z, M⁺ 116), major peaks found: 116, 71, 55, 43, 29. ¹H NMR (CDCl₃, 300 Hz) δ 0.95 (t, 3H, J = 7.2 Hz), 1.56-1.42 (m, 4H), 2.67-2.91 (m, 2H), 3.61 (dd, 1H, J = 12.6, 2.4 Hz), 3.91 (dd, 1H, J = 12.6, 2.4 Hz). ¹³C NMR (CDCl₃, 75 Hz) 13.9 (CH₃), 19.2 (CH₂), 33.5 (CH₂), 56.0 (CH), 58.5 (CH), 61.7 (CH₂).

Cinnamyl alcohol epoxide 2b.⁵ GC-MS (m/z, M⁺ 150), major peaks found: 150, 148, 132, 117, 105, 91, 77, 63, 51, 28. ¹H NMR (CD₃CN, 400 Hz) δ 7.73-7.34 (m, 5 H, Ph),

3.96 (m, 1H), 3.58-3.54 (m, 3H). ^{13}C NMR (CD_3CN , 101 Hz) δ 55.6 (CH), 61.2 (CH), 64.1 (CH_2), 125.6 (CH), 128.2 (CH), 128.4 (CH), 135.4 (C).

(*2-Methyl-3-phenyloxiran-2-yl*)methanol **2c**.⁶ GC-MS (m/z , $\text{M}^{+\bullet}$ 164), major peaks found: 164, 145, 131, 117, 107, 90, 79, 63, 51, 39, 29. ^1H NMR (CDCl_3 , 400 Hz) δ 1.2 (s, 3H), 2.01 (d, 1H, $J = 1.6$ Hz), 3.75-3.78 (m, 2H), 7.14-7.49 (m, 5H). ^{13}C NMR (CDCl_3 , 75 Hz) δ 13.5 (CH_3), 60.5 (CH), 64.1 (C), 65.2 (CH_2), 126.4 (CH), 127.6 (CH), 128.1 (CH), 135.7 (C).

1,2-Epoxyoctan-3-ol **2d**.⁴ GC-MS (m/z , $\text{M}^{+\bullet}$ 144), major peaks found: 144, 131, 116, 101, 83, 71, 55, 43, 29. ^1H NMR (CD_3CN , 300 Hz) δ 0.89 (t, 3H, $J = 6.6$ Hz), 1.17-1.30 (m, 8H), 2.31 (m, 1H), 2.48 (m, 1H), 2.71 (m, 1H), 3.80 (m, 1H). ^{13}C NMR (CD_3CN , 75 Hz) 73.1 (CH), 54.6 (CH), 43.5 (CH_2), 34.3 (CH_2), 31.8 (CH_2), 24.9 (CH_2), 22.5 (CH_2), 13.9 (CH_3).

2,3-Epoxygeraniol **2e**.⁷ GC-MS (m/z , $\text{M}^{+\bullet}$ 170), major peaks found: 170, 168, 152, 139, 121, 109, 95, 82, 69, 55, 41, 27. ^1H NMR (CD_3CN , 101 Hz) δ 1.38 (s, 3H), 1.26-1.32 (m, 2H), 1.43-1.50 (m, 2H), 1.60 (s, 3H), 1.68 (d, 3H, $J = 1.2$ Hz), 2.99 (dd, 1H, $J = 6.9, 4.5$ Hz), 3.66-3.84 (2H, m), 5.08 (m, 1H). ^{13}C NMR (CD_3CN , 75 Hz) δ 16.9 (CH_3), 17.8 (CH_3), 23.8 (CH_2), 25.8 (CH_3), 38.6 (CH_2), 61.3 (C), 61.6 (CH_2), 63.0 (CH), 123.5 (CH), 132.3 (C).

3-Phenyloxiranylmethyl acetate **2g**.⁸ GC-MS (m/z , $[\text{M}^{\bullet} - \text{H}]$ 191), major peaks found: 191, 176, 164, 149, 131, 123, 107, 91, 77, 43. ^1H NMR (CD_3CN , 400 Hz) δ 2.09 (s, 3H), 3.27-3.30 (m, 1H), 3.85 (d, 1H, $J = 2.0$ Hz), 4.00 (dd, 1H, $J = 6.4, 12.4$ Hz), 4.48 (dd, 1H, $J = 2.8, 12.4$ Hz), 7.26-7.40 (m, 5H). ^{13}C NMR (CD_3CN , 101 Hz) 21.1 (CH_3), 56.6 (CH), 60.1 (CH), 64.9 (CH_2), 126.7 (CH), 129.6 (CH), 128.9 (CH), 137.4 (C), 171.4 (C).

(*4-(Prop-1-en-2-yl)-7-oxabicyclo[4.1.0]heptan-1-yl*)methanol **2h**.⁹ GC-MS (m/z , $\text{M}^{+\bullet}$ 168), major peaks found: 168, 150, 137, 125, 109, 93, 79, 67, 55, 41. ^1H NMR (CD_3CN , 400 Hz) δ 1.10-1.30 (m, 3H), 1.55-1.80 (m, 4H), 1.71 (brs, 3H), 1.93-1.99 (m, 1H), 3.17 (m, 1H), 3.45 (m, 1H), 4.68-4.72 (m, 2H). ^{13}C NMR (CD_3CN , 101 Hz) 21.1 (CH_3), 25.4 (CH_2), 26.9 (CH_2), 29.5 (CH_2), 37.9 (CH), 57.9 (CH), 66.2 (CH_2), 68.9 (C), 109.5 (CH_2), 150.3 (C).

*Cinnamaldehyde 3b.*¹⁰ GC-MS (m/z, [M⁺-H] 131), major peaks found: 131.2, 103, 77, 51, 28. ¹H NMR (CD₃CN, 400 Hz) δ 7.20-7.46 (m, 7H), 9.93 (s, 1H). ¹³C NMR (CD₃CN, 101 Hz) δ 125.6(CH), 128.0 (CH), 128.2 (CH), 128.4 (CH), 135.4 (C), 150.1 (CH), 195.8 (CH).

*2-Methyl-3-phenylacrylaldehyde 3c.*¹¹ GC-MS (m/z, M⁺-H] 145), major peaks found: 145, 131, 115, 103, 91, 78, 63, 51, 39, 29. ¹H NMR (CDCl₃, 400 Hz) δ 1.96 (d, 3H, *J* = 1.6 Hz), 7.14-7.49 (m, 6H), 9.46 (s, 1H). ¹³C NMR (CDCl₃, 75 Hz) δ 13.5 (CH₃), 126.4 (CH), 127.6 (CH), 128.1 (CH), 135.7 (C), 138.3 (C), 150.1 (CH), 195.4 (CH).

*4-Nitro-cinnamaldehyde 3f.*¹⁰ GC-MS (m/z, M⁺ 177), major peaks found: 177, 160, 147, 130, 118, 102, 91, 77, 63, 51. ¹H NMR (CD₃CN, 400 Hz) δ 6.85 (dd, 1H, *J* = 7.6, 16.0 Hz), 7.61 (d, 2H, *J* = 8.8 Hz), 7.70 (d, 1H, *J* = 16.0 Hz), 8.27 (d, 2H, *J* = 8.8 Hz), 9.73 (d, 1H, *J* = 7.6 Hz). ¹³C NMR (CD₃CN, 75 Hz) δ 123.9 (CH), 124.3 (CH), 129.0 (CH), 130.5 (CH), 131.3 (CH), 147.9 (CH), 190.3 (CH).

*4-(Prop-1-en-yl)cyclohex-1-ene-1-carbaldehyde 3h.*¹² GC-MS (m/z, M⁺ 150), major peaks found: 150, 137., 121, 107, 93, 79, 67, 55, 41.

*(E)-2-benzylideneheptanal 3i.*¹³ GC-MS (m/z, [M⁺ -H] 201), major peaks found: 201, 189, 171, 159, 145, 131, 115, 107, 91, 79, 57, 41.

X-ray crystallographic data collection and structure refinement.

Crystal of **VO(acac)(H₂O)@4** with 0.14 x 0.12 x 0.12 mm as dimensions was selected and mounted on a MiTeGen MicroMount in Paratone oil and very quickly placed on a liquid nitrogen stream cooled at 90 K, to avoid the possible degradation upon dehydration or exposure to air. Diffraction data were collected on a Bruker-Nonius X8APEXII CCD area detector diffractometer using graphite-monochromated Mo-K α radiation (λ = 0.71073 Å), The data were processed through SAINT¹⁴ reduction and SADABS¹⁵ multi-scan absorption software. The structure was solved with the SHELXS structure solution program, using the Patterson method. The model was refined with version 2018/3 of SHELXL against *F*² on all data by full-matrix least squares.¹⁶

As reported in the main text, the robustness of the 3D network, allowed the resolution of the crystal structure of **VO(acac)(H₂O)@4** adsorbates, being their crystals suitable for X-ray diffraction, even over one-step process of crystal-to-crystal transformation. Indeed, as previously reported, compound **VO(acac)(H₂O)@4** was synthesised by soaking crystals of precursor **4** in an acetonitrile solution of the [VO(acac)₂] complex during three days in open air. After that, it is reasonable to observe a diffraction pattern sometimes affected by expected internal imperfections of the crystals and thus a quite expected difficulty to perform a perfect correction of anisotropy, mainly affected by highly flexible, and thus disordered, thioether chains as terminal moiety (*vide infra*).

In the refinement, all non-hydrogen atoms of the MOF net, except the highly thermal disordered diethyl thioether chains from the methox ligand, and encapsulated vanadyl compound atoms, were refined anisotropically. The use of some C-C and C-S bond lengths restrains as well as vanadium-oxygen distance restrains, during the refinement, has been reasonable imposed and related to extraordinary flexibility of diethyl thioether chains from the methionine residues, which are dynamic components of the frameworks. In the refinement of crystal structures some further restrains, to make the refinement more efficient, have been applied, for instance ADP components have been restrained to be similar to other related atoms, using SIMU 0.04 for disordered sections or EADP for group of atoms expected to have essentially similar ADPs. In particular, acac⁻ ligand exhibits statistical as well (see Fig. S7). Disordered sites for atoms C1V, C3V and C4V in refinement, belonging to the acetylacetonate ligand, reside in special positions resulting statistically disordered for symmetry reason. All the hydrogen atoms of the net were set in calculated position and refined isotropically using the riding model.

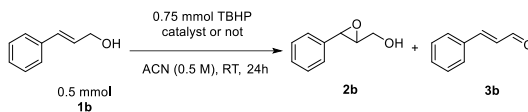
The occupancy factors of vanadium atoms have been defined in agreement with SEM and ICP–MS results (Table S2). The high thermal factors are likely related to the porosity of the net hosting vanadyl acetylacetonate complexes within very large pores.

The solvent molecules, as normally observed for such porous crystals, were highly disordered and only few of them were found from the ΔF map. The quite large channels featured by this series of MOFs likely account for that.

A summary of the crystallographic data and structure refinement for **VO(acac)(H₂O)₄** crystal structure is given in Table S3. The comments for the alerts A and B are described in the CIF using the validation reply form (vrf). CCDC reference number is 2122007.

The final geometrical calculations on free voids and the graphical manipulations were carried out with PLATON¹⁷ implemented in WinGX,¹⁸ and CRYSTAL MAKER¹⁹ programs, respectively.

Table S1. Blank experiments for cinnamyl alcohol epoxidation and dehydrogenation reactions, comparing homogeneous and heterogeneous catalysts. ACN: acetonitrile.



Entry	Catalyst	Conv% 1	Sel% 2	Sel% 3
1	None	7.3	19.5	80.5
2	VO(acac) ₂	87.7	22.9	77.1
3	4 ^a	15.3	26.1	73.9
4	VO(acac)(H ₂ O)@4 ^a	46.5	5.3	94.7

^a 48 h reaction time.

Table S2. Selected data from the ICP-MS^a and SEM/EDX^b analyses for VO(acac)(H₂O)@4 and VO(acac)₂ impregnated in MOFs 4 and 5.

VO(acac)(H ₂ O)@4				
Metal	% mass ^a	Metal stoichiometry ^a	% mass ^b	Metal stoichiometry ^b
Cu	20.65	6.00	20.62	5.99
Ca	2.13	0.98	2.24	1.03
V	2.79	1.01	2.73	0.99

VO(acac) ₂ impregnated in 4				
Metal	% mass ^a	Metal stoichiometry ^a	% mass ^b	Metal stoichiometry ^b
Cu	20.58	5.98	20.68	6.01
Ca	2.15	0.99	2.21	1.02
V	0.68	0.25	0.72	0.26

VO(acac) ₂ impregnated in 5				
Metal	% mass ^a	Metal stoichiometry ^a	% mass ^b	Metal stoichiometry ^b
Cu	17.40	6.00	17.31	5.97
Ca	1.92	1.05	1.83	1.00
V	0.84	0.36	0.82	0.35

Solid samples were digested with 0.5 mL of HNO₃ 69% at 60°C for 4 hours followed by the addition of 0.5 mL of HCl 37% and digestion 80°C for 1 hour. Metal stoichiometric is given according to formula unit.

Table S3. Summary of crystallographic data for **VO(acac)(H₂O)@4**

Compound	VO(acac)(H₂O)@4
Formula	C ₄₁ H ₇₇ CaCu ₆ N ₆ O ₃₃ S ₆ V
<i>M</i> (g mol ⁻¹)	1846.70
<i>λ</i> (Å)	0.71073
Crystal system	hexagonal
Space group	<i>P</i> 6 ₃
<i>a</i> (Å)	17.8884(17)
<i>c</i> (Å)	12.8853(13)
<i>V</i> (Å ³)	3570.8(8)
<i>Z</i>	2
<i>ρ</i> _{calc} (g cm ⁻³)	1.718
<i>μ</i> (mm ⁻¹)	2.211
<i>T</i> (K)	90
<i>θ</i> range for data collection (°)	2.277 to 26.175
Completeness to <i>θ</i> = 25.0	100%
Measured reflections	41658
Unique reflections (Rint)	4766 (0.0762)
Observed reflections [<i>I</i> > 2σ(<i>I</i>)]	2967
Goof	1.029
Absolute structure parameter (Flack)	0.20(3)
<i>R</i> ^a [<i>I</i> > 2σ(<i>I</i>)] (all data)	0.0775 (0.1332)
<i>wR</i> ^b [<i>I</i> > 2σ(<i>I</i>)] (all data)	0.2076 (0.2494)
CCDC	2122007

$$^a R = \sum(|F_o| - |F_c|) / \sum |F_o|, \quad ^b wR = [\sum w(|F_o| - |F_c|)^2 / \sum w|F_o|^2]^{1/2}.$$

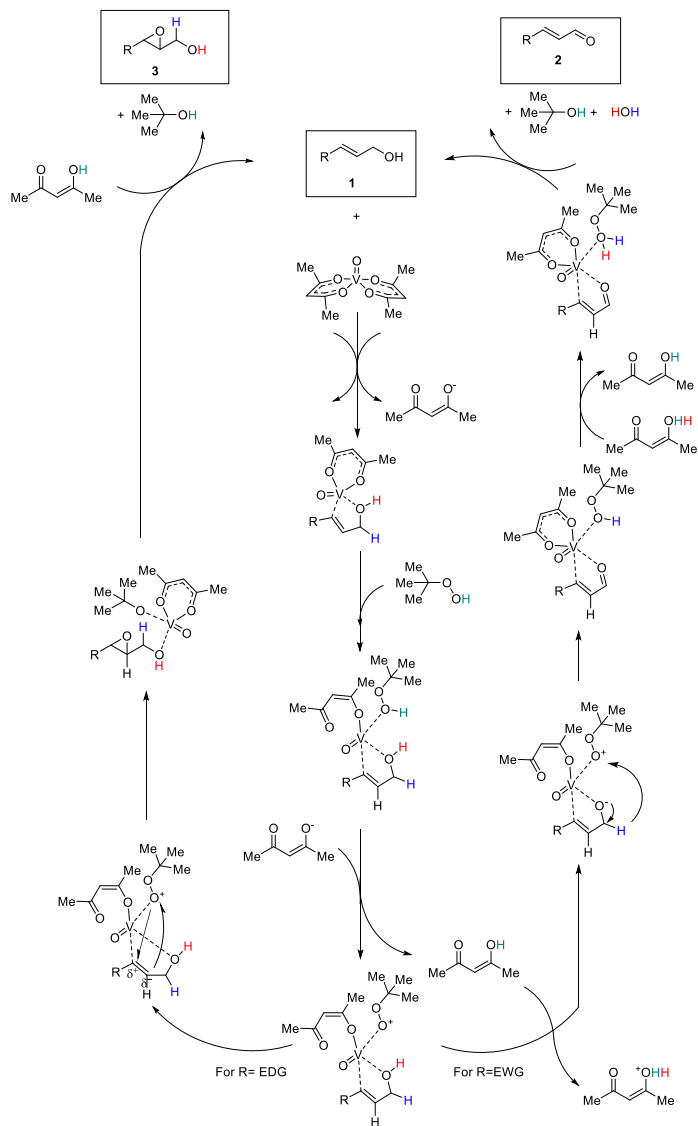
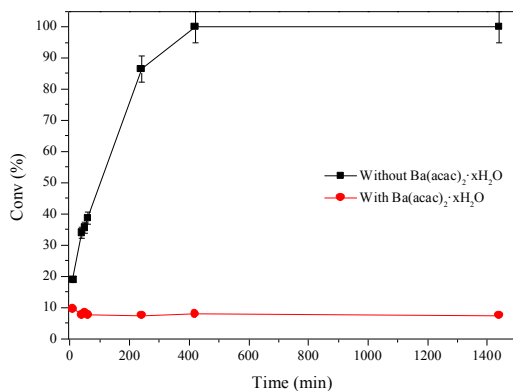


Fig. S1. Plausible reaction mechanism for allylic alcohol epoxidation and dehydrogenation catalyzed by $\text{VO}(\text{acac})_3$, and chemoselective rationalization.

a)



b)

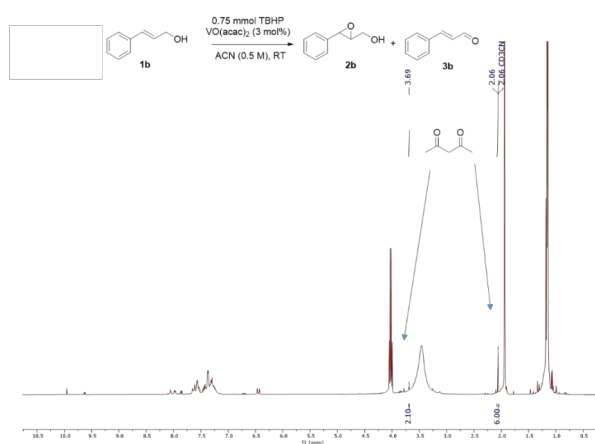


Fig. S2. (a) Kinetics for the hydrogenation of **1b** (0.5 M) with TBHP (1.2 equivalents) catalyzed by VO(acac)₂ to give **2b** and **3b** in acetonitrile at room temperature (black squares), and other in the same conditions adding Ba(acac)₂·xH₂O (1.1 equivalent) (red circles). Error bars account for a 10% uncertainty. (b) ¹H NMR of the reaction crude with the corresponding signals of the acetylacetonate ligands in solution, indicated by the arrows.

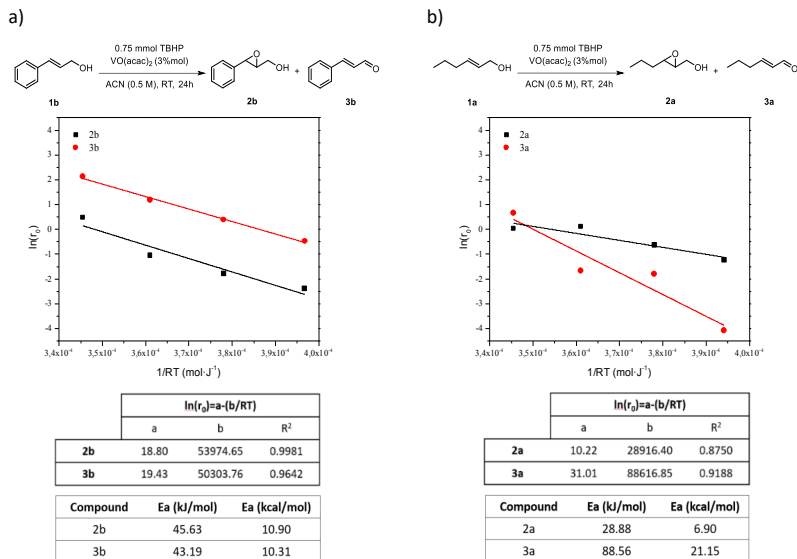
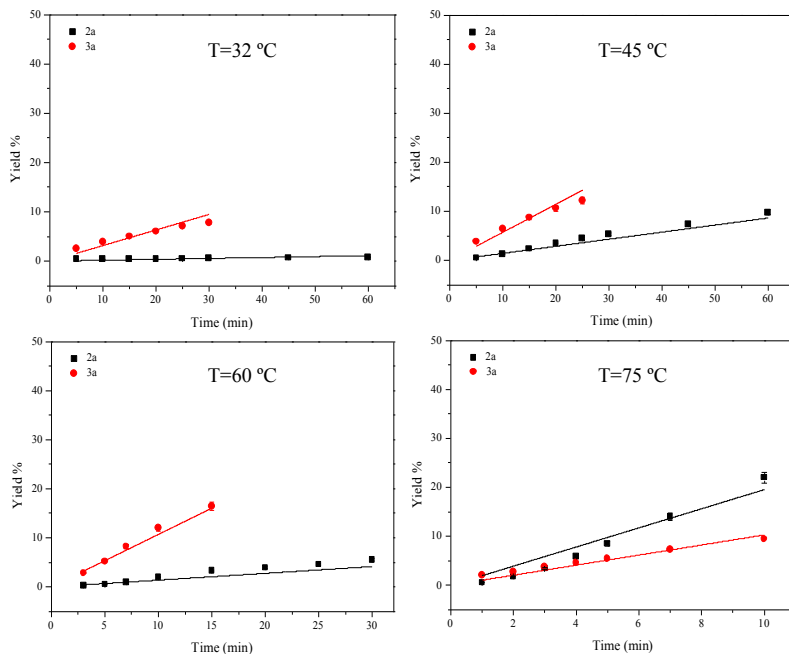
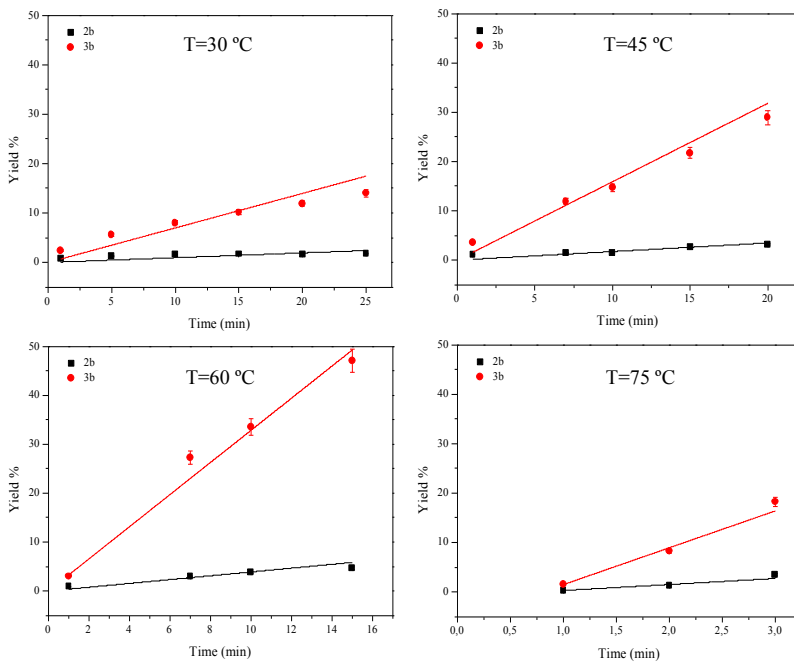


Fig. S3. Activation energies calculated for the epoxidation and dehydrogenation of cinnamyl alcohol **1b** (a) and 2-hexenol **1a** (b) under the indicated reaction conditions at different temperatures.



Temperature	Product	Yield(%)=a+b·t(min)		
		a	b	R ²
32	2a	0	0.289	0.9808
	3a	0	0.017	0.9119
45	2a	0	0.531	0.9895
	3a	0	0.166	0.9975
60	2a	0	1.122	0.9972
	3a	0	0.187	0.9921
75	2a	0	1.028	0.9854
	3a	0	1.952	0.9697

Fig. S4. Kinetic profiles to calculate the initial rates of reaction, calculated by linear regression for each temperature and measured for the alkene **1a** using VO(acac)₂ in solution.



Temperature	Product	Yield(%)=a+b·t(min)		
		a	b	R ²
30	2b	0	0.090	0.8409
	3b	0	0.618	0.9708
45	2b	0	0.166	0.9545
	3b	0	1.468	0.9955
60	2b	0	0.348	0.9798
	3b	0	3.288	0.9941
75	2b	-1.6	1.581	0.9564
	3b	-7.4	8.342	0.9870

Fig. S5. Kinetic profiles to calculate the initial rates of reaction, calculated by linear regression for each temperature and measured for the alkene **1b** using VO(acac)₂ in solution.

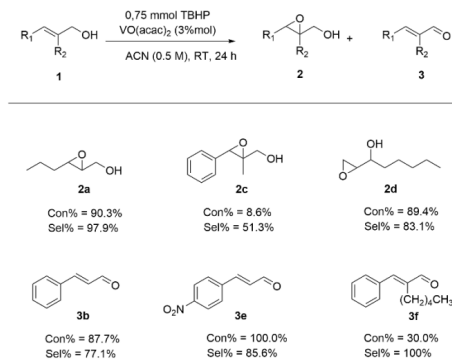


Fig. S6. Scope of reactivity for different allylic alcohols under the indicated reaction conditions. We observed epoxides were formed when the allyl alcohol possess electron donating groups on the alkene (products **2a**, **2c**, and **2d**), while aldehyde formation was favoured with electron withdrawing groups (**3b**, **3e**, and **3f**). Also, it was further validated that even a small change in the structure of the substrate is enough to favour the epoxidation, which agree with the slow difference in activation energy.

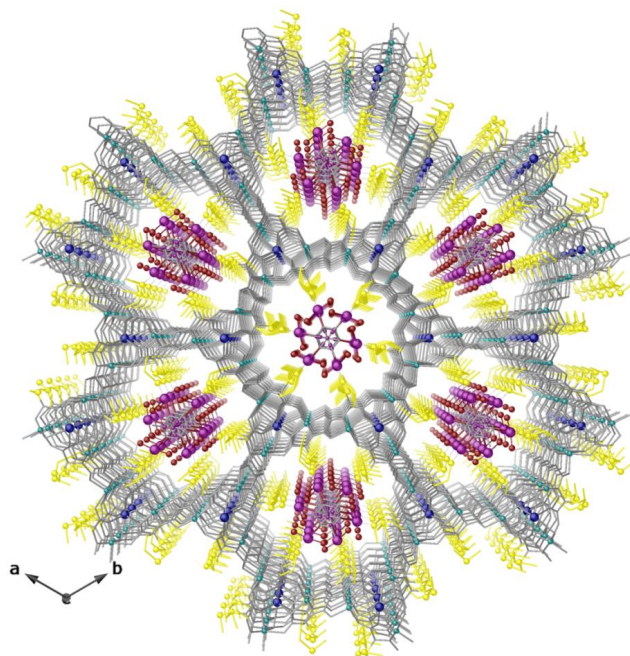


Fig. S7. Perspective view of the crystal structure of $\text{VO}(\text{acac})(\text{H}_2\text{O})^+$ @4 along c crystallographic axis, showing $\text{VO}(\text{acac})(\text{H}_2\text{O})^+$ complexes well-packed within pores of the MOF 4. The 3D network is depicted as grey sticks, with the exception of copper and calcium, depicted as cyan and blue spheres, and ethyl chain and sulphur atoms from the methionine residue, which are represented as yellow sticks (carbon) and yellow spheres (sulphur). For the guest $\text{VO}(\text{acac})(\text{H}_2\text{O})^+$ species hosted in the channels, vanadium, carbon and oxygen atoms are represented as purple, grey and red spheres, respectively. Crystallization water molecules have been omitted for the sake of clarity.

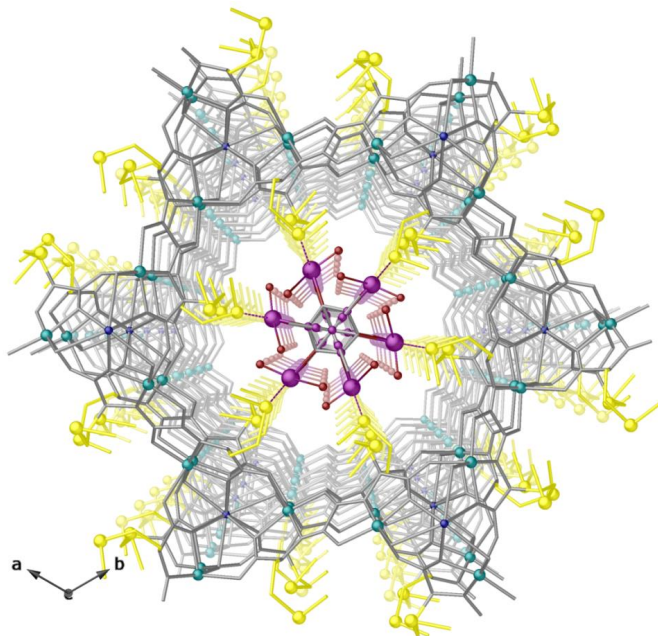


Fig. S8. Perspective details of a single pore of the crystal structure of $\text{VO}(\text{acac})(\text{H}_2\text{O})@4$ along c crystallographic axis. The 3D network is depicted as grey sticks, with the exception of copper and calcium, depicted as cyan and blue spheres, and ethyl chain and sulphur atoms from the methionine residue, which are represented as yellow sticks (carbon) and yellow spheres (sulphur). For the guest $\text{VO}(\text{acac})(\text{H}_2\text{O})^+$ species hosted in the channels, vanadium, carbon and oxygen atoms are represented as purple, grey and red spheres, respectively. Crystallization water molecules have been omitted for the sake of clarity.

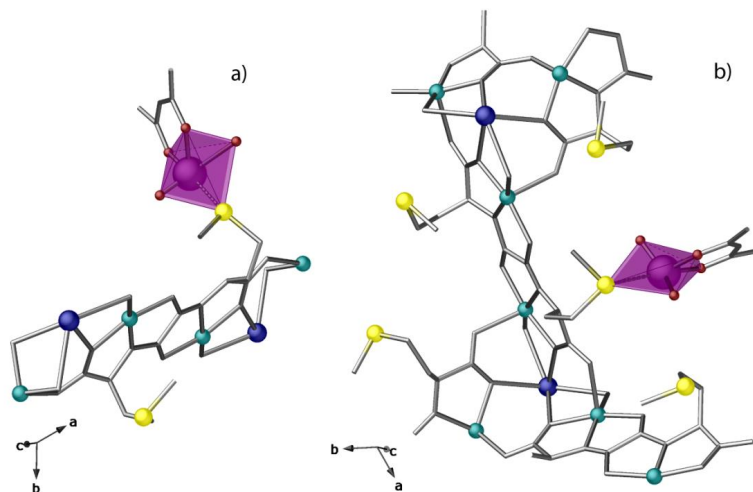


Fig. S9. Top (a) and side (b) view of fragments of $\text{VO}(\text{acac})(\text{H}_2\text{O})@4$ crystal structure highlighting the highly distorted coordination geometry around vanadium. The 3D network is depicted as grey sticks, with the exception of copper and calcium, depicted as cyan and blue spheres, and ethyl chain and sulphur atoms from the methionine residue, which are represented as yellow sticks (carbon) and yellow spheres (sulphur). For the guest $\text{VO}(\text{acac})(\text{H}_2\text{O})^+$ species hosted in the channels, vanadium, carbon and oxygen atoms are represented as purple, grey and red spheres, respectively.

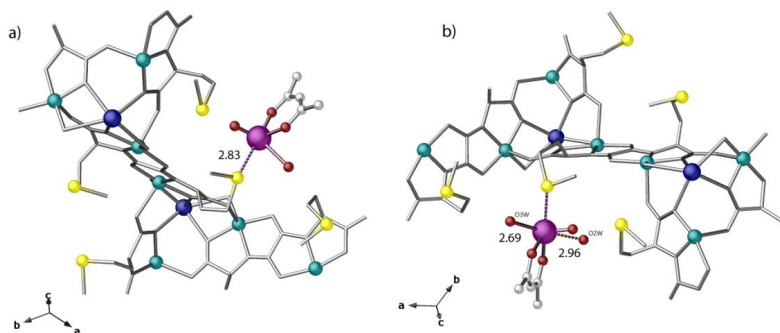


Fig. S10. Details of host-guest interactions in $\text{VO}(\text{acac})(\text{H}_2\text{O})@4$: $\text{V}\cdots\text{S}$ interaction (purple dashed line) in $\text{VO}(\text{acac})(\text{H}_2\text{O})^+$ a) and further $\text{V}\cdots\text{O}_{\text{water}}$ interaction with a second water molecule (red dashed line) residing near to the $\text{VO}(\text{acac})(\text{H}_2\text{O})$ moiety at a distance of 2.96(3) Å. The 3D network is depicted as grey sticks, with copper and calcium, depicted as cyan and blue spheres, and ethyl chain and sulphur atoms from the methionine residue, represented as yellow sticks (carbon) and yellow spheres (sulphur). For the guest $\text{VO}(\text{acac})(\text{H}_2\text{O})^+$ species hosted in the channels, vanadium, carbon and oxygen atoms are represented as purple, grey and red spheres, respectively.

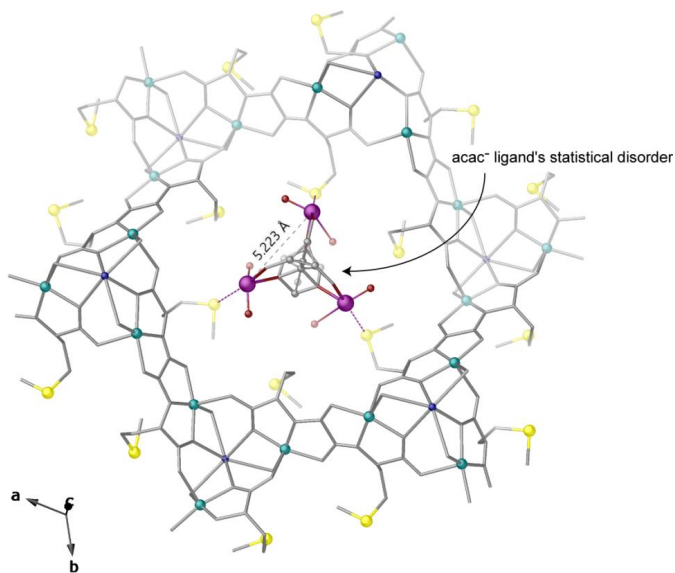


Fig. S11. Details of $\text{VO}(\text{acac})(\text{H}_2\text{O})^+$ arrangement within pores and overlapping of some carbon atoms related to statistical disorder. The 3D network is depicted as grey sticks, with copper and calcium, depicted as cyan and blue spheres, and ethyl chain and sulphur atoms from the methionine residue, represented as yellow sticks (carbon) and yellow spheres (sulphur). For the guest $\text{VO}(\text{acac})(\text{H}_2\text{O})^+$ species hosted in the channels, vanadium, carbon and oxygen atoms are represented as purple, grey and red spheres, respectively.

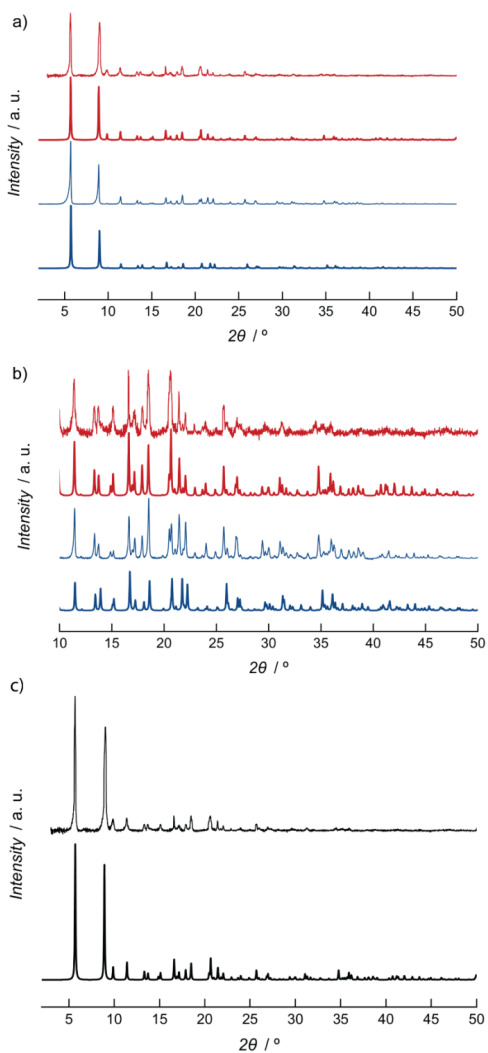


Fig. S12. (a) Calculated (bold lines) and experimental (solid lines) PXRD pattern profiles of **4** (blue) and **VO(acac)(H₂O)@4** (red) in the 2θ range 2.0–50.0° at room temperature, and enlarged image in the range 10.0–50.0° (b). (c) Calculated (bold lines) and experimental (solid lines) PXRD pattern profile of **VO(acac)(H₂O)@4** after seven reuses in the catalytic epoxidation of **1c** in the range 2.0–50.0°.

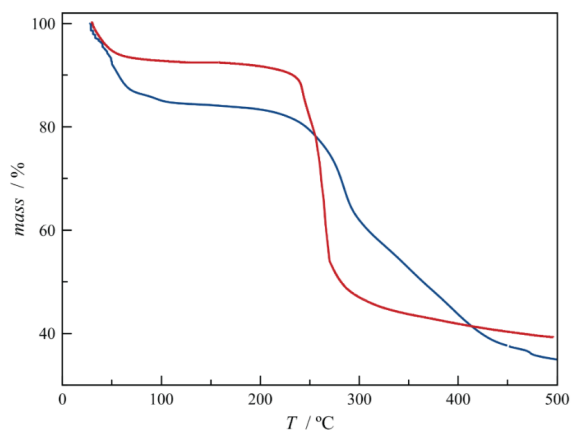


Fig. S13. Thermo-Gravimetric Analyses (TGA) of **4** (blue) and **VO(acac)(H₂O)@4** (red) under dry N₂ atmosphere.

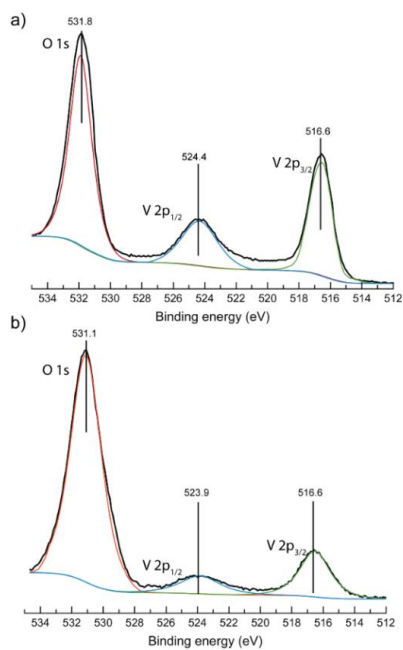


Fig. S14. XPS spectra of VO(acac)₂ (a) and VO(acac)(H₂O)@4 (b).

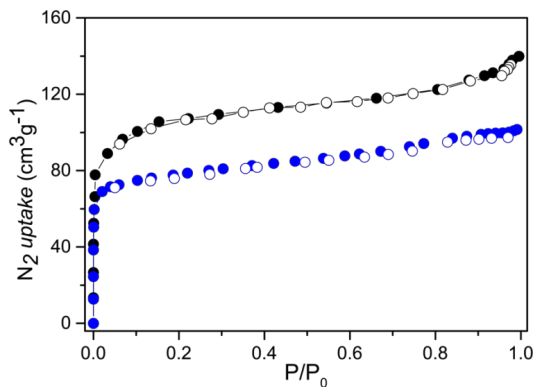
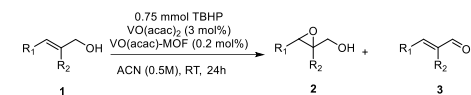


Fig. S15. N₂ (77 K) adsorption isotherm for the activated compounds **4** (black) and VO(acac)(H₂O)@**4** (blue). Filled and empty symbols indicate the adsorption and desorption isotherms, respectively. The samples were activated at 348 K under reduced pressure for 19 h prior to carry out the sorption measurements. Both, **4** and VO(acac)(H₂O)@**4**, exhibited an isotherm characteristic for microporous materials, with estimated Brunauer-Emmett-Teller (BET) surface areas of 455 (**4**) and 337 (VO(acac)(H₂O)@**4**) m² g⁻¹. As expected, after the VO(acac)(H₂O) encapsulation we observed a reduction of N₂ uptake in VO(acac)(H₂O)@**4**, respect **4**. Nevertheless, VO(acac)(H₂O)@**4** still presents a sizeable porosity.



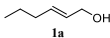
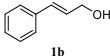
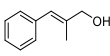
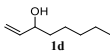
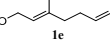
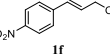
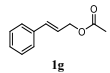
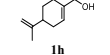
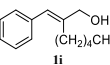
Entry	Reactive	Catalyst	Conv% 1	Sel% 2	Sel% 3
1		VO(acac) ₂	90.3	97.9	2.1
		MOF*	36.0	50.0	50.0
2		VO(acac) ₂	100	22.9	77.1
		MOF*	46.5	5.3	94.7
3		VO(acac) ₂	8.6	51.3	48.7
		MOF	92.7	75.7	24.3
4		VO(acac) ₂	89.4	83.1	16.9
		MOF*	46.4	84.8	15.2
5		VO(acac) ₂	99.0	96.4	3.6
		MOF	88.6	84.9	15.1
6		VO(acac) ₂	100	0	85.6
		MOF*	32.5	0	100
7		VO(acac) ₂	2.5	81.0	0
		MOF*	10.7	78.0	0
8		VO(acac) ₂	91.0	41.1	31.0
		MOF*	87.4	52.1	31.3
9		VO(acac) ₂	30.0	0.0	100
		MOF*	12.6	0.0	100

Fig. S16. Scope of the reaction using **VO(acac)H₂O@4** or **VO(acac)₂** as catalysts.

* 48 h reaction time.

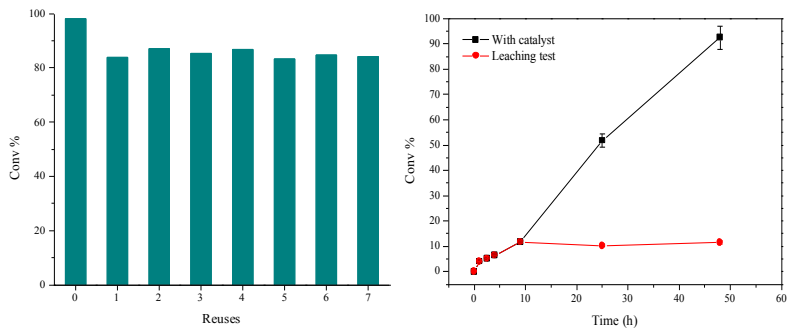


Fig. S17. Left: Reuse of $\text{VO}(\text{acac})(\text{H}_2\text{O})@4$ after washing with acetonitrile and drying. Right: Kinetics for the epoxidation of **1c** (0.5 M) with TBHP (1.2 equivalents) catalysed by $\text{VO}(\text{acac})(\text{H}_2\text{O})@4$ to give **2c** and **3c** in acetonitrile at room temperature (black squares) and after filtering the catalyst at 9 h reaction time (red circles).

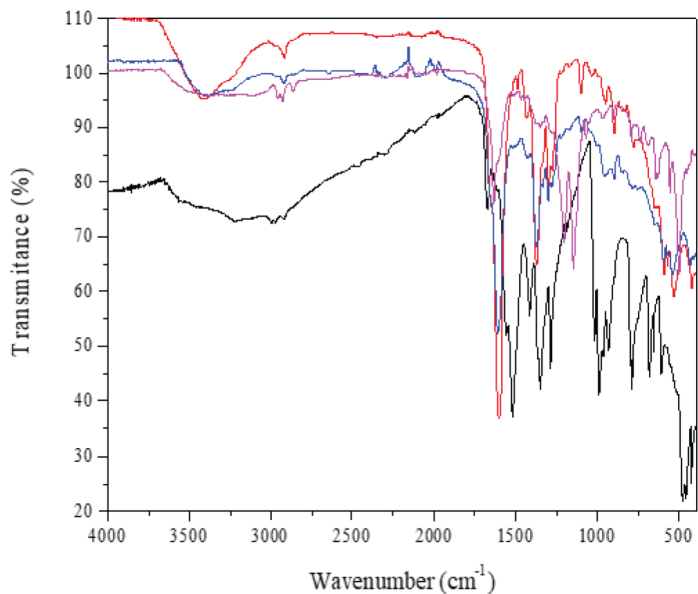


Fig. S18. FT-IR spectra of **4** (red line), the fresh **VO(acac)(H₂O)@4** (blue line) and after being used (pink line), are shown together with **VO(acac)₂** (black line). At 960 cm^{-1} , we observe the stretching vibration frequency of vanadyl group ($\text{V}=\text{O}$). It is one of the most intense and most characteristic. At 1280 cm^{-1} , the stretching symmetric vibration of the ring ($\text{C}-\text{C}-\text{C}$) appears. In contrast, the stretching asymmetric vibration appears at 1520 cm^{-1} . Finally, the stretching asymmetric vibration of $\text{C}-\text{O}$ of the ring ($\text{C}-\text{C}-\text{C}$) can be seen at 1430 cm^{-1} .²⁰

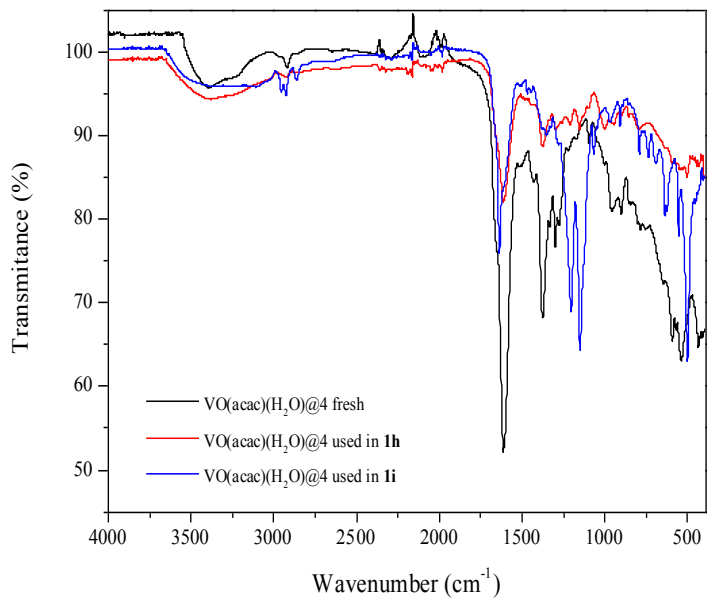


Fig. S19. FT-IR spectra of VO(acac)(H₂O)@4 before (fresh) and after used in different reactions (1h and 1i as starting materials).

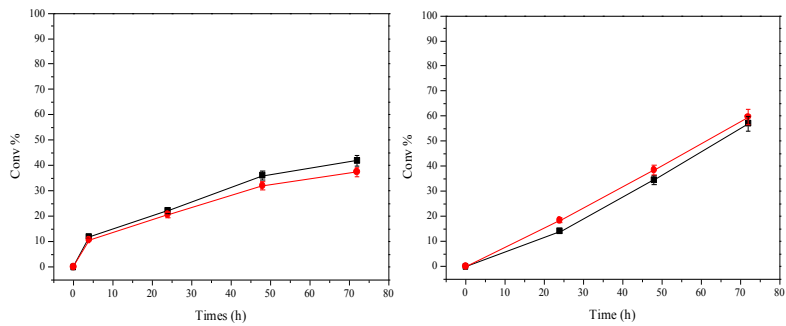


Fig. S20. Catalytic results for the allylic alcohol epoxidation/dehydrogenation of aliphatic **1a** (left) and aromatic **1b** (right) alkenes using VO(acac)₂ impregnated on **4** (black squares) and **5** (red dots).

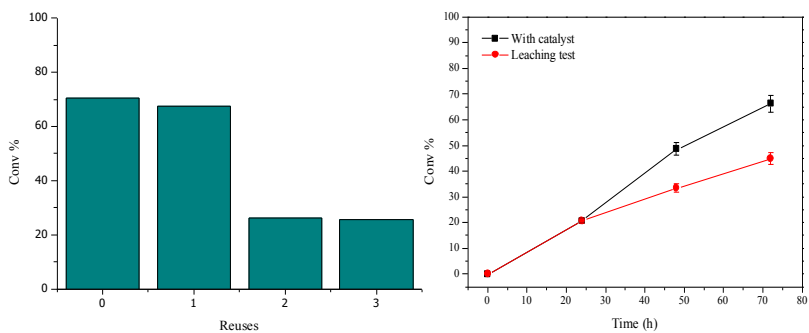


Fig. S21. Left: Reuse of $\text{VO}(\text{acac})_2$ impregnated on **5** after washing with acetonitrile and drying. Right: Kinetics for the epoxidation of **1c** (0.5 M) with TBHP (1.2 equivalents) catalyzed by $\text{VO}(\text{acac})_2$ impregnated on **4** to give **2c** and **3c** in acetonitrile at room temperature (black squares), and after filtering the catalyst at 24 h reaction time (red circles).

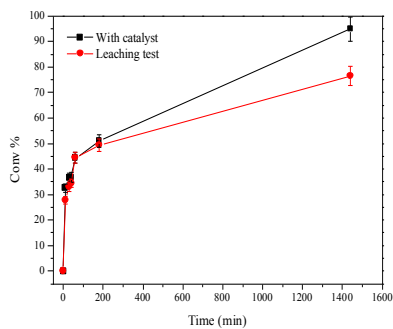
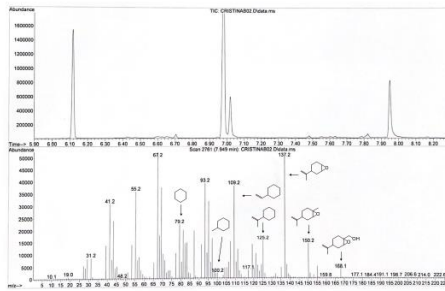
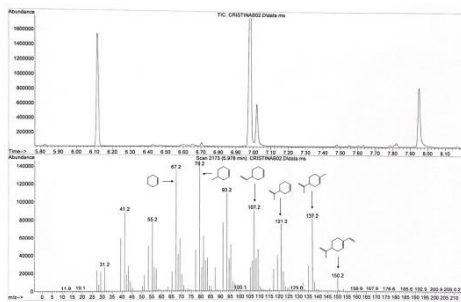


Fig. S22. Kinetics for the epoxidation of **1c** (0.5 M) with TBHP (1.2 equivalents) catalyzed by **VO(acac)₂@SiO₂** to give **2e** and **3c** in acetonitrile at room temperature (black squares), and after filtering the catalyst at 50 min reaction time (red circles).

Product 2h:



Product 3h:



Product 3i:

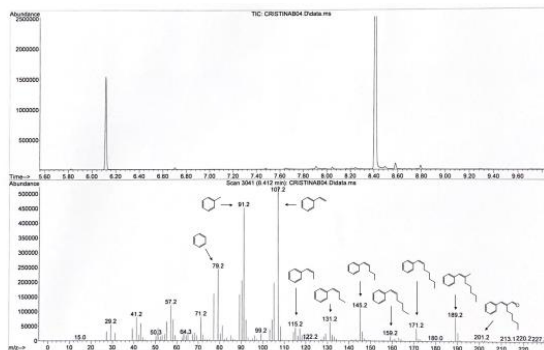
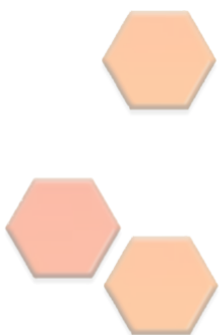


Fig. S23. GC-MS of products 2h, 3h and 3i.

References

- [1] M. Mon, J. Ferrando-Soria, T. Grancha, F. R. Fortea-Pérez, J. Gascon, A. Leyva-Pérez, D. Armentano, E. Pardo, *J. Am. Chem. Soc.* 2016, **138**, 7864–7867.
- [2] M. Mon, R. Bruno, R. Elliani, A. Tagarelli, X. Qu, S. Chen, J. Ferrando-Soria, D. Armentano, E. Pardo, *Inorg. Chem.* 2018, **57**, 13895–13900.
- [3] B. Jarrais, C. Pereira, A. R. Silva, A. P. Carvalho, J. Pires, C. Freire, *Polyedron* 2009, **28**, 994–1000.
- [4] S. K. Maiti, S. Dinda and R. Bhattacharyya, *Tetrahedron Lett.* 2008, **49**, 6205–6208.
- [5] H. Pettersson, A. Gogoll and J. E. Baeckvall, *J. Org. Chem.* 1992, **57**, 6025–6031.
- [6] X. Li and B. Borhan, *J. Am. Chem. Soc.* 2008, **130**, 16126–16127.
- [7] R. Saladino, R. Bernini, V. Neri and C. Crestini, *Appl. Catal. A* 2009, **360**, 171–176.
- [8] M. Klawonn, M. K. Tse, S. Bhor, C. Döbler and M. Beller, *J. Mol. Catal. A* 2004, **218**, 13–19.
- [9] W. B. Cunningham, J. D. Tibbetts, M. Hutchby, K. A. Maltby, M. G. Davidson, U. Hintermair, P. Plucinski and S. D. Bull, *Green Chem.* 2020, **22**, 513–524.
- [10] J. Zhu, J. Liu, R. Ma, H. Xie, J. Li, H. Jiang and W. Wang, *Adv. Synth. Catal.* 2009, **351**, 1229–1232.
- [11] G. Pelletier, W. S. Bechara and A. B. Charette, *J. Am. Chem. Soc.* 2010, **132**, 12817–12819.
- [12] Y. Zou, Q. Wang and A. Goeke, *Chem.–Eur. J.* 2008, **14**, 5335–5345.
- [13] N. Lahmar, J. Aatar, T. Ben Ayed, H. Amri and M. Bellassoued, *J. Organomet. Chem.* 2006, **691**, 3018–3026.
- [14] SAINT, version 6.45, Bruker Analytical X-ray Systems, Madison, WI, 2003.
- [15] G.M. Sheldrick, SADABS Program for Absorption Correction, version 2.10, Analytical X-ray Systems, Madison, WI, 2003.

- [16] (a) G. M. Sheldrick, *Acta Cryst. C* 2015, **71**, 3. (b) G. M. Sheldrick, *Acta Cryst. A* 2008, **64**, 112. (c) SHELXTL-2013/4, Bruker Analytical X-ray Instruments, Madison, WI, 2013.
- [17] (a) A. L. Spek, *Acta Crystallogr. Sect. C-Struct. Chem.* 2015, **71**, 9–18. (b) A. L. Spek, *Acta Crystallogr. Sect. D, Biol. Crystallogr.* 2009, **65**, 148–155.
- [18] L. J. Farrugia, *J. Appl. Crystallogr.* 1999, **32**, 837–838.
- [19] D. Palmer, CRYSTAL MAKER, Cambridge University Technical Services, C. No Title, 1996.
- [20] P. Van Der Voort, I. V. Babitch, P. J. Grobet, A. A. Verberckmoes and E. F. Vansant, *J. Chem. Soc., Faraday Trans.* 1996, **92**, 3635-3642.



PUBLICATION 2: Exploring the Role of Amino Acid-Derived Multivariate Metal-Organic Frameworks as Catalyst in (Hemi)-Ketalization Reactions



Exploring the Role of Amino Acid-Derived Multivariate Metal–Organic Frameworks as Catalysts in Hemiketalization Reactions

Cristina Negro,^{||} Sergio Sanz-Navarro,^{||} Antonio Leyva-Pérez,^{*} Donatella Armentano,^{*} Jesús Ferrando-Soria,^{*} and Emilio Pardo^{*}

Cite This: <https://doi.org/10.1021/acs.inorgchem.3c00495>

Read Online

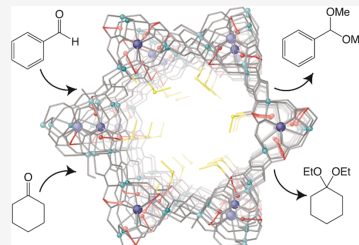
ACCESS |

Metrics & More

Article Recommendations

Supporting Information

ABSTRACT: Understanding the host–guest chemistry in MOFs represents a research field with outstanding potential to develop in a rational manner novel porous materials with improved performances in fields such as heterogeneous catalysis. Herein, we report a family of three isorecticular MOFs derived from amino acids and study the influence of the number and nature of functional groups decorating the channels as a catalyst in hemiketalization reactions. In particular, a multivariate (MTV) MOF 3, prepared by using equal percentages of amino acids L-serine and L-mecysteine, in comparison to single-component (“traditional”) MOFs, derived from either L-serine or L-mecysteine (MOFs 1 and 2), exhibits the most efficient catalytic conversions for the hemiketalization of different aldehydes and ketalization of cyclohexanone. On the basis of the experimental data reported, the good catalytic performance of MTV-MOF 3 is attributed to the intrinsic heterogeneity of MTV-MOFs. These results highlight the potential of MTV-MOFs as strong candidates to mimic natural nonacidic enzymes, such as glycosidases, and to unveil novel catalytic mechanisms not so easily accessible with other microporous materials.



INTRODUCTION

Multivariate metal–organic frameworks (MTV-MOFs)^{1–7} represent a novel generation of porous crystalline materials within MOFs, constituted of linkers with identical backbones but different functionalities decorating the ligand, where heterogeneity and complexity of composition have opened the way to synergetic behaviors and thus to novel and/or enhanced properties compared with single-component (“traditional”) MOFs.^{8–10} Nevertheless, it is difficult to obtain precise atomic information on the location and distribution of the different functionalities decorating the MTV-MOF channels, and further work adapting/improving existing characterization techniques or implementing new ones will be needed.^{11–13} The exciting properties exhibited by MTV-MOFs in different applications overcome this uncertainty, and it has not been a limitation for the growing interest in developing novel MTV-MOFs.^{14–19}

Elegant application examples of taking advantage of the heterogeneity of MTV-MOFs have been reported for heterogeneous catalysis.^{20–23} Indeed, such complex porous platforms are a step closer to engendering materials that mimic the existing complexity and functionality of enzymes.^{24,25} A beautiful example is the seminal work reported by Fracaroli et al.,²⁰ where, in an MTV-MOF, up to seven postsynthetic modifications were performed to lead to more complex MTV-MOFs with channels decorated with a tripeptide. In particular,

the one with the H₂N-Cys-His-Asp-CONHL sequence (Cys = cysteine, His = histidine, Asp = aspartic acid, and L = organic backbone) of the endopeptidase enzyme tobacco etch virus (TEV) was investigated as a mimic of this enzyme for the sequence-specific bond cleavage of a pentapeptide. Despite the low conversion achieved, this work illustrated that it is possible to transfer the compositional heterogeneity of MTV-MOFs into a complex target application.

One of our main research lines has been devoted to exploring the development of MTV-MOFs with amidato-based ligands derived from amino acids, with the main aim to take advantage of the heterogeneity of composition and the intrinsic flexibility of the residues decorating the MTV-MOF channels toward more complex applications. So far, we have observed a successful transfer from the complexity of composition to the improvement of performance in water remediation.^{14,18,26,27} In particular, an MTV-MOF {Ca^{II}Cu^I}_6¹¹[(S,S)-methox]_{1.43–1.46}[(S,S)-seri-

Received: February 14, 2023

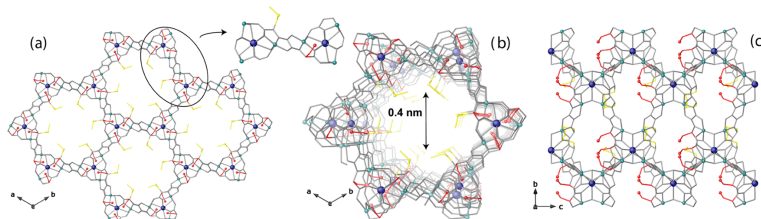


Figure 1. (a) View of the porous structure of **3** along the *c* crystallographic axis (inset emphasizes the dianionic bis(hydroxo) dicopper(II) building blocks). (b, c) Views of a single channel for the porous structure of MTV-MOF **3** along the *b* (b) and *a* (c) axes (the crystallization water molecules are omitted for clarity). Copper(II) and strontium(II) ions from the network are represented as cyan and blue spheres, respectively. Oxygen and sulfur atoms from the residues are shown as red and yellow spheres, respectively. The organic ligands are represented as gray sticks, with the exception of L-serine ($-\text{CH}_2\text{OH}$) and L-methylcysteine ($-\text{CH}_2\text{SCH}_3$) residues, which are represented as red and yellow sticks, respectively.

$\text{mox}]_{1.57-1.54}(\text{OH})_2(\text{H}_2\text{O})\cdot 30\text{H}_2\text{O}$ (where methox = bis[(*S*-methionine)oxalyl diamide and serimox = bis[(*S*-serine)oxalyl diamide) with functional channels decorated with approximately 50% of hydroxyl groups and 50% thioalkyl ones derived from natural amino acids L-serine and L-methionine, respectively, has proven very efficient in the simultaneous capture of contaminants with inorganic and organic nature.¹⁴ Also, this has been further validated with an isorecticular MTV-MOF $\{\text{Sr}^{\text{II}}\text{Cu}_6^{\text{II}}[(\text{S},\text{S})\text{-methox}]_{1.50}[(\text{S},\text{S})\text{-mecs-mox}]_{1.50}(\text{OH})_2(\text{H}_2\text{O})\cdot 36\text{H}_2\text{O}$ (where methox = bis[(*S*-methionine)oxalyl diamide), which outperforms single-component MOFs in the removal of emergent neonicotinoid contaminants from water.¹⁸

On this basis and with the background inspiration of the active centers of enzymes, where different organic functionalities are able to act synergistically to interact, adapt, and efficiently catalyze the transformation of specific substrates, the aim of this investigation has been to explore within a family of isorecticular MOFs the role and influence of the presence and absence of functional channels decorated with more than one distinct amino acid residue in catalysis. To this end, we have focused on the use of two previously reported MOFs, with formulas $\{\text{Sr}^{\text{II}}\text{Cu}_6^{\text{II}}[(\text{S},\text{S})\text{-serimox}]_3(\text{OH})_2(\text{H}_2\text{O})\cdot 38\text{H}_2\text{O}$ (**1**)^{28,29} and $\{\text{Sr}^{\text{II}}\text{Cu}_6^{\text{II}}[(\text{S},\text{S})\text{-mecs-mox}]_3(\text{OH})_2(\text{H}_2\text{O})\cdot 15\text{H}_2\text{O}$ (**2**),³⁰ and a novel MTV-MOF of formula $\{\text{Sr}^{\text{II}}\text{Cu}_6^{\text{II}}[(\text{S},\text{S})\text{-serimox}]_{1.50}[(\text{S},\text{S})\text{-mecs-mox}]_{1.50}(\text{OH})_2(\text{H}_2\text{O})\cdot 12\text{H}_2\text{O}$ (**3**) (Scheme S1 and Figure S1) as catalysts for hemiketalization and ketalization reactions.

The addition of alcohols to the carbonyl group of aldehydes and ketones is an essential reaction in nature³¹ and industrial synthesis,³² since the electronic density of the carbonyl group is completely switched from electron-rich to electron-poor. Hemiketalization and ketalization reactions have been traditionally used in organic synthesis to protect the aldehyde and ketone groups during other reactions, which are regenerated after simple water-acidic treatment.³³ However, the acid-catalyzed conditions required for hemiketalization and ketalization reactions are not always compatible with other groups. Indeed, it is not surprising to find in the literature synthetic routes where a functional group is previously protected by other methodologies before the carbonyl group is protected under acid-catalyzed conditions.³⁴ Thus, any catalytic method for hemiketalization and ketalization reactions based on nonacidic conditions is of interest.

Nature makes use of nonacid enzymes, such as glycosidases, to catalyze hemiketalization and ketalization reactions by the cooperative action of two different pocketed base groups, *i.e.*, carboxylates.³⁵ In this context, we have recently reported that MOF **1** is able to selectively hydrolyze ketal groups in complex organic molecules under nonacid conditions, by the combined action of the alcohol groups from serine residues within the MOF channels in the presence of water.³⁶ Since ketalization reactions are reversible, we hypothesized that the same MOF **1** could catalyze the formation of ketal under anhydrous conditions. Unfortunately, this reaction only occurred to a very minor extent.³⁵ Thus, at this point, on the basis of the efficient σ -hole interactions observed on MOFs containing thioether residues on the recognition and capture of organic contaminants,¹⁸ as well as the fact that cyclic thiols in stoichiometric amounts, after forming dithianes, have been traditionally used to protect carbonyl groups,³⁷ we turned our attention to MOF **2**. However, despite these *a priori* optimal conditions, **2** has not been revealed as a very efficient catalyst. Intrigued by these results, we aimed to take advantage of the heterogenization and synergistic effect observed in MTV-MOFs, to explore the possibility that the MTV-MOF **3** could be active for hemiketalization and ketalization reactions, since the combination of $-\text{CH}_2\text{OH}$ and $-\text{CH}_2\text{SCH}_3$ groups in **3** could help in carbonyl group activation. Thus, the amino acid residues containing alcohol and thioether groups in MTV-MOF **3** will not form permanent bonds but could cooperatively activate the carbonyl group in the presence of external alcohol, in a way similar to glycosidases. The catalytic mechanism of this microporous bifunctional solid will significantly differ from previous examples with microporous solids, *i.e.*, zeolites^{38,39} and MOFs,⁴⁰ based on amine/acid and other functional groups. We present below that this strategy works and that MTV-MOF **3** catalyzes hemiketalization and ketalization reactions within its confined space more efficiently than MOFs **1** and **2**.

RESULTS AND DISCUSSION

Synthesis and Characterization. In this work, we show an expansion of the application of the metalloligand design strategy to synthesize a novel water-stable tridimensional (3D) MTV-MOF, with formula $\{\text{Sr}^{\text{II}}\text{Cu}_6^{\text{II}}[(\text{S},\text{S})\text{-serimox}]_{1.50}[(\text{S},\text{S})\text{-mecs-mox}]_{1.50}(\text{OH})_2(\text{H}_2\text{O})\cdot 12\text{H}_2\text{O}$ (**3**), obtained as green prisms by slow diffusion in H-shaped tubes at room temperature of aqueous solutions containing stoichiometric

B

<https://doi.org/10.1021/acs.inorgchem.3c00495>
Inorg. Chem. XXXX, XXX, XXX–XXX

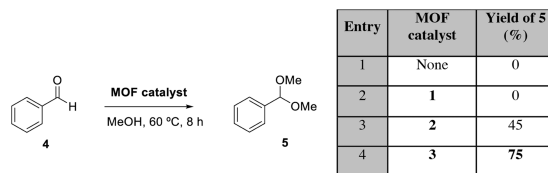


Figure 2. Results for the MOF-catalyzed hemiketalization reaction of benzaldehyde 4 with methanol. Selectivity to 5 is 100% (conversion equals yield). GC yields.

amounts of an equimolar mixture of $(\text{Me}_4\text{N})_2\{\text{Cu}_2[(\text{S},\text{S})\text{-serimox}](\text{OH})_2\}\cdot\text{SH}_2\text{O}$ and $(\text{Me}_4\text{N})_2\{\text{Cu}_2[(\text{S},\text{S})\text{-mecysmox}](\text{OH})_2\}\cdot\text{SH}_2\text{O}$ in one arm and $\text{Sr}(\text{NO}_3)_2$ in the other.

The crystal structure of 3 determined by single-crystal X-ray diffraction (SCXRD) consists of a chiral honeycomb-like 3D strontium (II)/copper (II) network featuring functional hexagonal channels of approximately 0.4 nm, developing along the *c* crystallographic axis, where the methylenethio-methyl chains of methylcysteine derivatives are located (Figure 1). It is an aca uninodal sixfold-connected net (4⁹.6⁶), built from trans-oxamidato-bridged dicopper(II) units of $\{\text{Cu}_2^{\text{II}}[(\text{S},\text{S})\text{-serimox}]\}$ and $\{\text{Cu}_2^{\text{II}}[(\text{S},\text{S})\text{-mecysmox}]\}$ (Scheme S1 and Figures 1 and S1–S3), which are expected to be statistically disordered in the crystal structure. They act as linkers between the Sr^{II} ions through carboxylate groups (Figure 1a,b). Neighboring Cu^{2+} and $\text{Cu}^{2+}/\text{Sr}^{2+}$ ions are auxiliary interconnected, in a μ_3 fashion, by aqua/hydroxo groups (in a 1:2 statistical distribution) (inset Figure 1a). As previously tested for the refinement of best model in the crystal structure of the isorecticular MTV-MOF $\{\text{Ca}^{\text{II}}\text{Cu}_6^{\text{II}}[(\text{S},\text{S})\text{-methox}]_{1.43-1.46}[(\text{S},\text{S})\text{-serimox}]_{1.57-1.54}(\text{OH})_2(\text{H}_2\text{O})\}\cdot 30\text{H}_2\text{O}$,¹⁴ a similar percentage of mixed serimox and mecysmox (confirmed by the composition analysis, vide infra C, H, S, N in the Experimental Section and Supporting Information) lead to superimposed snapshots of mixed $\{\text{Cu}_2^{\text{II}}[(\text{S},\text{S})\text{-mecysmox}/\text{serimox}]\}$ metalloligands. Thus, once more, the disorder in 3 has been modeled as an averaged view of the crystal structure, which is the spatial average of all molecule/fragment structures in the crystal *via* only one unit cell (see crystallographic details in the Supporting Information). This, even if it could seem counterintuitive, it is a better description of the real situation, where pure copper(II) metalloligands of each amino acid-derived ligand are randomly distributed (with 1:1 ratio) within the net (see crystallographic details in the Supporting Information). Looking at such modeled crystal structure of 3, the two “arms” decorated with serine and methylcysteine derivatives, respectively, show different orientations, with the methylcysteine one being more distended, within the largest octagonal pores, and the serine one bent and confined in the smallest channels developing along the *a* crystallographic axis (Figures 1b,c and S3). Here, it is worth noting that MTV-MOFs, as already underlined in our previous works,^{14,18,26,27} show as a thrilling feature an impressive flexibility of the functional arms confined within the pores, exhibiting different conformations depending on the target molecules captured in pores. Thus, loaded reactants of a given catalytic reaction might have an effect on the final conformation adopted by the flexible aminoacidic arms decorating the pores. Indeed, it depends on host–guest interactions, which are at the origin of the stabilization of such species within confined spaces.

Finally, the estimated empty volume for 3, without the crystallization water molecules, is 1764.7 (1) Å³, which represents 48.3% of potential void per unit cell volume [$V = 3653.9$ Å³].

In addition to the structural characterization and elemental analysis, the nature and identity of MTV-MOF 3 were also established by powder X-ray diffraction (PXRD), N₂ adsorption isotherm at 77 K, and thermogravimetric analyses (TGAs) (see the Supporting Information). The experimental PXRD pattern of 3 is consistent with the theoretical one, extracted from SCXRD (Figure S4), which confirms the homogeneity and purity of the powder sample. The permanent porosity of 3 was supported by measuring the N₂ adsorption isotherm at 77 K and compared to the adsorption isotherms of traditional MOFs 1 and 2 (Figure S5). They confirm the permanent porosity for all three materials, with N₂ adsorbed amounts for 3 between the ones of 1 and 2, but closer to 2, which is consistent with the accessible void spaces shown in the crystal structures. The solvent content of 3 was established by TGA (Figure S6), with a calculated percentage weight loss value of 85% at 388 K, which corresponds to 12 water molecules. 3 is stable up to 200 °C when decomposition starts.

Catalytic Studies. Figure 2 shows the catalytic results for the hemiketalization reaction of benzaldehyde 4 with methanol. After screening some reaction conditions, the best results were obtained at 60 °C after an 8 h reaction time. Under these reaction conditions, it can be seen that MOF 1 is completely inactive for the reaction (entries 1 and 2), as observed before,³⁶ and that MOF 2 shows some activity, to afford a 45% yield of hemiacetal 5 (entry 3). In contrast, MTV-MOF 3 catalyzes the reaction much more efficiently to afford product 5 in 75% yield (entry 4). The selectivity of the reaction is complete since other products are not observed, and the fact that the transformation does not advance further is probably due to reaching equilibrium. Magnesium sulfate was added to the reaction media in order to adsorb the water formed during the reaction, further shifting the equilibrium toward the hemiketal product 5. However, the addition of MgSO_4 did not improve the yield of 5, since the generated water is probably retained in the highly polar MOF pores and reacts back with 5 at high conversions of 4.

In order to confirm the retention of the structural integrity of 1–3 under catalytic conditions, as well as to rule out the possibility of partial/total structural collapse in 1 and 2, N₂ adsorption isotherms at 77 K and PXRD were also performed after catalytic experiments (Figures S5b and S7). From PXRD, it can be concluded that all materials are robust enough to maintain their structural integrity under reaction conditions. In an analogous way, the similarity of Brunauer–Emmett–Teller (BET)⁴¹ surface areas before [791(1), 633(2), and 682(3) m²/g] and after [763(1), 609(2), and 670(3) m²/g] catalysis

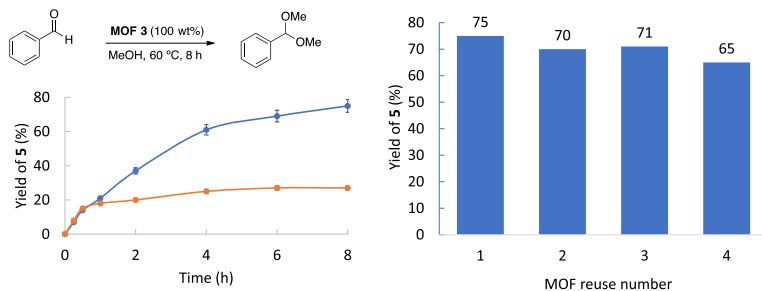


Figure 3. (Left) Hot filtration test for MTV-MOF 3 during the hemiketalization reaction of benzaldehyde 4 with MeOH under optimized reaction conditions. Error bars account for a 5% uncertainty. (Right) Reuse of MTV-MOF 3 under the same reaction conditions. GC yields.

support the retention of porosity and further reflect the stability of 1–3. The stability of MTV-MOF 3 in aqueous and nonaqueous solvents was further validated by PXRD (Figure S8) of polycrystalline samples of 3 immersed for 24 h in hot water, dimethylformamide, methanol, and acetonitrile.

Figure 3 (left) shows the hot filtration test for the reaction catalyzed by the MTV-MOF 3, where it can be seen that the hemiketalization reaction of benzaldehyde 4 stops after the solid catalyst is filtered off. In accordance, Figure 3 (right) shows that MTV-MOF 3 could be reused up to 3 times without appreciable depletion of the final yield of 5.

The scope of aldehydes was then assessed for the hemiketalization reaction catalyzed by MTV-MOF 3, under the optimized reaction conditions. The results are shown in Figure 4. It can be seen that aromatic aldehydes with halide and methoxy substituents in different positions of the aryl ring can be obtained in good yields (products 5b–g) and that alkyl aldehydes are even better reactive (products 5h–i), including acid-sensitive propargyl aldehydes (5j). These results support the ability of MTV-MOF 3 to catalyze the hemiketalization reaction of aldehydes with disparate electronics.

Ketones are more unreactive than aldehydes in ketalization reactions; however, they were also tested with the MOF catalysts. Figure 5 shows the catalytic results for cyclohexanone 6. In accordance with the lower reactivity of ketones, a higher reaction temperature (80 °C) was needed to get significant conversions, and EtOH instead of MeOH was used as a nucleophile to avoid overpressure in the reaction. The results show that again MTV-MOF 3 was the best catalyst, although with just a slight difference from MOF 2 (compare entries 3 and 4), to afford 50% of product 7 with complete selectivity. Thus, MTV-MOF 3 can be considered as a general catalyst for the hemiketalization reaction of simple carbonyl compounds (aldehydes and ketones).

CONCLUSIONS

Here, we have presented the synthesis and crystal structure of a novel component of the oxamidato-based ligands derived from the amino acid 3D MTV-MOFs family, and we have reported the influence of the functionalization of the channels, with one or two types of distinct functional groups decorating the channels, on the hemiketalization reaction of different simple carbonyl compounds. On the basis of the obtained results, we can confirm that the heterogeneity present in MTV-MOF 3 is translated well into a more efficient catalytic behavior on the

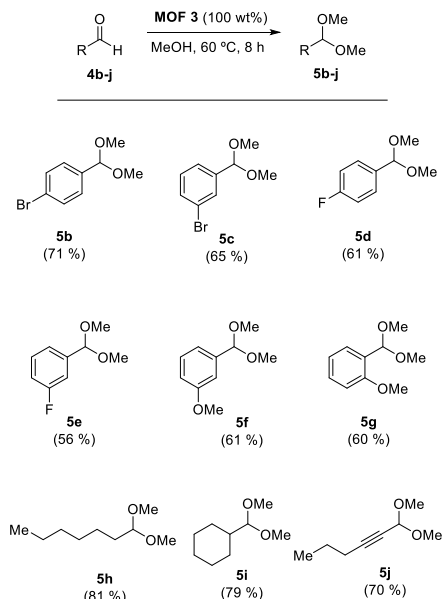


Figure 4. Scope of aldehydes for the hemiketalization reaction catalyzed by MTV-MOF 3. GC yields.

reactions under study. Thus, these results also illustrate the potential of MTV-MOFs to somehow mimic natural nonacidic enzymes and to uncover novel catalytic mechanisms not accessible with traditional microporous materials or single-component MOFs. Nevertheless, further work will be needed to fully uncover the key role that the distinct functional groups play in MTV-MOFs, and how the subtle modification of their proportions and/or spatial arrangement has a massive influence on their functionality, in a similar manner as it occurs in natural enzymes.

D

<https://doi.org/10.1021/acs.inorgchem.3c00495>
Inorg. Chem. XXXX, XXX, XXX–XXX

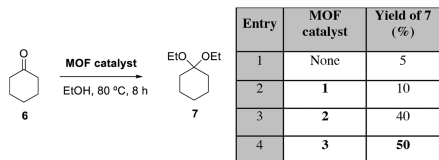


Figure 5. Results for the MOF-catalyzed hemiketalization reaction of cyclohexanone **6** with ethanol. Selectivity to **7** is 100% (conversion equals yield). GC yields.

EXPERIMENTAL SECTION

Materials. Reagents were obtained from commercial sources (Merck-Aldrich) and used without further purification unless otherwise indicated. Anhydrous solvents were obtained from a resin-exchanger apparatus. Reactions were performed in conventional round-bottomed flasks or sealed vials equipped with a magnetic stirrer. All of the products were characterized by gas chromatography-mass spectrometry (GC-MS). $\{Sr^{II}Cu_6^{II}[(S,S)\text{-serimox}]_2(OH)_2(H_2O)\}_2 \cdot 38H_2O$ (**1**) and $\{Sr^{II}Cu_6^{II}[(S,S)\text{-mecs-mox}]_2(OH)_2(H_2O)\}_2 \cdot 15H_2O$ (**2**) were prepared following a previously reported procedure.

Physical Techniques. Elemental (C, H, S, N) analyses were performed at the Microanalytical Service of the Universitat de València. FT-IR spectra were recorded on a Perkin Elmer 882 spectrophotometer as KBr pellets. The thermogravimetric analysis was performed on crystalline samples under a dry N_2 atmosphere with a Mettler Toledo TGA/STDA 851⁺ thermobalance operating at a heating rate of $10\text{ }^\circ\text{C min}^{-1}$.

Preparation of $\{Sr^{II}Cu_6^{II}[(S,S)\text{-serimox}]_{1.50}[(S,S)\text{-mecs-mox}]_{1.50}(OH)_2(H_2O)\}_2 \cdot 12H_2O$ (3**).** Suitable well-shaped prisms of **3** for SCXRD were synthesized by slow diffusion in H-shaped tubes of aqueous solutions containing stoichiometric amounts of an equimolar mixture of $(Me_4N)_2[Cu_2[(S,S)\text{-serimox}](OH)_2] \cdot 5H_2O$ (0.118 g, 0.18 mmol) and $(Me_4N)_2[Cu_2[(S,S)\text{-mecs-mox}](OH)_2] \cdot 5H_2O$ (0.129 g, 0.18 mmol) in one arm and $Sr(NO_3)_2$ (0.025 g, 0.12 mmol) in the other. They were isolated by filtration on paper and air-dried. Alternatively, a gram-scale procedure can also be successfully followed by mixing greater amounts of $(Me_4N)_2[Cu_2[(S,S)\text{-serimox}](OH)_2] \cdot 5H_2O$ (3.96 g, 6.0 mmol) and $(Me_4N)_2[Cu_2[(S,S)\text{-mecs-mox}](OH)_2] \cdot 5H_2O$ (4.32 g, 6 mmol) in water (50 mL) and adding dropwise another aqueous solution of $Sr(NO_3)_2$ (0.846 g, 4.0 mmol). After allowing the final mixture of reaction to react, under stirring for 6 h, a green polycrystalline powder was isolated by filtration and characterized by C, H, S, N analysis to obtain the final formula of $\{Sr^{II}Cu_6^{II}[(S,S)\text{-serimox}]_{1.50}[(S,S)\text{-mecs-mox}]_{1.50}(OH)_2(H_2O)\}_2 \cdot 12H_2O$. Anal. calcd for **3**: $C_{27}Cu_6SrS_7H_{66}N_6O_{40}$ (1679.92): C, 19.30; H, 3.96; S, 5.73; N, 5.00%. Found: C, 19.63; H, 3.91; S, 5.78; N, 5.03%. IR (KBr): 1605 and 1602 cm^{-1} (C=O).

Gas Adsorption. The N_2 adsorption-desorption isotherms at 77 K were obtained for the polycrystalline samples of **3** with a BELSORP-mini-X instrument. The samples were first activated with methanol and then evacuated at 348 K for 16 h under 10^{-6} Torr prior to their analysis.

X-ray Powder Diffraction Measurements. A polycrystalline sample of **3** was introduced into a 0.5 mm borosilicate capillary prior to being mounted and aligned on an Empyrean PANalytical powder diffractometer using Cu $K\alpha$ radiation ($\lambda = 1.54056\text{ \AA}$). Five repeated measurements were collected at room temperature ($2\theta = 2-45^\circ$) and merged in a single diffractogram. A polycrystalline sample of **3** was also measured after catalysis following the same procedure.

X-ray Crystallographic Data Collection and Structure Refinement. Crystal of **3** with $0.16\text{ mm} \times 0.14\text{ mm} \times 0.12\text{ mm}$ as dimensions was selected and mounted on a MiTeGen MicroMount in Paratone oil and very quickly placed on a liquid nitrogen stream cooled at 90 K, to avoid the possible degradation upon dehydration or exposure to air. Diffraction data were collected on a Bruker-Niuis

X8APEXII CCD area detector diffractometer using graphite-monochromated Mo $K\alpha$ radiation ($\lambda = 0.71073\text{ \AA}$). The data were processed through SAINT reduction and SADABS multiscan absorption software. The structure was solved with the SHELXS structure solution program using the Patterson method. The model was refined with version 2018/3 of SHELXL against F^2 on all data by full-matrix least squares.

In the refinement of **3**, all non-hydrogen atoms were refined anisotropically except for some highly dynamically disordered atoms of methylcysteine and serine arms and solvent water molecules. The use of some bond length restraints, applied on atoms belonging to highly dynamic moieties, has been reasonably imposed and related to the expected thermal motion, likely depending on the large size of the huge cages of the frameworks (DFIX and ISOR). For instance, EADP for a group of atoms of the fragments expected to have essentially similar ADPs has been applied. All of the hydrogen atoms of the ligand were set in a calculated position and refined isotropically using the riding model. Hydrogen atoms on thermally disordered solvent water molecules were neither found nor calculated.

As stated in the main text, the oxamidato-bridged dicopper(II) units of $\{Cu_2^{II}[(S,S)\text{-serimox}]\}$ and $\{Cu_2^{II}[(S,S)\text{-mecs-mox}]\}$, added in a 1:1 ratio in **3**, exhibit a statistical disorder in the crystal structure, where a very similar percentage of serimox and mecs-mox leads to a completely superimposed snapshot of mixed $\{Cu_2^{II}[(S,S)\text{-mecs-mox/serimox}]\}$ dimers (see the inset of Figure 1a).

A summary of the crystallographic data and structure refinement for the crystal structure of **3** is given in Table S1. The comments for alerts A and B are described in the CIF using the validation reply form (vrf). CCDC reference number is 2241172.

The final geometrical calculations on free voids and the graphical manipulations were carried out with PLATON⁴² implemented in WinGX⁴³ and CRYSTAL MAKER programs,⁴⁴ respectively.

Typical Catalytic Reaction Procedure. MOFs **1** and **2** or MTV-MOF **3** (25 mg, 100 wt %) were placed in a 2 mL vial equipped with a magnetic stir bar, and the corresponding amount of MeOH (1 mL) was added. Then, the corresponding aldehyde (for example, 26 μL , 0.24 mmol, for **4**) was added via a syringe at room temperature. The mixture was sealed and magnetically stirred in a preheated oil bath at $60\text{ }^\circ\text{C}$ for 8 h. For kinetic experiments, individual reactions were placed for each point and aliquots of 0.125 mL were periodically taken. After that, the reaction mixture was poured into AcOEt (1 mL), *n*-dodecane (11 mL, 0.05 mmol) was added as an external standard, and the mixture was passed through a filter syringe and subjected to GC and GC-MS analysis.

ASSOCIATED CONTENT

Supporting Information

The Supporting Information is available free of charge at <https://pubs.acs.org/doi/10.1021/acs.inorgchem.3c00495>.

Preparation and physical characterization data, crystallographic refinement details for **3**, and catalytic results (Scheme S1, Figures S1–S6, and Table S1) (PDF)

Accession Codes

CCDC 2241172 contains the supplementary crystallographic data for this paper. These data can be obtained free of charge via www.ccdc.cam.ac.uk/data_request/cif, or by emailing data_request@ccdc.cam.ac.uk, or by contacting The Cambridge Crystallographic Data Centre, 12 Union Road, Cambridge CB2 1EZ, UK; fax: +44 1223 336033.

AUTHOR INFORMATION

Corresponding Authors

Antonio Leyva-Pérez – Instituto de Tecnología Química (UPV-CSIC), Universidad Politécnica de Valencia–Consejo Superior de Investigaciones Científicas, 46022 Valencia,

E

<https://doi.org/10.1021/acs.inorgchem.3c00495>
Inorg. Chem. XXXX, XXX, XXX–XXX

Spain; orcid.org/0000-0003-1063-5811;
Email: anleyva@itq.upv.es

Donatella Armentano – Dipartimento di Chimica e
Tecnologie Chimiche (CTC), Università della Calabria,
Rende 87036, Italy; orcid.org/0000-0002-8502-8074;
Email: donatella.armentano@unical.it

Jesús Ferrando-Soria – Instituto de Ciencia Molecular
(ICMol), Universidad de Valencia, 46980 Valencia, Spain;
orcid.org/0000-0003-0987-2764;
Email: jesus.ferrando@uv.es

Emilio Pardo – Instituto de Ciencia Molecular (ICMol),
Universidad de Valencia, 46980 Valencia, Spain;
orcid.org/0000-0002-1394-2553; Email: emilio.pardo@uv.es

Authors

Cristina Negro – Instituto de Ciencia Molecular (ICMol),
Universidad de Valencia, 46980 Valencia, Spain

Sergio Sanz-Navarro – Instituto de Tecnología Química
(UPV-CSIC), Universidad Politécnica de Valencia–Consejo
Superior de Investigaciones Científicas, 46022 Valencia, Spain

Complete contact information is available at:

<https://pubs.acs.org/10.1021/acs.inorgchem.3c00495>

Author Contributions

||C.N. and S.S.-N. contributed equally to this work.

Notes

The authors declare no competing financial interest.

ACKNOWLEDGMENTS

This work was supported by the MICINN (Spain) (Projects PID2019-104778GB-I00, PID2020-115100GB-I00, Excellence Unit “Maria de Maeztu” CEX2019-000919-M and Severo Ochoa Centre of Excellence Program CEX2021-001230-S) and the Ministero dell’Istruzione, dell’Università e della Ricerca (Italy). The work has also been funded by Generalitat Valenciana, Prometeo Grupos de Investigación de Excelencia (PROMETEU/2021/054). D.A. also acknowledges the financial support of the European Union NextGenerationEU under the National Recovery and Resilience Plan (NRRP) of Ministero dell’Università e della Ricerca (MUR) (Project code PE0000021, “Network 4 Energy Sustainable Transition, NEST). Thanks are also extended to the 2019 Postdoctoral Junior Leader-Retaining Fellowship, la Caixa Foundation (ID100010434 and fellowship code LCF/BQ/PR19/11700011), the “Generalitat Valenciana” (SEJI/2020/034), and the “Ramón y Cajal” program (RYC2019-027940-1) (J.F.-S.). E.P. acknowledges the financial support of the European Research Council under the European Union’s Horizon 2020 research and innovation programme/ERC Grant Agreement No 814804, MOF-reactors. S.S.-N. thanks the fellowship from MINECO (project number CTQ_2017-86735-P). This study forms part of the Advanced Materials programme (MFA/2022/048) and was supported by MCIN with funding from European Union NextGenerationEU (PRTR-C17.11) and by Generalitat Valenciana.

REFERENCES

- (1) Deng, H.; Doonan, C. J.; Furukawa, H.; Ferreira, R. B.; Towne, J.; Knobler, C. B.; Wang, B.; Yaghi, O. M. Multiple Functional Groups of Varying Ratios in Metal-Organic Frameworks. *Science* **2010**, *327*, 846–850.
- (2) Furukawa, H.; Müller, U.; Yaghi, O. M. “Heterogeneity within Order” in Metal-Organic Frameworks. *Angew. Chem., Int. Ed.* **2015**, *54*, 3417–3430.
- (3) Helal, A.; Yamani, Z. H.; Cordova, K. E.; Yaghi, O. M. Multivariate Metal-Organic Frameworks. *Natl. Sci. Rev.* **2017**, *4*, 296–298.
- (4) Osborn Popp, T. M.; Yaghi, O. M. Sequence-Dependent Materials. *Acc. Chem. Res.* **2017**, *50*, 532–534.
- (5) Jiao, J.; Gong, W.; Wu, X.; Yang, S.; Cui, Y. Multivariate Crystalline Porous Materials: Synthesis, Property and Potential Application. *Coord. Chem. Rev.* **2019**, *385*, 174–190.
- (6) Feng, L.; Wang, K.-Y.; Day, G. S.; Zhou, H.-C. The Chemistry of Multi-Component and Hierarchical Framework Compounds. *Chem. Soc. Rev.* **2019**, *48*, 4823–4853.
- (7) Viciano-Chumillas, M.; Liu, X.; Leyva-Pérez, A.; Armentano, D.; Ferrando-Soria, J.; Pardo, E. Mixed Component Metal-Organic Frameworks: Heterogeneity and Complexity at the Service of Application Performances. *Coord. Chem. Rev.* **2022**, *451*, No. 214273.
- (8) Furukawa, H.; Cordova, K. E.; O’Keeffe, M.; Yaghi, O. M. The Chemistry and Applications of Metal-Organic Frameworks. *Science* **2013**, *341*, No. 6149.
- (9) Maurin, G.; Serre, C.; Cooper, A.; Férey, G. The New Age of MOFs and of Their Porous-Related Solids. *Chem. Soc. Rev.* **2017**, *46*, 3104–3107.
- (10) Zhang, X.; Wang, B.; Alsalmé, A.; Xiang, S.; Zhang, Z.; Chen, B. Design and Applications of Water-Stable Metal-Organic Frameworks: Status and Challenges. *Coord. Chem. Rev.* **2020**, *423*, No. 213507.
- (11) Castillo-Blas, C.; de la Peña-O’Shea, V. A.; Puente-Orench, I.; de Paz, J. R.; Sáez-Puche, R.; Gutiérrez-Puebla, E.; Gándara, F.; Monge, A. Addressed Realization of Multication Complex Arrangements in Metal-Organic Frameworks. *Sci. Adv.* **2017**, *3*, No. e1700773.
- (12) Schrimpf, W.; Jiang, J.; Ji, Z.; Hirschle, P.; Lamb, D. C.; Yaghi, O. M.; Wuttke, S. Chemical Diversity in a Metal-Organic Framework Revealed by Fluorescence Lifetime Imaging. *Nat. Commun.* **2018**, *9*, No. 1647.
- (13) Ji, Z.; Li, T.; Yaghi, O. M. Sequencing of Metals in Multivariate Metal-Organic Frameworks. *Science* **2020**, *369*, 674–680.
- (14) Mon, M.; Bruno, R.; Tiburcio, E.; Viciano-Chumillas, M.; Kalinke, L. H. G.; Ferrando-Soria, J.; Armentano, D.; Pardo, E. Multivariate Metal-Organic Frameworks for the Simultaneous Capture of Organic and Inorganic Contaminants from Water. *J. Am. Chem. Soc.* **2019**, *141*, 13601–13609.
- (15) Fan, W.; Yuan, S.; Wang, W.; Feng, L.; Liu, X.; Zhang, X.; Wang, X.; Kang, Z.; Dai, F.; Yuan, D.; Sun, D.; Zhou, H.-C. Optimizing Multivariate Metal-Organic Frameworks for Efficient C₂H₂/CO₂ Separation. *J. Am. Chem. Soc.* **2020**, *142*, 8728–8737.
- (16) Ma, R.; Jiang, H.; Wang, C.; Zhao, C.; Deng, H. Multivariate MOFs for Laser Writing of Alloy Nanoparticle Patterns. *Chem. Commun.* **2020**, *56*, 2715–2718.
- (17) Nandi, F. S.; Wang, S.; Wahiduzzaman, M.; Yadav, V.; Taksande, K.; Maurin, G.; Serre, C.; Devautour-Vinot, S. Multivariate Sulfonic-based Titanium Metal-Organic Frameworks as Superprotonic Conductors. *ACS Appl. Mater. Interfaces* **2021**, *13*, 20194–20200.
- (18) Negro, C.; Martínez Pérez-Cejuela, H.; Simó-Alfonso, E. F.; Herrero-Martínez, J. M.; Bruno, R.; Armentano, D.; Ferrando-Soria, J.; Pardo, E. Highly Efficient Removal of Neonicotinoid Insecticides by Thioether-Based (Multivariate) Metal-Organic Frameworks. *ACS Appl. Mater. Interfaces* **2021**, *13*, 28424–28432.
- (19) Canossa, S.; Ji, Z.; Gropp, C.; Rong, Z.; Ploetz, E.; Wuttke, S.; Yaghi, O. M. System of Sequences in Multivariate Reticular Structures. *Nat. Rev. Mater.* **2022**, *1–10*.
- (20) Fracaroli, A. M.; Siman, P.; Nagib, D. A.; Suzuki, M.; Furukawa, H.; Toste, F. D.; Yaghi, O. M. Seven Post-synthetic Covalent Reactions in Tandem Leading to Enzyme-like Complexity within Metal-Organic Framework Crystals. *J. Am. Chem. Soc.* **2016**, *138*, 8352–8355.

F

<https://doi.org/10.1021/acs.inorgchem.3c00495>
Inorg. Chem. XXXX, XXX, XXX–XXX

- (21) Xia, Q.; Li, Z.; Tan, C.; Liu, Y.; Gong, W.; Cui, Y. Multivariate Metal–Organic Frameworks as Multifunctional Heterogeneous Asymmetric Catalysts for Sequential Reactions. *J. Am. Chem. Soc.* **2017**, *139*, 8259–8266.
- (22) Liang, J.; Xie, Y.-Q.; Wu, Q.; Wang, X.-Y.; Liu, T.-T.; Li, H.-F.; Huang, Y.-B.; Cao, R. Zinc Porphyrin/Imidazolium Integrated Multivariate Zirconium Metal–Organic Frameworks for Transformation of CO₂ Into Cyclic Carbonates. *Inorg. Chem.* **2018**, *57*, 2584–2593.
- (23) Liu, T.-T.; Liang, J.; Xu, R.; Huang, Y.-B.; Cao, R. Salen-Co(III) Insertion in Multivariate Cationic Metal–Organic Frameworks for the Enhanced Cycloaddition Reaction of Carbon Dioxide. *Chem. Commun.* **2019**, *55*, 4063–4066.
- (24) Okamoto, Y.; Ward, T. R. Supramolecular Enzyme Mimics. In *Comprehensive Supramolecular Chemistry II*; Atwood, J., Ed.; Elsevier: Oxford, 2017; pp 459–510.
- (25) Schramm, V. L. Introduction: Principles of Enzymatic Catalysis. *Chem. Rev.* **2006**, *106*, 3029–3030.
- (26) Baratta, M.; Mastropietro, T. F.; Bruno, R.; Tursi, A.; Negro, C.; Ferrando-Soria, J.; Mashin, A. I.; Nezhadanov, A.; Nicoletta, F. P.; De Filipo, G.; Pardo, E.; Armentano, D. Multivariate Metal–Organic Framework/Single-Walled Carbon Nanotube Buckypaper for Selective Lead Decantation. *ACS Appl. Nano Mater.* **2022**, *5*, 5223–5233.
- (27) Negro, C.; Pérez-Cejuela, H. M.; Simó-Alfonso, E. F.; Iqbal, W.; Herrero-Martínez, J. M.; Armentano, D.; Ferrando-Soria, J.; Pardo, E. (Multivariate)-Metal–Organic Framework for Highly Efficient Capture from Aquatic Environmental Matrices. *ACS Appl. Mater. Interfaces* **2023**, *15*, 3069–3076.
- (28) Mon, M.; Bruno, R.; Ferrando-Soria, J.; Bartella, L.; Di Donna, L.; Talia, M.; Lappano, R.; Maggolini, M.; Armentano, D.; Pardo, E. Crystallographic Snapshots of Host–Guest Interactions in Drugs@Metal–Organic Frameworks: Towards Mimicking Molecular Recognition Processes. *Mater. Horiz.* **2018**, *5*, 683–690.
- (29) Mon, M.; Bruno, R.; Elliani, R.; Tagarelli, A.; Qu, X.; Chen, S.; Ferrando-Soria, J.; Armentano, D.; Pardo, E. Lanthanide Discrimination with Hydroxyl-Decorated Flexible Metal–Organic Frameworks. *Inorg. Chem.* **2018**, *57*, 13895–13900.
- (30) Tiburcio, E.; Greco, R.; Mon, M.; Ballesteros-Soberanas, J.; Ferrando-Soria, J.; López-Haro, M.; Hernández-Garrido, J. C.; Oliver-Meseguer, J.; Marini, C.; Boronat, M.; Armentano, D.; Leyva-Pérez, A.; Pardo, E. Soluble/MOF-Supported Palladium Single Atoms Catalyze the Ligand-, Additive-, and Solvent-Free Aerobic Oxidation of Benzyl Alcohols to Benzoic Acids. *J. Am. Chem. Soc.* **2021**, *143*, 2581–2592.
- (31) Sinnott, M. L. Catalytic mechanisms of enzymatic glycosyl transfer. *Chem. Rev.* **1990**, *90*, 1171–1202.
- (32) Ruiz, V. R.; Velly, A.; Santos, L. L.; Leyva-Pérez, A.; Sabater, M. J.; Iborra, S.; Corma, A. Gold catalysts and solid catalysts for biomass transformations: Valorization of glycerol and glycerol–water mixtures through formation of cyclic acetals. *J. Catal.* **2010**, *271*, 351–357.
- (33) Ley, S. V.; Polara, A. A fascination with 1,2-diacetals. *J. Org. Chem.* **2007**, *72*, 5943–5959.
- (34) Veitch, G. E.; Beckmann, E.; Burke, B. J.; Boyer, A.; Maslen, S. L.; Ley, S. V. Synthesis of Azadirachtin: A Long but Successful Journey. *Angew. Chem., Int. Ed.* **2007**, *46*, 7629–7632.
- (35) Davies, G.; Henrissat, B. Structures and mechanisms of glycosyl hydrolases. *Structure* **1995**, *3*, 853–859.
- (36) Mon, M.; Bruno, R.; Sanz-Navarro, S.; Negro, C.; Ferrando-Soria, J.; Bartella, L.; Di Donna, L.; Prejano, M.; Marino, T.; Leyva-Pérez, A.; Armentano, D.; Pardo, E. Hydrolase-like catalysis and structural resolution of natural products by a metal–organic framework. *Nat. Commun.* **2020**, *11*, No. 3080.
- (37) Gaunt, M. J.; Sneddon, H. F.; Hewitt, P. R.; Orsini, P.; Hook, D. F.; Ley, S. V. Development of β -keto 1,3-dithianes as versatile intermediates for organic synthesis. *Org. Biomol. Chem.* **2003**, *1*, 15–16.
- (38) Lewis, J. D.; Van de Vyver, S.; Román-Leshkov, Y. Acid-Base Pairs in Lewis Acidic Zeolites Promote Direct Aldol Reactions by Soft Enolization. *Angew. Chem., Int. Ed.* **2015**, *54*, 9835–9838.
- (39) Corma, A.; Díaz, U.; García, T.; Sastre, G.; Velly, A. Multifunctional Hybrid Organic–Inorganic Catalytic Materials with a Hierarchical System of Well-Defined Micro- and Mesopores. *J. Am. Chem. Soc.* **2010**, *132*, 15011–15021.
- (40) Zhou, G.; Wang, B.; Cao, R. Acid Catalysis in Confined Channels of Metal–Organic Frameworks: Boosting Orthoformate Hydrolysis in Basic Solutions. *J. Am. Chem. Soc.* **2020**, *142*, 14848–14853.
- (41) Rouquerol, J.; Avnir, D.; Fairbridge, C. W.; Everett, D. H.; Haynes, J. H.; Pernicone, N.; Ramsay, J. D. F.; Sing, K. S. W.; Unger, K. K. Recommendations for the Characterization of Porous Solids. *Pure Appl. Chem.* **1994**, *66*, 1739–1758.
- (42) (a) Spek, A. L. PLATON SQUEEZE: a tool for the calculation of the disordered solvent contribution to the calculated structure factors. *Acta Crystallogr., Sect. C: Struct. Chem.* **2015**, *71*, 9–18. (b) Spek, A. L. Structure validation in chemical crystallography. *Acta Crystallogr., Sect. D: Biol. Crystallogr.* **2009**, *65*, 148–155.
- (43) Farrugia, L. J. WinGX suite for small-molecule single-crystal crystallography. *J. Appl. Crystallogr.* **1999**, *32*, 837–838.
- (44) Palmer, D. C. Zeitschrift für Krist. Z. Kristallogr. - Cryst. Mater. **2015**, *230*, 559–572.

Recommended by ACS

Off-Lattice Coarse-Grained Model of Surface-Confined Metal–Organic Architectures

Vitaly A. Gorbunov, Alexander V. Mshlyavtsev, et al.

APRIL 25, 2023

THE JOURNAL OF PHYSICAL CHEMISTRY C

READ 

Neutrophil-Membrane-Coated Biomaterialized Metal–Organic Framework Nanoparticles for Atherosclerosis Treatment by Targeting Gene Silencing

Yi Liu, Xia Chu, et al.

APRIL 06, 2023

ACS NANO

READ 

Comparative Study on Adsorptive Desulfurization of Thiophenic Compounds over Terephthalic Acid-Based and Trimesic Acid-Based Metal–Organic Frameworks

Mahya Ghassa, Saeed Soltanali, et al.

APRIL 18, 2023

ENERGY & FUELS

READ 

Understanding the Hydrocracking of Polycyclic Aromatic Hydrocarbons within FAU Zeolites: Hydrogen Splitting Catalyzed by the Frustrated Lewis Pair

Peng Liu, Donghai Mei, et al.

APRIL 26, 2023

THE JOURNAL OF PHYSICAL CHEMISTRY C

READ 

Get More Suggestions >

Supporting Information (SI) for the manuscript:

**Exploring the Role of Amino Acid-Derived
Multivariate-Metal-Organic Frameworks as Catalyst
in (Hemi)-Ketalization Reactions**

Cristina Negro,^{a†} Sergio Sanz-Navarro,^{b†} Antonio Leyva-Pérez,^{*b} Donatella

Armentano,^{*c} Jesús Ferrando-Soria,^{*a} and Emilio Pardo^{*a}

^aInstituto de Ciencia Molecular (ICMol), Universidad de Valencia, 46980 Valencia, Spain.

^b Instituto de Tecnología Química (UPV-CSIC), Universidad Politècnica de València–Consejo Superior de Investigaciones Científicas, Avda. de los Naranjos s/n, 46022 Valencia, Spain.

^cDipartimento di Chimica e Tecnologie Chimiche (CTC), Università della Calabria, Rende 87036, Italy.

Corresponding authors emails: Antonio Leyva-Pérez (anleyva@itq.upv.es), Donatella Armentano (donatella.armentano@unical.it), Jesús Ferrando-Soria (jesus.ferrando@uv.es) and Emilio Pardo (emilio.pardo@uv.es).

Materials. Reagents were obtained from commercial sources (Merck-Aldrich) and used without further purification otherwise indicated. Anhydrous solvents were obtained from a resin-exchanger apparatus. Reactions were performed in conventional round-bottomed flasks or sealed vials equipped with a magnetic stirrer. All the products were characterized by gas chromatography-mass spectrometry (GC-MS). $\{\text{Sr}^{\text{II}}\text{Cu}^{\text{II}}_6[(S,S)\text{-serimox}]_3(\text{OH})_2(\text{H}_2\text{O})\} \cdot 38 \text{ H}_2\text{O}$ (**1**) and $\{\text{Sr}^{\text{II}}\text{Cu}^{\text{II}}_6[(S,S)\text{-Mecysmox}]_3(\text{OH})_2(\text{H}_2\text{O})\} \cdot 15 \text{ H}_2\text{O}$ (**2**) were prepared following a previously reported procedure.^{1,2}

Physical Techniques. Elemental (C, H, S, N) analyses were performed at the Microanalytical Service of the Universitat de València. FT-IR spectra were recorded on a Perkin-Elmer 882 spectrophotometer as KBr pellets. The thermogravimetric analysis was performed on crystalline samples under a dry N_2 atmosphere with a Mettler Toledo TGA/STDA 851° thermobalance operating at a heating rate of $10 \text{ }^\circ\text{C min}^{-1}$.

Preparation of $\{\text{Sr}^{\text{II}}\text{Cu}^{\text{II}}_6[(S,S)\text{-serimox}]_{1.50}[(S,S)\text{-Mecysmox}]_{1.50}(\text{OH})_2(\text{H}_2\text{O})\} \cdot 12 \text{ H}_2\text{O}$ (3**).** Suitable well-shaped prisms of **3** for SCXRD were synthesized by slow diffusion in H-shaped tubes of aqueous solutions containing stoichiometric amounts of an equimolar mixture of $(\text{Me}_4\text{N})_2\{\text{Cu}_2[(S,S)\text{-serimox}](\text{OH})_2\} \cdot 5\text{H}_2\text{O}$ (0.118 g, 0.18 mmol) and $(\text{Me}_4\text{N})_2\{\text{Cu}_2[(S,S)\text{-Mecysmox}](\text{OH})_2\} \cdot 5\text{H}_2\text{O}$ (0.129 g, 0.18 mmol) in one arm and $\text{Sr}(\text{NO}_3)_2$ (0.025 g, 0.12 mmol) in the other. They were isolated by filtration on paper and air-dried. Alternatively, a gram-scale procedure can be also successfully followed by mixing greater amounts of $(\text{Me}_4\text{N})_2\{\text{Cu}_2[(S,S)\text{-serimox}](\text{OH})_2\} \cdot 5\text{H}_2\text{O}$ (3.96 g, 6.0 mmol) and $(\text{Me}_4\text{N})_2\{\text{Cu}_2[(S,S)\text{-Mecysmox}](\text{OH})_2\} \cdot 5\text{H}_2\text{O}$ (4.32 g, 6 mmol) in water (50 mL), and dropwise adding another aqueous solution of $\text{Sr}(\text{NO}_3)_2$ (0.846 g, 4.0 mmol). After allowing to react the final mixture of reaction, under stirring, for 6 h, a green polycrystalline powder was isolated by filtration and

characterised by C, H, S, N analysis to give the final formula of $\{\text{Sr}^{\text{II}}\text{Cu}^{\text{II}}_6[(S,S)\text{-serimox}]_{1.50}[(S,S)\text{-Mecysmox}]_{1.50}(\text{OH})_2(\text{H}_2\text{O})\} \cdot 12 \text{ H}_2\text{O}$. Anal. Calcd for **3**: $\text{C}_{27}\text{Cu}_6\text{SrS}_3\text{H}_{66}\text{N}_6\text{O}_{40}$ (1679.92): C, 19.30; H, 3.96; S, 5.73; N, 5.00 %. Found: C, 19.63; H, 3.91; S, 5.78; N, 5.03%. IR (KBr): = 1605 and 1602 cm^{-1} (C=O)

Gas adsorption. The N_2 adsorption-desorption isotherms at 77 K were carried out on polycrystalline samples of **3** with a BELSORP-mini-X instrument. Samples were first activated with methanol and then evacuated at 348 K during 16 hours under 10^{-6} Torr prior to their analysis.

X-ray Powder Diffraction Measurements. Polycrystalline samples of **3** was introduced into a 0.5 mm borosilicate capillar prior to being mounted and aligned on a Empyrean PANalytical powder diffractometer, using Cu $K\alpha$ radiation ($\lambda = 1.54056 \text{ \AA}$). Five repeated measurements were collected at room temperature ($2\theta = 2\text{--}45^\circ$) and merged in a single diffractogram. A polycrystalline sample of **3** was also measured after catalysis following the same procedure.

X-ray Crystallographic Data Collection and Structure Refinement. Crystal of **3** with 0.16 x 0.14 x 0.12 mm as dimensions was selected and mounted on a MiTeGen MicroMount in Paratone oil and very quickly placed on a liquid nitrogen stream cooled at 90 K, to avoid the possible degradation upon dehydration or exposure to air. Diffraction data were collected on a Bruker-Nonius X8APEXII CCD area detector diffractometer using graphite-monochromated Mo- $K\alpha$ radiation ($\lambda = 0.71073 \text{ \AA}$). The data were processed through SAINT reduction and SADABS multi-scan absorption software.³ The structure was solved with the SHELXS structure solution program, using the Patterson method. The model was refined with version 2018/3 of SHELXL against F^2 on all data by full-matrix least squares.^{4,5}

In the refinement of **3**, all non-hydrogen atoms were refined anisotropically except some highly dynamically disordered atoms of methycysteine and serine arms and solvent water molecules. The use of some bond lengths restraints, applied on atoms belonging to highly dynamic moieties, has been reasonably imposed and related to the expected thermal motion, likely depending on the large size of the huge cages of the frameworks (DFIX and ISOR). For instance, EADP for group of atoms of the fragments expected to have essentially similar ADPs have been applied. All the hydrogen atoms of the ligand were set in calculated position and refined isotropically using the riding model. Hydrogen atoms on thermally disordered solvent water molecules were neither found nor calculated.

As stated in main text, the oxamidato-bridged dicopper(II) units of $\{\text{Cu}^{\text{II}}_2[(S,S)\text{-serimox}]\}$ and $\{\text{Cu}^{\text{II}}_2[(S,S)\text{-mecysmox}]\}$, inserted with a 1:1 ratio in **3**, exhibit a statistically disorder in the crystal structure, where the very similar percentage of serimox and mecysmox leads to a completely superimposed snapshot of mixed $\{\text{Cu}^{\text{II}}_2[(S,S)\text{-mecysmox/serimox}]\}$ dimers (see inset of Figure 1a).

A summary of the crystallographic data and structure refinement for **3** crystal structure is given in Table S1. The comments for the alerts A and B are described in the CIF using the validation reply form (vrf). CCDC reference number is 2241172.

The final geometrical calculations on free voids and the graphical manipulations were carried out with PLATON⁶ implemented in WinGX,⁷ and CRYSTAL MAKER programs,⁸ respectively.

Catalytic experiments.

Leaching test. MTV-MOF **3** (25 mg, 100 wt%) was placed in a 2 ml vial equipped with a magnetic stir bar, and the corresponding amount of MeOH (1 mL) was added.

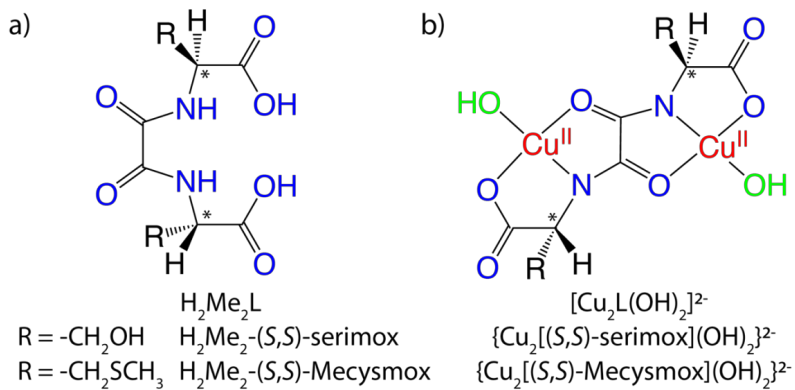
Then, benzaldehyde **4** (26 μL , 0.24 mmol) was added via syringe at room temperature. The mixture was sealed and magnetically stirred in a pre-heated oil bath at 60 $^{\circ}\text{C}$. After 30 min reaction time, the solid catalyst was filtered off and the filtrates were magnetically stirred in a pre-heated oil bath at 60 $^{\circ}\text{C}$ for 7 h 30 min, taking periodically aliquots of 0.125 mL to be analysed by GC. The kinetic results were compared with the reaction containing MTV-MOF **3**.

Reuses of the solid catalyst. The general reaction procedure above was followed. After the reaction time, the solid catalyst was recovered by filtration and washed with hexane. After drying, MTV-MOF **3** was weighted and benzaldehyde **4** added in proportional amount to keep the initial relative molar ratios.

Table S1. Summary of Crystallographic Data for **3**.

Compound	3
Formula	C ₂₇ Cu ₆ SrS ₃ H ₆₆ N ₆ O ₄₀
<i>M</i> (g mol ⁻¹)	1679.89
λ (Å)	0.71073
Crystal system	Hexagonal
Space group	<i>P</i> 6 ₃
<i>a</i> (Å)	17.9936(10)
<i>c</i> (Å)	13.0313(8)
<i>V</i> (Å ³)	3653.9(5)
<i>Z</i>	2
ρ_{calc} (g cm ⁻³)	1.527
μ (mm ⁻¹)	2.608
<i>T</i> (K)	293
θ range for data collection (°)	2.614 to 26.279
Completeness to $\theta = 25.0$	100%
Measured reflections	66317
Unique reflections (Rint)	4938 (0.0632)
Observed reflections [<i>I</i> > 2 σ (<i>I</i>)]	3830
Goof	1.054
Absolute structure parameter (Flack)	0.046(5)
<i>R</i> ^a [<i>I</i> > 2 σ (<i>I</i>)] (all data)	0.0670 (0.0870)
<i>wR</i> ^b [<i>I</i> > 2 σ (<i>I</i>)] (all data)	0.1982 (0.2179)
Largest diff. peak and hole	1.496 and -0.566 e.Å ⁻³

^a $R = \sum(|F_o| - |F_c|) / \sum |F_o|$. ^b $wR = [\sum w(|F_o| - |F_c|)^2 / \sum w|F_o|^2]^{1/2}$. ^c The poor quality of the crystals of **2** allowed only cell parameters determination.



Scheme S1. Chemical structures of the chiral bis(amino acid)oxalamide ligands (a), highlighting the potential coordination sites and chiral centers (*) and the corresponding dianionic bis(hydroxo)dicopper(II) complexes (b).

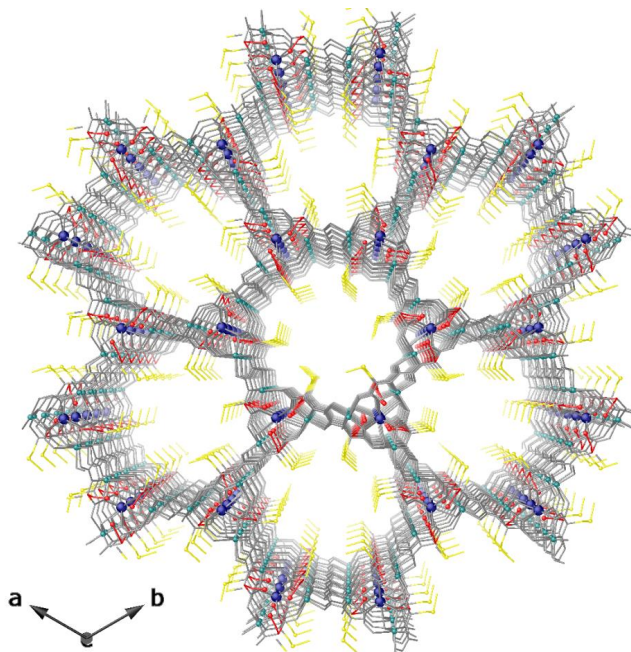


Figure S1. Perspective view of the crystal of **3** along *c* crystallographic axes. Copper(II) and strontium(II) ions from the network are represented as cyan and blue spheres, respectively. Oxygen and sulfur atoms from the residues are shown as red and yellow spheres, respectively. The organic ligands are represented as gray sticks, with the exception of *L*-serine ($-\text{CH}_2\text{OH}$) and *L*-methylcysteine ($-\text{CH}_2\text{SCH}_3$) residues, which are represented as red and yellow sticks, respectively.

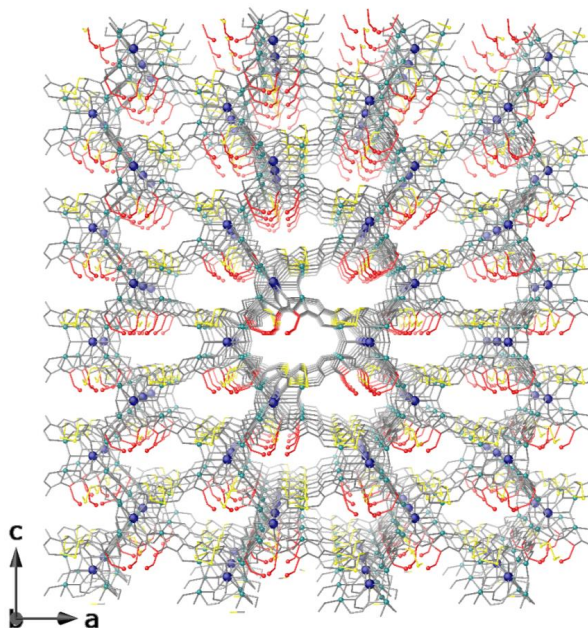


Figure S2. Perspective view of the crystal of **3** along *b* crystallographic axes. Copper(II) and strontium(II) ions from the network are represented as cyan and blue spheres, respectively. Oxygen and sulfur atoms from the residues are shown as red and yellow spheres, respectively. The organic ligands are represented as gray sticks, with the exception of *L*-serine ($-\text{CH}_2\text{OH}$) and *L*-methylcysteine ($-\text{CH}_2\text{SCH}_3$) residues, which are represented as red and yellow sticks, respectively.

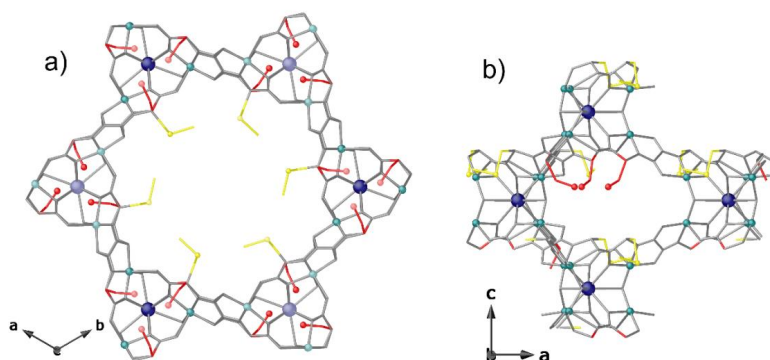


Figure S3. Details of conformations and distribution of *L*-serine ($-\text{CH}_2\text{OH}$) and *L*-methylcysteine ($-\text{CH}_2\text{SCH}_3$) residues a) along *c* and b) *b* crystallographic axis, respectively, pointing towards big pores and smallest voids in **3**. The organic ligands are represented as gray sticks, with the exception of *L*-serine ($-\text{CH}_2\text{OH}$) and *L*-methylcysteine ($-\text{CH}_2\text{SCH}_3$) residues, which are represented as red and yellow sticks, respectively.

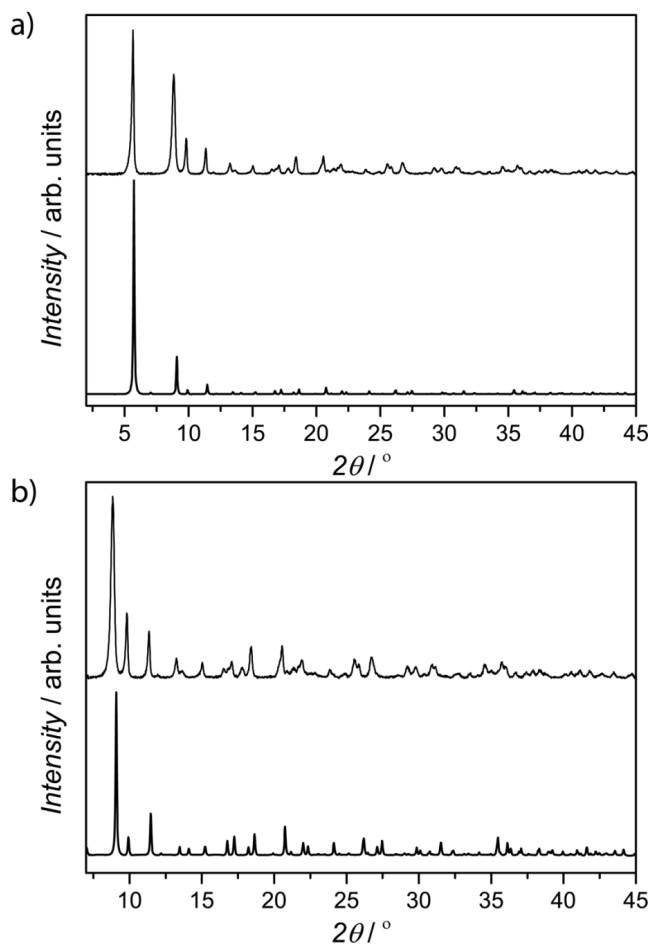


Figure S4. Theoretical (bottom) and experimental (top) PXRD patterns of **3** in the $2.0-45.0^\circ$ (a) and $7.0-45.0^\circ$ (b) 2θ range measured at room temperature.

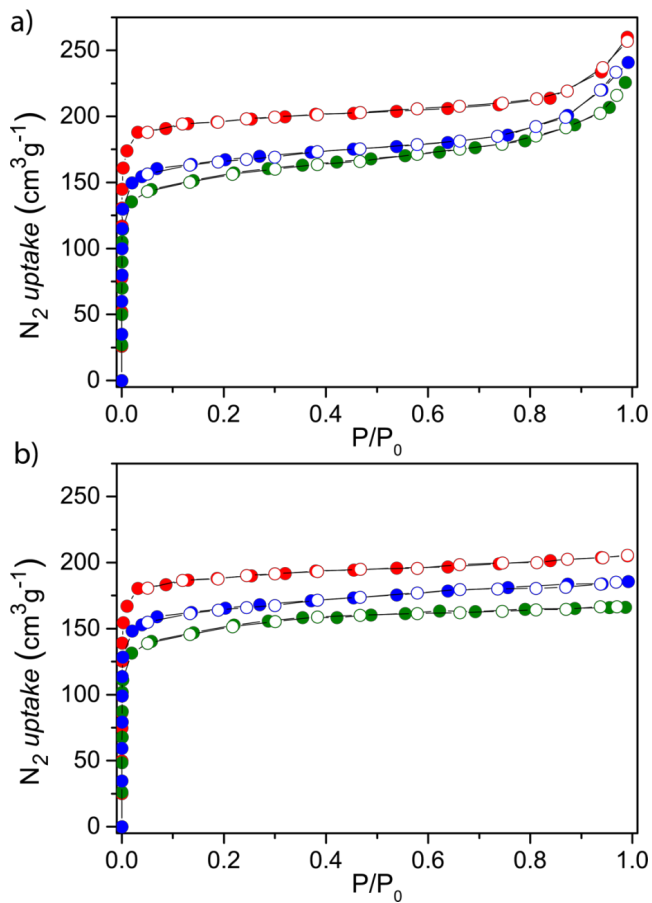


Figure S5. (a) N_2 (77 K) adsorption isotherms for the activated compounds 1 (red), 2 (green) and 3 (blue). (b) N_2 (77 K) adsorption isotherms for the activated compounds 1 (red), 2 (green) and 3 (blue) after catalytic experiments. Filled and empty symbols indicate the adsorption and desorption isotherms, respectively. The samples were activated at 70 °C under reduced pressure for 16 h prior to carry out the sorption measurements.

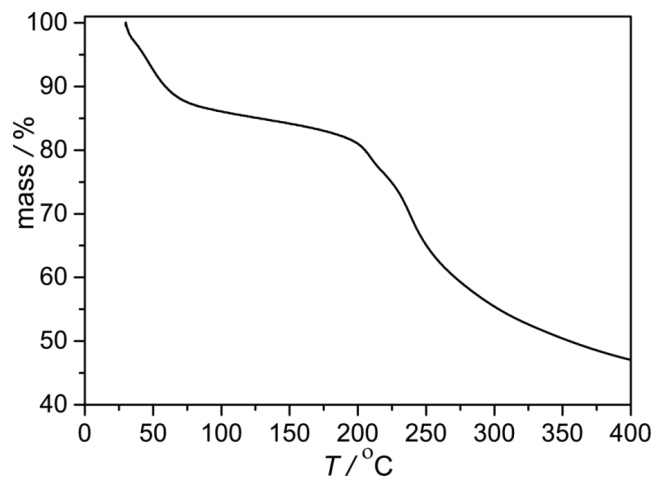


Figure S6. Thermo-Gravimetric analysis (TGA) of **3** under dry N₂ atmosphere.

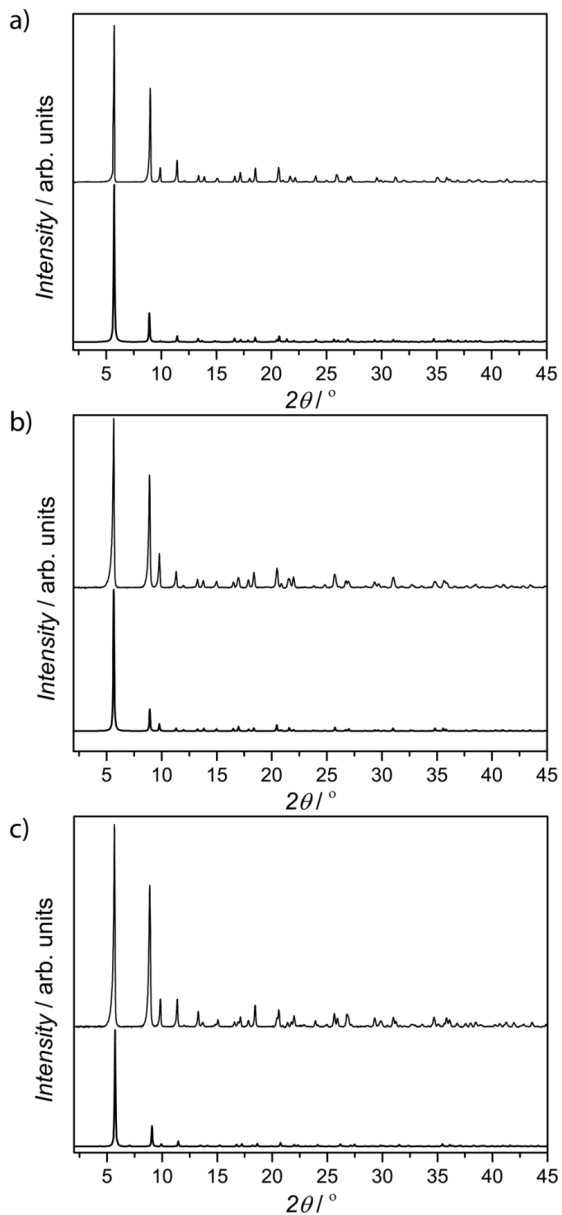


Figure S7. Theoretical (bottom) and experimental (top) PXRD patterns of **1** (a), **2** (b) and **3** (c) after catalysis in the 2.0–45.0° 2θ range measured at room temperature.

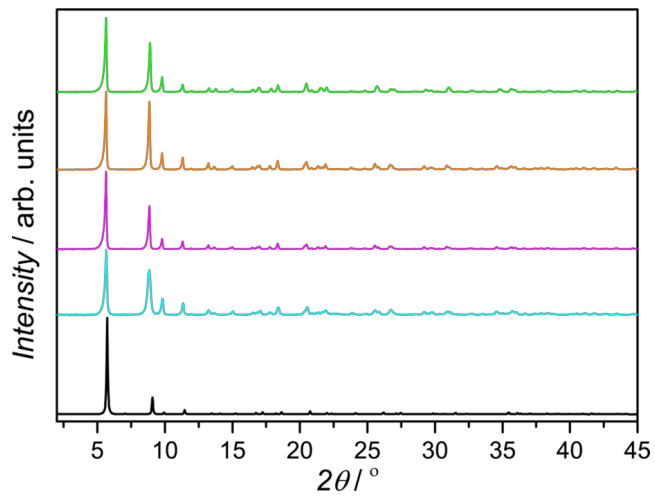


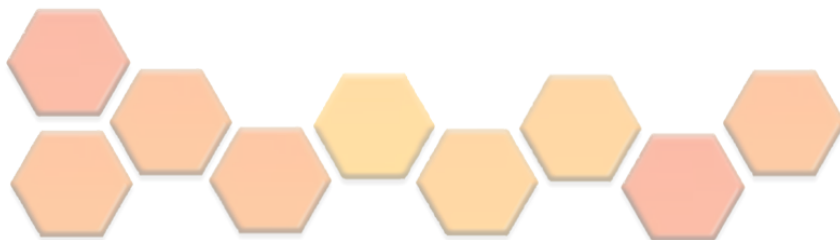
Figure S8. Theoretical (bottom) and experimental (top) PXRD patterns of **3** after being immersed in hot water (cyan), dimethylformamide (purple), methanol (orange) and acetonitrile (light green) in the 2.0–45.0° 2θ range measured at room temperature.

References

1. (a) Mon, M.; Bruno, R.; Ferrando-Soria, J.; Bartella, L.; Di Donna, L.; Talia, M.; Lappano, R.; Maggiolini, M.; Armentano, D.; Pardo, E. Crystallographic Snapshots of Host–Guest Interactions in Drugs@metal–Organic Frameworks: Towards Mimicking Molecular Recognition Processes. *Mater. Horizons* **2018**, *5*, 683–690. (b) Mon, M.; Bruno, R.; Elliani, R.; Tagarelli, A.; Qu, X.; Chen, S.; Ferrando-Soria, J.; Armentano, D.; Pardo, E. Lanthanide Discrimination with Hydroxyl-Decorated Flexible Metal–Organic Frameworks. *Inorg. Chem.* **2018**, *57*, 13895–13900
2. Tiburcio, E.; Greco, R.; Mon, M.; Ballesteros-Soberanas, J.; Ferrando-Soria, J.; López-Haro, M.; Hernández-Garrido, J. C.; Oliver-Meseguer, J.; Marini, C.; Boronat, M.; Armentano, D.; Leyva-Pérez, A.; Pardo, E. Soluble/MOF-Supported Palladium Single Atoms Catalyze the Ligand-, Additive-, and Solvent-Free Aerobic Oxidation of Benzyl Alcohols to Benzoic Acids. *J. Am. Chem. Soc.* **2021**, *143*, 2581–2592.
3. Sheldrick, G. M. *SADABS Program for Absorption Correction*, ver. 2.10; Analytical X-ray Systems: Madison, WI, 1998.
4. Sheldrick, G. M. A short history of SHELX. *Acta. Crystallogr., Sect. A: Found. Crystallogr.* **2008**, *64*, 112–122.
5. Sheldrick, G. M. Crystal structure refinement with SHELXL. *Acta. Crystallogr., Sect. C: Struct. Chem.* **2015**, *71*, 3–8.
6. Parsons, S.; Flack, H. D.; Wagner, T. Use of intensity quotients and differences in absolute structure refinement. *Acta Crystallogr., Sect. B: Struct. Sci., Cryst. Eng. Mater.* **2013**, *69*, 249–259.
7. (a) Farrugia, L. J. WinGX suite for small-molecule single-crystal crystallography. *J. Appl. Crystallogr.* **1999**, *32*, 837–838. (b) Farrugia, L. J. WinGX and ORTEP for Windows: An Update. *J. Appl. Crystallogr.* **2012**, *45*, 849–854.
8. Palmer, D. C. Zeitschrift für Krist. *Z. Kristallogr. – Cryst. Mater.* **2015**, *230*, 559–572.



**PUBLICATION 3: Metal-Organic Frameworks
as Unique Platforms to Gain Insight of σ -Hole
Interactions for the Removal of Organic Dyes
from Aquatic Ecosystems**



FULL PAPER

Metal-Organic Frameworks as Unique Platforms to Gain Insight of σ -Hole Interactions for the Removal of Organic Dyes from Aquatic Ecosystems

Cristina Negro,^{[a],†} Paula Escamilla,^{[a],†} Rosaria Bruno,^[b] Jesus Ferrando-Soria,^{*,[a]} Donatella Armentano,^{*,[b]} and Emilio Pardo^{*,[a]}

Abstract: The combination in metal-organic frameworks (MOFs) of rich host-guest chemistry and high crystallinity have situated them in an advantageous position respect traditional porous materials, to gain insight on specific and barely exploited weak noncovalent supramolecular interactions. In particular, sulfur σ -hole interactions are known to be key in the biological activity of living beings as well as on relevant molecular recognitions processes, but they have been barely explored so far. Here we describe how the combination of the intrinsic features of MOFs, especially the possibility of using single-crystal X-ray crystallography (SCXRD) can be an extremely valuable tool to gain insight on sulfur σ -hole interactions, and how their rational exploitation can be enormously useful in the efficient removal of organic dyes from aquatic ecosystems. Thus, we have used a 3D MOF, prepared from the amino acid *L*-methionine and possessing channels decorated with $-\text{CH}_2\text{CH}_2\text{SCH}_3$ thioalkyl chains, to remove a family of organic dyes at very low concentrations (10 ppm) from water. This MOF is able to efficiently capture the four dyes in a very fast manner, reaching within five minutes nearly the maximum removal. Remarkably, the crystal structure of the different organic dyes within MOFs channels could be determined by SCXRD. This have enabled us to directly visualize the key role sulfur σ -hole interactions play on the removal of organic dyes from aqueous solutions, representing one of the first studies on the rational exploitation of σ -hole interactions for water remediation.

Introduction

Weak noncovalent interactions are ubiquitous in many relevant processes occurring in living beings, and represent one of the most important tools in Supramolecular Chemistry to mimic/emulate them.^[1–4] Among them, σ -hole interactions are of particular interest. A σ -hole is the region of electron deficiency that appears in the outer lobe of an orbital, when an atom from the group V–VII –with half-filled *p* orbitals–, participate in a covalent bond.^[5–7] This σ -hole could create a region of positive electrostatic potential –if the rest of the molecule presents a relatively sufficient electron-withdrawing nature respect the group V–VII atom, and this one is sufficiently polarizable– able to interact with electron donors, such as nitrogen and oxygen, and even, π -systems. Despite this interaction is present in key supramolecular recognitions processes and is very relevant in biological activity, somehow their importance has been underestimated in comparison to hydrogen-bonds, with the exception of halogen ones.^[7] For example, this is the case of sulfur σ -hole interaction, which mainly has been described in post-analysis of close contacts in protein data bank or as stabilizing agent of desired conformations of drugs for interacting with receptors.^[8–12] However, the rational use of such interaction for specific applications has been barely explored.^[13–20]

Metal-organic frameworks (MOFs)^[21–28] are a class of crystalline porous inorganic-organic materials, whose rich host-guest chemistry^[29–35] and high crystallinity,^[36–38] together with the possibility to have –to a certain extent– a control of their dimensionality, topology and functionality by chemical design,^[39–45] have situated them in an advantageous position among other porous materials. This has been clearly exemplified by the continuous growth of novel aesthetically pleasant crystal structures,^[46–49] as well as by the wide range of applications where they have shown successful –e.g. gas storage and separation, catalysis, drug delivery, conductivity, molecular recognition of small molecules, encapsulation of functional moieties, magnetism, chemical nanoreactors and water remediation.^[50–61] Indeed, relevant advances performed in MOFs chemistry have been, mainly, consequence of the combined possibility to tailor the functionalities decorating MOFs channels by chemical design and the application of single-crystal X-ray diffraction (SCXRD) as basic characterization tool.^[62–67] This has demonstrated as a powerful approach to understand/rationalize host-guest interactions, and eventually found structure-properties relationships that have enabled positive feedback of knowledge to develop more performant MOFs.^[68] Thus, MOFs are, *a priori*, excellent test benches to gain insight of specific molecular recognitions interactions, such as sulfur σ -hole, and to try to exploit them towards a targeted application.

Contamination of aquatic ecosystems with organic dyes represent a severe environmental problem, having a negative impact on the quality of aquatic ecosystems –i.e. avoiding the photoactivity of plants and algae, and representing a health threat for fish as consequence of their teratogenic, mutagenic and carcinogenic character– and consequently on humans life.^[69] Different technologies have been studied for the removal of organic dyes from wastewater streams.^[70–72] Among them, the use of MOFs for their capture and/or photodegradation has revealed as a very promising approach.^[70,73–76] This is mainly due to the intrinsic characteristic properties of MOFs highlighted above. However, despite the great structural, compositional and functional diversity of MOFs, its potential has been poorly explored and somehow underdeveloped so far in this field, and consequently more research efforts are needed to fully unleash them.

^a Departamento de Química Inorgánica, Instituto de Ciencia Molecular (ICMol), Catedrático José Beltrán Martínez, 2, Universidad de Valencia, 46100 Paterna, Valencia, Spain.

^b Dipartimento di Chimica e Tecnologia Chimiche (CTC), Università della Calabria, via P. Bucci, 12, Rende 87036, Cosenza, Italy.

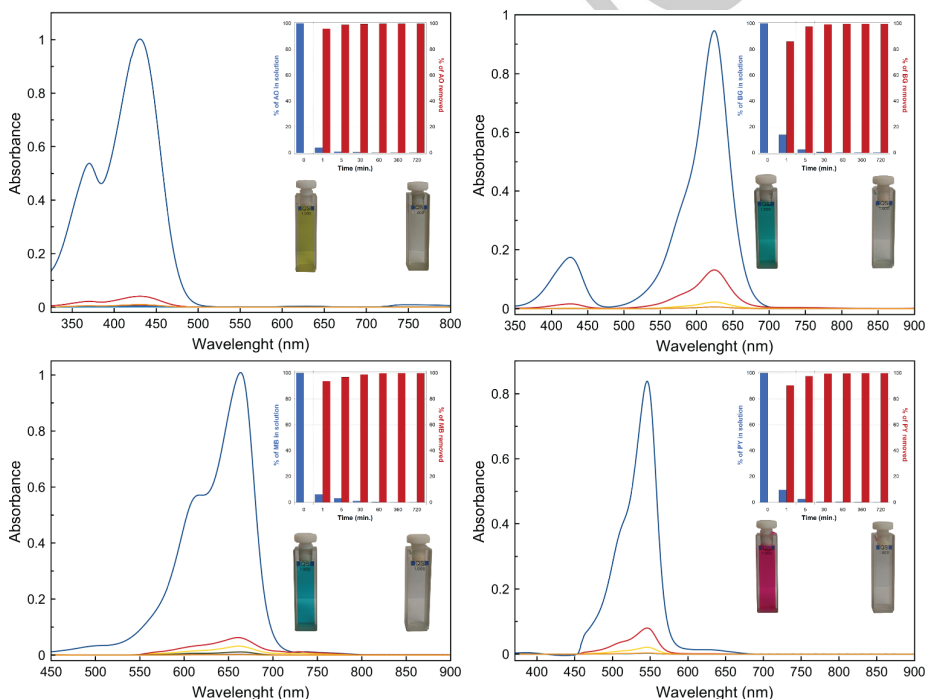
[†] These two authors have equally contributed to this work.

Corresponding authors' emails: donatella.armentano@unical.it, emilio.pardo@uv.es, jesus.ferrando@uv.es. Supporting information for this article is given via a link at the end of the document. Crystallographic data: CCDC 2132442-2132446.

FULL PAPER

One of our research lines is focused on exploiting the differentiating features of MOFs toward catalytic and water remediation applications.^[62,70] Along the development of our investigations, we have realized of the relevance in the developed materials of considerably underestimated sulfur σ -hole interactions.^[13–20] In this context, we aim here to extend our knowledge on them, through their rational application for the removal of organic dyes from aquatic ecosystems. In order to do so, we have taken advantage of a neutral 3D MOF, with formula $\{\text{Sr}^{\text{II}}\text{Cu}_6^{\text{II}}[(\text{S},\text{S})\text{-methox}]_3(\text{OH})_2(\text{H}_2\text{O})\} \cdot 16\text{H}_2\text{O}$ (**1**; methox = bis[(*S*)-methionine]oxalyl diamide), constructed with oxamate ligands derived from the natural amino acid *L*-methionine (see Experimental Section for synthetic details).^[13,14,16,19] The selection of **1** has not been innocent. This has been based on our previous reports in an isorecticular MOF to **1** –with calcium instead of

recognition properties –for distinct metal ions and some neonicotinoids– and high crystallinity –which have enabled to unveil the crystal structure of diverse and unique host-guest assemblies.^[15,18] In this work, we have observed **1** is capable to remove, efficiently, four organic dyes (Auramine O (AO), Brilliant Green (BG), Methylene Blue (MB) and Pyronin Y (PY)) at very low concentrations (10 ppm) from water (Scheme S1). Indeed, this process takes place with a very fast kinetics, improving, notably, the performance of a related reported MOF with serine hydroxyl-residues functionalizing the pores,^[77] which, *a priori*, would be expected to interact more efficiently with organic molecules through hydrogen-bonds. Thanks to the high degree of crystallinity of **1** and application of cutting-edge single-crystal X-ray crystallography techniques, we have been able to get unique snapshots of the assembled host-guest systems, which have



strontium.^[13,14] This MOF exhibited functional channels decorated with flexible $-\text{CH}_2\text{CH}_2\text{SCH}_3$ thioalkyl chains with nice molecular

allowed to rationalize the nice removal efficiency of **1**, and more importantly, improve our knowledge on sulfur σ -hole interaction.

Figure 1. Evolution with time of the UV-Vis absorption spectra of 10 ppm solutions of AO (a), BG (b), MB (c) and PY (d) in real water samples from Turia river when using 50 mg of pellets of **1** as adsorbent. Colors code: Blue: $t = 0$; Red: $t = 1$ min.; Yellow: $t = 5$ min.; Orange: $t = 30$ min.; Light blue: $t = 360$ min.; Green: $t = 720$ minutes. The insets show the kinetic of adsorption for each dye. The photographs illustrate the colors of the solutions at the beginning (left) and after only one minute of the dye removal experiments (right).

Results and Discussion

Removal Experiments of Organic Dyes.

FULL PAPER

In order to evaluate the removal efficiency of **1** toward the four selected organic dyes –Auramine O (AO), Brilliant Green (BG), Methylene Blue (MB) and Pyronin Y (PY)– we processed **1** in the form of extruded pellets, by mixing polycrystalline powders of **1** with commercial Matrimid in 80:20 ratios (Experimental Section). The structuration of MOFs is a very interesting and necessary topic of research, which allows to possess materials with improved applicability as consequence of their better handling and longer lifetime.^[76] However, in some cases it is difficult to retain the chemical/physical properties of the selected MOF. To preclude this option, we have performed PXRD pattern of the prepared pellets of **1**, which evidence that is isostructural to polycrystalline powders of **1** (Figure S1).

Then, using the prepared pellets of **1** (50 mg), we have studied its removal efficiency of organic dyes using individual spiked solutions of each of them (10 mL, 10 ppm) in real water samples from Turia river (Valencia, Spain). These processes were followed with UV-vis spectroscopy (Figure 1), measuring the decrease in the intensity of the respective characteristic/principal absorption band in the visible region at different times (1, 5, 30, 60, 360 and 720 min). The kinetic profile obtained (inset of Figure 1 and Table S2) evidenced the efficient and fast adsorption of all four tested dyes, reaching nearly 90 % of removal after only 5 min. This contrast with the serine-based MOF, which need nearly 24 hours to reach the same capture efficiency.^[77] This removal efficiency and kinetics of adsorption was even maintained when using a multi-dye mixture solution, 10 ppm of each of all four dyes (Figure S2, Table S3 and Experimental Section). Here, it is

noteworthy to remark the relevance of the observed results by **1**, which not only is capable to capture these organic contaminants at very low concentration –similar to the ones found in industrial wastewaters– in a very efficient and fast manner, but also in samples where the presence of other ions could interfere the adsorption process.

Recyclability, maximum uptake and scale-up.

The reusability and structural and physical integrity of any adsorbent are parameters of main relevance in order to fully characterize them and think toward real-world applications. We observed **1** could be easily regenerated by immersing the extruded pellets in a methanol solution for 15 min, while retaining the crystallinity –as PXRD in Figure S1 evidenced– and maintaining the removal efficiency in the next capture experiment (Table S4). To evaluate the maximum loading capacity of **1** for each organic dye, we prepared aqueous saturated solutions of each dye and soaked **1** for two weeks while replacing the saturated solution every 12 hours. Maximum uptakes of 598.85, 786.80, 554.01 and 542.56 mg g⁻¹ were obtained for AO, BG, MB and PY, respectively –see Experimental Section for characterization details. Overall, these features together with the easiness to produce **1** at multigram-scale (see Experimental Section) and environmentally benign nature of its components, makes **1** an attracting candidate to be tested in pilot plants or structured in mixed-matrix membranes.

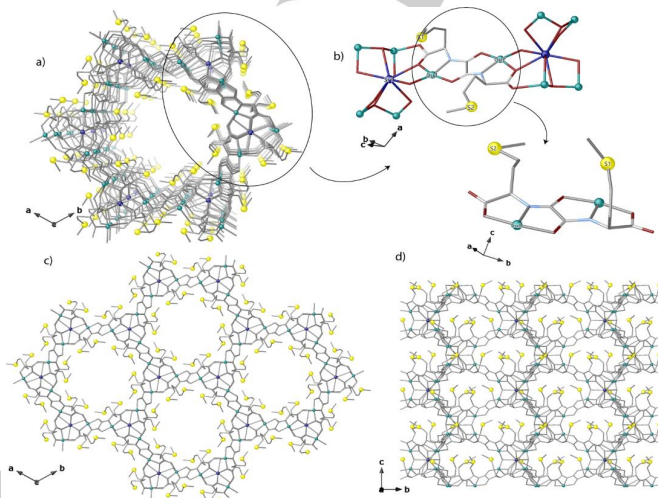


Figure 2. Crystal structure of **1**: (a) Perspective view along *c* crystallographic axis of a single channel in crystal structure of **1**. (b) Fragments of **1** showing the diatomic bis(hydroxo) dicopper(II) building blocks. Views of a fragment of **1** in the *ab* (c) and *bc* (d) planes, respectively. Copper, strontium and sulphur atoms are represented by cyan, blue and yellow spheres, respectively, whereas the ligands (except sulphur) are depicted as sticks (carbon: gray, oxygen: red and nitrogen: blue).

FULL PAPER

X-ray Crystal Structure.

In order to elucidate the host-guest interactions established between **1** (structure shown in Figure 2) and the captured organic dyes –playing special attention to sulfur σ -hole ones–, crystals of **1** were soaked in saturated acetonitrile solutions of each organic dye for one week. After that period, crystals of enough quality to solve the crystal structure of four host-guest systems by means of single-crystal X-ray diffraction could be obtained (Table S1). Their formula, supported by CHSN elemental analysis, inductively coupled plasma mass spectrometry (ICP-MS) and thermogravimetric analysis (TGA) (see Experimental Section and Supporting Information), are: $\text{AO}@\{\text{Sr}^{\text{II}}\text{Cu}_6^{\text{II}}[(\text{S},\text{S})\text{-methox}]_3(\text{OH})_2(\text{H}_2\text{O})\} \cdot 6\text{H}_2\text{O}$ (**AO@1**), $\text{BG}@\{\text{Sr}^{\text{II}}\text{Cu}_6^{\text{II}}[(\text{S},\text{S})\text{-methox}]_3(\text{OH})_2(\text{H}_2\text{O})\} \cdot 5\text{H}_2\text{O}$ (**BG@1**), $\text{MB}@\{\text{Sr}^{\text{II}}\text{Cu}_6^{\text{II}}[(\text{S},\text{S})\text{-methox}]_3(\text{OH})_2(\text{H}_2\text{O})\} \cdot 6\text{H}_2\text{O}$ (**MB@1**) and $\text{PY}@\{\text{Sr}^{\text{II}}\text{Cu}_6^{\text{II}}[(\text{S},\text{S})\text{-methox}]_3(\text{OH})_2(\text{H}_2\text{O})\} \cdot 6\text{H}_2\text{O}$ (**PY@1**). The resolution of the crystal structure of adsorbates allowed the atomically-precise visualization of the main host-guest interactions, likely at the origin of the efficient captures of pollutant dyes by the thio-alkyl residues decorating the framework (Figures 3, 4 and S3-S9).

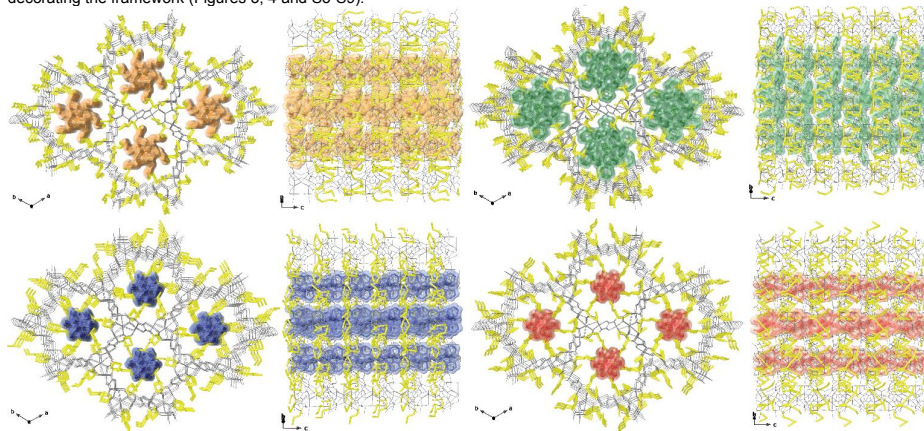


Figure 3. Perspective views in the *ab* (left) and *bc* (right) planes of the host-guest assemblies of **AO@1** (a), **BG@1** (b), **MB@1** (c) and **PY@1** (d). The networks are represented as light gray sticks with $-\text{CH}_2\text{CH}_2\text{SCH}_3$ ethylthiomethyl residues as yellow sticks and guest organic dyes as orange (AO), green (BG), blue (MB) and red (PY) solid surfaces. Free water molecules have been omitted for clarity.

As far as **AO@1**, **MB@1** and **PY@1** is concerned, the capture of Cl^- anions, nicely blocked in the most hindered voids of the MOF by directly $\text{S}\cdots\text{Cl}$ interaction [2.43, 2.20 and 2.87 Å, for **AO@1**, **MB@1** and **PY@1**, respectively], can be seen as a driving force to the further insertion of cationic dye molecules, which are captured thanks to $\text{S}\cdots\pi$ interactions, supported also by those electrostatic interactions (Figures 4, S6 and S8).

In **AO@1** and **PY@1** the network host displayed a more open structure when compared with **MB@1** and especially with **BG@1**. The bigger size and/or less efficient packing of the latter dyes likely accounting for that. Indeed, in **PY@1** methionine arms

The four compounds **AO@1**, **BG@1**, **MB@1** and **PY@1** are isomorphous to **1**, crystallizing in the $P6_3$ chiral space group of the hexagonal system. This behaviour confirms the robustness of **1** as hosting matrix. They are built by uni-nodal **acs** six-connected three-dimensional (3D) strontium(II)-copper(II) porous networks, decorated by highly flexible $\text{CH}_2\text{CH}_2\text{SCH}_3$ thioalkyl chains, which are capable to act as receptors towards guest dyes (Figures 2-4, S4, S6 and S8). The four crystal structures undoubtedly evidence that AO, BG, MB and PY guest molecules are encapsulated in the nanopores of **1**, where they are recognized by the thioether arms of the methionine residues. As expected for loaded-porous structures, the dye molecules displayed a severe disorder in pores, both dynamical and statistic (see Experimental Section). All the crystal structures exhibit different allocations of guests with a 1:3 statistical distribution (Figures S3, S5, S7 and S9) strictly dependent on the size and chemical nature of the dye. The main host-guest interactions are assured by sulfur atoms directly interacting either with Cl^- anions in **AO@1**, **MB@1** and **PY@1** or with aromatic rings via the low-lying σ^* orbitals of the C-S bond (σ -hole) –available for interaction with electron donors such as the four dyes π -systems.

are distended to interact through $\text{S}\cdots\text{H-C}$ weak interactions [shortest $\text{S}\cdots\text{H-C}$ distances of 2.88 and 3.16 Å], which anchor external aromatic rings to the walls of the MOF. The severe statistic and thermal disorder did not allow us to model terminal $-\text{N}(\text{CH}_3)_2$ (see Experimental Section for details). However, the defined orientations gave clues on potential $\text{C-H}\cdots\text{N}$ intermolecular interactions involving adjacent molecules. Indeed, supramolecular chains of Pyronin Y molecules evidence a propagation along the direction of channels, as imposed by the hosting matrix, which not only host but also align guests.

FULL PAPER

More evident σ -hole interactions are detected in **AO@1** crystal structure, where $-\text{CH}_2\text{CH}_2\text{SCH}_3$ methionine arms point toward the $-\text{NH}_2^+$ group of the Auramine O organic dye [S...N distance of 4.44 Å] (Figure 4). Further stabilizing host-guest interactions occur between $-\text{CH}_2\text{CH}_2\text{SCH}_3$ ethylthiomethyl chains and aromatic rings of AO dye molecule [centroid...C distances of 3.40, 3.56 and 3.72 Å] (Figure 4). Despite the unresolved disorder

—that does not allow to spot any further details and neither defining the messy $-\text{N}(\text{CH}_3)_2$ terminal group of the organic dye and a lattice water molecule—, it can be inferred implications of the free rotation of the two phenyl rings in reducing the strength of the interactions, which, even if detected, it appears weak when looking at distances —although they must be imagined as averaged in the crystal.

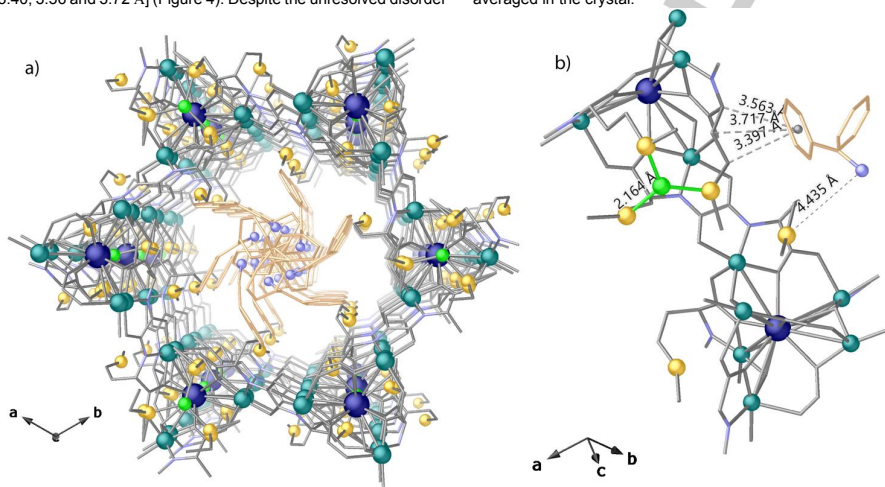


Figure 4. Details of host-guest interactions in **AO@1**: (a) Perspective view of a single channel of X-ray crystal structure of **AO@1** along *c* crystallographic axis emphasizing pores filled by Auramine O and (b) details of host-guest interactions (S...Cl and AO...S represented as green and grey dashed lines, respectively). Copper and calcium are represented by cyan and blue spheres respectively, whereas the ligands and guest molecules are depicted as grey and gold sticks except for sulfur atoms of methoxy moieties and nitrogen atoms of guest molecule, which are represented by yellow and blue-sky spheres, respectively. Free water molecules are omitted for clarity.

In **BG@1** and **MB@1** crystal structures, the size of BG and MB and/or their worst self-packing impose a more contracted conformation of the methionine derivatives arms. BG crystal structure, exhibits a very nice interlock between BG molecules and hosting matrix, based on S... π interactions [centroid...C distance of 3.14 Å] (Figure S4). As far as for **MB@1** is concerned, we have to underline a direct bond involving methionine-sulphur and nitrogen atoms belonging to the MB molecule at a distance of 1.79 Å, in agreement with similar bonds reported in literature,^[15] which packed dye molecules confining sulphur atoms of the dye molecule at the center of the pores (Figure S6). Also in these cases, due to dynamic disorder, terminal $-\text{N}(\text{CH}_2\text{CH}_3)_2$ groups present in **BG@1** and $-\text{N}(\text{CH}_3)_2$ in **MB@1** and have not been modelled (see Experimental Section for details). However, the core of the dye molecules —although with disorder— has been defined, suggesting the main interactions with terminal $-\text{N}(\text{CH}_2\text{CH}_3)_2$ and $-\text{N}(\text{CH}_3)_2$ groups likely involve dye intermolecular ones. Surprisingly, for all dyes, the high degree of loading in the confined space is the same. Each dye molecule does displace almost all water molecules from pores in order to reach the

observed close-packing. The totally fill of the channels makes the adsorbates very stable at air and room temperature for months.

The good performance of **1** for chosen dye capture could be understood analyzing non-covalent interactions within the final aggregates with the help of X-ray crystallography. As stated above, it is known that σ -hole bonding plays a pivotal role in the 3D organization of crystalline structures and in various molecular scaffolds. Indeed, these interactions, frequently unnoticed or identified as secondary contacts, can be highly predictable and generally present. In this work we considered and used them as a novel and efficient tool to reach high performance in capture of pollutant dyes. Studies on this subject have worked dramatically to interpret and rationalize properties of **1**. In fact, the importance of such interactions is clearly manifested in a multitude of biological phenomena.^[17] In all the four adsorbates **AO@1**, **BG@1**, **MB@1** and **PY@1** a kind of S... π interactions, together with S...Cl interactions in **AO@1**, **MB@1** and **PY@1**, have been detected. Certainly, although an aromatic π -system can be electron-rich or electron-deficient, it can be non-covalently bonded to a σ -hole-containing molecule —as in the cases reported here containing molecule... π -system interactions. The σ -hole term is assigned to

FULL PAPER

the area of positive or less negative electrostatic potential emerging on the outer surface of the covalently bonded sulfur atom. In this scenario, σ -hole interactions found in **AO@1**, **BG@1**, **MB@1** and **PY@1**, even if different in nature and discussed in the context of other electrostatic interactions, are the main forces at the origin of efficient capture of dyes in **1**. Their density of propagation, through the confined space ensured by **1**, represent the power of encapsulation of the system, being reminiscent of peptide-based methionine. In such supramolecular aggregates, these bonds rely to a large extent also on polarization and charge transfer effects, accompanied by dispersive forces –even if the precise mix of these different components varies from one bond to another. Thus, it is clear that a particular sort of hole does not have to be present in the isolated monomer, but it will be active when cooperative and polarizing forces can occur.

Thermogravimetric Analysis, N₂ Isotherm Adsorption and X-Ray Powder Diffraction.

The water content of **1**, **AO@1**, **BG@1**, **MB@1** and **PY@1** was determined by thermogravimetric analysis (TGA) under a dry N₂ atmosphere. All of them show a small loss of solvent from room temperature, in comparison with **1**, which agrees with the fact that the channels are filled with organic dyes. In particular, they showed a weight loss of 15.86 (**1**), 5.30 (**AO@1**), 4.35 (**BG@1**), 5.25 (**MB@1**) and 5.22 % (**PY@1**), that correspond with 16, 6, 5, 6 and 6 water molecules, respectively, which is in line with CHSN analyses (Figure S10). The N₂ adsorption at 77K of **AO@1**, **BG@1**, **MB@1** and **PY@1** showed a considerable reduction respect **1**, which further support that the channels are occupied by organic dyes molecules (Figure S11). The experimental powder X-ray diffraction (PXRD) patterns of polycrystalline sample of **1**, **AO@1**, **BG@1**, **MB@1** and **PY@1** confirm the purity and homogeneity of the bulk samples (Figure S12). As it was previously observed, the slight increase in relative intensity at the higher-angle peaks of dyes@**1**, respect **1**, are most likely consequence of the increase of the electronic density in the channels filled with organic dyes.

Conclusions

Here we have presented our recent advances on the relevance of σ -hole interactions toward applications. In particular, we have gained insight by means of single-crystal X-ray crystallography of the importance of such poorly investigated interactions for the removal of four organic dyes from real river waters. In doing so, we have precisely characterized four host-guest adsorbates, where the main interactions between the organic dyes and the framework allowed us to rationalize the appealing removal properties of **1**. In an indirect manner, we have taken this MOF one step closer to real world applications by both its structuration as extruded pellets and the scale-up synthesis. This work represents an interesting beginning of a research line, which currently we are developing to integrate **1** in a decontamination pilot plant.

Acknowledgements

This work was supported by the Ministerio de Ciencia e Innovación (Spain) (Projects PID2019–104778GB–I00 and Excellence Unit "Maria de Maeztu" CEX2019–000919–M), the Generalitat Valenciana (Project PROMETEO/2021/054) and the Ministero dell'Istruzione, dell'Università e della Ricerca (Italy). R. B. thank Fondazione CARIPLO (Project code: 2019–2090, "Economia Circolare: ricerca per un futuro sostenibile" 2019, MOCA) for postdoctoral grant. Thanks are also extended to the "2019 Post-doctoral Junior Leader–Retaining Fellowship, la Caixa Foundation (ID100010434 and fellowship code LCF/BQ/PR19/11700011", "Subvenciones concedidas a la excelencia científica de juniors investigadores, SEJI/2020/034" and "Ramon y Cajal Programme" (J. F.-S.). E.P. acknowledges the financial support of the European Research Council under the European Union's Horizon 2020 research and innovation programme / ERC Grant Agreement No 814804, MOF-reactors. MM was supported by Fondazione AIRC (IG 21322). RL and MM acknowledge (i) the special award namely 'Department of Excellence 2018–2022' (Italian Law 232/2016) to the Department of Pharmacy, Health and Nutritional Sciences of the University of Calabria (Italy), (ii) the 'Sistema Integrato di Laboratori per L'Ambiente—(SILA) PONa3_00341'.

Experimental Section

Materials. All chemicals were of reagent grade quality. They were purchased from commercial sources and used as received. H₂Me₂-(S,S)-methox and (Me₄N)₂[Cu₂[(S,S)-methox](OH)₂] · 4H₂O were prepared as early reported.^[13]

Physical Techniques. Elemental (C, H, S, N) analyses were performed at the Microanalytical Service of the Universitat de València. ¹H NMR spectra were recorded at room temperature on a Bruker AC 200 (200.1 MHz) spectrometer. FT–IR spectra were recorded on a Perkin-Elmer 882 spectrophotometer as KBr pellets. Thermogravimetric analysis (TGA) data were recorded on an SDT-Q600 analyzer from TA instruments. The temperature varied from RT to 490 °C at a heating rate of 10 °C.min⁻¹. Measurements were carried out on samples in open platinum crucibles under a flow of air.

Preparation of (Sr^{II}Cu^I)₆[(S,S)-methox]₃(OH)₂(H₂O)) · 16H₂O (1**):** To 50 mL solution of (Me₄N)₂[Cu₂[(S,S)-methox](OH)₂] · 4H₂O (4.37 g, 6.0 mmol) was added dropwise under stirring another aqueous solution (10 mL) containing Sr(NO₃)₂ (0.423 g, 2 mmol). After further stirring for 24 h at room temperature a green polycrystalline powder was obtained by filtration. Yield: 3.04 g, 82% Anal. calcd for C₃₆Cu₆SrH₈₄S₆N₆O₃₇ (1854.35): C, 23.32; H, 4.57; S, 10.37; N, 4.53%. Found: C, 23.28; H, 4.62; S, 10.44; N, 4.67%; IR (KBr): ν = 1602 cm⁻¹ (C=O). Well-shaped hexagonal green prisms of **1** suitable for X-ray structural analysis were obtained by slow diffusion in an H-shaped tube of aqueous solutions containing stoichiometric amounts of

FULL PAPER

(Me₄N)₂[Cu₂((S,S)-methox)(OH)₂] · 4H₂O (0.13 g, 0.18 mmol) in one arm and Sr(NO₃)₂ (0.013 g, 0.06 mmol) in the other.

Preparation of extruded pellets of 1. Extruded pellets of **1** were prepared by following an already reported procedure.^[60] 250 mg of **1** in the form of polycrystalline powder sample were dispersed in 5 mL of a Dichloromethane (CH₂Cl₂)/N-Methyl-2-pyrrolidone (NMP) (2:1) and ultrasonicated for 20 min. (power = 50 W and frequency = 60 Hz). Then, a CH₂Cl₂/NMP solution (5 mL) of the polyimide Matrimid®5218 (62.50 mg), previously degassed, was added dropwise to the previous suspension under vigorous stirring at room temperature, to obtain a final mass ratio MOF/matrimid of 80/20. After further stirring during 30 min., the resulting viscous suspension was poured on a water solution (15 mL) and shaped as extruded pellets. After several minutes, they were isolated by filtration on paper and air-dried. Yield: 280 mg, 90%; Anal. calcd for C_{64.2}Cl_{0.6}SrH_{104.3}Se_{0.1}N_{7.6}O_{11.1} (2305.13): C, 32.18; H, 4.56; S, 8.35; N, 4.62%. Found: C, 33.52; H, 4.61; S, 8.30; N, 4.67%. IR (KBr): $\nu = 1702, 1670$ and 1606 cm^{-1} (C=O).

Preparation of AO@{Sr^{II}Cu₆[(S,S)-methox]₃(OH)₂(H₂O)} · 6H₂O (AO@1), BG@{Sr^{II}Cu₆[(S,S)-methox]₃(OH)₂(H₂O)} · 5H₂O (BG@1), MB@{Sr^{II}Cu₆[(S,S)-methox]₃(OH)₂(H₂O)} · 6H₂O (MB@1) and PY@{Sr^{II}Cu₆[(S,S)-methox]₃(OH)₂(H₂O)} · 6H₂O (PY@1). Well-formed hexagonal prisms of **AO@1**, **BG@1**, **MB@1** and **PY@1** suitable for X-ray structural analysis were obtained by soaking crystals of **1** (ca. 5 mg) in saturated acetone solutions of Auramine O (AO), Brilliant Green (BG), Methylene Blue (MB) and Pyronin Y (PY), respectively, for one week. Then, the crystals were isolated by filtration on paper and air-dried. **AO@1**: Anal. calcd for C₅₃Cl_{0.6}SrH₈₆Se_{0.1}N_{7.6}O₂₇ (1974.59): C, 32.18; H, 4.38; S, 9.73; N, 6.37%. Found: C, 32.18; H, 4.22; S, 10.04; N, 6.46%; IR (KBr): $\nu = 1601\text{ cm}^{-1}$ (C=O). **BG@1**: Anal. calcd for C₅₃Cu₆SrH₈₆S₇N₈O₃₀ (2138.65): C, 35.38; H, 4.52; S, 10.49; N, 5.24%. Found: C, 35.16; H, 4.42; S, 10.29; N, 5.26%; IR (KBr): $\nu = 1607\text{ cm}^{-1}$ (C=O). **MB@1**: Anal. calcd for C₅₂Cl_{0.6}SrH₈₂S₇N₈O₂₇ (1991.51): C, 31.32; H, 4.14; S, 11.26; N, 6.32%. Found: C, 31.22; H, 4.22; S, 11.29; N, 6.30%; IR (KBr): $\nu = 1603\text{ cm}^{-1}$ (C=O). **PY@1**: Anal. calcd for C₅₃Cl_{0.6}SrH₈₃Se_{0.1}N₈O₂₈ (1973.51): C, 32.20; H, 4.23; S, 9.73; N, 5.67%. Found: C, 32.10; H, 4.32; S, 9.62; N, 5.64%; IR (KBr): $\nu = 1600\text{ cm}^{-1}$ (C=O).

Kinetic profile of the water dye removal. 50 mg of extruded pellets of **1** were soaked in each of four 10 mL solutions of 10 ppm spiked real water sample from Turia river (Valencia, Spain) with Auramine O (AO), Brilliant Green (BG), Methylene Blue (MB) and Pyronin Y (PY). Each mixture was stirred at room temperature and the concentration of the supernatant solutions were estimated through UV-vis spectroscopy at the given time intervals (see main text, Figure 1 and Table S2 and S4). The same experiment was repeated for a multidye solution containing 10 ppm of each dye (Figure S11 and Table S3). The water sample from Turia river were collected in dark glass bottles at (39.504095, -0.473712; Valencia) and stored at 4 °C until analysis. The samples were spiked after reaching room temperature and used without any additional pretreatment step.

Maximum uptake capacity of 1. In order to evaluate this, ca. 50 mg of **1** were soaked in aqueous saturated solutions of the respective dye [Auramine O (AO), Brilliant Green (BG), Methylene Blue (MB) and Pyronin Y (PY)] during two weeks. The saturated solutions were replaced each day with the intention to secure the maximum dye loading. Then, each **dye@1** was filtered off and gently washed with water. The dye content for each **dye@1** was determined by the combination of C, H, S, N analyses and UV-vis spectroscopy. Dealing with the spectroscopic approach, 25 mg of each **dye@1** were suspended in methanol during 24 h. After that time, **1** recover the pristine color and it was considered the 100% of the dye was eluted. The concentration of each dye was evaluated by UV-vis spectroscopy. The results obtained following this approach were very close to the ones obtained from C, H, S, N analyses.

C, H, S, N analyses: **AO + 1**: Anal. calcd for C_{92.1}Cl_{3.3}Cu₆SrH_{134.6}Se_{1.6}N_{15.9}O₂₆ (2658.83): C, 41.60; H, 5.10; S, 7.24; N, 8.38%. Found: C, 41.48; H, 5.02; S, 7.34; N, 8.46%. **BG + 1**: Anal. calcd for C_{108.9}Cu₆SrH_{153.8}S_{8.7}N_{11.4}O_{36.8} (2959.30): C, 44.20; H, 5.24; S, 9.43; N, 5.40%. Found: C, 44.16; H, 5.22; S, 9.39; N, 5.46%. **MB + 1**: Anal. calcd for C_{92.4}Cl_{2.9}Cu₆SrH_{116.2}S_{8.9}N_{14.7}O₂₇ (2601.77): C, 38.04; H, 4.50; S, 10.97; N, 7.91%. Found: C, 38.12; H, 4.56; S, 10.79; N, 7.80%. **PY@1**: Anal. calcd for C₆₇Cl₃Cu₆SrH₁₂₁Se₁N₁₂O₃₀ (2582.60): C, 40.46; H, 4.72; S, 7.45; N, 6.51%. Found: C, 40.40; H, 4.72; S, 7.42; N, 6.54%.

Scale-up of 1. A multigram scale synthetic procedure have been adapted to obtain **1** in higher amounts. In order to do so, a 350 mL solution of (Me₄N)₂[Cu₂((S,S)-methox)(OH)₂] · 4H₂O (20.0 g, 27.5 mmol) was added dropwise under stirring another aqueous solution (40 mL) containing Sr(NO₃)₂ (1.94 g, 9.2 mmol). After further stirring for 24 h at room temperature a green polycrystalline powder was obtained by filtration. The process was repeated five times. Average yield: 14.33 g, 84% Anal. calcd for C₃₆Cu₆SrH₈₄Se_{0.1}N₈O₃₇ (1854.35): C, 23.32; H, 4.57; S, 10.37; N, 4.53%. Found: C, 23.42; H, 4.65; S, 10.31; N, 4.56%; IR (KBr): $\nu = 1601\text{ cm}^{-1}$ (C=O).

X-ray Powder Diffraction Measurements. Polycrystalline samples of **1**, **AO@1**, **BG@1**, **MB@1** and **PY@1** were introduced into 0.5 mm borosilicate capillaries prior to being mounted and aligned on a Bruker D8 Discover powder diffractometer, using Cu K α radiation ($\lambda = 1.54056\text{ \AA}$). Extruded pellets of **1** were measured in a diffraction plate using the same diffractometer. For each sample, five repeated measurements were collected at room temperature ($2\theta = 2-45^\circ$) and merged in a single diffractogram. The simulated powder pattern was calculated from single-crystal X-ray diffraction data and processed by the Mercury program (Version 4.2.0) provided by the Cambridge Crystallographic Data Centre.^[61]

Gas adsorption. The N₂ adsorption-desorption isotherms at 77 K, were carried out on a polycrystalline sample of **1** with a BELSORP-miniX instrument. Sample was first activated with

FULL PAPER

methanol and then evacuated at 348 K during 19 hours under 10^{-6} Torr prior to their analysis.

UV-vis spectroscopy. UV-vis spectra were recorded, at room temperature, with a Jasco V 670 spectrometer.

Single-Crystal X-ray Diffraction. Crystals of **1**, **AO@1**, **BG@1**, **MB@1** and **PY@1** adsorbates were selected and mounted on a MITIGEN holder in Paratone oil. Diffraction data were collected on a Bruker-Nonius X8APEXII CCD area detector diffractometer, at room temperature, except for **1**, which was measured at 100 K under nitrogen stream, using graphite-monochromated Mo- K_{α} radiation ($\lambda = 0.71073$ Å). The data were processed through the SAINT^[82] reduction and SADABS^[83] multi-scan absorption software. The structure was solved with the SHELXS structure solution program, using the Patterson method. The model was refined with version 2013/4 of SHELXL against R^2 on all data by full-matrix least squares.^[84–86]

As reported in the main text, even after a single-crystal to single-crystal process, the retained crystallinity of the 3D network of **1**, allowed the resolution of the crystal structures of **AO@1**, **BG@1**, **MB@1** and **PY@1**. Hence, for these samples, it is reasonable to expect somewhat mismatches from the routine expected diffraction patterns.

In all samples **–1**, **AO@1**, **BG@1**, **MB@1** and **PY@1**– all non-hydrogen atoms of the net were refined anisotropically. It is not the same for some highly dynamically disordered carbon atoms belonging to the methionine residues pointing within huge pores or lattice water molecules atoms and atoms of guest molecules. All the hydrogen atoms of the net were set in calculated position and refined isotropically using the riding model. Hydrogen atoms on the guest molecules, and for solvent lattice molecules were neither found nor calculated. These show, in all structures, severe disorder as a direct consequence of their high thermal motion and also statistic disorder. It is well known that a crystal structure is the *spatial average*, representing all molecules, together with all their possible orientations averaged in the crystal *via* only one-unit cell. In all cases, as the present one of as synthesized porous materials, where obviously not all unit cells are identical and a variety of orientations are allowed, the description became more challenging.

Firstly, the occupancies of the guests in the pores, have been defined by a combination of CHSN analyses, UV-vis spectroscopy and thermal factors, and then imposed as occupancy factors in structures refinement. We strongly believe that it is the more reliable way to accurately define loading instead of taking into account merely thermal factors, which can be affected by a lot of issues above all severe disorder. Then, the use of some C-C, C-N, C-O and C-S bond lengths restraints of highly disordered atoms for guest molecules during the refinements in all adsorbate crystal structures has been reasonably imposed, as well as related to the expected and severe thermal motion, likely depending on the large size of the huge pores of the frameworks (SAME, DFIX, RIGU, SIMU, DELU

and ISOR). In all adsorbate samples **–AO@1**, **BG@1**, **MB@1** and **PY@1**– guest molecules are severely disordered, especially for the guest's fragments pointing towards the center of the pores where, undoubtedly, the degrees of freedom, related to diverse possible conformations, significantly increase. For those reasons, in some cases we constrained even thermal factors. Moreover, in general for the four messy organic molecules, counter-anions Cl^- and HSO_4^- and some terminal fragments were not found from ΔF map.

In **AO@1** the whole terminal moieties $-\text{N}(\text{CH}_3)_2$ were not found, furthermore guest molecule results close to the position of a lattice water molecule, which has been modelled with an occupancy factor complementary to that of AO molecule. (see Figure S3 for details of statistical disorder).

The same happens in **BG@1** where the two $-\text{N}(\text{CH}_2\text{CH}_3)_2$ groups ethyl moieties were not found. (see Figure S5 for details of statistical disorder).

In **MB@1** the two $-\text{N}(\text{CH}_3)_2$ groups were not found, the overlap between different orientations on terminal carbon atoms makes them disordered with carbon sites (see Figure S7).

In **PY@1** the two $-\text{N}(\text{CH}_3)_2$ groups were not modelled as they fall in a disordered region when carbon atoms from different conformations of the guest molecules overlap. The oxygen atom O1L resides in special position, thus resulting shared by the three conformations. (see Figure S9).

As a consequence of the severe disorder, Alert A in the checkcif, also related to short intermolecular C \cdots C of guests and net or equivalent positions generated by overlapping various geometry, are detected, but are unavoidable. The solvent molecules were disordered as well –some refined double positions are detected as Alerts A in the checkcif– some of them virtually occupying assigned sites overlapping guest molecules, as for O1w **AO@1**. Here the occupancy has been assigned in accordance with occupancy guest's one, just because all pore's content is averaged on one-unit cell. Again, the quite large channels featured by the MOFs likely account for that. However even if not all the ones detected by TGA analysis, they have been somehow modelled in all the adsorbates (Alert level B for **1**, related to mismatch in the ratio of given/expected molecular weight) – **AO@1**, **BG@1**, **MB@1** and **PY@1**. As indicated above, in all the four **AO@1**, **BG@1**, **MB@1** and **PY@1** adsorbates, fragments of molecules overlapped on the symmetrically generated ones by the 6-fold rotation operation, and thus guest molecules are also statistically disordered. A detail of kind of disorder related to guest molecules in **AO@1**, **BG@1**, **MB@1** and **PY@1** crystal structures have been showed in Figs. S3, S5, S7 and S9.

Overall the "Alert A" notifications found in the validation program CheckCIF are related either to intrinsic imperfections and disorder (as the presence of large outliers in the data set), quite normal for crystals that suffered a single-crystal to single-crystal process, or from short intermolecular contacts between water molecules and

FULL PAPER

guest molecules or water molecules or guest molecules and the whole network, which are unavoidable due to the expected severe disorder of both solvent and guest molecules. The comments for the alerts are described in the CIFs using the validation response form (vrf).

A summary of the crystallographic data and structure refinement for the five compounds is given in Table S1. CCDC reference numbers are 2132442–2132446 for **1**, **AO@1**, **BG@1**, **MB@1** and **PY@1**, respectively.

The final geometrical calculations on free voids and the graphical manipulations were carried out with PLATON^[87,88] implemented in WinGX^[89] and CRYSTAL MAKER^[90] programs, respectively.

Keywords: water remediation • metal-organic frameworks • organic dyes • σ -Hole Interaction • host-guest chemistry

- [1] J.-M. Lehn, *Supramolecular Chemistry*, Wiley, 1995.
- [2] G. Vantomme, E. W. Meijer, *Science* **2019**, *363*, 1396–1397.
- [3] D. B. Amabilino, P. A. Gale, *Chem. Soc. Rev.* **2017**, *46*, 2376–2377.
- [4] W. Liu, J. F. Stoddart, *Chem* **2021**, *7*, 919–947.
- [5] J. S. Murray, P. Lane, P. Politzer, *Int. J. Quantum Chem.* **2008**, *108*, 2770–2781.
- [6] S. Scheiner, U. Adhikari, *J. Phys. Chem. A* **2011**, *115*, 11101–11110.
- [7] P. Politzer, J. S. Murray, T. Clark, *Phys. Chem. Chem. Phys.* **2013**, *15*, 11178.
- [8] A. Obata, H. Kawazura, H. Miyamae, *Acta Crystallogr. Sect. C Cryst. Struct. Commun.* **1984**, *40*, 45–48.
- [9] Y. Nagao, T. Hirata, S. Goto, S. Sano, A. Kakehi, K. Iizuka, M. Shiro, *J. Am. Chem. Soc.* **1998**, *120*, 3104–3110.
- [10] M. Iwaoka, S. Takemoto, S. Tomoda, *J. Am. Chem. Soc.* **2002**, *124*, 10613–10620.
- [11] B. M. Hudson, E. Nguyen, D. J. Tantillo, *Org. Biomol. Chem.* **2016**, *14*, 3975–3980.
- [12] S. P. Thomas, D. Jayatilaka, T. N. Guru Row, *Phys. Chem. Chem. Phys.* **2015**, *17*, 25411–25420.
- [13] M. Mon, J. Ferrando-Soria, T. Granchar, F. R. Fortea-Pérez, J. Gascon, A. Leyva-Pérez, D. Armentano, E. Pardo, *J. Am. Chem. Soc.* **2016**, *138*, 7864–7867.
- [14] M. Mon, F. Lloret, J. Ferrando-Soria, C. Martí-Gastaldo, D. Armentano, E. Pardo, *Angew. Chem. Int. Ed.* **2016**, *55*, 11167–11172.
- [15] M. Mon, R. Bruno, E. Tiburcio, M. Viciano-Chumillas, L. H. G. Kalinke, J. Ferrando-Soria, D. Armentano, E. Pardo, *J. Am. Chem. Soc.* **2019**, *141*, 13601–13609.
- [16] M. Mon, X. Qu, J. Ferrando-Soria, I. Pellicer-Carreño, A. Sepúlveda-Escribano, E. V. Ramos-Fernandez, J. C. Jansen, D. Armentano, E. Pardo, *J. Mater. Chem. A* **2017**, *5*, 20120–20125.
- [17] M. Mon, M. A. Rivero-Crespo, J. Ferrando-Soria, A. Vidal-Moya, M. Boronat, A. Leyva-Pérez, A. Corma, J. C. Hernández-Garrido, M. López-Haro, J. J. Calvino, et al., *Angew. Chem. Int. Ed.* **2018**, *57*, 6186–6191.
- [18] C. Negro, H. Martínez Pérez-Cejuela, E. F. Simó-Alfonso, J. M. Herrero-Martínez, R. Bruno, D. Armentano, J. Ferrando-Soria, E. Pardo, *ACS Appl. Mater. Interfaces* **2021**, *13*, 28424–28432.
- [19] R. Bruno, M. Mon, P. Escamilla, J. Ferrando-Soria, E. Esposito, A. Fuoco, M. Monteleone, J. C. Jansen, R. Elliani, A. Tagarelli, et al., *Adv. Funct. Mater.* **2021**, *31*, 2008499.
- [20] E. Tiburcio, R. Greco, M. Mon, J. Ballesteros-Soberanas, J. Ferrando-Soria, M. López-Haro, J. C. Hernández-Garrido, J. Oliver-Meseguer, C. Marini, M. Boronat, et al., *J. Am. Chem. Soc.* **2021**, *143*, 2581–2592.
- [21] H. Furukawa, K. E. Cordova, M. O’Keeffe, O. M. Yaghi, *Science* **2013**, *341*, 974.
- [22] H.-C. Zhou, S. Kitagawa, *Chem. Soc. Rev.* **2014**, *43*, 5415–5418.
- [23] B. Seoane, S. Castellanos, A. Dikhtiarenko, F. Kapteijn, J. Gascon, *Coord. Chem. Rev.* **2016**, *307*, 147–187.
- [24] G. Maurin, C. Serre, A. Cooper, G. Férey, *Chem. Soc. Rev.* **2017**, *46*, 3104–3107.
- [25] O. M. Yaghi, M. J. Kalmuzki, C. S. Diercks, *Introduction to Reticular Chemistry*, Wiley, 2019.
- [26] X. Zhang, B. Wang, A. Alsalm, S. Xiang, Z. Zhang, B. Chen, *Coord. Chem. Rev.* **2020**, *423*, 213507.
- [27] W. Xu, B. Tu, Q. Liu, Y. Shu, C.-C. Liang, C. S. Diercks, O. M. Yaghi, Y.-B. Zhang, H. Deng, Q. Li, *Nat. Rev. Mater.* **2020**, *5*, 764–779.
- [28] R. Freund, O. Zaremba, G. Amnats, R. Ameloot, G. Skorupskii, M. Dincă, A. Bavykina, J. Gascon, A. Ejsmont, J. Goscianska, et al., *Angew. Chem. Int. Ed.* **2021**, *60*, 23975–24001.
- [29] H. Deng, S. Grunder, K. E. Cordova, C. Valente, H. Furukawa, M. Hmadeh, F. Gandara, A. C. Whalley, Z. Liu, S. Asahina, et al., *Science* **2012**, *336*, 1018–1023.
- [30] D. Antypov, A. Shkurenko, P. M. Bhatt, Y. Belmabkhout, K. Adil, A. Cadiau, M. Suyetin, M. Eddaoudi, M. J. Rosseinsky, M. S. Dyer, *Nat. Commun.* **2020**, *11*, 6099.
- [31] Z. Ji, H. Wang, S. Canossa, S. Wuttke, O. M. Yaghi, *Adv. Funct. Mater.* **2020**, *30*, 2000238.
- [32] H. Wang, Z. Shi, J. Yang, T. Sun, B. Rungtaweeworant, H. Lyu, Y. Zhang, O. M. Yaghi, *Angew. Chem. Int. Ed.* **2021**, *60*, 3417–3421.
- [33] M. Mon, R. Bruno, S. Sanz-Navarro, C. Negro, J. Ferrando-Soria, L. Bartella, L. Di Donna, M. Prejanò, T. Marino, A. Leyva-Pérez, et al., *Nat. Commun.* **2020**, *11*, 3080.
- [34] M. Mon, R. Bruno, E. Tiburcio, A. Grau-Atienza, A. Sepúlveda-Escribano, E. V. Ramos-Fernandez, A. Fuoco, E. Esposito, M. Monteleone, J. C. Jansen, et al., *Chem. Mater.* **2019**, *31*, 5856–5866.
- [35] M. Mon, R. Bruno, J. Ferrando-Soria, L. Bartella, L. Di Donna, M. Talia, R. Lappano, M. Maggolini, D. Armentano, E. Pardo, *Mater. Horizons* **2018**, *5*, 683–690.
- [36] Y. Inokuma, T. Arai, M. Fujita, *Nat. Chem.* **2010**, *2*, 780–783.
- [37] Y. Inokuma, S. Yoshioka, J. Ariyoshi, T. Arai, M. Fujita, *Nat. Protoc.* **2014**, *9*, 246–252.
- [38] N. Zigon, M. Hoshino, S. Yoshioka, Y. Inokuma, M. Fujita, *Angew. Chem. Int. Ed.* **2015**, *54*, 9033–9037.
- [39] V. Guillemin, M. Eddaoudi, *Acc. Chem. Res.* **2021**, *54*, 3298–3312.
- [40] H. Jiang, D. Alezi, M. Eddaoudi, *Nat. Rev. Mater.* **2021**, *6*, 466–487.
- [41] R. Freund, S. Canossa, S. M. Cohen, W. Yan, H. Deng, V. Guillemin, M. Eddaoudi, D. G. Madden, D. Fairen-Jimenez, H. Lyu, et al.,

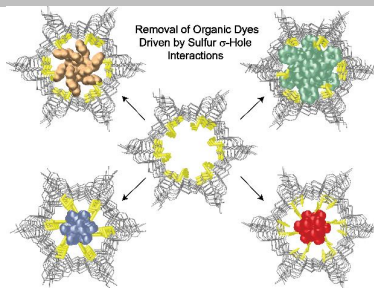
FULL PAPER

- Angew. Chem. Int. Ed.* **2021**, *60*, 23946–23974.
- [42] L. Feng, G. S. Day, K.-Y. Wang, S. Yuan, H.-C. Zhou, *Chem* **2020**, *6*, 2902–2923.
- [43] Z. Chen, H. Jiang, M. Li, M. O’Keeffe, M. Eddoudi, *Chem. Rev.* **2020**, *120*, 8039–8065.
- [44] M. Li, D. Li, M. O’Keeffe, O. M. Yaghi, *Chem. Rev.* **2014**, *114*, 1343–1370.
- [45] M. O’Keeffe, O. M. Yaghi, *Chem. Rev.* **2012**, *112*, 675–702.
- [46] Y. Isaka, Y. Kawase, Y. Kuwahara, K. Mori, H. Yamashita, *Angew. Chem. Int. Ed.* **2019**, *58*, 5402–5406.
- [47] H. Jiang, J. Jia, A. Shkurenko, Z. Chen, K. Adil, Y. Belmabkhout, L. J. Weselinski, A. H. Assen, D.-X. Xue, M. O’Keeffe, et al., *J. Am. Chem. Soc.* **2018**, *140*, 8858–8867.
- [48] P. Li, N. A. Vermeulen, C. D. Malliakas, D. A. Gómez-Gualdrón, A. J. Howarth, B. L. Mehdi, A. Dohnalkova, N. D. Browning, M. O’Keeffe, O. K. Farha, *Science* **2017**, *356*, 624–627.
- [49] F. R. Fortea-Pérez, M. Mon, J. Ferrando-Soria, M. Boronat, A. Leyva-Pérez, A. Corma, J. M. Herrera, D. Osadchii, J. Gascon, D. Armentano, et al., *Nat. Mater.* **2017**, *16*, 760–766.
- [50] R. Li, S. Alomari, T. Islamoglu, O. K. Farha, S. Fernando, S. M. Thagard, T. M. Holsen, M. Wriedt, *Environ. Sci. Technol.* **2021**, *55*, 15162–15171.
- [51] Z. Jiang, X. Xu, Y. Ma, H. S. Cho, D. Ding, C. Wang, J. Wu, P. Oleynikov, M. Jia, J. Cheng, et al., *Nature* **2020**, *586*, 549–554.
- [52] M. Viciano-Chumillas, M. Mon, J. Ferrando-Soria, A. Corma, A. Leyva-Pérez, D. Armentano, E. Pardo, *Acc. Chem. Res.* **2020**, *53*, 520–531.
- [53] R. J. Young, M. T. Huxley, E. Pardo, N. R. Champness, C. J. Sumbly, C. J. Doonan, *Chem. Sci.* **2020**, *11*, 4031–4050.
- [54] M. I. Gonzalez, A. B. Turkiewicz, L. E. Darago, J. Oktawiec, K. Bustillo, F. Grandjean, G. J. Long, J. R. Long, *Nature* **2020**, *577*, 64–68.
- [55] N. Hanikel, M. S. Prévot, O. M. Yaghi, *Nat. Nanotechnol.* **2020**, *15*, 348–355.
- [56] A. Bavykina, N. Kolobov, I. S. Khan, J. A. Bau, A. Ramirez, J. Gascon, *Chem. Rev.* **2020**, *120*, 8468–8535.
- [57] Z. Chen, P. Li, R. Anderson, X. Wang, X. Zhang, L. Robison, L. R. Redfern, S. Moribe, T. Islamoglu, D. A. Gómez-Gualdrón, et al., *Science* **2020**, *368*, 297–303.
- [58] R.-B. Lin, S. Xiang, W. Zhou, B. Chen, *Chem* **2020**, *6*, 337–363.
- [59] L. S. Xie, G. Skorupkii, M. Dincă, *Chem. Rev.* **2020**, *120*, 8536–8580.
- [60] Q. Hu, J. Yu, M. Liu, A. Liu, Z. Dou, Y. Yang, *J. Med. Chem.* **2014**, *57*, 5679–5685.
- [61] M. Viciano-Chumillas, X. Liu, A. Leyva-Pérez, D. Armentano, J. Ferrando-Soria, E. Pardo, *Coord. Chem. Rev.* **2022**, *451*, 214273.
- [62] W. M. Bloch, A. Burgun, C. J. Coghlan, R. Lee, M. L. Coote, C. J. Doonan, C. J. Sumbly, *Nat. Chem.* **2014**, *6*, 906–912.
- [63] W. M. Bloch, N. R. Champness, C. J. Doonan, *Angew. Chem. Int. Ed.* **2015**, *54*, 12860–12867.
- [64] A. Burgun, C. J. Coghlan, D. M. Huang, W. Chen, S. Horike, S. Kitagawa, J. F. Alvino, G. F. Metha, C. J. Sumbly, C. J. Doonan, *Angew. Chem. Int. Ed.* **2017**, *56*, 8412–8416.
- [65] R.-W. Huang, Y.-S. Wei, X.-Y. Dong, X.-H. Wu, C.-X. Du, S.-Q. Zang, T. C. W. Mak, *Nat. Chem.* **2017**, *9*, 689–697.
- [66] K. Rissanen, *Chem. Soc. Rev.* **2017**, *46*, 2638–2648.
- [67] R. Adam, M. Mon, R. Greco, L. H. G. Kalinke, A. Vidal-Moya, A. Fernandez, R. E. P. Winpenny, A. Doménech-Carbó, A. Leyva-Pérez, D. Armentano, et al., *J. Am. Chem. Soc.* **2019**, *141*, 10350–10360.
- [68] N. Hanikel, X. Pei, S. Chheda, H. Lyu, W. Jeong, J. Sauer, L. Gagliardi, O. M. Yaghi, *Science* **2021**, *374*, 454–459.
- [69] A. Tkaczyk, K. Mitrowska, A. Posylniak, *Sci. Total Environ.* **2020**, *717*, 137222.
- [70] M. Mon, R. Bruno, J. Ferrando-Soria, D. Armentano, E. Pardo, *J. Mater. Chem. A* **2018**, *6*, 4912–4947.
- [71] A. Ahmad, S. H. Mohd-Setapar, C. S. Chuong, A. Khatoon, W. A. Wani, R. Kumar, M. Rafatullah, *RSC Adv.* **2015**, *5*, 30801–30818.
- [72] E. Brillas, C. A. Martínez-Huitle, *Appl. Catal. B Environ.* **2015**, *166–167*, 603–643.
- [73] C.-C. Wang, J.-R. Li, X.-L. Lv, Y.-Q. Zhang, G. Guo, *Energy Environ. Sci.* **2014**, *7*, 2831–2867.
- [74] D. Jiang, M. Chen, H. Wang, G. Zeng, D. Huang, M. Cheng, Y. Liu, W. Xue, Z. Wang, *Coord. Chem. Rev.* **2019**, *380*, 471–483.
- [75] E. M. Dias, C. Petit, *J. Mater. Chem. A* **2015**, *3*, 22484–22506.
- [76] Y. Wen, P. Zhang, V. K. Sharma, X. Ma, H.-C. Zhou, *Cell Reports Phys. Sci.* **2021**, *2*, 100348.
- [77] M. Mon, R. Bruno, E. Tiburcio, P.-E. Casteran, J. Ferrando-Soria, D. Armentano, E. Pardo, *Chem. Eur. J.* **2018**, *24*, 17712–17718.
- [78] A. Knebel, A. Bavykina, S. J. Datta, L. Sundermann, L. Garzon-Tovar, Y. Lebedev, S. Durini, R. Ahmad, S. M. Kozlov, G. Shterk, et al., *Nat. Mater.* **2020**, *19*, 1346–1353.
- [79] M. S. Smith, E. E. K. Lawrence, W. M. Billings, K. S. Larsen, N. A. Bécar, J. L. Price, *ACS Chem. Biol.* **2017**, *12*, 2535–2537.
- [80] T. Granchar, J. Ferrando-Soria, J. Cano, P. Amorós, B. Seoane, J. Gascon, M. Bazaga-García, E. R. Losilla, A. Cabeza, D. Armentano, et al., *Chem. Mater.* **2016**, *28*, 4608–4615.
- [81] C. F. Macrae, I. J. Bruno, J. A. Chisholm, P. R. Edgington, P. McCabe, E. Pidcock, L. Rodriguez-Monge, R. Taylor, J. van de Streek, P. A. Wood, *J. Appl. Crystallogr.* **2008**, *41*, 466–470.
- [82] W. SAINT, version 6.45, Bruker Analytical X-ray Systems, Madison, **2003**.
- [83] W. Sheldrick G.M. SADABS Program for Absorption Correction, version 2.10, Analytical X-ray Systems, Madison, **2003**.
- [84] G. M. Sheldrick, *Acta Crystallogr. Sect. C Struct. Chem.* **2015**, *71*, 3–8.
- [85] G. M. Sheldrick, *Acta Crystallogr. A* **2008**, *64*, 112–22.
- [86] W. S.-2013/4 B. A. X. I. Madison, **2013**.
- [87] A. L. Spek, *Acta Crystallogr. Sect. D Biol. Crystallogr.* **2009**, *65*, 148–155.
- [88] A. L. Spek, *Acta Crystallogr. Sect. C Struct. Chem.* **2015**, *71*, 9–18.
- [89] L. J. Farrugia, *J. Appl. Crystallogr.* **1999**, *32*, 837–838.
- [90] C. Palmer, D. CRYSTAL MAKER, Cambridge University Technical Services, **1996**.

Entry for the Table of Contents

COMMUNICATION

A metal-organic framework, with functional channels decorated with $-\text{CH}_2\text{CH}_2\text{SCH}_3$ thioalkyl chains, does not only exhibit outstanding capture properties for organic dyes but also allows to establish that sulfur σ -hole interactions play a prominent role with the help of single crystal X-Ray diffraction.



*Cristina Negro, Paula Escamilla,
Rosaria Bruno, Jesus Ferrando
Soria,* Donatella Armentano,*
and Emilio Pardo**

Page No. – Page No.

**Metal-Organic Frameworks as
Unique Platforms to Gain
Insight of σ -Hole Interactions
for the Removal of Organic
Dyes from Aquatic
Ecosystems**

Supporting Information for the manuscript:

**Metal-Organic Frameworks as Unique Platforms to Gain Insight
of σ -Hole Interactions for the Removal of Organic Dyes from
Aquatic Ecosystems**

Cristina Negro, Paula Escamilla, Rosaria Bruno, Jesus Ferrando Soria,*
Donatella Armentano,* and Emilio Pardo*

Table S1. Summary of Crystallographic Data for **1**, **AO@1**, **BG@1**, **MB@1** and **PY@1**.

Compound	1	AO@1	BG@1	MB@1	PY@1
Formula	C ₃₆ Cu ₆ SrH ₈₄ N ₆ O ₃ S ₆	C ₅₃ ClCu ₆ SrH ₁₈₆ N ₉ O ₂₇ S ₆	C ₆₃ Cu ₆ SrH ₁₀₂ N ₈ O ₃₀ S ₇	C ₅₃ ClCu ₆ SrH ₈₂ N ₉ O ₂₇ S ₇	C ₅₃ ClCu ₆ SrH ₈₃ N ₈ O ₂₈ S ₆
<i>M</i> (g mol ⁻¹)	1.854.31	1977.97	2138.75	1991.51	1973.51
λ (Å)	0.71073	0.71073	0.71073	0.71073	0.71073
Crystal system	Hexagonal	Hexagonal	Hexagonal	Hexagonal	Hexagonal
Space group	<i>P</i> 6 ₃	<i>P</i> 6 ₃	<i>P</i> 6 ₃	<i>P</i> 6 ₃	<i>P</i> 6 ₃
<i>a</i> (Å)	17.786(5)	17.594(3)	17.6474(19)	17.575(13)	17.7980(16)
<i>c</i> (Å)	12.894(6)	13.706(3)	13.909(2)	13.837(11)	13.6194(14)
<i>V</i> (Å ³)	3532(3)	3674.3(13)	3751.4(10)	3701(6)	3736.2(8)
<i>Z</i>	2	2	2	2	2
ρ^{calc} (g cm ⁻³)	1.743	1.788	1.893	1.678	1.754
μ (mm ⁻¹)	2.789	2.714	2.661	2.715	2.664
<i>T</i> (K)	100	293	296	296	296
θ range for data collection (°)	1.322 – 26.510	2.315- 26.427	2.665- 26.540	1.338- 26.499	1.32 - 26.5
Completeness to $\theta = 25.0$	100	100 %	100 %	100 %	100 %
Measured reflections	53941	49384	75182	23443	83359
Unique reflections (Rint)	4870	5011 (0.0717)	5107 (0.0354)	4998 (0.1065)	5109 (0.0657)
Observed reflections [<i>I</i> > 2 σ (<i>I</i>)]	3573	3257	4118	2736	3159
Goof	1.134	1.062	1.013	1.264	1.034
Absolute structure parameter (Flack)	0.48(1)	0.18(2)	0.06(1)	0.16(2)	0.23(2)
<i>R</i> ^a [<i>I</i> > 2 σ (<i>I</i>)] (all data)	0.0896 (0.1042)	0.0741 (0.1191)	0.0642 (0.0832)	0.0753 (0.1502)	0.0757 (0.1357)
<i>wR</i> ^b [<i>I</i> > 2 σ (<i>I</i>)] (all data)	0.2706 (0.2869)	0.2095 (0.2474)	0.2015 (0.2205)	0.2107 (0.2468)	0.2249 (0.2792)

^a $R = \sum(|F_o| - |F_c|) / \sum |F_o|$. ^b $wR = [\sum w(|F_o| - |F_c|)^2 / \sum w|F_o|^2]^{1/2}$.

Table S2. Selected data for the dye adsorption,^a obtained from the UV-vis measurements, of individual dye solutions with real water samples from Turia river (Valencia, Spain) spiked with 10 ppm of AO, BG, MB and PY, after soaking 50 mg of extruded pellets of **1**.

Time (min.)	<i>Auramine O (%)</i>	<i>Brilliant Green (%)</i>	<i>Methylene Blue (%)</i>	<i>Pyronin Y (%)</i>
1	95.93	86.08	93.82	90.44
5	99.06	97.62	96.84	97.49
30	99.67	99.11	98.97	98.59
60	99.87	99.67	99.29	99.29
360	99.97	99.73	99.39	99.67
720	99.98	99.81	99.65	99.89

^a Dye uptake (in %) extracted from the UV-vis measurements.

Table S3. Selected data for the dye adsorption,^a obtained from the UV-vis measurements, of a multidye solution with real water sample from Turia river (Valencia, Spain) spiked with 10 ppm of AO, BG, MB and PY, after soaking 50 mg of extruded pellets of **1**.

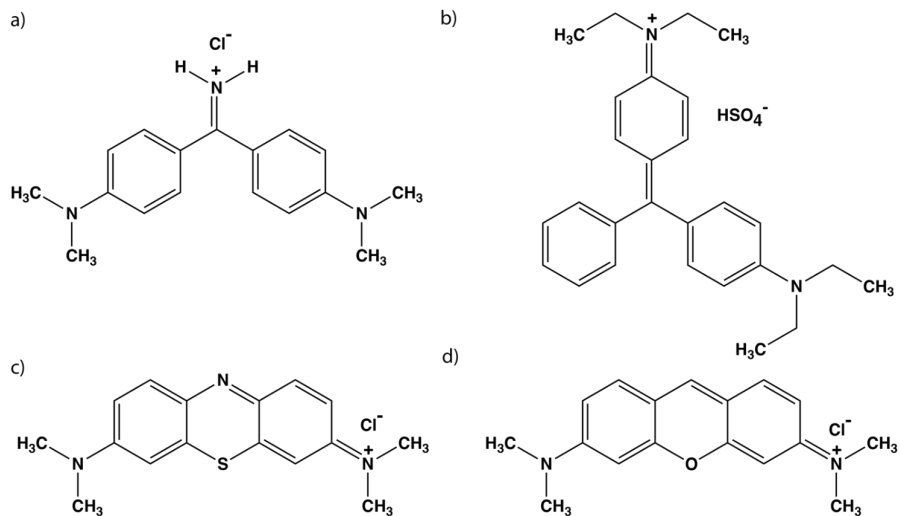
Time (min.)	<i>Auramine O (%)</i>	<i>Brilliant Green (%)</i>	<i>Methylene Blue (%)</i>	<i>Pyronin Y (%)</i>
1	96.33	89.36	93.32	92.44
5	98.11	96.11	97.87	95.34
30	98.89	98.79	99.11	97.11
60	99.11	99.37	99.67	98.89
360	99.77	99.65	99.79	99.79
720	99.83	99.69	99.83	99.82

^a Dye uptake (in %) extracted from the UV-vis measurements.

Table S4. Selected data for the dye adsorption,^a obtained from the UV-vis measurements, of individual dye solutions with real water samples from Turia river (Valencia, Spain) spiked with 10 ppm of AO, BG, MB and PY, after soaking 50 mg of recycled extruded pellets of **1**.

Time (min.)	<i>Auramine O (%)</i>	<i>Brilliant Green (%)</i>	<i>Methylene Blue (%)</i>	<i>Pyronin Y (%)</i>
1	94.34	84.65	95.54	92.36
5	96.55	87.26	96.00	95.65
30	97.11	93.14	97.97	97.56
60	98.23	96.67	98.24	98.29
360	99.00	97.32	98.39	99.00
720	99.11	98.61	99.03	98.99

^a Dye uptake (in %) extracted from the UV-vis measurements.



Scheme S1. Chemical structures of Auramine O (a), Brilliant Green (b), Methylene Blue (c) and Pyronin Y (d).

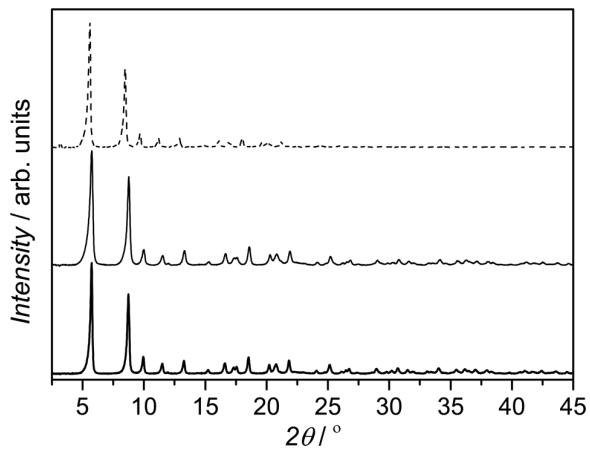


Figure S1. Experimental PXRD pattern profiles of **1** in the form of polycrystalline powder (bold lines), extruded pellets (normal lines) and recycled extruded pellets (dotted lines) in the 2θ range 2.0–45.0.

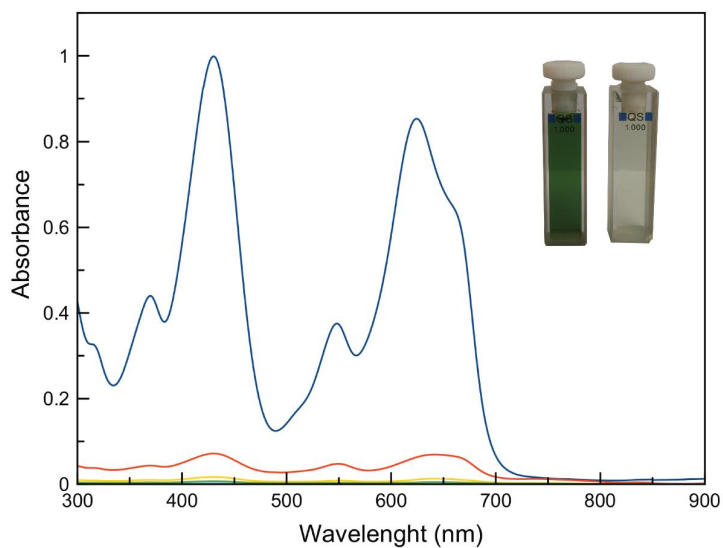


Figure S2. Evolution with time of the UV-Vis absorption spectra of a multidyedye solution containing 10 ppm solutions of Auramine O, Brilliant green, Methylene blue and Pyronin Y in real water samples from Turia river in the presence of 50 mg of pellets of **1**. Blue: $t = 0$; Red: $t = 1$ min.; Yellow: $t = 5$ min.; Orange $t = 30$ min.; Light blue $t = 360$ min.; Green: $t = 720$ min. The photographs show the colours of the solutions at the beginning (left) and after only one minute of exposure of the multidyedye solution with MOF **1** (right).

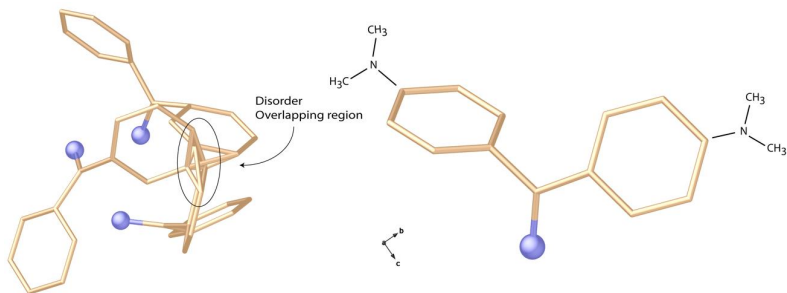


Figure S3. (a) Details of the three sets of guest conformations statistically disordered in AO@1. All possible orientations are included. (b) Details of a modelled set of AO in crystal structure of AO@1 with scheme of undetected fragments from ΔF maps.

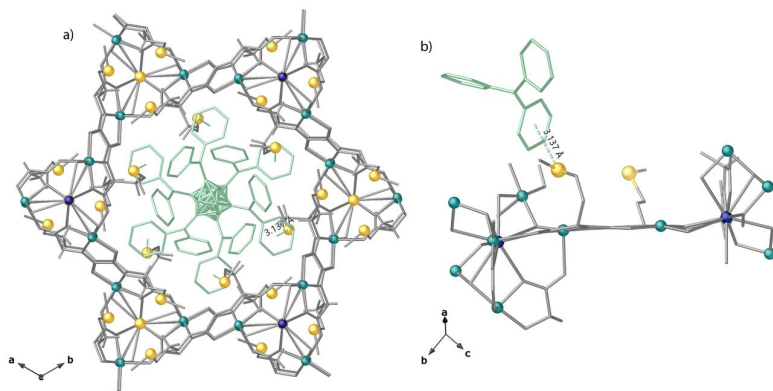


Figure S4. Details of host-guest interactions in **BG@1**: (a) Perspective view of a single channel of X-ray crystal structure of **BG@1** along *c* crystallographic axis emphasizing pores filled by Brilliant Green and (b) details of host-guest interactions (BG···S represented as green dashed lines). Copper and calcium are represented by cyan and blue spheres respectively, whereas the ligands and guest molecules are depicted as grey and green sticks except for sulfur atoms of methoxy moieties, which are represented by yellow spheres. Free water molecules are omitted for clarity.

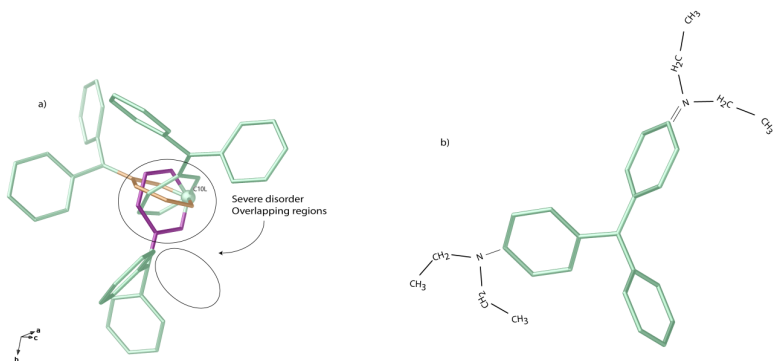


Figure S5. (a) Details of the three sets of guest conformations statistically disordered in **BG@1**. All possible orientations are included for the overlapping region, sharing C10L atom, represented in purple, gold-brown and green colors. (b) Details of a modelled set of BG in crystal structure of **BG@1** with scheme of undetected fragments from ΔF maps.

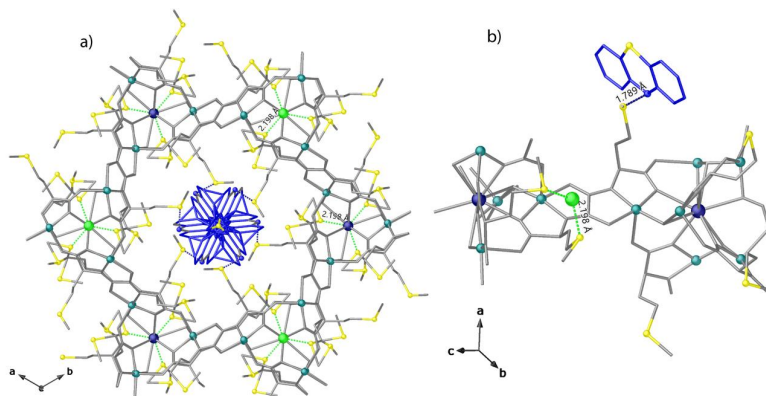


Figure S6. Details of host-guest interactions in **MB@1**: (a) Perspective view of a single channel of X-ray crystal structure of **MB@1** along *c* crystallographic axis emphasizing pores filled by Methylene Blue and (b) details of host-guest interactions ($S \cdots Cl$ and $MB \cdots S$ represented as green and blue dashed lines, respectively). Copper and calcium are represented by cyan and blue spheres respectively, whereas the ligands and guest molecules are depicted as grey and blue sticks except for sulfur atoms of methoxy moieties and guest molecule, which are represented by yellow spheres. Free water molecules are omitted for clarity.

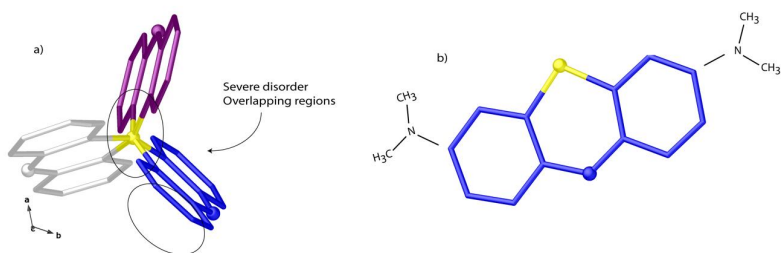


Figure S7. (a) Details of the three sets of guest conformations statistically disordered in **MB@1**. All possible orientations are included, represented in blue, magenta and white colors. (b) Details of a modelled set of MB in crystal structure of **MB@1** with scheme of undetected fragments from ΔF maps.

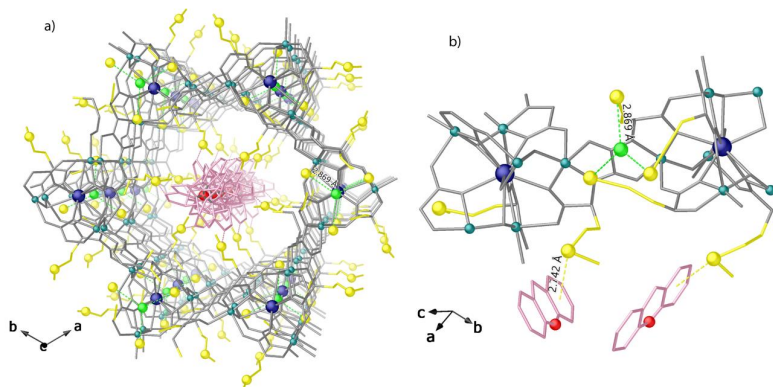


Figure S8. Details of host-guest interactions in **PY@1**: (a) Perspective view of a single channel of X-ray crystal structure of **PY@1** along *c* crystallographic axis emphasizing pores filled by Pyronin Y and (b) details of host-guest interactions ($S\cdots Cl$ and $PY\cdots S$ represented as green and pink dashed lines, respectively). Copper and calcium are represented by cyan and blue spheres respectively, whereas the ligands and guest molecules are depicted as grey and pink sticks for carbon and nitrogen respectively. Sulfur atoms of methoxy moieties and oxygen atoms of guest molecule are represented by yellow and red spheres, respectively. Free water molecules are omitted for clarity.

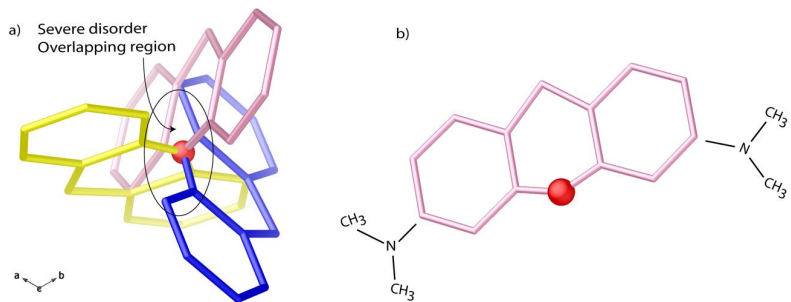


Figure S9. (a) Details of the three sets of guest conformations statistically disordered in **PY@1**. (All possible orientations are included, represented in blue, yellow and pink colors). (b) Details of a modelled set of PY in crystal structure of **PY@1** with scheme of undetected fragments from ΔF maps.

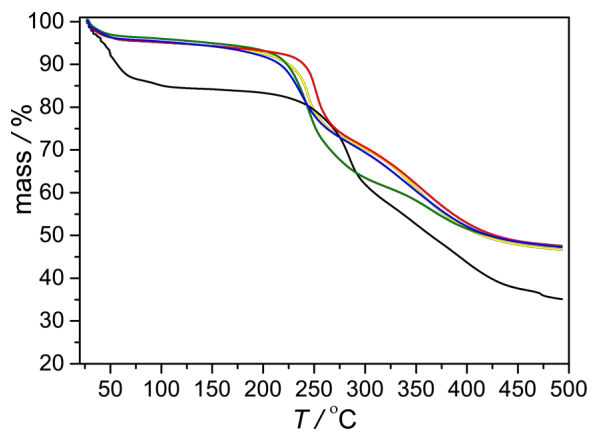


Figure S10. Thermo-Gravimetric Analyses (TGA) of **1** (black), **AO@1** (yellow), **BG@1** (green), **MB@1** (blue) and **PY@1** (red) under a dry N₂ atmosphere.

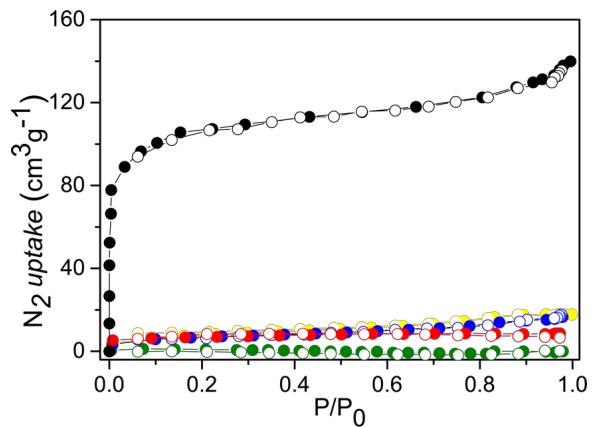


Figure S11. N₂ (77 K) adsorption isotherm for the activated compounds **1** (black), **AO@1** (yellow), **BG@1** (green), **MB@1** (blue) and **PY@1** (red). Filled and empty symbols indicate the adsorption and desorption isotherms, respectively. The samples were activated at 348 K under reduced pressure for 19 h prior to carry out the sorption measurements.

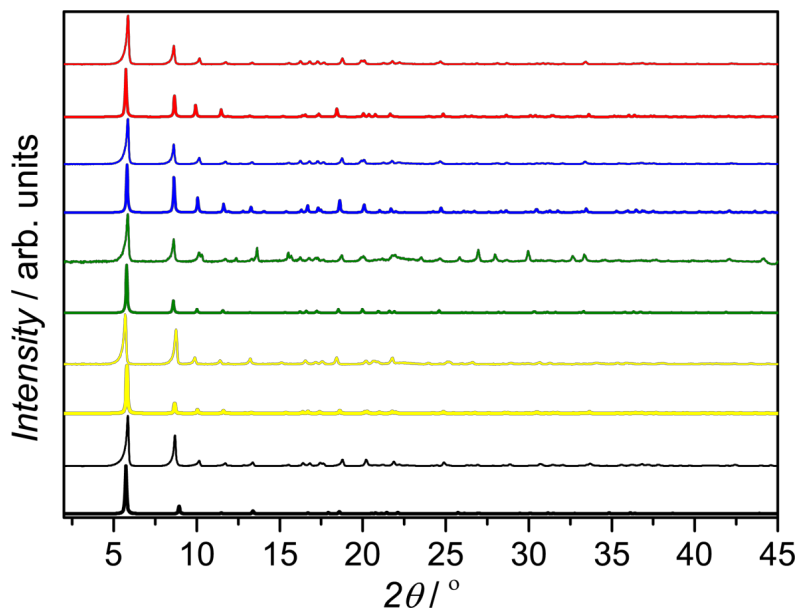
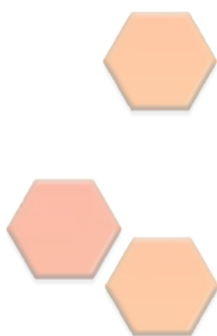


Figure S12. Calculated (bold lines) and experimental (normal lines) PXRD pattern profiles of **1** (black), **AO@1** (yellow), **BG@1** (green) and **MB@1** (blue) and **PY@1** (red) in the 2θ range 2.0–45.0.



PUBLICATION 4: Highly Efficient Removal of Neonicotinoid Insecticides by Thioether-Based (Multivariate) Metal–Organic Frameworks



Highly Efficient Removal of Neonicotinoid Insecticides by Thioether-Based (Multivariate) Metal–Organic Frameworks

Cristina Negro,[#] Héctor Martínez Pérez-Cejuela,[#] Ernesto F. Simó-Alfonso, José Manuel Herrero-Martínez,^{*} Rosaria Bruno, Donatella Armentano,^{*} Jesús Ferrando-Soria,^{*} and Emilio Pardo^{*}

Cite This: <https://doi.org/10.1021/acsami.1c08833>

Read Online

ACCESS |

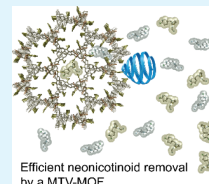
Metrics & More

Article Recommendations

Supporting Information

ABSTRACT: Circumventing the impact of agrochemicals on aquatic environments has become a necessity for health and ecological reasons. Herein, we report the use of a family of five eco-friendly water-stable isorecticular metal–organic frameworks (MOFs), prepared from amino acids, as adsorbents for the removal of neonicotinoid insecticides (thiamethoxam, clothianidin, imidacloprid, acetamiprid, and thiacloprid) from water. Among them, the three MOFs containing thioether-based residues show remarkable removal efficiency. In particular, the novel multivariate MOF $\{Sr^{II}Cu^{II}_4[(S,S)\text{-methox}]_{1.5}[(S,S)\text{-Mecysmox}]_{1.50}(\text{OH})_2(\text{H}_2\text{O})\} \cdot 36\text{H}_2\text{O}$ (**S**), featuring narrow functional channels decorated with both $-\text{CH}_2\text{SCH}_3$ and $-\text{CH}_2\text{CH}_2\text{SCH}_3$ thioalkyl chains—from L-methionine and L-methylcysteine amino acid-derived ligands, respectively—stands out and exhibits the higher removal efficiency, being capable to capture 100% of acetamiprid and thiacloprid in a single capture step under dynamic solid-phase extraction conditions—less than 30 s. Such unusual combination of outstanding efficiency, high stability in environmental conditions, and low-cost straightforward synthesis in 5 places this material among the most attractive adsorbents reported for the removal of this type of contaminants.

KEYWORDS: multivariate metal–organic frameworks, amino acids, water remediation, neonicotinoid insecticides, host–guest chemistry, crystal structures



Efficient neonicotinoid removal by a MTV-MOF

INTRODUCTION

Neonicotinoids¹ (NEOs)—so-called because of their chemical resemblance to nicotine alkaloid—are a widely used type of insecticides that, despite some recent restrictions,² have extensively spread throughout the world in the past decades because of their high efficiency in controlling insect pests. However, their use is also associated with significant environmental concerns.¹ Thus, despite low toxicity for beneficial insects was reported initially, subsequent studies demonstrated potential toxicity to beneficial insects³—such as honeybee colonies—as well as an alarming impact on avian species biodiversity, especially on grassland and insectivorous bird populations.⁴ In this context, another feature of NEO insecticides, which explain to a certain extent their popularity, is their moderate water solubility, which facilitates their application to soils and plant adsorptions.¹ This point also constitutes a problem, from an environmental point of view, because of the concomitant contamination of aquatic environments.⁵ As a consequence, it is clear that as long as NEOs are not definitely banned, efficient capture technologies are needed.

Different technologies have been proposed for the removal/degradation of pesticides and insecticides.^{6,7} These include precipitation, coagulation/flocculation, membrane technologies, use of biological processes, advanced oxidation processes, or adsorption by porous sorbents.^{5,8–10} Among them, the

removal of these contaminants by a porous material offers potential advantages over other technologies, such as, for example, preventing the formation of secondary contaminants and offering the possibility to implement economically viable decontamination protocols worldwide—which is of main relevance, especially in developing countries, giving a global application character to this potent technology.¹¹

Metal–organic frameworks^{12–16} (MOFs) are porous crystalline materials that, among many other properties, have already demonstrated to be highly efficient in the removal of both organic and inorganic contaminants.^{6,11,17–25} Main reasons for such efficiency are high water and structural stability,^{26,27} microporosity that can be functionalized pre- or postsynthetically,²⁸ to increase affinity for contaminants, and a certain degree of flexibility and/or adaptability that may play a key role capturing and accommodating the guest target contaminant.^{29,30} Moreover, unlike other porous materials, such thrilling host–guest chemistry can be visualized with the

Received: May 17, 2021

Accepted: June 6, 2021

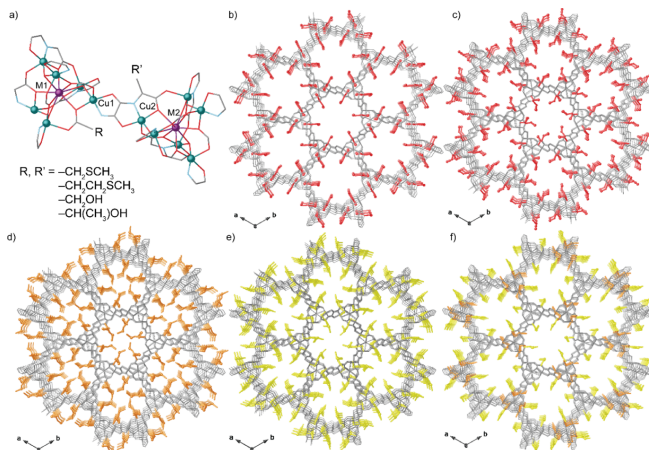


Figure 1. (a) Fragment of the structure of MOFs 1–5 emphasizing the common dicopper(II) building block. Copper and calcium/strontium (M) atoms from the network are represented by cyan and purple spheres, respectively, whereas organic ligands are depicted as gray (C), blue (N), and red (O) sticks. Perspective views of MOFs 1 (b), 2 (c), 3 (d), 4 (e), and 5 (f) along the *c* axes. Metals and organic ligands are depicted as gray sticks, whereas the amino acid residues are represented with the following color code: $-\text{CH}_2\text{OH}$ (1)/ $-\text{CH}(\text{CH}_3)\text{OH}$ (2) (red), $-\text{CH}_2\text{CH}_2\text{SCH}_3$ (3 and 5) (orange), and $-\text{CH}_2\text{SCH}_3$ (4 and 5) (yellow).

precious help of single-crystal X-ray diffraction^{31,32} (SCXRD), given the high crystallinity of these porous materials.^{33,34} This last point has been demonstrated to be extremely useful to unveil host–guest interaction governing the mechanism of the capture processes. More recently, a particular type of MOFs, the so-called multivariate MOFs^{35–37} (MTV-MOFs), which combine organic linkers with different functional groups decorating their channels, has emerged strongly in different fields that include water remediation.¹¹ However, despite all these remarkable features, the use of MOFs for the sensing^{38–41} and/or removal of pesticides/insecticides has been only barely explored.^{42–48}

In this work, we explore the performance of a family of five water-stable highly crystalline three-dimensional (3D) isoreticular MOFs (one of them is MTV-MOFs) in the removal of different NEOs of environmental concern from water. In particular, we have focused on the use of four previously reported MOFs, with formulas $\{\text{Ca}^{\text{II}}\text{Cu}^{\text{II}}_6[(\text{S},\text{S})\text{-serimox}]_3(\text{OH})_2(\text{H}_2\text{O})\} \cdot 39\text{H}_2\text{O}$ ⁴⁹ (1), $\{\text{Sr}^{\text{II}}\text{Cu}^{\text{II}}_6[(\text{S},\text{S})\text{-threomox}]_3(\text{OH})_2(\text{H}_2\text{O})\} \cdot 36\text{H}_2\text{O}$ ⁵⁰ (2), $\{\text{Ca}^{\text{II}}\text{Cu}^{\text{II}}_6[(\text{S},\text{S})\text{-methox}]_3(\text{OH})_2(\text{H}_2\text{O})\} \cdot 16\text{H}_2\text{O}$ ^{29,30} (3), and $\{\text{Ca}^{\text{II}}\text{Cu}^{\text{II}}_6[(\text{S},\text{S})\text{-Mecysmox}]_3(\text{OH})_2(\text{H}_2\text{O})\} \cdot 16\text{H}_2\text{O}$ ^{31,52} (4) (where serimox = bis[(*S*)-serine]oxalyl diamide; threomox = bis[(*S*)-threonine]oxalyl diamide; methox = bis[(*S*)-methionine]oxalyl diamide; and Mecysmox = bis[*S*-methylcysteine]oxalyl diamide), and a novel MTV-MOF of formula $\{\text{Sr}^{\text{II}}\text{Cu}^{\text{II}}_6[(\text{S},\text{S})\text{-methox}]_{1.5}[(\text{S},\text{S})\text{-Mecysmox}]_{1.50}(\text{OH})_2(\text{H}_2\text{O})\} \cdot 36\text{H}_2\text{O}$ (5) (Scheme S1 and Figure 1). The selection of this family of MOFs is not accidental. This is based on their good mechanical properties, which have already permitted their processability as pellets²⁹ or mixed matrix membranes,⁵¹ their proven air and water stability⁵³ (neutral and basic media), and their excellent performances in the removal of both

inorganic^{29,51} (Hg^{2+}) and organic contaminants (dyes⁵⁴ or vitamins,^{49,55} recently reported for 1–4, in the presence of other metal cations and inorganic anions usually present in potable drinking water.^{29,30,35,54} The main reasons that lie at the origin of such remarkable capture properties are twofold: (i) these MOFs feature channels decorated with different functional groups, which can be tuned depending on the nature of the chosen amino acid residue ($-\text{CH}_2\text{OH}$, $-\text{CH}(\text{CH}_3)\text{OH}$, $-\text{CH}_2\text{SCH}_3$, and/or $-\text{CH}_2\text{CH}_2\text{SCH}_3$); and (ii) these amino acid residues exhibit a high degree of adaptability,⁵⁶ being capable of accommodating and adjusting to guest molecules by maximizing host–guest interactions with the contaminant.

RESULTS AND DISCUSSION

We report here the efficiency of the whole family of MOFs, as solid-phase extraction (SPE) sorbents, toward five well-known NEOs like thiamethoxam, clothianidin, imidacloprid, acetamiprid, and thiacloprid (Scheme S2 and Table S1).¹ Overall, the three thioether-derived isoreticular MOFs (3–5) are capable of capturing, very efficiently, NEOs in a single loading step—within 30 s. In particular, the novel MTV-MOF 5—featuring functional pores tailored with, approximately, a 50% of $-\text{CH}_2\text{CH}_2\text{SCH}_3$ groups and another 50% of the $-\text{CH}_2\text{SCH}_3$ residues from the amino acids *L*-methionine and *S*-methyl-*L*-cysteine (Figure 1f), respectively—shows the best performance for all the NEOs, being capable of capturing 99–100% of acetamiprid and thiacloprid in a single capture process. In addition, it has been possible to solve the crystal structures of the resulting host–guest adsorbates with acetamiprid and thiacloprid that help to unveil the mechanism of the capture process of MTV-MOF 5.

B

<https://doi.org/10.1021/acsami.1c08833>
ACS Appl. Mater. Interfaces XXXX, XXX, XXX–XXX

Figure 1 shows the crystal structures of 1–5. They all are isomorphous, crystallizing in the chiral $P6_3$ space group of the hexagonal system, and exhibit chiral 3D calcium(II)/strontium(II)–copper(II) networks featuring hexagonal channels, where the different adaptable amino acid residues are depicted in different colors (see color code in Figure 1). The crystal structure of the novel material reported here $\{Sr^{II}Cu^{II}_6[(S,S)\text{-methox}]_{1.5}[(S,S)\text{-Mecys-mox}]_{1.50}(\text{OH})_2(\text{H}_2\text{O})\}\cdot 36\text{H}_2\text{O}$ (5) has been determined by SCXRD measurements—using synchrotron radiation at the I19 beamline of the Diamond Light Source (Table S2). Well-shaped crystals of 5 were grown with a slow diffusion technique (see the Supporting Information). 5 presents an uninodal *acs* six-connected 3D strontium(II)–copper(II) network with functional hexagonal channels—virtual diameters of ca. 1 nm—decorated by the two types of flexible amino acid residues, the ethylene- ($-\text{CH}_2\text{CH}_2\text{SCH}_3$) and the methylene-thiomethyl ($-\text{CH}_2\text{SCH}_3$), belonging to methionine and methyl cysteine amino acids, respectively (Figures 1 and S1).

Similarly to single-ligand parent compounds 3 and 4, MTV-MOF 5 shows also a highly stable 3D porous network, with flexibility confined only in pores, where highly bendable arms are prone to adopt different conformations of the thioether chains depending on the different chemical environments determined by guest's nature (Figure S1c,d). In particular, the crystal structure of 5 shows methionine arms more bent than methyl-cysteine ones (Figures 1 and S1a,b), featuring available sulfur groups for interaction—mainly based on σ -hole—with electron donors—including oxygen and nitrogen atoms^{57–61} and π -systems (vide infra).⁶² Thus, they encapsulate the targeted guest molecules assuming the favorite conformation, in each case, to maximize the host–guest interactions. The channel size in 5 (Figure S1b) is similar to those in 3 and 4, with the added value of chemical diversity confined in the same pores, guaranteed by diverse length and electron density for $-\text{CH}_2\text{CH}_2\text{SCH}_3$ and $-\text{CH}_2\text{SCH}_3$ groups. The crystal structure of the chiral network 5 unveils statistically disordered *trans*-oxamidato-bridged dicopper(II) units of $\{\text{Cu}^{II}_2[(S,S)\text{-Mecys-mox}]\}$ and $\{\text{Cu}^{II}_2[(S,S)\text{-methox}]\}$ (Figure S1 inset,c), which build the 3D motif. As stated above, SCXRD measurements on 5 have been performed using synchrotron radiation. This was done with the aim to safeguard the desirable high quality of data set in case of such statistical disordered. In this respect, the best final model found for the crystal structure is based on the most realistic assumption that there is a random distribution of methyl-cysteine and methionine moieties (with 1:1 ratio) within the net (see crystallographic details in the Supporting Information), as previously reported by us for an analogue MTV-MOF.³⁵ In so doing, the spatial average, of all fragments and all their possible orientations averaged in the crystal via only one unit cell (see crystallographic details in the Supporting Information), discloses basically the crystal structure of 5, which is constructed from the self-assembly of copper(II) dimers and Sr^{II} ions, through the carboxylate groups of the ligands (Figure S1). Aqua/hydroxo groups (in a 1:2 statistical distribution) contribute to further connect neighboring Cu^{2+} and $\text{Cu}^{2+}/\text{Sr}^{2+}$ ions finally linked in a μ_3 fashion (Figures S1c,d). Indeed, it must be the comparable percentage of Mecysmox and methox that gives back to superimposed snapshot of mixed $\{\text{Cu}^{II}_2[(S,S)\text{-methox}/\text{Mecys-mox}]\}$ dimers, which is also supported by the experimental results of composition analysis (vide infra C, H, S, N, and Supporting Information).

Besides the structural characterization and elemental analysis, the chemical identity of 5 was further established by powder X-ray diffraction (PXRD), electronic microscopy, and thermogravimetric analyses (TGAs) (see the Supporting Information).

Figure S2 shows the experimental PXRD pattern of 5. It is identical to the theoretical one, which confirms that the bulk sample is pure and homogeneous. Moreover, the structural stability of 5 was tested after being soaked, for 48 h, in neutral (Figure S3b), basic (Figure S3c, pH = 12), and acid (Figure S3d, pH = 5 and Figure S3e, pH = 2) aqueous media (Figure S3). This test confirmed that 5 is stable in basic and moderately acid media. The permanent porosity of 5 was verified by measuring their N_2 adsorption isotherm at 77 K, which is also compared to those adsorption isotherms of related MOFs 3 and 4 (Figure S4). Overall, they confirm permanent porosity for 3–5, with larger N_2 adsorbed amounts for 4 and 5, which is consistent with higher accessible void spaces, as suggested by the crystal structures (Figure 1). The solvent content of 5 was, however, definitively established by TGA (see Figure S5), which also confirms that 5 is stable up to 250 °C, when decomposition starts. The reported analyses performed both on the bulk and on the crystal sample of MTV-MOF 5 unveil similar composition to that used in the reaction mixture, validating the hypothesis that there were no significant ligand preferences giving nature and stability of both 3 and 4 parent MOFs. These results, together with previously reported ones,³⁵ confirm a successful protocol, which proposes that the composition can be controlled through the relative reactant concentrations in this family of materials.

For the evaluation of the NEO capture properties, SPE devices were prepared by packing 25 mg of the corresponding MOF (1–5) between two frits into 1 mL of empty propylene cartridges. First of all, activation and equilibration of the sorbent were done with 1 mL of MeOH and 1 mL of H_2O , consecutively. Then, 1 mL of aqueous mixtures of thiamethoxam, clothianidin, imidacloprid, acetamiprid, and thiacloprid at four levels of concentrations (0.1, 1, 10, and 100 mg L^{-1}) was percolated through the SPE cartridges. Then, a washing step was carried out with 1 mL of H_2O . After that, elution of the retained analytes was accomplished with MeOH (5 mL). All SPE fractions were collected and filtered (membrane with pore size of 0.22 μm) prior to their injection in HPLC system, and the NEO content was established (see also Experimental Section).

Following this procedure, the efficiency of the NEO capture was, initially, evaluated for 1–5 using a mixture of the five NEOs (at 1 mg L^{-1} each), and the results are collected in Table S3. Overall, the five MOFs showed distinct behaviors, and they can be classified in two clearly distinct groups. The serine- (1) and threonine-derived (2) MOFs—for which a high capture efficiency of organic dyes was reported previously—exhibit, by far, much worse capture properties than the thioalkyl MOFs (3–5) (Table S3). 1 and 2 do not surpass 20% of removal efficiency for any of the NEOs. In turn, 3, 4, and, especially, the MTV-MOF 5 show much higher efficiencies. On this basis, MOFs 3–5 were subjected to further capture experiments using different contents of the five NEOs (0.1, 10, and 100 mg L^{-1}). In so doing, it was observed that, overall, the three MOFs capture, very efficiently, thiacloprid and acetamiprid and, moderately well, clothianidin, imidacloprid, and thiamethoxam (Table 1). In particular, MTV-MOF 5 exhibits outstanding capture properties,

C

<https://doi.org/10.1021/acsami.1c08833>
ACS Appl. Mater. Interfaces XXXX, XXX, XXX–XXX

Table 1. Removal Values (%) for NEOs from Different Aqueous Samples (at Three Levels of Concentration) Using MOFs 3–5 ($n = 3$)

NEOs	concentration (mg L ⁻¹)	MOF		
		3	4	5
thiamethoxam	0.1	66	45	71
	10	30	28	33
	100	33	25	30
clothianidin	0.1	60	48	86
	10	64	48	74
	100	47	43	61
imidacloprid	0.1	65	50	86
	10	50	42	57
	100	38	41	60
acetamiprid	0.1	95	91	99
	10	96	91	99
	100	86	94	100
thiacloprid	0.1	93	96	100
	10	91	96	100
	100	87	98	100

especially at very diluted conditions. Thus, 5 captures, in a single step, 100% of thiacloprid and acetamiprid in any condition and 71–86%, at the most diluted conditions, of clothianidin, imidacloprid, and thiamethoxam.

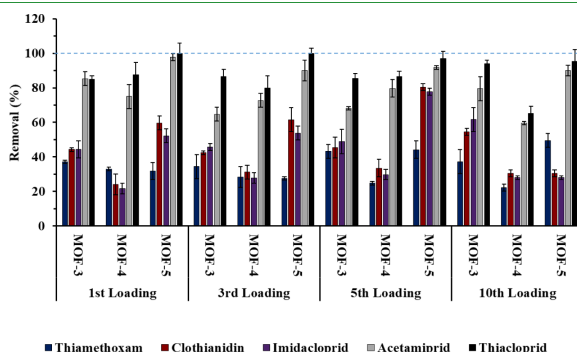
To further confirm the applicability of the developed method in removing NEOs from environmental matrices with possible competing species, a real water samples from river (Turia river; 39.504095, -0.473712; Valencia) were analyzed. For real sample analysis (river water), the same SPE protocol described above was used. None of the target pollutants were found in the samples using the optimized protocol (see [Experimental Section](#)). Therefore, the river water was spiked at 5 mg L⁻¹ with each of the five NEOs. As it can be seen in [Figure S6](#), a significant decrease in the signal was observed after SPE treatment with MOFs 3–5 as sorbents, indicating the suitable removal efficiency of these MOFs for organic pollutants in environmental waters ([Table S4](#)). Furthermore, the reproducibility of these sorbents was

evaluated, as relative standard deviation, showing values lower than 9% for all the analytes ([Table S5](#)).

In order to evaluate the reusability of the MOFs, up to 10 capture cycles—using a mixture of the five NEOs (at 1 mg L⁻¹ level)—were performed for 3–5 ([Figure 2](#)). For this purpose, the same SPE-optimized protocol, used before (see [Experimental Section](#)), was followed using an aqueous standard mixture of the five NEOs, at 1 μg mL⁻¹. It can be observed that, at least for 10 cycles, the three MOFs maintain the efficiency for the removal of the five NEOs, showing a similar capture performance. [Figure S7](#) shows the PXRD patterns, after 10 consecutive NEO sorption/desorption cycles, which confirm that 3–5 maintain the structural integrity. Moreover, no metal leaching could be observed in any of the sorption/desorption cycles.

Finally, we evaluated the maximum loading capacity of the best performing materials (3–5) toward each of the selected NEOs. Thus, polycrystalline samples of 3–5 were soaked in saturated water/acetonitrile (1:1) solutions of thiamethoxam, clothianidin, imidacloprid, acetamiprid, and thiacloprid for 1 week, replacing each saturated solution every 24 h (see [Experimental Section](#)). In so doing, maximum uptakes of 275, 312, 356, 426, and 411 (3); 402, 321, 399, 423, and 415 (4); and 447, 379, 402, 445, and 499 (5) mg g⁻¹ were determined for thiamethoxam, clothianidin, imidacloprid, acetamiprid, and thiacloprid, respectively. Maximum loadings observed for 5 closely corresponds to up to three guest molecules per SrCu₆ formula unit.

On the basis of these results and aiming at elucidating the mechanisms involved in the capture processes of the best performing material, insertion experiments were also carried out on single crystals of MTV-MOF 5 (see the [Supporting Information](#) and [Experimental Section](#)). Remarkably, suitable samples of host–guest aggregates of 5 with acetamiprid and thiacloprid for SCXRD were obtained, and the crystal structure of acetamiprid@5 and thiacloprid@5 could be determined ([Table S2](#)), which allowed the atomically precise visualization on the interaction of the two most efficiently captured NEO pollutants with the thioalkyl residues decorating the framework. The chemical formulas were finally established with the help of CHNS and SEM/EDX analyses (see [Experimental](#)

**Figure 2.** Reuses of 3–5 for the removal (%) of thiamethoxam, clothianidin, imidacloprid, acetamiprid, and thiacloprid using a 1 mg L⁻¹ mixture of NEOs.

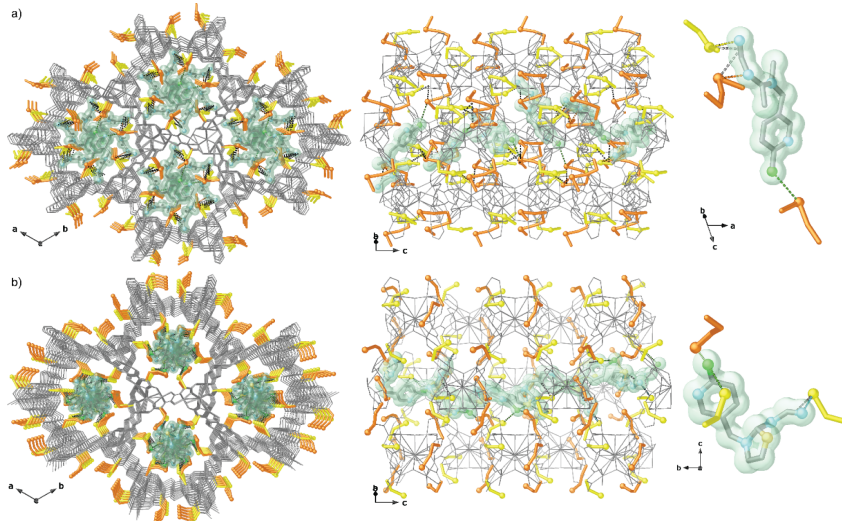


Figure 3. Perspective views in the *ab* (left) and *bc* (middle) planes of the porous structures of **acetamidrid@5** (a) and **thiacloprid@5** (b). Metals and organic ligands from the network are represented as in **Figure 1**, whereas the guest NEO molecules are represented as light blue (nitrogen), green (chloride), pale yellow (sulfur) ball-and-stick, and gray (carbon) sticks. Guest molecules are also represented as green solid surfaces with the same color code for atoms. The guest molecule structures are shown in detail in the right side of the porous structures.

Section and the **Supporting Information**), and the solvent contents were estimated by TGA: **acetamidrid@5** [$\text{Sr}^{\text{II}}\text{Cu}_6^{\text{II}}[(S,S)\text{-methox}]_{1.50}[(S,S)\text{-Mecysmox}]_{1.50}(\text{OH})_2(\text{H}_2\text{O})\} \cdot 9\text{H}_2\text{O}$ (**acetamidrid@5**) and **thiacloprid@5** [$\text{Sr}^{\text{II}}\text{Cu}_6^{\text{II}}[(S,S)\text{-methox}]_{1.50}[(S,S)\text{-Mecysmox}]_{1.50}(\text{OH})_2(\text{H}_2\text{O})\} \cdot 18\text{H}_2\text{O}$ (**thiacloprid@5**) (**Figures 3** and **S5**).

Compounds **acetamidrid@5** and **thiacloprid@5** are isomorphous to **5** and crystallize in the $P6_3$ chiral space group of the hexagonal system, confirming the preservation of the 3D network of the hosting matrix **5** even after the guests' capture. The crystal structures clearly evidence that **acetamidrid** and **thiacloprid** guest molecules are encapsulated in the nanopores of **5**, where they are simultaneously recognized by the thioether arms of the methyl-cysteine and methionine residues. The most stabilizing forces are assured by sulfur atoms interacting either with nitrile groups or with Cl atoms as electron donors. Although the different chemical nature of **acetamidrid** and **thiacloprid**—featuring nitrile groups—among the whole family of tested NEOs, seems a priori to be discriminant, it is not supported by host–guest interactions visualized by SCXRD. Indeed, it is pretty interesting to observe that in **acetamidrid@5** both methyl-cysteine and methionine arms distend their conformation within pores pointing toward nitrile groups, while in **thiacloprid@5**, the S⋯Cl interaction is observed as prominent—with molecules orienting in such a way to confine the $-\text{CN}$ moieties toward the hidden center of the pores (**Figures 2** and **S8–S11**). Although both **acetamidrid** and **thiacloprid** molecules were disordered in the pores, we succeeded to get their possible configurations and locations (see **Supporting Information** for structural details) as well as

details on their interaction sites with the hosting matrix MTV-MOF **5** (**Figures S8–S13**).

Details of **acetamidrid@5** crystal structure show molecules statistically disordered on three configuration sets (see **Figures S8** and **S12**) residing in the pores, packed via straight S⋯N–CN—involving only methionine residues—[S⋯N distances of 3.18(1) Å] and S⋯nitrile interactions—involving both kind of arms—which block **acetamidrid** terminal moieties at almost identical distance [S⋯CN_{centroid} distances of 3.67(1) and 3.82(1) Å, for methyl-cysteine and methionine residues, respectively] (**Figure S9**). On the contrary, in **thiacloprid@5** crystal structure (**Figure S10**), the two kinds of amino acid residues are involved in different contacts. **Thiacloprid** molecules, statistically disordered as well on three configuration sets (**Figure S13**), are captured via either methionine residues, which involve sulfur atoms to interact with Cl [S⋯Cl distance of 3.10 (1) Å] or methyl-cysteine residues, which contribute with interactions of the type S⋯S held with thiazolidine ring of pollutant molecules [S⋯S distance of 2.76(1) Å] (**Figure S11**). Both contact distances fall in the range of those found in the literature for similar S interactions,⁶¹ although the last distance, exhibiting a value lower than the sum of van der Waals radii, has been rarely observed.⁶³ The arrangement of the NEO molecules is clearly driven by the pore's size as well, which imposes preferential configurations. Indeed, despite their structural similarity, the molecular orientation found in the nanoconfined space for **acetamidrid** and **thiacloprid** is surprisingly different. It is worth to note also the high loading of guests, which displace almost all water molecules from the pores, and it is at the origin of the

E

<https://doi.org/10.1021/acscami.1c08833>
ACS Appl. Mater. Interfaces XXXX, XXX, XXX–XXX

close-packing observed. In fact, **acetamidrid@5** and **thiacloprid@5** almost totally fill channels (Figures S8 and S10), making extremely robust the adsorbates being stable at air and room temperature for 4 weeks. This, indeed, represents an added value for a more safe storage and handling of a scavenger material like that, for which only the regeneration process, based on the use of appropriate solvent, will cause the release of captured pollutants.

The high performance of **5** for some NEO capture could be understood with the help of X-ray crystallography. Interactions found in **acetamidrid@5** and **thiacloprid@5**, discussed in the context of both sulfur-containing ligands, have a prominent role because of their extensive propagation in the nanoconfined space ensured by **5**, exactly as observed for peptide-based methionine, cysteine, and cysteine moieties—where associations extend beyond that of simple hydrophobic interactions. Both intra- and intermolecular interactions—involving low-lying sulfur σ^* orbitals—are known to be implicated in chemical reactivity, with electronic characteristics of chemical systems responsible, in part, for specific kinetic, regiochemical, or even stereochemical outcomes. Indeed, it is also known that electron-deficient bivalent sulfur atoms have two areas of positive electrostatic potential, as a consequence of the low-lying σ^* orbitals of the C–S bond (the so-called σ -hole),^{62,64} which are available for interaction with electron donors such as nitrogen atoms or, as in the present case, nitrile groups and, even, π -systems. The present results, together with the previously reported by us,^{20,25–27} represent the first examples of a judicious exploitation of these sulfur-based interactions. Intramolecular interactions are by far the most common manifestation of this effect, which offers a means of modulating the conformational preferences of a molecule. Although it is a well-documented phenomenon, a priori applications in rational capture are relatively sparse, and this interaction, which is often isosteric with an intramolecular hydrogen-bonding interaction, appears to be underappreciated by the applied chemistry community. The majority of the examples of this kind of sulfur interaction have been noted in post facto analyses of crystallographic or other structural information, and there are relatively few examples reported in the literature where this interaction has been exploited in a prospective fashion.⁶⁵

CONCLUSIONS

In summary, we report the one-step efficient capture of NEO insecticides by a family of isoreticular thioether-based MOFs derived from amino acids *L*-methionine and *S*-methyl-L-cysteine. In particular, the novel MTV-MOF **5**—combining both amino acids in equal proportions—exhibits outstanding capture properties, being capable to remove, in a single step, 100% of acetamidrid and thiacloprid at different conditions and 71–86%, at the most diluted conditions, of clothianidin, imidacloprid, and thiamethoxam. In addition, the capture properties are maintained during, at least 10 cycles. Remarkably, the crystal structures of the two host–guest aggregates of **5** with acetamidrid and thiacloprid could be resolved, which allowed to visualize how both NEOs are encapsulated and immobilized. Also, it enables to unveil the synergistic interactions of both types of thioether groups with the guest molecules, which are ultimately responsible for such capture efficiency. This family of thioether-containing MOFs arise as an alternative for more traditional materials, such as

activated carbons,^{66–68} for the capture of this type of emerging contaminants.

EXPERIMENTAL SECTION

Preparation of $\{Sr^{II}Cu^{II}_6[(S,S)\text{-methox}]_{1,5}[(S,S)\text{-Mecysmox}]_{1,50}(\text{OH})_2(\text{H}_2\text{O})\}_n \cdot 36\text{H}_2\text{O}$ (5**).** Well-shaped hexagonal prisms of **5**, suitable for SCXRD, were obtained by slow diffusion in H-shaped tubes of aqueous solutions containing stoichiometric amounts of $(\text{Me}_4\text{N})_2\text{Cu}_2[(S,S)\text{-methox}](\text{OH})_2 \cdot 4\text{H}_2\text{O}$ (0.131 g, 0.18 mmol) and $(\text{Me}_4\text{N})_2\text{Cu}_2[(S,S)\text{-Mecysmox}](\text{OH})_2 \cdot 5\text{H}_2\text{O}$ (0.129 g, 0.18 mmol) in one arm and $\text{Sr}(\text{NO}_3)_2$ (0.025 g, 0.12 mmol) in the other. They were isolated by filtration on paper and air-dried. A gram-scale procedure was also carried out successfully by mixing greater amounts of $(\text{Me}_4\text{N})_2\text{Cu}_2[(S,S)\text{-methox}](\text{OH})_2 \cdot 4\text{H}_2\text{O}$ (4.37 g, 6 mmol) and $(\text{Me}_4\text{N})_2\text{Cu}_2[(S,S)\text{-Mecysmox}](\text{OH})_2 \cdot 5\text{H}_2\text{O}$ (4.32 g, 6 mmol) in water (60 mL). Another aqueous solution of $\text{Sr}(\text{NO}_3)_2$ (0.846 g, 4 mmol) was added dropwise to the resulting deep green solution, and the final mix was allowed to react, under stirring, for 6 h. Afterward, the material was isolated by filtration and characterized by C, H, N, S analyses to give a final formula of $\{Sr^{II}Cu^{II}_6[(S,S)\text{-methox}]_{1,5}[(S,S)\text{-Mecysmox}]_{1,50}(\text{OH})_2(\text{H}_2\text{O})\}_n \cdot 30\text{H}_2\text{O}$. Anal. Calcd for **5**: $\text{C}_{43}\text{Cu}_6\text{Sr}_6\text{H}_{118}\text{N}_{10}\text{O}_{39}$ (2172.6): C, 18.24; H, 5.47; S, 8.86; N, 3.87%. Found: C, 18.13; H, 5.52; S, 8.82; N, 3.93%; IR (KBr): $\nu = 1611$ and 1606 cm^{-1} (C=O).

Preparation of Acetamidrid@ $\{Sr^{II}Cu^{II}_6[(S,S)\text{-methox}]_{1,5}[(S,S)\text{-Mecysmox}]_{1,50}(\text{OH})_2(\text{H}_2\text{O})\}_n \cdot 9\text{H}_2\text{O}$ (Acetamidrid@5**) and Thiacloprid@ $\{Sr^{II}Cu^{II}_6[(S,S)\text{-methox}]_{1,5}[(S,S)\text{-Mecysmox}]_{1,50}(\text{OH})_2(\text{H}_2\text{O})\}_n \cdot 18\text{H}_2\text{O}$ (Thiacloprid@**5**).** Well-shaped hexagonal prisms of **acetamidrid@5** and **thiacloprid@5**, suitable for SCXRD, could be obtained by soaking crystals of **5** (ca. 5.0 mg) for a week in saturated acetonitrile solutions containing acetamidrid and thiacloprid (recharging fresh saturated solutions daily). After this period, they were isolated by filtration, air-dried, and characterized by SCXRD, C, H, N, S, and TGA analyses to give, as final formulas, **acetamidrid@ $\{Sr^{II}Cu^{II}_6[(S,S)\text{-methox}]_{1,5}[(S,S)\text{-Mecysmox}]_{1,50}(\text{OH})_2(\text{H}_2\text{O})\}_n \cdot 9\text{H}_2\text{O}$ (acetamidrid@**5**)** and **thiacloprid@ $\{Sr^{II}Cu^{II}_6[(S,S)\text{-methox}]_{1,5}[(S,S)\text{-Mecysmox}]_{1,50}(\text{OH})_2(\text{H}_2\text{O})\}_n \cdot 18\text{H}_2\text{O}$ (thiacloprid@**5**)**. The same synthetic was carried out, with identical results, with larger amounts of polycrystalline samples. Anal. Calcd for **acetamidrid@5**: $\text{C}_{43}\text{Cu}_6\text{ClSr}_6\text{H}_{118}\text{N}_{10}\text{O}_{39}$ (1908.9): C, 27.06; H, 3.96; S, 10.08; N, 7.34%. Found: C, 27.09; H, 3.77; S, 10.02; N, 7.38%; IR (KBr): $\nu = 2233$ (C≡N), 1641 (C=N), and 1611 and 1606 cm^{-1} (C=O). Anal. Calcd for **thiacloprid@5**: $\text{C}_{43}\text{Cu}_6\text{ClSr}_6\text{H}_{99}\text{N}_{10}\text{O}_{39}$ (2101.0): C, 24.58; H, 4.37; S, 10.68; N, 6.66%. Found: C, 24.59; H, 4.31; S, 10.59; N, 6.69%; IR (KBr): $\nu = 2238$ (C≡N), 1645 (C=N), and 16011 and 1609 cm^{-1} (C=O).

Well-shaped hexagonal prisms of **acetamidrid@5** and **thiacloprid@5**, suitable for SCXRD, could be obtained by soaking crystals of **5** (ca. 5.0 mg) for a week in saturated acetonitrile solutions containing acetamidrid and thiacloprid (recharging fresh saturated solutions daily). After this period, they were isolated by filtration, air-dried, and characterized by SCXRD, C, H, N, S, and TGA analyses to give, as final formulas, **acetamidrid@ $\{Sr^{II}Cu^{II}_6[(S,S)\text{-methox}]_{1,5}[(S,S)\text{-Mecysmox}]_{1,50}(\text{OH})_2(\text{H}_2\text{O})\}_n \cdot 9\text{H}_2\text{O}$ (acetamidrid@**5**)** and **thiacloprid@ $\{Sr^{II}Cu^{II}_6[(S,S)\text{-methox}]_{1,5}[(S,S)\text{-Mecysmox}]_{1,50}(\text{OH})_2(\text{H}_2\text{O})\}_n \cdot 18\text{H}_2\text{O}$ (thiacloprid@**5**)**. The same synthetic was carried out, with identical results, with larger amounts of polycrystalline samples. Anal. Calcd for **acetamidrid@5**: $\text{C}_{43}\text{Cu}_6\text{ClSr}_6\text{H}_{118}\text{N}_{10}\text{O}_{39}$ (1908.9): C, 27.06; H, 3.96; S, 10.08; N, 7.34%. Found: C, 27.09; H, 3.77; S, 10.02; N, 7.38%; IR (KBr): $\nu = 2233$ (C≡N), 1641 (C=N), and 1611 and 1606 cm^{-1} (C=O). Anal. Calcd for **thiacloprid@5**: $\text{C}_{43}\text{Cu}_6\text{ClSr}_6\text{H}_{99}\text{N}_{10}\text{O}_{39}$ (2101.0): C, 24.58; H, 4.37; S, 10.68; N, 6.66%. Found: C, 24.59; H, 4.31; S, 10.59; N, 6.69%; IR (KBr): $\nu = 2238$ (C≡N), 1645 (C=N), and 16011 and 1609 cm^{-1} (C=O).

Capture Experiments. Selected NEOs (thiamethoxam, clothianidin, imidacloprid, acetamidrid, and thiacloprid) in this study were obtained from Sigma-Aldrich (St. Louis, MO, USA). See details and structures in Table S1. All the solvents (e.g., methanol (MeOH) or acetonitrile (MeCN) and others) were of HPLC grade and purchased from VWR International Eurolab (Barcelona, Spain). Nanopure water

F

<https://doi.org/10.1021/acsmi.1c08833>
ACS Appl. Mater. Interfaces XXXX, XXX, XXX–XXX

was purified in Crystal B30 EDI Adrona deionizer (Riga, Latvia). Other nonspecific reagents were of analytical grade unless otherwise stated. SPE propylene cartridges of 1 mL (internal volume) and their respective frits (1/16", 20 μm) were provided from Análisis Vínicos (Tomelloso, Spain). Individual standard solutions (at 1000 mg L⁻¹) of NEOs were prepared in fresh MeOH and kept until their use at 4 °C. For daily work, standard mixtures were prepared by dilution from the stock solutions. Water samples from Turia river (39.504095, -0.473712; Valencia) were collected in dark glass bottles and stored at 4 °C until analysis. For real sample analysis (river water), the same SPE protocol was done. River water samples were spiked after reaching room temperature, and no more additional pretreatment steps were needed.

General SPE Protocol. SPE cartridges were prepared as stated above. First, 1 mL of aqueous standard mixtures of contaminants, at the appropriate concentration, was loaded to the cartridge. Then, a washing step was carried out using 1 mL of water. After that, the elution was accomplished with 5 mL of pure MeOH. An additional step was performed for reconditioning the extraction unit passing through the cartridge 1 mL of MeOH and 1 mL of water. The process was repeated until a significant signal decrease was achieved. All the fractions were filtered (using a nylon membrane, 0.23 μm) previous to their injection to the HPLC-UV system.

Maximum Loading Experiments. The maximum loading capacities of MOFs 3–5 toward each of the selected NEOs were determined by soaking polycrystalline samples of 3–5, in saturated water/acetonitrile (1:1) solutions of thiamethoxam, clothianidin, imidacloprid, acetamiprid, and thiacloprid for 1 week. Each saturated solution was replaced every 24 h. After 1 week, polycrystalline samples were filtered, and the number of guest molecules was estimated by determining the Cu₂Sr/Cl ratio with ICP-MS analyses (data not shown).

X-ray Crystallographic Data Collection and Structure Refinement. Crystals of 5, acetamiprid@5, and thiacloprid@5 were selected and mounted on a MITIGEN holder in Paratone oil, and then quickly placed in a nitrogen stream cooled at 100 K to extract the best data set avoiding the possible degradation upon desolvation or exposure to air. Nevertheless, crystals of both acetamiprid@5 and thiacloprid@5 samples displayed an outstanding stability at air and room temperature for at least 4 weeks, as demonstrated by their diffraction patterns measured at 296 K as well, without displaying any important crystal decay. Diffraction data for 5 were collected using synchrotron radiation at I19 beamline of the Diamond Light Source at $\lambda = 0.6889$ Å, whereas for acetamiprid@5 and thiacloprid@5 data were acquired on a Bruker-Nonius X8APEXII CCD area detector diffractometer using graphite-monochromated Mo K α radiation ($\lambda = 0.71073$ Å), as a significant beam damage was observed for both single crystals under synchrotron radiation. Further crystallographic details can be found in the Supporting Information.

X-ray Powder Diffraction Measurements. Fresh polycrystalline samples of 5, acetamiprid@5, and thiacloprid@5 were introduced into 0.5 mm of borosilicate capillaries prior to being mounted and aligned on an Empyrean PANalytical powder diffractometer, using Cu K α radiation ($\lambda = 1.54056$ Å). For each sample, five repeated measurements were collected at room temperature ($2\theta = 2^\circ$ – 60°) and merged in a single diffractogram.

The same procedure was carried out for polycrystalline samples of 3, 4, and 5, after 10 sorption/desorption cycles with the solution containing the five NEOs simultaneously.

■ ASSOCIATED CONTENT

Supporting Information

The Supporting Information is available free of charge at <https://pubs.acs.org/doi/10.1021/acsami.1c08833>.

Experimental preparation, analytical characterization; Tables S1–S5, Schemes S1 and S2, and Figures S1–S13 (PDF)

CCDC reference numbers CCDC 2072807-2072809 (CIF), (CIF) and (CIF)

■ AUTHOR INFORMATION

Corresponding Authors

José Manuel Herrero-Martínez – Departamento de Química Analítica, Universitat de Valencia, 46100 Valencia, Spain; Email: jmherrer@uv.es

Donatella Armentano – Dipartimento di Chimica e Tecnologie Chimiche (CTC), Università della Calabria, Rende 87036, Italy; orcid.org/0000-0002-8502-8074; Email: donatella.armentano@unical.it

Jesús Ferrando-Soria – Instituto de Ciencia Molecular (ICMol), Universidad de Valencia, 46980 Valencia, Spain; Email: jesus.ferrando@uv.es

Emilio Pardo – Instituto de Ciencia Molecular (ICMol), Universidad de Valencia, 46980 Valencia, Spain; orcid.org/0000-0002-1394-2553; Email: emilio.pardo@uv.es

Authors

Cristina Negro – Instituto de Ciencia Molecular (ICMol), Universidad de Valencia, 46980 Valencia, Spain

Héctor Martínez Pérez-Cejuela – Departamento de Química Analítica, Universitat de Valencia, 46100 Valencia, Spain

Ernesto F. Simó-Alfonso – Departamento de Química Analítica, Universitat de Valencia, 46100 Valencia, Spain

Rosaria Bruno – Dipartimento di Chimica e Tecnologie Chimiche (CTC), Università della Calabria, Rende 87036, Italy

Complete contact information is available at: <https://pubs.acs.org/doi/10.1021/acsami.1c08833>

Author Contributions

#C.N. and H.M.P.-C. have equally contributed to this work.

Notes

The authors declare no competing financial interest.

■ ACKNOWLEDGMENTS

This work was supported by the Ministero dell'Istruzione, dell'Università e della Ricerca (Italy) and the MINECO (Spain) (Projects RTI2018-095536-B-I00, PID2019-104778GB-I00, and Excellence Unit "María de Maeztu" CEX2019-000919-M). D.A. acknowledges the financial support of the Fondazione CARIPLO/"Economia Circolare: ricerca per un futuro sostenibile" 2019, Project code: 2019-2090; MOCA and Diamond Light Source for awarded beamtime and provision of synchrotron radiation facilities; and thank Dr. David Allan and Sarah Barnett for their assistance at I19 beamline (Proposal no. CY22411-1). Thanks are also extended to the 2019 Post-doctoral Junior Leader-Retaining Fellowship, la Caixa Foundation (ID100010434 and fellowship code LCF/BQ/PR19/11700011), and "Generalitat Valenciana" (SEJ1/2020/034) (J.F.–S.). E.P. acknowledges the financial support of the European Research Council under the European Union's Horizon 2020 research and innovation programme/ERC Grant Agreement no. 814804, MOF-reactors. H.M.P.-C. thanks the MSIU for a PhD FPU grant.

REFERENCES

- (1) Goulson, D. REVIEW: An Overview of the Environmental Risks Posed by Neonicotinoid Insecticides. *J. Appl. Ecol.* **2013**, *50*, 977–987.
- (2) European Food Safety Authority. Conclusion on the Peer Review of the Pesticide Risk Assessment for Bees for the Active Substance Clothianidin. *EFSA J.* **2013**, *11*, No. 3066.
- (3) Schmuck, R.; Lewis, G. Review of Field and Monitoring Studies Investigating the Role of Nitro-Substituted Neonicotinoid Insecticides in the Reported Losses of Honey Bee Colonies (*Apis Mellifera*). *Ecotoxicology* **2016**, *25*, 1617–1629.
- (4) Li, Y.; Miao, R.; Khanna, M. Neonicotinoids and Decline in Bird Biodiversity in the United States. *Nat. Sustain.* **2020**, *3*, 1027–1035.
- (5) Castillo, M. D. P.; Torstensson, L.; Stenström, J. Biobeds for Environmental Protection from Pesticide Use Review. *J. Agric. Food Chem.* **2008**, *56*, 6206–6219.
- (6) Bolisetty, S.; Peydayesh, M.; Mezzenga, R. Sustainable Technologies for Water Purification from Heavy Metals: Review and Analysis. *Chem. Soc. Rev.* **2019**, *48*, 463–487.
- (7) Patel, M.; Kumar, R.; Kishor, K.; Mlsna, T.; Pittman, C. U.; Mohan, D. Pharmaceuticals of Emerging Concern in Aquatic Systems: Chemistry, Occurrence, Effects, and Removal Methods. *Chem. Rev.* **2019**, *119*, 3510–3673.
- (8) Vagi, M. C.; Petsas, A. S.; Kostopoulou, M. N.; Lekkas, T. D. Adsorption and Desorption Processes of the Organophosphorus Pesticides, Dimethoate and Fenthion, onto Three Greek Agricultural Soils. *Int. J. Environ. Anal. Chem.* **2010**, *90*, 369–389.
- (9) Rodríguez-Castillo, G.; Molina-Rodríguez, M.; Cambronero-Henrichs, J. C.; Quirós-Fournier, J. P.; Lizano-Fallas, V.; Jiménez-Rojas, C.; Masis-Mora, M.; Castro-Gutiérrez, V.; Mata-Araya, I.; Rodríguez-Rodríguez, C. E. Simultaneous Removal of Neonicotinoid Insecticides by a Microbial Degrading Consortium: Detoxification at Reactor Scale. *Chemosphere* **2019**, *235*, 1097–1106.
- (10) González, T.; Dominguez, J. R.; Correia, S. Neonicotinoids Removal by Associated Binary, Tertiary and Quaternary Advanced Oxidation Processes: Synergistic Effects, Kinetics and Mineralization. *J. Environ. Manage.* **2020**, *261*, No. 110156.
- (11) Mon, M.; Bruno, R.; Ferrando-Soria, J.; Armentano, D.; Pardo, E. Metal–Organic Framework Technologies for Water Remediation: Towards a Sustainable Ecosystem. *J. Mater. Chem. A* **2018**, *6*, 4912–4947.
- (12) Kitagawa, S.; Matsuda, R. Chemistry of Coordination Space of Porous Coordination Polymers. *Coord. Chem. Rev.* **2007**, *251*, 2490–2509.
- (13) Férey, G. Hybrid Porous Solids: Past, Present, Future. *Chem. Soc. Rev.* **2008**, *37*, 191–214.
- (14) Long, J. R.; Yaghi, O. M. The Pervasive Chemistry of Metal–Organic Frameworks. *Chem. Soc. Rev.* **2009**, *38*, 1213–1214.
- (15) Farha, O. K.; Hupp, J. T. Rational Design, Synthesis, Purification, and Activation of Metal–Organic Framework Materials. *Acc. Chem. Res.* **2010**, *43*, 1166–1175.
- (16) Furukawa, H.; Cordova, K. E.; O’Keeffe, M.; Yaghi, O. M. The Chemistry and Applications of Metal–Organic Frameworks. *Science* **2013**, *341*, No. 1230444.
- (17) Li, J.; Wang, X.; Zhao, G.; Chen, C.; Chai, Z.; Alsaedi, A.; Hayat, T.; Wang, X. Metal–Organic Framework-Based Materials: Superior Adsorbents for the Capture of Toxic and Radioactive Metal Ions. *Chem. Soc. Rev.* **2018**, *47*, 2322–2356.
- (18) Feng, M.; Zhang, P.; Zhou, H.-C.; Sharma, V. K. Water-Stable Metal–Organic Frameworks for Aqueous Removal of Heavy Metals and Radionuclides: A Review. *Chemosphere* **2018**, *209*, 783–800.
- (19) Kobielska, P. A.; Howarth, A. J.; Farha, O. K.; Nayak, S. Metal–Organic Frameworks for Heavy Metal Removal from Water. *Coord. Chem. Rev.* **2018**, *358*, 92–107.
- (20) Rojas, S.; Horcajada, P. Metal–Organic Frameworks for the Removal of Emerging Organic Contaminants in Water. *Chem. Rev.* **2020**, *120*, 8378–8415.
- (21) Dias, E. M.; Petit, C. Towards the Use of Metal–Organic Frameworks for Water Reuse: A Review of the Recent Advances in the Field of Organic Pollutants Removal and Degradation and the next Steps in the Field. *J. Mater. Chem. A* **2015**, *3*, 22484–22506.
- (22) Martínez-Pérez-Cejuela, H.; Mompó-Roselló, Ó.; Crespi-Sánchez, N.; Palomino Cabello, C.; Catalá-Icardo, M.; Simó-Alfonso, E. F.; Herrero-Martínez, J. M. Determination of Benzothiazolones in Environmental Complex Samples by Combining Zeolitic Imidazolate Framework-8-Based Solid-Phase Extraction and High-Performance Liquid Chromatography with UV Detection. *J. Chromatogr. A* **2020**, *1631*, No. 461580.
- (23) Martínez-Pérez-Cejuela, H.; Guñe, M.; Simó-Alfonso, E. F.; Amorós, P.; El Haskouri, J.; Herrero-Martínez, J. M. In Situ Growth of Metal–Organic Framework HKUST-1 in an Organic Polymer as Sorbent for Nitrated and Oxygenated Polycyclic Aromatic Hydrocarbon in Environmental Water Samples Prior to Quantitation by HPLC-UV. *Microchim. Acta* **2020**, *187*, No. 301.
- (24) Ghosh, S. K. *Metal–Organic Frameworks (MOFs) for Environmental Applications*; Elsevier, 2019.
- (25) Yoo, D. K.; Bhadra, B. N.; Jhung, S. H. Adsorptive Removal of Hazardous Organics from Water and Fuel with Functionalized Metal–Organic Frameworks: Contribution of Functional Groups. *J. Hazard. Mater.* **2021**, *403*, No. 123655.
- (26) Ding, M.; Cai, X.; Jiang, H.-L. Improving MOF Stability: Approaches and Applications. *Chem. Sci.* **2019**, *10*, 10209–10230.
- (27) Burtch, N. C.; Jasuja, H.; Walton, K. S. Water Stability and Adsorption in Metal–Organic Frameworks. *Chem. Rev.* **2014**, *114*, 10575–10612.
- (28) Cohen, S. M. The Postsynthetic Renaissance in Porous Solids. *J. Am. Chem. Soc.* **2017**, *139*, 2855–2863.
- (29) Mon, M.; Lloret, F.; Ferrando-Soria, J.; Martí-Gastaldo, C.; Armentano, D.; Pardo, E. Selective and Efficient Removal of Mercury from Aqueous Media with the Highly Flexible Arms of a BioMOF. *Angew. Chem., Int. Ed.* **2016**, *55*, 11167–11172.
- (30) Mon, M.; Ferrando-Soria, J.; Grancha, T.; Fortea-Pérez, F. R.; Gascon, J.; Leyva-Pérez, A.; Armentano, D.; Pardo, E. Selective Gold Recovery and Catalysis in a Highly Flexible Methionine-Decorated Metal–Organic Framework. *J. Am. Chem. Soc.* **2016**, *138*, 7864–7867.
- (31) Inokuma, Y.; Kawano, M.; Fujita, M. Crystalline Molecular Frameworks. *Nat. Chem.* **2011**, *3*, 349–358.
- (32) Bloch, W. M.; Champness, N. R.; Doonan, C. J. X-ray Crystallography in Open-Framework Materials. *Angew. Chem., Int. Ed.* **2015**, *54*, 12860–12867.
- (33) Young, R. J.; Huxley, M. T.; Pardo, E.; Champness, N. R.; Sumbly, C. J.; Doonan, C. J. Isolating Reactive Metal-Based Species in Metal–Organic Frameworks – Viable Strategies and Opportunities. *Chem. Sci.* **2020**, *11*, 4031–4050.
- (34) Viciano-Chumillas, M.; Mon, M.; Ferrando-Soria, J.; Corma, A.; Leyva-Pérez, A.; Armentano, D.; Pardo, E. Metal–Organic Frameworks as Chemical Nanoreactors: Synthesis and Stabilization of Catalytically Active Metal Species in Confined Spaces. *Acc. Chem. Res.* **2020**, *53*, 520–531.
- (35) Mon, M.; Bruno, R.; Tiburcio, E.; Viciano-Chumillas, M.; Kalinke, L. H. G.; Ferrando-Soria, J.; Armentano, D.; Pardo, E. Multivariate Metal–Organic Frameworks for the Simultaneous Capture of Organic and Inorganic Contaminants from Water. *J. Am. Chem. Soc.* **2019**, *141*, 13601–13609.
- (36) Kong, X.; Deng, H.; Yan, F.; Kim, J.; Swisher, J. A.; Smit, B.; Yaghi, O. M.; Reimer, J. A. Mapping of Functional Groups in Metal–Organic Frameworks. *Science* **2013**, *341*, 882–885.
- (37) Deng, H.; Doonan, C. J.; Furukawa, H.; Ferreira, R. B.; Towne, J.; Knobler, C. B.; Wang, B.; Yaghi, O. M. Multiple Functional Groups of Varying Ratios in Metal–Organic Frameworks. *Science* **2010**, *327*, 846–850.
- (38) Yang, Q.; Wang, J.; Chen, X.; Yang, W.; Pei, H.; Hu, N.; Li, Z.; Suo, Y.; Li, T.; Wang, J. The Simultaneous Detection and Removal of Organophosphorus Pesticides by a Novel Zr-MOF Based Smart Adsorbent. *J. Mater. Chem. A* **2018**, *6*, 2184–2192.
- (39) Kumar, P.; Paul, A. K.; Deep, A. Sensitive Chemosensing of Nitro Group Containing Organophosphate Pesticides with MOF-5. *Microporous Mesoporous Mater.* **2014**, *195*, 60–66.

H

<https://doi.org/10.1021/acsami.1c08833>
ACS Appl. Mater. Interfaces XXXX, XXX, XXX–XXX

- (40) Wang, G.-D.; Li, Y.-Z.; Shi, W.-J.; Zhang, B.; Hou, L.; Wang, Y.-Y. A Robust Cluster-Based Eu-MOF as Multi-Functional Fluorescence Sensor for Detection of Antibiotics and Pesticides in Water. *Sens. Actuators, B* **2021**, *331*, No. 129377.
- (41) Liu, G.; Li, L.; Huang, X.; Zheng, S.; Xu, D.; Xu, X.; Zhang, Y.; Lin, H. Determination of Triazole Pesticides in Aqueous Solution Based on Magnetic Graphene Oxide Functionalized MOF-199 as Solid Phase Extraction Sorbents. *Microporous Mesoporous Mater.* **2018**, *270*, 258–264.
- (42) Jung, B. K.; Hasan, Z.; Jhung, S. H. Adsorptive Removal of 2,4-Dichlorophenoxyacetic Acid (2,4-D) from Water with a Metal–Organic Framework. *Chem. Eng. J.* **2013**, *234*, 99–105.
- (43) Cao, X.; Liu, G.; She, Y.; Jiang, Z.; Jin, F.; Jin, M.; Du, P.; Zhao, F.; Zhang, Y.; Wang, J. Preparation of Magnetic Metal Organic Framework Composites for the Extraction of Neonicotinoid Insecticides from Environmental Water Samples. *RSC Adv.* **2016**, *6*, 113144–113151.
- (44) Liu, G.; Li, L.; Xu, D.; Huang, X.; Xu, X.; Zheng, S.; Zhang, Y.; Lin, H. Metal–Organic Framework Preparation Using Magnetic Graphene Oxide- β -Cyclodextrin for Neonicotinoid Pesticide Adsorption and Removal. *Carbohydr. Polym.* **2017**, *175*, S84–S91.
- (45) Zhu, X.; Li, B.; Yang, J.; Li, Y.; Zhao, W.; Shi, J.; Gu, J. Effective Adsorption and Enhanced Removal of Organophosphorus Pesticides from Aqueous Solution by Zr-Based MOFs of UiO-67. *ACS Appl. Mater. Interfaces.* **2015**, *7*, 223–231.
- (46) Seo, Y. S.; Khan, N. A.; Jhung, S. H. Adsorptive Removal of Methylchlorophenoxypropionic Acid from Water with a Metal–Organic Framework. *Chem. Eng. J.* **2015**, *270*, 22–27.
- (47) Fu, Q.; Wen, L.; Zhang, L.; Chen, X.; Pun, D.; Ahmed, A.; Yang, Y.; Zhang, H. Preparation of Ice-Templated MOF–Polymer Composite Monoliths and Their Application for Wastewater Treatment with High Capacity and Easy Recycling. *ACS Appl. Mater. Interfaces.* **2017**, *9*, 33979–33988.
- (48) Yang, J.; Trickett, C. A.; Alahmadi, S. B.; Alshammari, A. S.; Yaghi, O. M.; Calcium, L. Lactate Frameworks as Naturally Degradable Carriers for Pesticides. *J. Am. Chem. Soc.* **2017**, *139*, 8118–8121.
- (49) Mon, M.; Bruno, R.; Ferrando-Soria, J.; Bartella, L.; Di Donna, L.; Talia, M.; Lappano, R.; Maggolini, M.; Armentano, D.; Pardo, E. Crystallographic Snapshots of Host–Guest Interactions in Drugs@metal–Organic Frameworks: Towards Mimicking Molecular Recognition Processes. *Mater. Horizons* **2018**, *5*, 683–690.
- (50) Mon, M.; Bruno, R.; Elliani, R.; Tagarelli, A.; Qu, X.; Chen, S.; Ferrando-Soria, J.; Armentano, D.; Pardo, E. Lanthanide Discrimination with Hydroxyl-Decorated Flexible Metal–Organic Frameworks. *Inorg. Chem.* **2018**, *57*, 13895–13900.
- (51) Bruno, R.; Mon, M.; Escamilla, P.; Ferrando-Soria, J.; Esposito, E.; Fuoco, A.; Monteleone, M.; Jansen, J. C.; Elliani, R.; Tagarelli, A.; Armentano, D.; Pardo, E. Bioinspired Metal–Organic Frameworks in Mixed Matrix Membranes for Efficient Static/Dynamic Removal of Mercury from Water. *Adv. Funct. Mater.* **2021**, *31*, No. 2008499.
- (52) Tiburcio, E.; Greco, R.; Mon, M.; Ballesteros-Soberanas, J.; Ferrando-Soria, J.; López-Haro, M.; Hernández-Garrido, J. C.; Oliver-Meseguer, J.; Marini, C.; Boronat, M.; Armentano, D.; Leyva-Pérez, A.; Pardo, E. Soluble/MOF-Supported Palladium Single Atoms Catalyze the Ligand-, Additive-, and Solvent-Free Aerobic Oxidation of Benzyl Alcohols to Benzoic Acids. *J. Am. Chem. Soc.* **2021**, *143*, 2581–2592.
- (53) Grancha, T.; Ferrando-Soria, J.; Cano, J.; Amorós, P.; Seoane, B.; Gascon, J.; Bazaga-García, M.; Losilla, E. R.; Cabeza, A.; Armentano, D.; Pardo, E. Insights into the Dynamics of Grothuss Mechanism in a Proton-Conducting Chiral Bio MOF. *Chem. Mater.* **2016**, *28*, 4608–4615.
- (54) Mon, M.; Bruno, R.; Tiburcio, E.; Casteran, P.-E.; Ferrando-Soria, J.; Armentano, D.; Pardo, E. Efficient Capture of Organic Dyes and Crystallographic Snapshots by a Highly Crystalline Amino-Acid-Derived Metal–Organic Framework. *Chem. – Eur. J.* **2018**, *24*, 17712–17718.
- (55) Pérez-Cejuela, H. M.; Mon, M.; Ferrando-Soria, J.; Pardo, E.; Armentano, D.; Simó-Alfonso, E. F.; Herrero-Martínez, J. M. Bio-Metal–Organic Frameworks for Molecular Recognition and Sorbent Extraction of Hydrophilic Vitamins Followed by Their Determination Using HPLC–UV. *Microchim. Acta* **2020**, *187*, No. 201.
- (56) Yan, Y.; Carrington, E. J.; Pétuya, R.; Whitehead, G. F. S.; Verma, A.; Hylton, R. K.; Tang, C. C.; Berry, N. G.; Darling, G. R.; Dyer, M. S.; Antypov, D.; Katsoulidis, A. P.; Rosseinsky, M. J. Amino Acid Residues Determine the Response of Flexible Metal–Organic Frameworks to Guests. *J. Am. Chem. Soc.* **2020**, *142*, 14903–14913.
- (57) Nagao, Y.; Hirata, T.; Goto, S.; Sano, S.; Kakehi, A.; Iizuka, K.; Shiro, M. Intramolecular Nonbonded S \cdots O Interaction Recognized in (Acylimino)Thiadiazoline Derivatives as Angiotensin II Receptor Antagonists and Related Compounds. *J. Am. Chem. Soc.* **1998**, *120*, 3104–3110.
- (58) Iwaoka, M.; Takamoto, S.; Tomoda, S. Statistical and Theoretical Investigations on the Directionality of Nonbonded S–O Interactions. Implications for Molecular Design and Protein Engineering. *J. Am. Chem. Soc.* **2002**, *124*, 10613–10620.
- (59) Adhikari, U.; Scheiner, S. Substituent Effects on Cl \cdots N, S \cdots N, and P \cdots N Noncovalent Bonds. *J. Phys. Chem. A* **2012**, *116*, 3487–3497.
- (60) Thomas, S. P.; Jayatilaka, D.; Guru Row, T. N. S \cdots O Chalcogen Bonding in Sulfa Drugs: Insights from Multiple Charge Density and X-Ray Wavereflection of Acetazolamide. *Phys. Chem. Chem. Phys.* **2015**, *17*, 25411–25420.
- (61) Hudson, B. M.; Nguyen, E.; Tantillo, D. J. The Influence of Intramolecular Sulfur–Lone Pair Interactions on Small-Molecule Drug Design and Receptor Binding. *Org. Biomol. Chem.* **2016**, *14*, 3975–3980.
- (62) Politzer, P.; Murray, J. S.; Clark, T. Halogen Bonding and Other σ -Hole Interactions: A Perspective. *Phys. Chem. Chem. Phys.* **2013**, *15*, No. 11178.
- (63) Obata, A.; Kawazura, H.; Miyamae, H. Structure of a Novel One-Dimensional Chlorpromazine–Copper(II) Complex Salt, [C $_{17}$ H $_{20}$ ClN $_2$ S $_2$][CuCl $_2$]. *Acta Crystallogr. Sect. C Cryst. Struct. Commun.* **1984**, *40*, 45–48.
- (64) Murray, J. S.; Lane, P.; Politzer, P. Simultaneous σ -Hole and Hydrogen Bonding by Sulfur- and Selenium-Containing Heterocycles. *Int. J. Quantum Chem.* **2008**, *108*, 2770–2781.
- (65) Lin, S.; Wroblewski, S. T.; Hynes, J.; Pitt, S.; Zhang, R.; Fan, Y.; Doweiko, A. M.; Kish, K. F.; Sack, J. S.; Malley, M. F.; Kiefer, S. E.; Newitt, J. A.; McKinnon, M.; Trzaskos, J.; Barrish, J. C.; Dodd, J. H.; Schieven, G. L.; Leftheris, K. Utilization of a Nitrogen–Sulfur Nonbonding Interaction in the Design of New 2-Aminothiazol-5-Yl-Pyrimidines as P38 α MAP Kinase Inhibitors. *Bioorg. Med. Chem. Lett.* **2010**, *20*, 5864–5868.
- (66) Nawaz, A.; Niaz, A.; Ilyas, M.; Shah, S. S. H.; Asi, M. R.; Ahmad, Z. A. Determination and Extraction of Acetamidiprid Residues in Fruits and Vegetables. *Int. J. Food Allied Sci.* **2015**, *1*, 63–66.
- (67) Webb, D. T.; Nagorzanski, M. R.; Powers, M. M.; Cwiertny, D. M.; Hladik, M. L.; LeFevre, G. H. Differences in Neonicotinoid and Metabolite Sorption to Activated Carbon Are Driven by Alterations to the Insecticidal Pharmacophore. *Environ. Sci. Technol.* **2020**, *54*, 14694–14705.
- (68) Mohammad, S. G.; Ahmed, S. M.; Amr, A. E.-G. E.; Kamel, A. H. Porous Activated Carbon from Lignocellulosic Agricultural Waste for the Removal of Acetamidiprid Pesticide from Aqueous Solutions. *Molecules* **2020**, *25*, No. 2339.

Supporting Information (SI) for the manuscript:

**Highly Efficient Removal of Neonicotinoid Insecticides by
Thioether–Based (Multivariate) Metal–Organic
Frameworks**

Cristina Negro,[†] Hector Martínez Pérez-Cejuela,[‡] Ernesto F. Simó-
Alfonso,[‡] Jose Manuel Herrero-Martínez^{*,‡}, Rosaria Bruno,[§] Donatella
Armentano,^{*,§} Jesús Ferrando–Soria^{*,†} and Emilio Pardo^{*,†}

[†]Instituto de Ciencia Molecular (ICMol), Universidad de Valencia, 46980 Paterna, Valencia, Spain.

[‡]Departamento de Química Analítica, Universitat de València, c/Dr. Moliner, 50, 46100 Burjassot, Valencia, Spain.

[§]Dipartimento di Chimica e Tecnologie Chimiche (CTC), Università della Calabria, Rende 87036, Cosenza, Italy

Experimental Section

Materials. All chemicals were of reagent grade quality. They were purchased from commercial sources and used as received.^{1,2} MOFs **1**, **2**, **3** and **4** were prepared as previously reported. Dinuclear precursor complexes $[(\text{Me}_4\text{N})_2\{\text{Cu}_2(\text{S,S})\text{-serimox}\}(\text{OH})_2] \cdot 5\text{H}_2\text{O}$, $[(\text{Me}_4\text{N})_2\{\text{Cu}_2(\text{S,S})\text{-threomox}\}(\text{OH})_2] \cdot 4\text{H}_2\text{O}$, $[(\text{Me}_4\text{N})_2\{\text{Cu}_2(\text{S,S})\text{-methox}\}(\text{OH})_2] \cdot 4\text{H}_2\text{O}$ and $[(\text{Me}_4\text{N})_2\{\text{Cu}_2(\text{S,S})\text{-Mecysmox}\}(\text{OH})_2] \cdot 4\text{H}_2\text{O}$ were prepared as previously reported.²

Physical Techniques: Elemental (C, H, S, N), SEM-EDX and ICP-MS analyses were performed at the Microanalytical Service of the Universitat de València. FT-IR spectra were recorded on a Perkin-Elmer 882 spectrophotometer as KBr pellets. The thermogravimetric analyses were performed on crystalline samples under a dry N_2 atmosphere with a Mettler Toledo TGA/STDA 851^e thermobalance operating at a heating rate of $10\text{ }^\circ\text{C min}^{-1}$. Scanning Electron Microscopy coupled with Energy Dispersive X-ray (SEM/EDX) was carried out with a XL 30 ESEM (PHILIPS) microscope equipped with a home-made EDX energy dispersive x-ray detector. The N_2 adsorption-desorption isotherms at 77 K were carried out on crystalline samples of **5**, **acetamidrid@5** and **thiacloprid@5** with a Micromeritics ASAP2020 instrument. Samples were activated at $70\text{ }^\circ\text{C}$ under reduced pressure (10^{-6} Torr) for 16 h prior to carry out the sorption measurements.

Analytical experiments:

- Instrumentation:

For the solid-phase extraction (SPE) protocols, manifold (VacElut) with twelve positions (Agilent Technologies, Waldbronn, Germany,) and pump for vacuum N938 Laboport (KNF, Freiburg, Germany) were used. For HPLC conditions, an 1100 series

liquid chromatograph (Agilent Technologies) provided with a quaternary pump, a degasser, a thermostated column compartment, an automatic sampler and equipped with diode-array (DAD) detection. Separation was accomplished with a Kinetex EVO C18 (250 × 4.6 mm, 5 μm particle size, Phenomenex). The mobile phases consisted of water (A) and MeCN (B) delivered at 1 mL min⁻¹. Isocratic elution mode was used to achieve the chromatographic separation (74:26 A:B, v/v) during 15 min. The injection volume was 25 μL, no temperature control was needed and the detection wavelength were fixed at 244 and 270 nm.

X-ray crystallographic data collection and structure refinement: Crystals of **5**, **acetamidrid@5** and **thiacloprid@5** were selected and mounted on a MITIGEN holder in Paratone oil, then quickly placed in a nitrogen stream cooled at 100 K in order to extract the best data set avoiding the possible degradation upon desolvation or exposure to air. Nevertheless, crystals of both **acetamidrid@5** and **thiacloprid@5** and samples displayed an outstanding stability at air and room temperature for at least four weeks, as demonstrating by their diffraction patterns measured at 296 K as well, without displaying any important crystal decay. Diffraction data for **5** were collected using synchrotron radiation at I19 beamline of the Diamond Light Source at $\lambda = 0.6889 \text{ \AA}$, whereas for **acetamidrid@5** and **thiacloprid@5** data were acquired on a Bruker-Nonius X8APEXII CCD area detector diffractometer using graphite-monochromated Mo-K α radiation ($\lambda = 0.71073 \text{ \AA}$), as significant beam-damage was observed for both single crystals under synchrotron radiation. Bearing in mind that crystal structure of adsorbates **acetamidrid@5** and **thiacloprid@5** have been obtained measuring on crystals which suffered a single-crystal to single-crystal (SC to SC) process, it is reasonable. The data were processed through xia2 (**5**),³ or SAINT⁴ reduction and SADABS⁵ multi-scan absorption [**acetamidrid@5** and **thiacloprid@5**] software. The

structures were solved with the SHELXS structure solution program, using the Patterson method. The model was refined with version 2018/3 of SHELXL against F^2 on all data by full-matrix least squares.⁶

Indeed, we could measure on **5** at synchrotron, before loading guests, in order to go deep in the point of statistical disorder we observe for the whole series of Multivariate MOFs (MTV-MOFs). In **5**, **acetamiprid@5** and **thiacloprid@5** crystallographic analysis does give superimposed snapshots of reactant dimers averaged in mixed $\{\text{Cu}^{\text{II}}[(\text{S},\text{S})\text{-methox/mecysmox}]\}$ ones. Despite the highest data quality of data set for **5**, measured up to theta 36° (see Table S1), no appreciable variations in the final best model of crystal structure have been achieved for **5**.

In all samples, all non-hydrogen atoms of the networks were refined anisotropically, except some highly dynamically disordered atoms of guest molecules in **acetamiprid@5** and **thiacloprid@5**. For a such kind of single crystals, the lower data quality for adsorbates, embedding highly disordered guest molecules, makes the use of constraints and especially restraints essential. The use of some bond lengths restraints applied on atoms belonging to highly dynamic moieties, especially during the refinements in **acetamiprid@5** and **thiacloprid@5**, has been reasonably imposed and related to the expected thermal motion, likely depending on the large pore's size of the frameworks (FLAT, DFIX, DANG, SIMU, DELU and ISOR). In particular, aminoacidic chains in all the three samples have been systematically refined with restraints on C-C and C-S bond lengths. In the refinement of **acetamiprid@5** and **thiacloprid@5** crystal structures, some further restraints, to make the refinement more efficient, have been applied. For instance, ADP components have been restrained to be similar to other related atoms, using SIMU 0.04 for disordered sections or EADP for group of atoms of the guest molecules expected to have essentially similar ADPs. In **5**,

all the hydrogen atoms of the networks were set in calculated position and refined isotropically using the riding model. As far as for **acetamiprid@5** and **thiacloprid@5** crystal structure's refinement is concerned, hydrogen atoms on the guest molecules, and for found solvent lattice molecules were neither found nor calculated. Furthermore, while in **acetamiprid@5** they were calculated for the network, in **thiacloprid@5**, due to the impressive statistical disorder, other than dynamical one, where not defined neither for network nor for the guest molecules. In fact, it is often expected that guest molecules are severely disordered, as a direct consequence of their high thermal motion and also exhibited statistic disorder.

As reported in main text as well, the oxamidato-bridged dicopper(II) units of $\{\text{Cu}^{\text{II}}_2[(\text{S,S})\text{-mecysmox}]\}$ and $\{\text{Cu}^{\text{II}}_2[(\text{S,S})\text{-methox}]\}$ inserted with a 1:1 ratio in **5** exhibit a statistically disorder in the crystal structure (Figure S1, inset), where the very similar percentage of mecysmox and methox leads to a completely superimposed snapshot of mixed $\{\text{Cu}^{\text{II}}_2[(\text{S,S})\text{-methox/mecysmox}]\}$ dimers, synchrotron measurements on **5** sample unveiled the same issue for its crystal structure. In fact, such disorder gives a mixed view of **5**, understandable considering that a crystal structure is the *spatial average*, of all molecules/fragments, together with all their possible orientations averaged, in the crystal *via* only one unit cell. It should be also underlined that our best model has taken into account the most persistence conformations –within the additional complication– that even a low percentage, not taken into account, such as a 10% of a whole pesticides guest molecule, is still a significant amount of electron density, and whole-molecule disorder lurks everywhere in the inky shadows of structure refinement, affecting quality of the model.

Both in **acetamiprid@5** and **thiacloprid@5** the occupancies of the guests in the pores, have been defined by ICP-MS analyses and, in the crystal structure, fixed at

0.333. We strongly believe that it is the more reliable way to accurately define loading instead of taking into account merely thermal factors, which can be affected by a lot of issues above all severe disorder.

In **acetamidrid@5**, acetamidrid guest molecules are statistically disordered exhibiting three set of possible orientations of the guest molecules as detailed in Figure S8 and S12. Similarly, in **thiacloprid@5**, thiacloprid pollutants are severely thermally and statistically disordered (Figure S10 and S13), which is probably related to the different degrees of freedom, related to diverse possible conformations. This fact imposed to block atoms N3L, N4L, C11L and C1I terminal groups during the final refinement. In particular, the partial overlap between different orientations at atom sites, in both adsorbate structures, make them disordered with carbon and nitrogen sites (see Figures S8, S10, S12 and S13).

The contribution to the diffraction pattern from the highly disordered solvent molecules in **5**, located in the voids, was subtracted from the observed data through the SQUEEZE method, implemented in PLATON.⁷

Finally, the estimated empty volumes for **5**, **thiacloprid@5** and **acetamidrid@5** without the crystallization water molecules is 1233.2 (1), 829.6 (2) and 379.7 (3) Å³, values which represent *ca.* 34.6, 22.6 and 10.3 %, respectively, of potential void per unit cell volume [$V = 3562.68(3)$, $3672.6(2)$ and $3679.5(3)$ Å³]. In accordance with BET and SCXRD analysis, the channels of **5** are entirely filled by organic molecular guests with the help of solvent molecules.

A summary of the crystallographic data and structure refinement for the three compounds is given in Table S2. The comments for the alerts A and B are reported in the CIFs using the validation response form (vrf). CCDC reference numbers are 2072807-2072809 for **5**, **acetamidrid@5** and **thiacloprid@5**, respectively.

The final geometrical calculations on free voids and the graphical manipulations were carried out with PLATON⁷ implemented in WinGX,⁸ and CRYSTAL MAKER⁹ programs, respectively.

Table S1. Molecular structures of NEOs and their water/octanol partition coefficients.

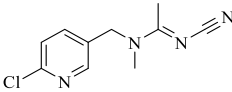
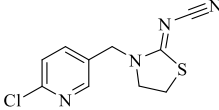
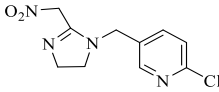
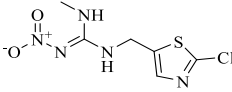
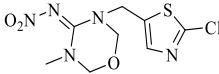
Name	Structure	Log P
Acetamiprid		0.80
Thiacloprid		1.26
Imidacloprid		0.57
Clothianidin		0.70
Thiamethoxan		-0.13

Table S2. Summary of Crystallographic Data for **5**, **acetamidrid@5** and **thiacloprid@5**

Compound	5	acetamidrid@5	thiacloprid@5
Formula	C ₃₃ H ₁₁₈ SrCu ₆ N ₆ O ₅₇ S ₆	C ₄₃ H ₇₅ SrCu ₆ ClN ₁₀ O ₃₀ S ₆	C ₄₃ H ₉₁ SrCu ₆ ClN ₁₀ O ₃₉ S ₇
<i>M</i> (g mol ⁻¹)	2172.55	1908.80	2100.98
λ (Å)	0.6889	0.71073	0.71073
Crystal system	hexagonal	hexagonal	hexagonal
Space group	<i>P</i> 6 ₃	<i>P</i> 6 ₃	<i>P</i> 6 ₃
<i>a</i> (Å)	17.82070(5)	18.0282(8)	18.0090(8)
<i>c</i> (Å)	12.95380(6)	13.0723(8)	13.0756(8)
<i>V</i> (Å ³)	3562.68(2)	3679.5(4)	3672.6(4)
<i>Z</i>	2	2	2
ρ_{calc} (g cm ⁻³)	2.025	1.723	1.900
μ (mm ⁻¹)	2.478	2.710	2.761
<i>T</i> (K)	100	100	100
θ range for data collection (°)	1.989 to 36.049	2.032 to 26.224	2.262 to 26.161
Completeness to $\theta = 25.0$	100%	100%	100%
Measured reflections	78315	50563	43839
Unique reflections (Rint)	11771 (0.0433)	4941 (0.0569)	4918 (0.0567)
Observed reflections [<i>I</i> > 2 σ (<i>I</i>)]	6217	3812	3629
Goof	0.981	1.075	1.575
Absolute structure parameter (Flack)	0.39(2)	0.44(2)	0.41(2)
<i>R</i> ^a [<i>I</i> > 2 σ (<i>I</i>)] (all data)	0.0574 (0.0929)	0.0835 (0.1060)	0.0693 (0.0949)
<i>wR</i> ^b [<i>I</i> > 2 σ (<i>I</i>)] (all data)	0.1847 (0.1718)	0.2488 (0.2761)	0.2149 (0.2274)
CCDC	2072807	2072808	2072809

$$^a R = \sum(|F_o| - |F_c|) / \sum |F_o|, \quad ^b wR = [\sum w(|F_o| - |F_c|)^2 / \sum w |F_o|^2]^{1/2}.$$

Table S3. Removal values for NEOs from 1 mg L⁻¹ of aqueous samples using different BioMOFs (n=3).

Neonicotinoids	Removal of different BioMOFs (%)				
	MOF-1	MOF-2	MOF-3	MOF-4	MOF-5
Thiamethoxam	2	11	20	10	36
Clothianidin	16	11	32	33	69
Imidacloprid	17	12	37	28	68
Acetamiprid	17	11	69	90	98
Thiacloprid	22	14	90	96	99

Experimental conditions: loading 1 mL of aqueous standards with 1 mg L⁻¹ of each contaminant, washing 1 mL of water and elution 5 mL of MeOH. The removal was quantified, after filtrating with nylon membrane 0.22 µm, by HPLC-UV.

Table S4. NEOs removal efficiencies¹ from river water using **MOF-3-5** (n=3).

Neonicotinoids	Removal of different BioMOFs (%)		
	MOF-3	MOF-4	MOF-5
Thiamethoxam	21	34	58
Clothianidin	45	42	77
Imidacloprid	40	42	78
Acetamiprid	96	77	100
Thiacloprid	99	95	100

¹Data obtained from Figure S6.

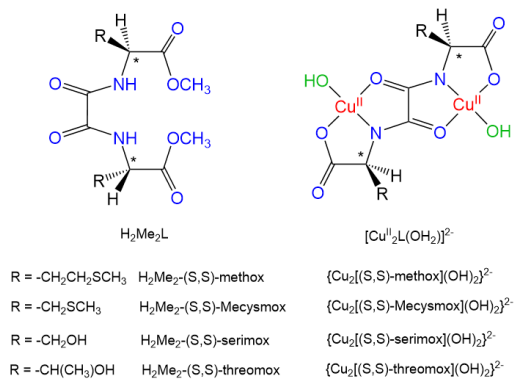
Experimental conditions: loading 1 mL of river water spiked with 5 mg L⁻¹ of each contaminant, washing 1 mL of water and elution 5 mL of MeOH. The removal was quantified, after filtrating with nylon membrane 0.22 µm, by HPLC-UV.

Table S5. Precision shown as maximum relative standard deviation of different BioMOFs as SPE sorbents in the analysis of NEOs.

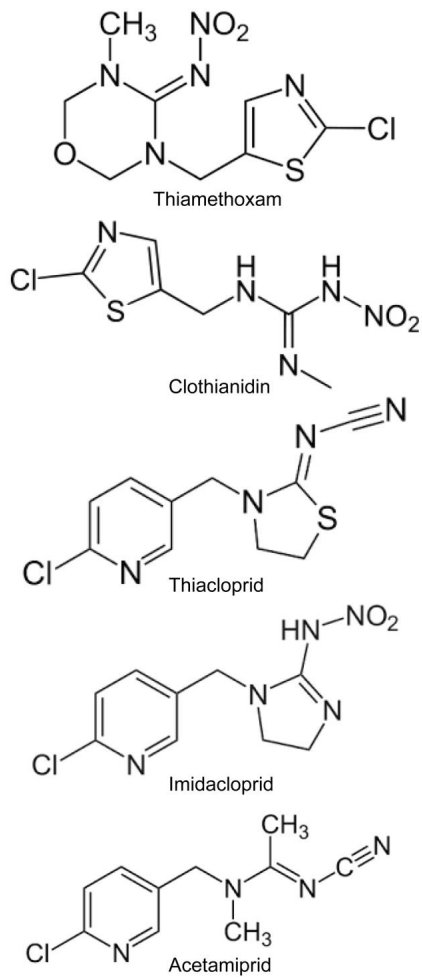
Compound	Precision, RSD (n=3)	
	Intra-device ^a	Inter-device
Thiamethoxam	2.3; 5.3	7.9
Clothianidin	4.0; 7.7	8.0
Imidacloprid	3.5; 7.5	8.6
Acetamiprid	4.2; 6.0	7.2
Thiacloprid	2.1; 3.9	6.7

^aAs intra- and inter-day RSD (n = 3)

The procedure was carried out using 1 mL of standard mixture (1 mg L⁻¹) of each NEO and the removal was quantified, after filtrating with nylon membrane 0.22 µm, by HPLC-UV.



Scheme S1. Chemical structures of the chiral bis(amino acid)oxalamide ligands (left), highlighting the potential coordination sites and chiral centers (*) and the corresponding dianionic bis(hydroxo) dicopper(II) complexes (right).



Scheme S2. Chemical structures of the neonicotinoids thiacloprid, acetamiprid, clothianidin, imidacloprid and thiamethoxam.

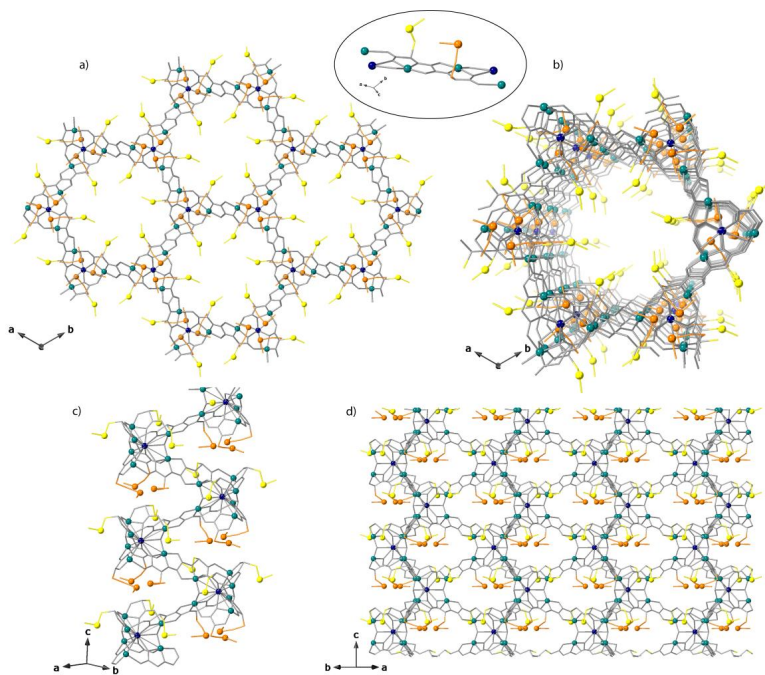


Figure S1. View down c axis of the porous structure of $\{\text{Sr}^{\text{II}}\text{Cu}^{\text{II}}[(S,S)\text{-methox}]_{1.50}[(S,S)\text{-Mecysmox}]_{1.50}(\text{OH})_2(\text{H}_2\text{O})\} \cdot 36\text{H}_2\text{O}$ **5**. (a) Perspective view along c crystallographic axis of a single channel of the MTV-MOF **5**. (b) Views along $[111]$ direction of (c) the chiral rods and (d) a portion of the porous crystal structure of MTV-MOF **5**. The crystallization water molecules are omitted for clarity. The inset shows the superimposed snapshot of mixed $\{\text{Cu}^{\text{II}}_2[(S,S)\text{-methox/mecysmox}]\}$ dimers, on which crystallographic model of **5** is based. Organic ligands are depicted as gray sticks, whereas the amino acid residues are represented with the following color code: $-\text{CH}_2\text{SCH}_3$ (yellow) and $-\text{CH}_2\text{CH}_2\text{SCH}_3$ (orange). Strontium, copper, and sulfur atoms are shown as blue, cyan, and yellow (for methionine fragment)/orange (for methionine fragment) spheres, respectively.

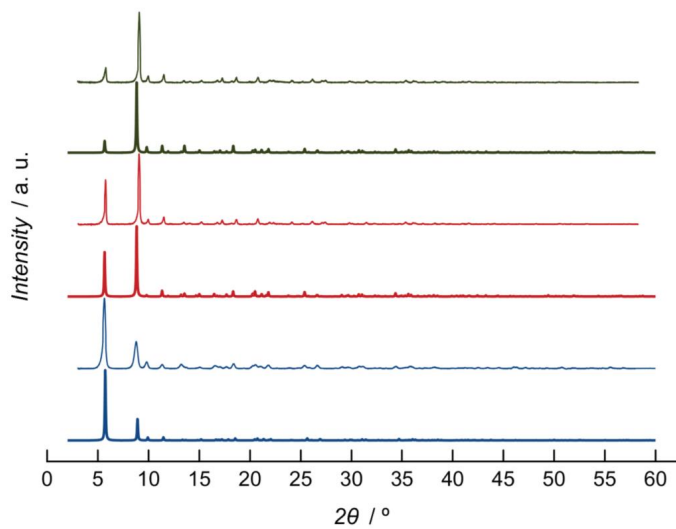


Figure S2. Theoretical (bottom) and experimental (top) PXRD patterns of **5** (blue), **acetamidrid@5** (red) and **thiacloprid@5** (green) in the 2.0–60.0°.

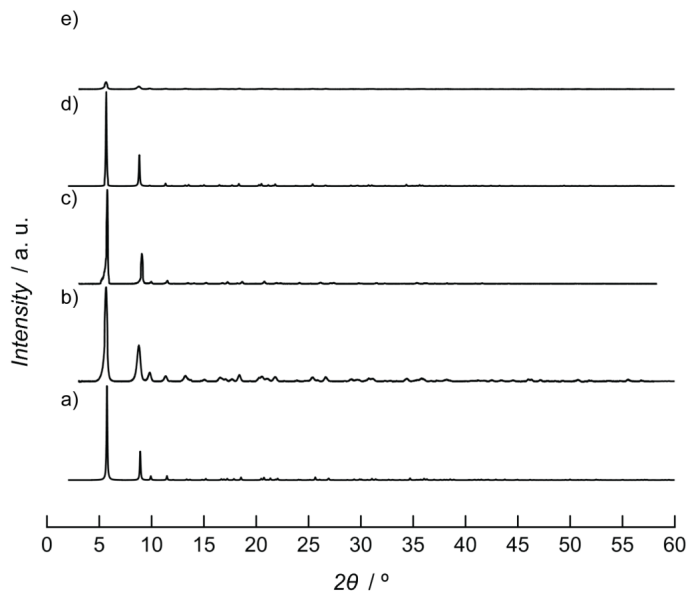


Figure S3. (a), Calculated PXRD pattern profile of **5**. PXRD pattern profiles of **5** after 48 h immersed in pH = 7 (b), pH = 12 (c), pH = 5 (d) and pH = 2 (e) aqueous solutions in the 2.0–60.0°.

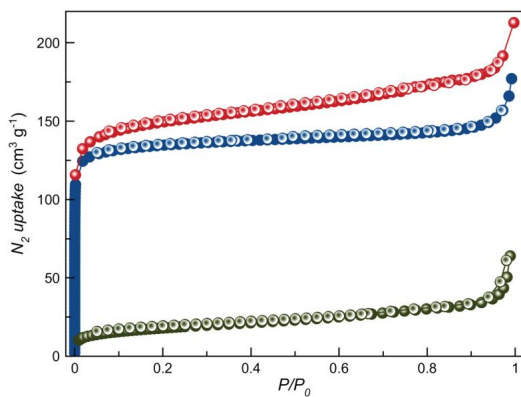


Figure S4. N_2 (77 K) adsorption isotherms for the activated compounds **3** (green), **4** (red) and **5** (blue). Filled and empty symbols indicate the adsorption and desorption isotherms, respectively. The samples were activated at 70 °C under reduced pressure for 16 h prior to carry out the sorption measurements.

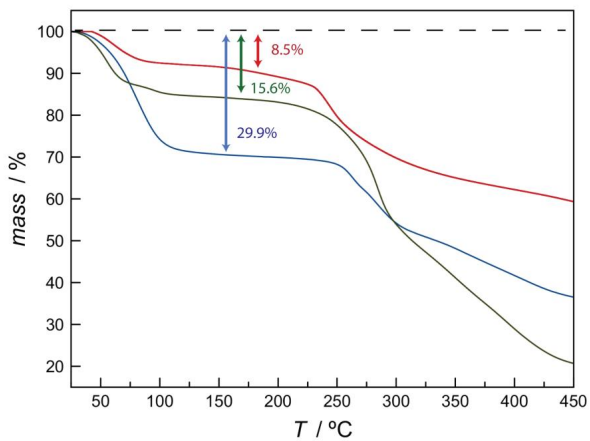


Figure S5. Thermo-Gravimetric Analysis (TGA) of **5** (blue), **acetamidrid@5** (red) and **thioclopid@5** (green) under dry N₂ atmosphere.

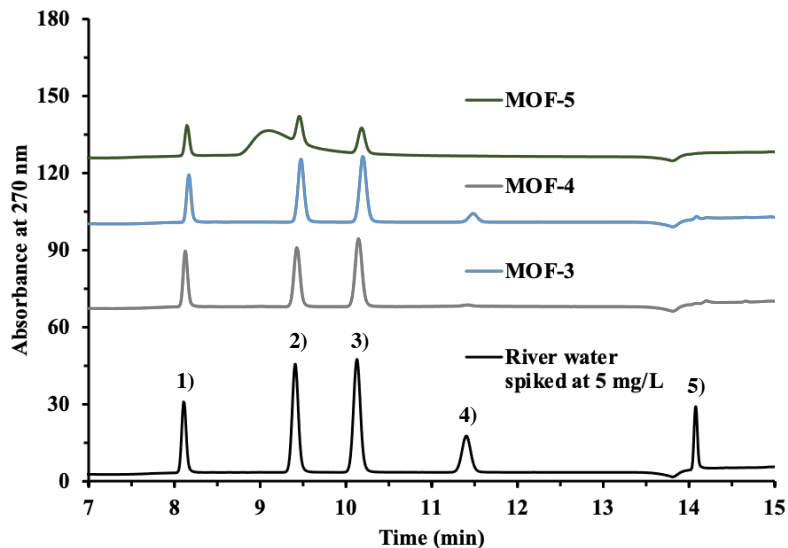


Figure S6. HPLC-DAD chromatograms from a river water spiking at 5 mg L^{-1} of each analyte without SPE treatment (black line) and with SPE treatment (grey, blue and green lines). Chromatographic details are given in the Experimental and Supplementary Section. Peak identification: 1) thiamethoxan; 2) clothianidin; 3) imidacloprid; 4) acetamiprid and 5) thiacloprid.

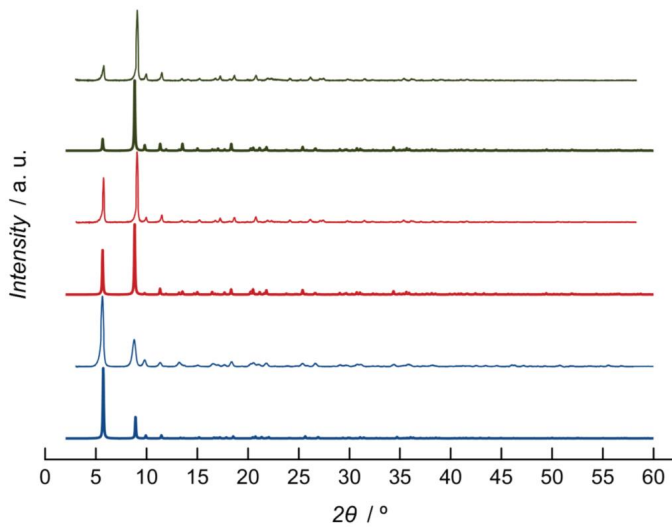


Figure S7. Theoretical (bottom) and experimental (top) PXR D patterns of **3** (blue), **4** (red) and **5** (green), after 10 sorption-desorption cycles in the 2.0–60.0° range.

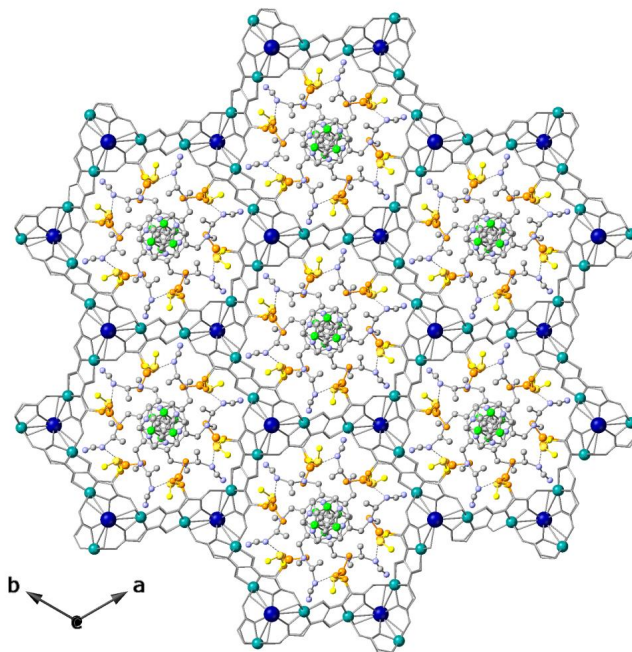


Figure S8. View of the crystal structure of **acetamiprid@5** along the c axis (the crystallization water molecules are omitted for clarity) undoubtedly showing pores filled by acetamiprid molecules as guests. Organic ligands of the network are depicted as gray sticks, whereas the amino acid residues are represented with the following color code: $-\text{CH}_2\text{SCH}_3$ (yellow) and $-\text{CH}_2\text{CH}_2\text{SCH}_3$ (orange). Guest molecules are depicted as balls and sticks with carbon grey, nitrogen light blue and chlorine green. Strontium, copper, and sulfur atoms are shown as blue, cyan, and yellow (for methionine fragment)/orange (for methionine fragment) spheres, respectively.

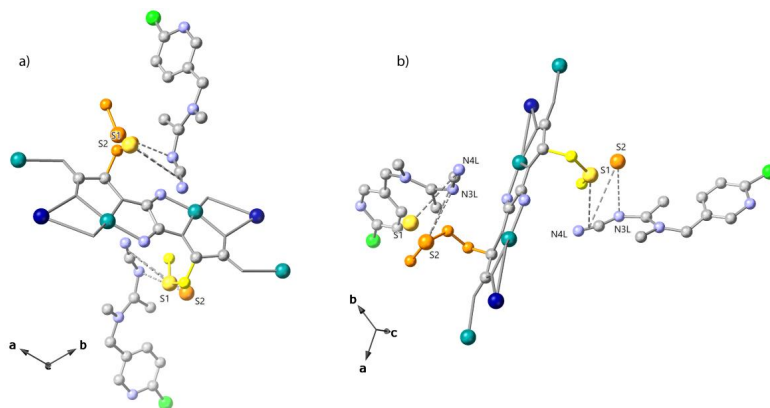


Figure S9. Details of host-guest interactions along *c* axis (a) and channel's propagation direction (b) in **acetamidrid@5**, unveiled by single crystal X-ray analysis. The $S \cdots N$ -CN involving only methionine residues [$S \cdots N$ distances of 3.18(1) Å] and $S \cdots$ nitrile interactions, involving both kind of *arms* blocking acetamidrid terminal moieties [$S \cdots CN_{\text{Centroid}}$ distances of 3.67(1) and 3.82(1) Å, for methyl-cysteine and methionine residues, respectively] are depicted with dashed lines. Organic ligands of the network and guest molecules are depicted as ball and sticks with carbon grey, nitrogen light blue and chlorine green. Strontium, copper and sulfur atoms are shown as blue, cyan and yellow (for methylcysteine fragment)/orange (for methionine fragment) spheres, respectively. The amino acid residues are represented with the following color code: $-\text{CH}_2\text{SCH}_3$ (yellow) and $-\text{CH}_2\text{CH}_2\text{SCH}_3$ (orange).

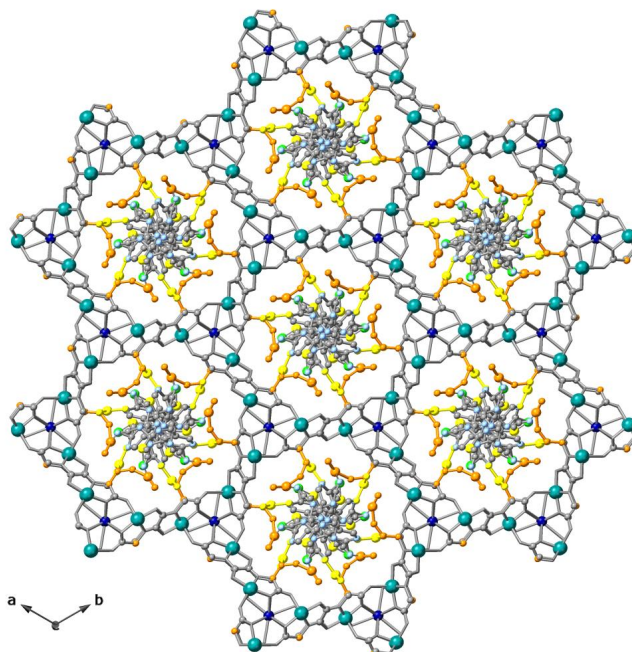


Figure S10. View of the crystal structure of **thiacloprid@5** along the *c* axis (the crystallization water molecules are omitted for clarity) markedly showing pores filled by thiacloprid molecules as guests. Organic ligands of the network are depicted as gray sticks whereas the amino acid residues are represented with the following color code: $-\text{CH}_2\text{SCH}_3$ (yellow) and $-\text{CH}_2\text{CH}_2\text{SCH}_3$ (orange). Guest molecules are depicted as balls and sticks with carbon grey, nitrogen light blue and chlorine green. Strontium, copper, and sulfur atoms are shown as blue, cyan and yellow (for methionine fragment)/orange (for methionine fragment) spheres, respectively.

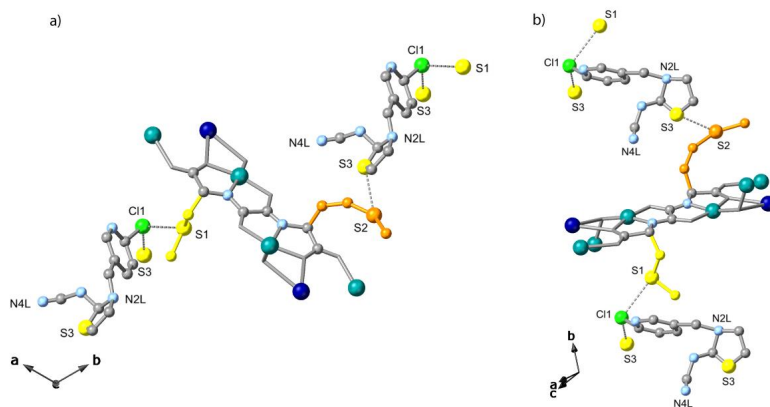


Figure S11. Details of host-guest interactions in **thiacloprid@5**, unveiled by single crystal X-ray analysis. The $S\cdots Cl$ interaction [distance of 3.10(1) Å] and the interactions of the type $S\cdots S$ held with thiazolidine ring of pollutants molecules at a $S\cdots S$ distance of 2.76(1) Å, are depicted with dashed lines. Strontium, copper, and sulfur atoms are shown as blue, cyan and yellow (for methylcysteine fragment)/orange (for methionine fragment) spheres, respectively.

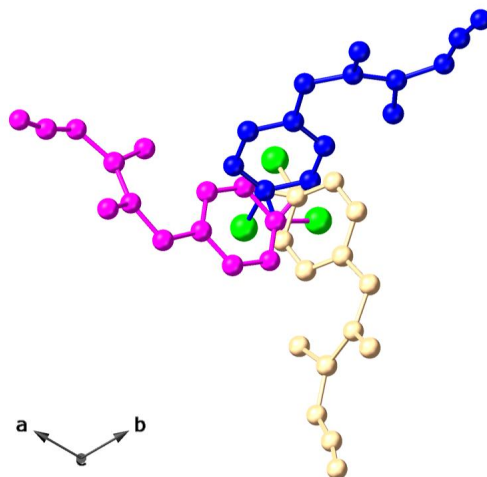


Figure S12. Details of disordered acetamidiprid guest's molecule. The three sets of different conformations allowed by $P6_3$ space group, are depicted in purple, blue and amber, respectively.

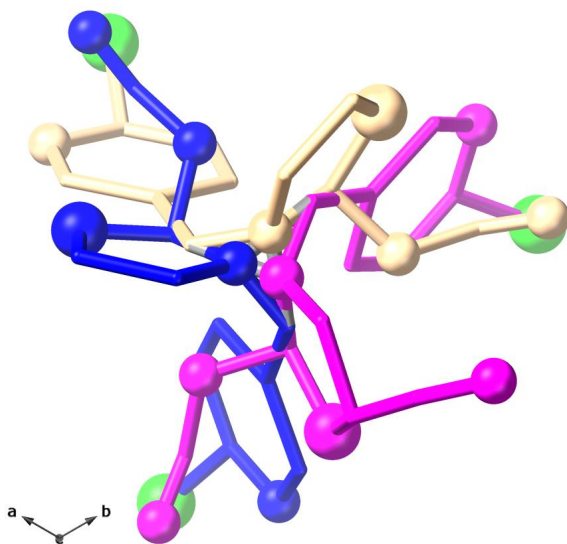


Figure S13. Details of disordered thiacloprid guest's molecules. The three sets of different conformations allowed by $P6_3$ space group, are depicted in purple, blue and amber, respectively.

References

- (1) (a) M. Mon, R. Bruno, J. Ferrando-Soria, L. Bartella, L. Di Donna, M. Talia, R. Lappano, M. Maggiolini, D. Armentano, E. Pardo, *Mater. Horizons* **2018**, *5*, 683–690. (b) M. Mon, R. Bruno, R. Elliani, A. Tagarelli, X. Qu, S. Chen, J. Ferrando-Soria, D. Armentano, E. Pardo, *Inorg. Chem.* **2018**, *57*, 13895–13900.
- (2) (a) E. Tiburcio, R. Greco, M. Mon, J. Ballesteros-Soberanas, J. Ferrando-Soria, M. López-Haro, J. C. Hernández-Garrido, J. Oliver-Meseguer, C. Marini, M. Boronat, et al., *J. Am. Chem. Soc.* **2021**, *143*, 2581–2592. (b) H. M. Pérez-Cejuela, M. Mon, J. Ferrando-Soria, E. Pardo, D. Armentano, E. F. Simó-Alfonso, J. M. Herrero-Martínez, *Microchim. Acta* **2020**, *187*, 201. (c) M. Mon, J. Ferrando-Soria, T. Grancha, F. R. Fortea-Pérez, J. Gascon, A. Leyva-Pérez, D. Armentano, E. Pardo, *J. Am. Chem. Soc.* **2016**, *138*, 7864–7867. (d) M. Mon, F. Lloret, J. Ferrando-Soria, C. Martí-Gastaldo, D. Armentano, E. Pardo, *Angew. Chemie Int. Ed.* **2016**, *55*, 11167–11172.
- (3) (a) Evans, P. Selaing and assessment of data quality. *Acta Cryst. D* **62**, 72–82 (2006). (b) Evans, P. R., Murshudov, G. N. How good are my data and what is the resolution?. *Acta Cryst. D* **69**, 1204–1214 (2013). (c) Winn, M. D.; Ballard, C. C.; Cowtan, K. D.; Dodson, E. J.; Emsley, P.; Evans, P. R.; Keegan, R. M.; Krissinel, E. B.; Leslie, A. G. W.; McCoy, A.; McNicholas, S. J.; Murshudov, G. N.; Pannu, N. S.; Potterton, E. A.; Powell, H. R.; Read, R. J.; Vagin, A.; Wilson K. S. Overview of the *CCP4* suite and current developments. *Acta Cryst. D* **67**, 235–242 (2011). (d) Winter, G. *xia2*: and expert system for macromolecular crystallography data reduction. *J. Appl. Cryst.* **43**, 186–190 (2010). (e) Winter, G.; Waterman, D. G.; Parkhurst, J. M.; Brewster, A. S.; Gildea, R. J.; Gerstel, M.; Fuentes-Montero, L.; Vollmar, M.; Michels-Clark, T.; Young, I. D.; Sauterb, N. K.; Evans, G. *DIALS*: implementation and evaluation of a new integration package *Acta Cryst.* **2018**, *D74*, 85–97
- (4) SAINT, version 6.45, Bruker Analytical X-ray Systems, Madison, WI, 2003.
- (5) Sheldrick G.M. SADABS Program for Absorption Correction, version 2.10, Analytical X-ray Systems, Madison, WI, 2003.
- (6) (a) Sheldrick, G. M. Crystal structure refinement with SHELXL. *Acta Cryst. C* **71**, 3–8 (2015). (b) Sheldrick, G. M. A short history of SHELX. *Acta Cryst. A* **64**, 112–122 (2008). (c) SHELXTL-2013/4, Bruker Analytical X-ray Instruments, Madison, WI, 2013.
- (7) (a) Spek, A. L. *PLATON SQUEEZE*: a tool for the calculation of the disordered solvent contribution to the calculated structure factors. *Acta Crystallogr. Sect. C-Struct. Chem.* **71**, 9–18 (2015). (b) Spek, A. L. Structure validation in chemical crystallography. *Acta Crystallogr. Sect. D, Biol. Crystallogr.* **65**, 148–155 (2009).
- (8) Farrugia, L. J. *WinGX* suite for small-molecule single-crystal crystallography. *J. Appl. Crystallogr.* **32**, 837–838 (1999).
- (9) Palmer, D. CRYSTAL MAKER, Cambridge University Technical Services, C. No Title, 1996.

